Lone Pair Ordering in Mixed Valence Oxide Perovskites and Superconductors

Jiale (Lance) Zhang

A thesis submitted to The University of Sydney in partial fulfilment of the requirements for the degree of:

Master of Philosophy (Science)

School of Chemistry

The University of Sydney

December 2025

Declaration of Authorship

I, Jiale Zhang, declare that this thesis entitled “Lone Pair Ordering in Mixed Valence Oxide Perovskites and Superconductors”, and the work presented herein, is my own except where otherwise acknowledged. During the preparation of this work, author used Copilot for the purposes of text enhancement.

Jiale Zhang – December 2025

Statement of Authorship Attribution

This dissertation fulfils the requirements for the degree of Master of Philosophy at the School of Chemistry, Faculty of Science, The University of Sydney. The research presented herein was conducted under the primary supervision of **Professor Brendan J. Kennedy** (School of Chemistry, The University of Sydney) from March 2024 to August 2025.

Projects in this work investigated the structure-property change within perovskite materials. The following work established with contributions:

Chapter 3 and **Chapter 4** describes studies of undoped and Pb-doped $BaBiO_3$. This work was conceptualised under the guidance of **Professor Brendan Kennedy** and **Dr. Frederick Marlton**.

- I performed the synthesis of all pristine and their doped derivatives.
- I conducted all conventional X-ray diffraction and STOE measurements. Synchrotron X-ray powder diffraction data were collected jointly by myself and **Professor Brendan Kennedy**, with operational support from beamline scientists at the Australian Synchrotron.
- Neutron total scattering data were acquired on the NOMAD and POWGEN beamlines at the Spallation Neutron Source (Oak Ridge National Laboratory, USA) under the scientific guidance of **Dr. Matt Tucker** and **Dr. Cheng Li**.
- I performed the primary data analysis and interpretation with intellectual and technical support from **Professor Brendan Kennedy**, **Dr. Frederick Marlton**, and **Mr. Caleb J. Bennett**.

Chapter 5 in this dissertation was published as the manuscript:

- Jiale Zhang; Sophie Fletcher; Wen Liang Tan; Fred Marlton; **Brendan J. Kennedy**. Structural Study of $Cs_2AgBiBr_6$ Double Perovskite. *Journal of Solid State Chemistry*, **2026**, 353, 125668.

This study was designed with help of Professor Brendan Kennedy.

- $Cs_2AgBiBr_6$ and other halide A_2AgBiX_6 (A = Rb, Cs; X = Cl; Br) was synthesized by myself.
- I performed all conventional X-ray diffraction and STOE measurements.
- Synchrotron X-ray powder diffraction data were collected by myself, **Ms. Sophie Fletcher**, and **Professor Brendan Kennedy**, under the guardianship of beamline scientist **Dr. Wen Liang Tan** at the Australian Synchrotron.
- Data analyses were conducted by **Professor Brendan Kennedy** and **Dr. Fred Marlton**.

Acknowledgements

The research presented in this Master's dissertation represents the culmination of extensive data refinement, simulation, and analysis. It is beyond doubt that without the support of many individuals and institutions, I could not have completed this academic journey.

First and foremost, I would like to express my deepest gratitude to my academic supervisor, **Professor Brendan Kennedy**, for his precise academic guidance and his meticulous responses to every question I posed. Throughout my Honour and postgraduate studies, his profound expertise has been instrumental in helping me overcome numerous challenges, while his objective and professional insights have shaped my ability to analyse and plan future work. His amiable personality and sense of humor have introduced me to a unique academic atmosphere. The very first English phrase that left a deep impression on me was "walking encyclopedia"—a description that, I believe, perfectly captures Brendan's breadth of knowledge and cultural perspective. It is difficult to fully express this brief expression of thanks can hardly encapsulate my deep-seated admiration for three years of mentorship.

I would also like to express my thanks to secondary academic supervisor, **Dr. Fred Marlton**. Although we have only worked together for less than a year, I have learned a great deal about PDF from him. I am extremely grateful for his help and encouragement. Due to the language barrier, it takes me more time to embrace new things. Fred's encouragement has helped me build confidence in learning PDF theory and conducting analysis. I cherish the casual conversation over a cup of coffee before meetings. Moreover, I sincerely hope I could have other research opportunities to continue our collaboration in future.

To **Solid State Chemistry Research Group**, the University of Sydney, I express my sincere gratitude to this research group for providing an academic environment that felt like home for three years. I am grateful to **Professor Chris Ling** as group leader for his professional feedback and thoughtful organization of our group meetings. Thank **Professor Sigegbert Schmid** for providing suggestions from different perspectives on my research work. I am also grateful to **Ms. Maria Nicholas** for her help as my "mentor" when I first joined the group in terms of

experiments and mental health. I also thank **Mr. Caleb Bennett** and **Dr. Bryce Mullen** for their assistance in data processing and analysis. Also thank to other members in group helped me understanding the meaning of "academic sibling". **Thanks to Dr. Alex Brown, Ms. Mia Brennan, Mr. Ahmadi (Didi) Permana, Mrs. Mueerah Almohareb, Ms. Mariá Sanchez, Ms. Yan Zheng, Mr. Artem Moskin, Ms. Kaylee Clark, Mr. Hao Chai** and **Ms. Sophie Fletcher**. I will always value the sense of belonging this group has given me, just as I missed home when I first travelled alone to Australia in 2017.

In addition, I would like to express my gratitude to the institution that has collaborated on my research project. My special thanks to **Professor Maxim Avdeev** from ANSTO for providing high-quality NPD data. Thanks to Oak Ridge National Laboratory, particularly indebted to **Dr. Yuanpeng Zhang** for his insightful RMC analysis approach, which gives us inspiration for investigation of mixed valence perovskites. I gratefully acknowledge the support from Australia Synchrotron for the halide double perovskite project and extend my appreciation to **Dr. Wen Liang Tan** for his invaluable assistance in synchrotron data collection and expert recommendations.

I am also deeply grateful to **Dr. René Macquart** from School of Chemistry, the University of Sydney for his assistance with the thermophysical instruments and providing essential guidance on PPMS during my Honours studies, it laid the foundation for my understanding of magnetic materials. Furthermore, I wish to acknowledge **Dr. Samuel Duyker**, **Dr. Paul Fitzgerald** and **Dr. William Lewis** from Sydney Analytical for their upkeep instruments meticulously and patient troubleshooting during every experimental session.

I would also like to acknowledge and thanks all scholarships funding and awards to supportive during my postgraduate degree. The *Postgraduate Research Support Scheme* (USYD), the *Society of Crystallographers in Australia and New Zealand* (SCANZ) for *Maslen Award*, the travel bursary to attend Crystal 35 in Perth, Australia, to Oak Ridge National Laboratory for *Neutron Beam Award at Spallation Neutron Source* (SNS).

Beyond my academic journey in Australia for past 8 years, I would like to express my deepest gratitude to my friends who provided unwavering encouragement and encouragement and support during my most challenging times. Thanks to my host, **Ms. Kirsten** offered invaluable

guidance during a period of academic difficulty; Thanks to my housemate **Yonghui Yun** for graciously provided me with temporary shelter in both initial and final year of my stay in Sydney.

At last, but not least, I would like to express my profound gratitude to my parents for their unwavering and selfless support of all my passionate pursuits. My deepest appreciation also goes to my wife, **Mrs. Weiwei Li**, for her decade-long steadfast companionship. With my academic endeavors in Australia now successfully concluded, a new chapter of life is about to commence.

Table of Contents

List of Figures

Chapter 1 Introduction

List of Tables

List of Abbreviations

Abbreviation	Definition
2D	Two Dimensions
3D	Three Dimensions
ADP	Atomic Displacement Parameter
ANSTO	The Australian Nuclear Science and Technology Organization
BCS	Bardeen–Cooper–Schrieffer theory
BVS	Bond Valence Sum
CD	Charge Disproportionation
CDW	Charge Density Wave
CMR	Colossal Magnetic Resistance
CO	Charge Ordering
CIF	Crystallographic Information File
DFT	Density Functional Theory
DoS	Density of States
FWHM	Full Width at Half Maximum
HTS	High-temperature Superconductor
ICSD	Inorganic Crystal Structural Database
LBCO	Lanthanum Barium Copper Oxide
LED	Light-Emitting Diode
MOS	Metal-oxide Semiconductors
NPD	Neutron Powder Diffraction
NPDF	Neutron Pair Distribution Function
NOMAD	Nanoscale-Ordered Materials Diffractometer
OIHP	Organic-inorganic Halide Perovskites
ORNL	Oak Ridge National Laboratory

PCE	Powder Conversion Efficiency
PDF	Pair Distribution Function
PDFgui	Powder Diffraction File Graphical User Interface
POWGEN	Powder Diffractometer BL-11A
PXRD	Powder *X*-ray Diffraction
PSC	Perovskite Solar Cell
RMC	Reverse Monte Carlo
SOC	Spin–orbit Coupling
SOFC	Solid-Oxide Fuel Cell
SXRD	Synchrotron X-Ray Diffraction
TI	Topological Insulators
ToF	Time-of-Flight
TOPAS	Total PAttern Solution
VESTA	Visualization for Electronic and STructural Analysis
XAS	X-ray Absorption Spectroscopy
XRD	X-Ray Diffraction

Abstract

$BaBiO_3$, as one of the most extensively studied oxide perovskites, exhibits numerous unexpected physical properties. The current scientific interest in $BaBiO_3$ centers on the influence of charge disproportionation on the symmetryand electronic properties. Bismuth is an example of a valence-skipping element, where the lower Bi^{3+} valence state has a $6s^2$ lone pair of electrons. These lone pair electrons can be stereochemically active and can modify the electronic structure of the material. Lone pair bearing cations are important for a wide range of functional materials, such as perovskite photovoltaics, ferroelectrics and thermoelectrics.

A wide range of chemical substitutions have been reported for Bismuth containing perovskites The extremely low toxicity of Bi makes this attractive across various fields. while exhibiting. The broad applicability of bismuth-based material is reflected in the significant research interest these attract. However, the structure-property relationship in substituted $BaBiO_3$, remains poorly understood. A local-scale distortions of structure that are “unseen” in the long-range average structure.

This dissertation describes investigations of $BaBiO_3$ and of its lead-doped counterparts, aiming to elucidate the relationship between charge disproportionation and structural change. To characterize the long-range average structures of these materials with varying temperatures, powder neutron diffraction data collected using the time-of-flights diffractometers NOMAD and POWGEN was analysed using the Rietveld method. These analyses were followed by neutron total scattering analysi,s from data measured on the same instruments, to obtain short-range local structural information, using pair distribution function methods.

The structure change of $BaBiO_3$ was observed, through variable temperature Rietveld refinement against neutron Bragg peak data. $BaBiO_3$ undergoes a number of phase transitions: $P2_1/n$ (~ 140 K)→ $I2/m$ (~ 405 K)→ $R\bar{3}$ (~ 750 K) → $Fm\bar{3}m$. During the phase transition process, the refinement results of $BaBiO_3$ were generally consistent with previous reports, wherein the unusual behavior of Bi-O bond length in the rhombohedral space group is attributed to the tilt angles formed by distinct BiO_6 octahedra. The variable-temperature

NPDF data indicates that bond length between Bi^{3+} and O atoms, represented as the first neighbouring peak ~ 2.2 Å becomes less distinct with temperature upon, and exhibits pronounced dynamic driven distortion.

The series of doped oxide perovskite $BaBi_{1-x}Pb_xO_3$ with $0 \leq x \leq 0.3$ were synthesized and the he structure distortion that occurred upon the addition of Pb resulted in a sequence of phase transitions identified as: *I*2/*m* (x = 0, 0.05, 0.1, 0.15, 0.2) → *Ibmm* (x = 0.25, 0.3), though Rietveld refinement against neutron Bragg peak data. The initial peak position of doublet for $BaBi_{0.9}Pb_{0.1}O_3$ observed in NPDF first neighbouring peak begins to shift, at room temperature, indicating the commencement of bond length contraction around the Bi^{3+} ions suggestive of a reduction in charge ordering. This observation contradicts pervious reports, and theoretical predictions suggest the charge ordering melting process occurs around x = ~0.2. The premature emergence of anomalous behavior was attributed to dynamic motion.

$BaBi_{0.7}Pb_{0.3}O_3$ exhibits the most robust superconducting properties within the $BaBi_{1-x}Pb_xO_3$ series and it recognized to traverse the boundary of charge density wave while undergoing charge ordering melting. Neutron Bragg peak data of $BaBi_{0.7}Pb_{0.3}O_3$ from room temperature to 600 Kshowed the co-existence of the *Ibmm* and *I*4/*mcm* phasesover a wide temperature range. Consequently, the phase transition sequence has been revised as: *Ibmm* (~298 K)→*Ibmm* + *I*4/*mcm* (~600 K) → *I*4/*mcm* (~800 K)→ $Pm\bar{3}m$. Temperature dependent neutron PDF indicates Bi^{3+}-O bond lengths are relatively insensitive to the extend of lead substitution in the series$BaBi_{1-x}Pb_xO_3$. The research focus on low-temperature $BaBi_{0.7}Pb_{0.3}O_3$ PDF investigation with varying symmetry structure fit. Although the local-scale fit shows a better agreement with the low-symmetry monoclinic structurese *I*2/*m* and $P2_1/n$, the *Ibmm* space group provides better fit for average structure, indicating that Bi-O bonds maintain as single average bond distance in BiO_6 octahedra. RMCprofile for 10 K $BaBi_{0.7}Pb_{0.3}O_3$ data, incorporating bond valence sum constraints successfully predict the theoretical charge ordering of Bi^{3+} and Bi^{5+} at positions identified in G(r) data, athrough the BVS constrained fit results a poorer agreement than expected. Correlating the temperature and composition dependent structural results with the these with superconducting properties and charge ordering melting, gives insight into the role of the $6s^2$ lone pair electrons of Bi^{3+} in inducing local distortions and driving temperature dependent structural transformations.

The last selection a preliminary variable temperature structural study of $Cs_2AgBiBr_6$ between 80–350 K is described. The structure was determined by Rietveld refinement of high-resolution synchrotron X-ray diffraction data. At room temperature, the material adopts a cubic $Fm\bar{3}m$ structure with rock-salt-like ordering of Ag^+ and Bi^{3+} cations, doubling the perovskite unit cell. Despite Ag^+ being larger than Bi^{3+} (1.15 vs 1.03 Å), the Ag–Br bond is slightly shorter than the Bi–Br bond (2.8103(8) vs 2.8229(8) Å), with nearly equal BO_6 octahedral volumes, suggesting greater covalency and distortion in $AgBr_6$ units. The Cs^+ cations are unbonded in the cubic phase and large anisotropic Br displacements perpendicular to Ag–Br–Bi chains, attributed to dynamic rotations of corner-sharing octahedra partially offsetting this underbonding. Below 120 K, the Br displacements freeze, inducing a continuous transition to a tetragonal $I4/m$ structure. The structural changes with temperature reflect the balance between ionic size, bonding character, and dynamic lattice effects.

Chapter 1 Introduction

1.1 Materials Science and Solid-State Chemistry

Materials science is an applied discipline that encompasses multiple fields, with applications from simple consumer products to aerospace engineering, on scales from microscopic to macroscopic. Materials science has significantly propelled the advancement of human civilization. Solid-state chemistry is the fundamental equivalent of materials science. As a discipline solid state chemistry sits at the interface of chemistry and physics and is underpinned by the theoretical framework of solid-state physics. It elucidates the principles underlying the emergence of specific physical, electronic and magnetic properties in materials at the macroscopic level. Solid state chemistry began to be systematically organized, as a distinct natural science around the 1940s, driven by the strong correlation between materials chemistry and industrial applications. Solid-state materials are numerous and include several major categories, e.g. metallic materials, ceramic materials and polymeric materials.[1, 2] The synthesis methods used to prepare solid state materials are equally diverse, with the synthesis of some perovskites detailed in Chapter 2 of this thesis. The unique properties of many solid-state materials is a consequence of their periodic atomic arrangements that is a feature of crystalline materials. Hence, the focus of this thesis is primarily on crystalline materials.

To be specific, the essence of materials chemistry lies in enhancing functionality by diverse processing techniques and considering the optimal integration of material properties with applications. The functionality of materials is intrinsically linked to their four fundamental properties: structure, electromagnetic characteristics, mechanical properties and thermal behaviour. Any variation in these can induce subtle alterations within the material that impact potential applications. Crucially, it is imperative to employ various characterization methods to elucidate the relationship between the structure and composition of a material and its respective properties. This step is essential for determining the potential applicability of materials across different fields, such as the use of titanium alloys with superior mechanical properties in aircraft exteriors or battery interlayers with electromagnetic capabilities. The

interaction between the material properties and its applications can be optimized through the study of solid-state chemistry.

1.1.1 Metal Oxides

Most metals are found as oxides in nature, although relatively few are found as simple binary oxides. The exceptional stability of metal oxides has seen them widely used in many important applications such as catalysis, corrosion-resistant materials and solar cells materials.[3-5] In many cases these are solid crystalline substances. It is generally possible to incorporate two or more metal cations into a single crystalline substance, and this compositional flexibility further expands the range of applications for metal oxides. Further flexibility emerges given the ability of metals to exist in different valence states in an oxide structure. Taking ternary metal oxides as example, the chemical formula is represented as $A_aB_bO_c$, where *A* and *B* represent different metal ions, and *a/b/c* are stoichiometric coefficients. Many ternary oxides show enhanced properties compared to the binary oxides, resulting in improved catalytic activity, enhanced corrosion resistance etc. In the catalysis industry, the use of ternary oxides such as Cu/ZnO for methanol synthesis is gradually replacing the first generation binary metal oxides.[6] However, while the incorporation of multiple elements in a material can increase the flexibility of a material's specific functionalities, it increases the complexity which may result in defects or structural distortions. Therefore, it is paramount to find the optimal balance between the structural and functional variations in mixed metal oxides.

1.2 Perovskite Structure

Perovskites are one of the most abundant structural families and perovskite-structural materials can display diverse properties through different elemental combinations. Perovskite is the name of the mineral $CaTiO_3$, but the term is often used to describe any material that has a similar

atomic arrangement. Most metallic cations can be incorporated into the perovskite structure which enables applications across various fields. The ability of the perovskite structure to host multiple functionalities has resulted in wide scientific interest.

Perovskites have been central to three major discoveries over the past 50 year. Bednorz and Müller won the 1987 Nobel Prize in physics for the discovery of high-temperature superconductivity in perovskite-type cuprates such as lanthanum barium copper oxide (LBCO).[7] The discovery of superconductivity in perovskite-type materials lead to nearly 40 years of intense research. Typically, perovskites support superconductivity in distorted or layered structures, with bismuth-based superconductors an obvious exception. Doping, lattice distortion and electron phase interactions are strongly correlated with superconducting behaviour. $YBa_2Cu_3O_{7-\delta}$ is a copper oxide-based perovskite, it achieves superconducting mode by involving oxygen vacancies that modulate the carrier density and critical current density.[8, 9] Colossal magnetic resistance (CMR) represents a distinctive property observed in manganese-based perovskite oxides, and was first described in the 1950's by Jonker and van Santen.[10] Ultimately Fert and Grünberg from Bell Labs won the 2007 Nobel Prize in Physics for the discovery of Giant Magnetoresistance in thin films an observation that can be traced back to the CMR observed in perovskites.[11] CMR involves a strong coupling of the magnetic and electronic properties such that it is possible to drive a change in electrical resistance by an external magnetic field. It is utilized in large-scale hard disk drives. $La_{1-x}Ca_xMnO_3$ exhibits CMR coupled with charge ordering. The electronic configuration transitions from an ordered arrangement to a charge disordered state if the Ca^{2+} content is larger than 0.5. This disrupts the internal magnetic interactions and results in an insulating ground state.[12, 13] The variation in resistivity is attributed to the strong coupling between the lattice and orbital degrees of freedom, doping and substitution of the cations in the perovskite-type lattice can facilitate precise adjustment in crystalline transport properties and magnetic characteristics.

$CsPbI_3$ is a textbook example of a halide perovskite material, it was initially employed in solar cell applications and subsequently catalysed extensive research on perovskite solar cells (PSCs). The break-through development of perovskite solar cell materials elevated the powder conversion efficiency (PCE) of PSCs from 3.8% to around 30% within two decades. Such

devices are considered superior in solar energy conversion efficiency and cost-effective processing compared with traditional silicon-based solar cell materials.[14-17] PSCs represent an innovative advance in green energy. Three distinctive properties underscore the adaptability inherent in perovskite structures, with different element substitution supporting diverse electronic configurations and bonding arrangements. Perovskites materials transcend a singular material classification, emerging as a versatile class of functional material capable of driving innovations in electromagnetic and energy technologies.

1.2.1 Simple Perovskite

Perovskite, with general formula ABX_3, is a crystalline material consisting of two different metal ions, and *X* is a negative charged oxide or halide ion which will bond with the two cations. In the ideal cubic structure, the *A*-type cation is larger than the *B*-type cation and the structure is based on corner sharing BX_6 octahedra. The *A*-type cation occupies the 12-coordinate cuboctahedral coordination site between the octahedra. The space group is $Pm\bar{3}m$. The Goldschmidt tolerance factor (*t*) provides an intuitive representation of the relationship between the ionic radii of the three ions and stability of the cubic perovskite structure. The tolerance factor *t* is given:

$$t = \frac{r_A + r_X}{\sqrt{2}(r_B + r_X)} \qquad (1.1)$$

Where r_A is the ionic radii for the *A*-site cation, r_B is the ionic radii for the *B*-site cation and r_X represents the ionic radii for *X*-site anion.

In the cubic perovskite structure, the *A*-site cation is located on the special symmetry-constrained Wyckoff position 1*a* at (0, 0, 0) which has no freedom of movement. The *B*-site cations occupy a similar symmetry-constrained Wyckoff position 1*b* (½, ½, ½) and *X*-site is at a third symmetry-constrained Wyckoff position 3*d* (½, 0, 0). In ideal conditions, the perovskite structure remain cubic. However, if the tolerance factor is significantly removed from one, distortion of the perovskite occurs.

The perovskite structure will remain cubic if the tolerance factor approaches one. If $t > 1$, the *A*-site cation is considered to be too large for optimal *A*-O bond in the AO_{12} cuboctahedral site, exerting chemical pressure on the surrounding BO_6 octahedral. This is relieved through the formation of edge or face-sharing octahedra, and the resulting structures are described as hexagonal perovskites. If $0.71 < t < 0.9$, the *A*-type cation is too small to fit into the cuboctahedral site of the cubic structure, and BX_6 octahedra will tilt about one of the principle axis, lowering the symmetry.

The small size of the *B*-site cations and, by extension, the *B*-O bonds means that the octahedra are relative rigid, although tilting can result in unequal *B*-*X* bond distance. The freedom of the *B*-site cation to displace from the high symmetry site forces a distortion in the structure, despite the approximately rigid octahedra. The Glazer notation is used to describe the octahedral tilting in perovskites.[18] The Glazer notation displays octahedral tilting in perovskites through setting an orthogonal crystal axes (*a*,*b*,*c*) at the centre of the octahedra, and using superscripts corresponding to in-phase tilting (+), out-of-phase tilting (-) or no tilting (0). As illustrated in Figure 1.1 (*a*), the tilting notation ($a^0a^0a^0$) represents an absence of tilting. In (b) the tilts are in-phase (+) about the *c*-axis as ($a^0a^0a^+$) and in (c) they are out-phase as ($a^0a^0a^-$). (*b*) and (*c*) correspond to a single tilt system. Tilts can exist about any of the three-axes and complex tilt patterns can contribute to the stability of a particular perovskite composition. Symmetry lowering can occur simultaneously around two or three axis and is often required to maintain the structural stability of a particular composition.

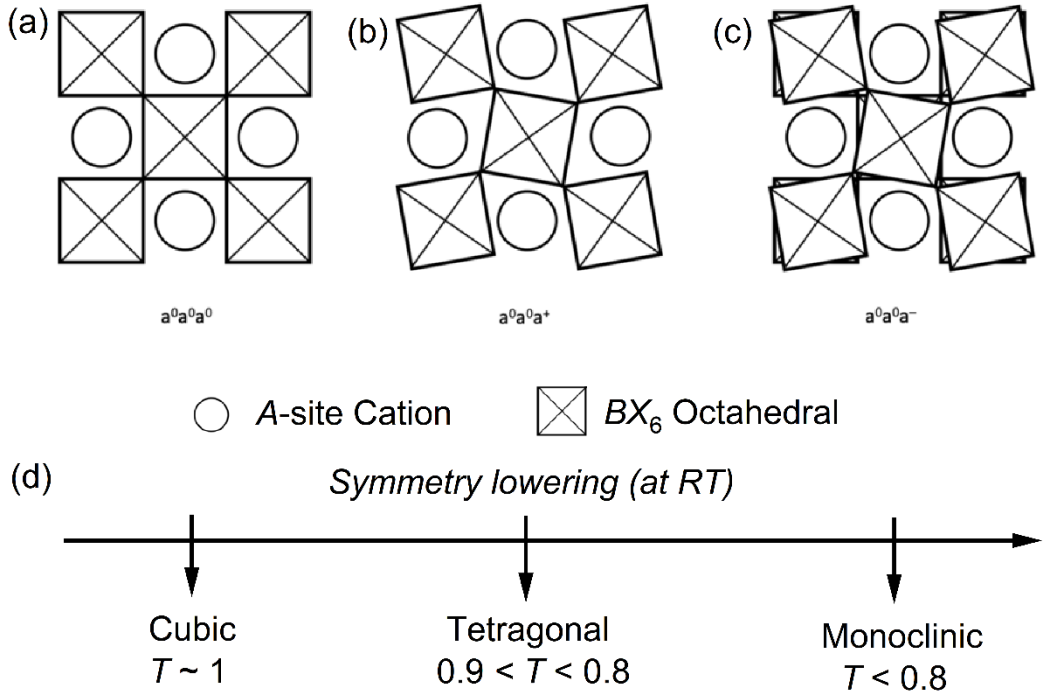

Figure 1.1: The schematic representation of octahedral tilting in the ABX_3 -type perovskite structure. (a) Cubic structure with no tilting Glazer notation ($a^0a^0a^0$). (b) Tetragonal structure with single in-phase tilt about the c-axis Glazer notation ($a^0a^0a^+$). (c) Tetragonal structure with single out-phase tilt about the c-axis Glazer notation ($a^0a^0a^-$). (d) indicates the relationship between tolerance factor and crystal structure.

$CaTiO_3$ has the orthorhombic space group *Pbnm* at room temperature and Glazer notation ($a^-b^+b^+$). This indicates that the TiO_6 octahedra exhibit out-phase tilts about the (100) direction and in-phase tilts about the (010) and (001) directions. If the tilts about (010) and (001) are equal, this is equivalent to in-phase tilting about the (011) direction. These distortions can remove the equality of the lattice parameter, and it results in lower symmetry. The correlation of the space group in the perovskite family and the octahedral tilt scheme was described using a group-subgroup relationship, see Figure 1.2. The diagram illustrates 15 possible space groups in ABX_3 type perovskites and show the nature of phase transitions between these.[19]

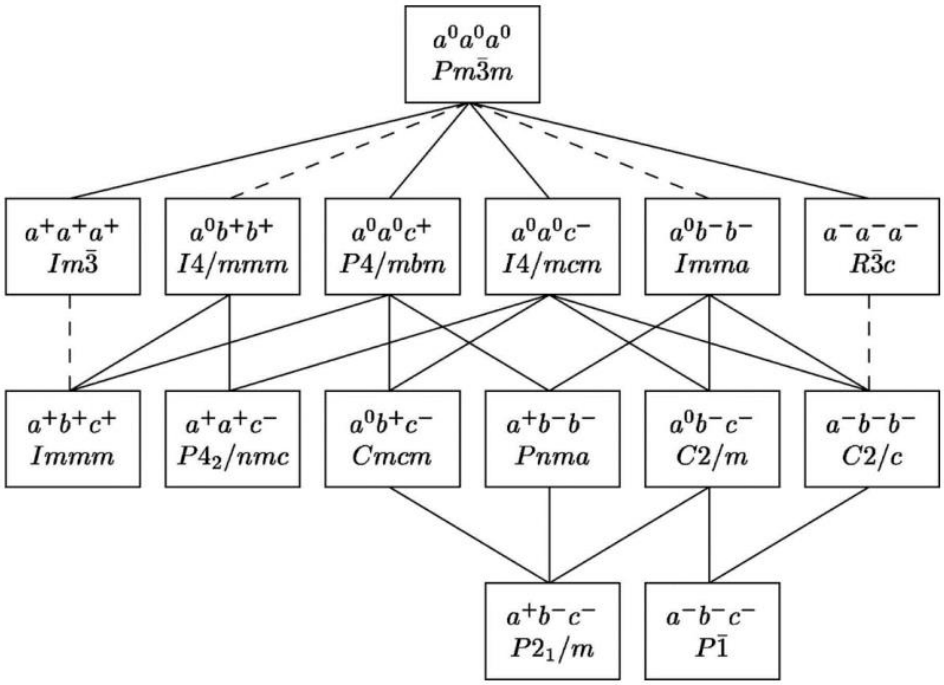

Figure 1.2: A schematic diagram indicating the group-subgroup relation in ABX_3 perovskites developed by Howard & Stokes. The dashed line represents a phase transition that must be 1st order by Landau theory. The solid line shows phase transition that can be continuous.[19]

1.2.2 Double Perovskites

The composition of the *B*-site metal cations in perovskite materials is flexible and when it contains two different metal ions it can be represented as $A_2BB'X_6$. If there are sufficient differences in the oxidation states and ionic radii between the two *B* cations, then long range ordering of these can occur. When the ratio of the two *B* cations is 1:1, the resulting structure is described as a rock-salt ordered double perovskite. It is possible for a vacancy to replace the *B*'-site cation, and this can result in a larger band gap.[20, 21] Although the *A*-site cations and *X*-site sublattice maintain the same arrangement, as observed in the $Pm\bar{3}m$ parent, the ordering of the *B*-site cations transforms the structure from a primitive unit cell to a face-cantered unit cell. Consequently, the cubic double perovskite structure has lower symmetry (space group $Fm\bar{3}m$ # 225) compared with archetypal $Pm\bar{3}m$ (#221) perovskite. The double perovskite structure retains corner sharing octahedra and if the tolerance factor is significantly reduced from one, symmetry lowering through cooperative tilting can occur. Figure 1.3 illustrates

group-subgroup relation for double perovskites.[22] Figure 1.4 illustrates representation of both the $Pm\bar{3}m$ and $Fm\bar{3}m$ cubic structures.

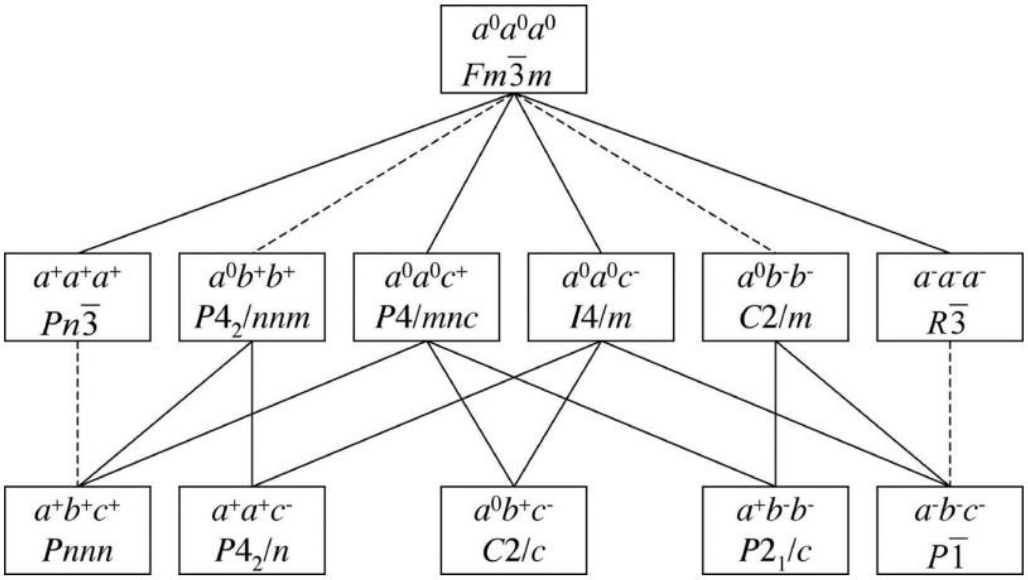

Figure 1.3: The group-subgroup relationship in rock-salt double perovskite illustrates the possible phase transition pathways are developed by Howard & Kennedy & Woodward. The dotted lines indicate 1st order transition, and the solid line is transition that allowed to be continuous.[19, 22] The Glazer notation is labelled above the space groups.

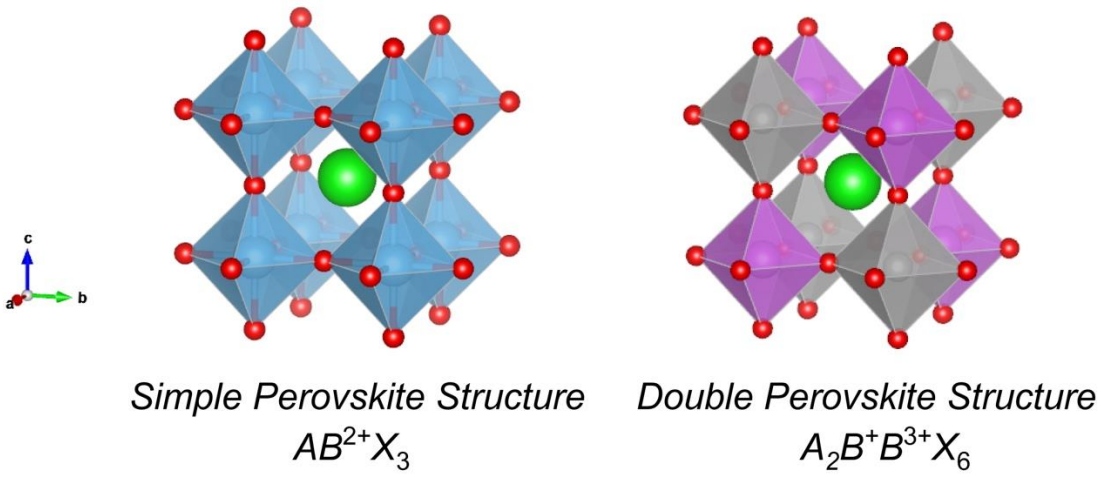

Figure 1.4: Representation of the structure of (a) simple perovskite and (b) double perovskite with two different *B*-site polyhedra. The rock-salt arrangement of the B^+ and B^{3+} cations in the double perovskite structure is apparent from the arrangement of the purple and grey polyhedral.

1.2.3 Halide Perovskites

The exceptional photophysical and electronic properties of hybrid and inorganic lead-halide perovskites with general formula ABX_3 (A = organic/inorganic cation, B = Pb^{2+}, and X = halide anion) has driven studies of their use in photovoltaics and other optoelectronic applications.[15, 23-25] The power conversion efficiency of devices based on such organic-inorganic halide perovskites (OIHP) is comparable to that of silicon-based solar cells reflecting their high carrier mobility, tuneable band gap, long diffusion lengths, and strong optical absorption. [26, 27]

Despite the excellent photovoltage performance of OIHP, there are two critical issues that limit the applicability of OIHP based devices. The first is the intrinsic instability of OIHP associated with the volatility of the organic components, and the second is the toxicity and adverse environmental impact of lead. To solve these problems, extensive efforts have been directed to identifying Pb-free inorganic perovskites. Sn and Bi have been identified as alternatives to Pb in many applications.[28, 29] Like Pb^{2+}, Sn^{2+} and Bi^{3+} have a lone pair of electrons that can lead to structural distortions and modification of the band gap by hybridized orbitals. The susceptibility of Sn^{2+} to oxidation to Sn^{4+} in air, results in a rapid decrease in the photovoltage performance of $CsSnI_3$-based solar cells.[30, 31] It seems unlikely that the Sn-based perovskites will ever have the stability to be commercially viable alternatives to the Pb-based perovskites. Incorporating Bi^{3+} at the octahedral site is not possible in ABX_3 OIHP.

1.3 The Wonder Metal – Bismuth

Bismuth (Bi Z = 83) is one of the most extensively studied heavier main group elements and has demonstrated remarkable potential in the field of optical materials over the past decade. This is attributed to its variable oxidation states. The electronic configuration of bismuth is [Xe]

$4f^{14}5d^{10}6s^26p^3$ and it is invariably encountered as Bi^{3+} and Bi^{5+} in oxides. The former is of particular interest as it has $6s^2$ lone pair electrons that can be stereochemically active. Unlike its neighbours Tl (Z = 81) Pb (Z = 82) and Po (Z = 84) Bi is generally regarded as non-toxic. Consequently, it has been promoted as a non-toxic and non-carcinogenic green metal and has emerged as a viable substitute for lead in many applications. The electron configuration of bismuth results in a pronounced spin-orbit coupling (SOC) effect. SOC influences the band structure of bismuth-containing oxides and impacts their semiconducting properties[32]. A detailed explanation of relationship between SOC and functionality will be provided in Section 1.3.2. From the perspective of optical properties, the primary rationale for using bismuth oxides as optical material reflects their broad absorption and emission bands, which has seen their luminescence investigated. In bismuth oxides the O 2*p* orbitals generally contribute to the ground state, and electronic transitions involve the excitation of an electron from the O 2*p* orbitals inter-band to an unfilled Bi 6*p* excited state. These properties give bismuth-based materials strong optical properties.[32]

1.4 Semiconductor and Superconductor in Oxides Metal

A semiconductor is a substance that has electrical conductivity intermediate between that of a metal and insulator. The conductivity of a semiconductor increases as the temperature increases, whereas that of a metal decrease with increasing temperature. $BaBiO_3$ is a quintessential exemplar of a *p*-type semiconductor. This perovskite exhibits two distinct BiO_6 octahedra with different Bi-O bond distances and valence states. Characterisation of $BaBiO_3$ indicates it has a relatively narrow band gap and a band structure that contributes to its *p*-type conductivity. It demonstrates significant potential for development in photovoltaic applications and photocatalysis.[33, 34] Scheelite-type $BiVO_4$ is a representative *n*-type semiconductor material that exhibits superior photoelectric properties compared to many *p*-type semiconductor. Its minimal environmental impact and simple reaction mechanisms have established $BiVO_4$ as a

target material in green chemistry. $BiVO_4$ not only displays promising potential as a photocatalyst, but it also holds significant research value in carbon dioxide photoreduction and ferroelectric properties.[35-37]

Band theory helps explain the conductivity of a material. In condensed matter, distinct energy levels are formed, the outermost valence electrons are involved in bonding and contribute to the so-called valence band. Electrons, in addition to those in the valence band, are critical in determining conductivity and these occupy the conduction band. The schematic representation in Figure 1.5 (*b*) indicates an energy gap devoid of electrons exists between valence bands and conduction bands. Consequently, current flow can be achieved through the provision of external energy to activate electron transition across the energy gap. Theunfilled states of the atomic electronic orbitals can be partially occupied if atoms undergo an electronic excitation. The configuration of active atom exhibits energy levels that approach the Fermi level and facilitating electron jumps though thermal excitation. The quantum state of electrons is fundamentally explained by the Fermi level and the Pauli exclusion principle.[38, 39]

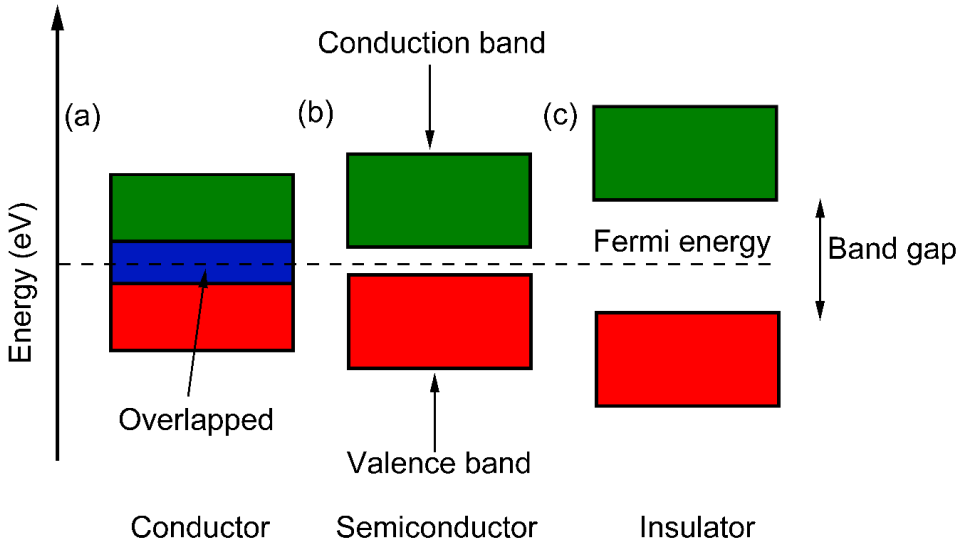

Figure 1.5: Representation of band gap existing between valence band and conduction band of (*a*) conductor, (*b*) semiconductor and (*c*) insulator. Blue area indicates the overlapped between band gaps. The band gap is approaching to Fermi energy.

Electrons in the valence band are not static, rather they can readily transition from the valence band to conduction band by acquiring sufficient energy, usually thermal energy. If there is no gap between the VB and CB or if they overlap, as indicated in Figure 1.5 (*a*), electrons can effortlessly transfer to conduction band. If the material is a conventional semiconductor, electron transition can also be induced through the application of electrical energy. When the band gap is excessively large, it requires a greater amount of energy to achieve conductivity, those material are classified as poor conductors or in the extreme insulators.[40]

Metal-oxide semiconductors (MOS) are used or being developed for many applications including to catalyse the photodegradation of organic pollutants, and for application in optoelectronics and biosensing.[41-43] The stability and insolubility of MOS materials are important considerations for replacing existing toxic materials such as CdS used as photovoltaics. TiO_2 exhibits promising application in the field of solid oxide fuel cells as an electrolyte with increasing the ionic conductivity. It contains the physical properties of semiconductor and characteristics of ionic fuel cells as a common material. The result of changing the ionic conductivity though Li interaction demonstrates the correlation between band structure modification and electron transport efficiency, which results in an oxygen vacancy.[44] This indicates that semiconductor research leads to a significant implication for industrial production.

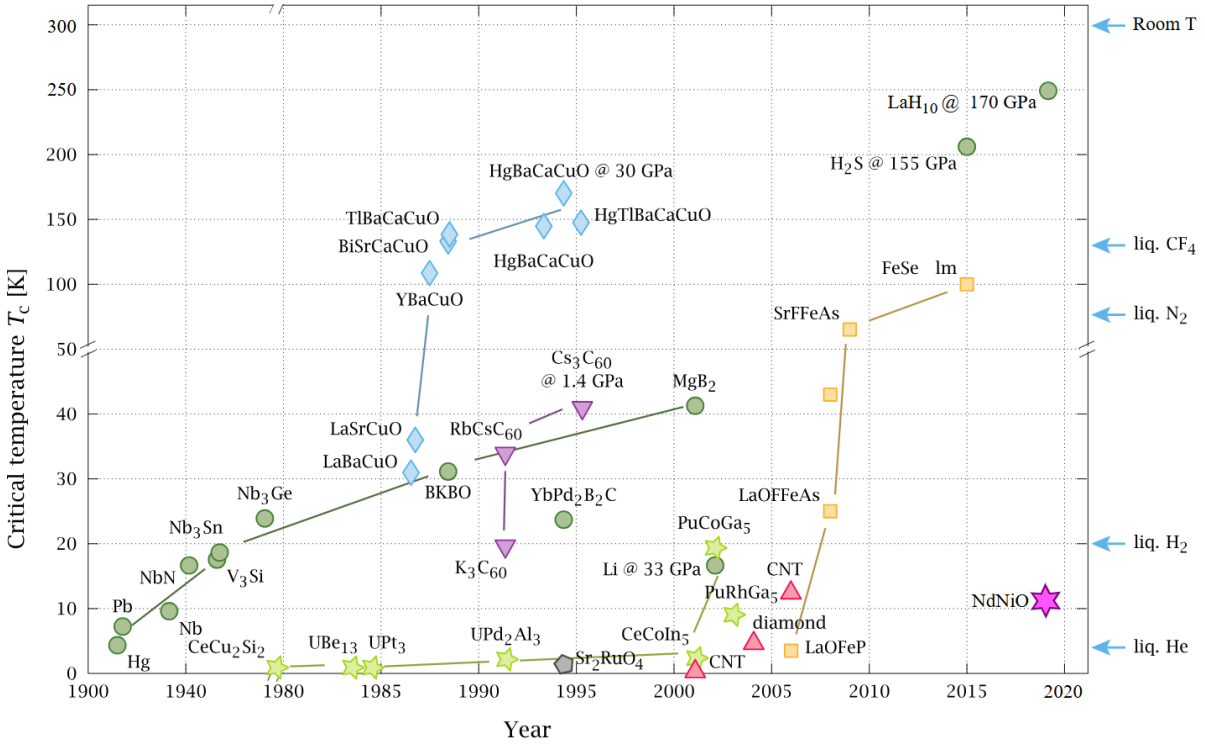

Figure 1.6: The graph illustrates relationship of each superconductor and critical temperature since 1911. Green circle shows superconductor have been identify as Bardeen–Cooper–Schrieffer (BCS) materials, blue diamond is copper-base oxide, orange square is iron-based oxide.[45, 46]

A superconductor is defined as a material that achieves zero electrical resistance, and the observation of superconductivity is limited to specific low-temperature or high-pressure conditions. The temperature at which superconductivity occurs is denoted as T_c. Common metallic conductors (like gold, silver and copper) possess zero band gap, but those materials still experience energy losses during electron movement. The resistance of such metals cannot be reduced lower than the "zero-resistance" value about 10^{-25} ohm ·mm^2/m. Not all metallic materials can be identified as superconductors. In theory, a superconducting material can sustain a persistent current without energy dissipation, as long as it remains below its critical temperature and magnetic field limits.[47] Superconductivity has been known since 1911, when Heike Onnes observed superconductivity by cooling mercury to approximately 4 K and this discovery has driven over a century of research attempting to find materials that superconduct near room temperature.[48] Superconductors are classified as either Type I or Type II. Type I superconductors, typically elemental metals like lead or mercury, exhibit complete magnetic field expulsion (the Meissner effect) but are limited to low critical fields. Type II

superconductors, which include metallic alloys and complex compounds such as high-temperature copper oxide superconductors, can maintain superconductivity under much higher magnetic fields. An example of a type II superconductor Pb doped $BaBiO_3$ will be discussed in this thesis.

Doping is a crucial technique for improving the transport efficiency of semiconductors and employed to enhance the properties of superconductors. Doping involves the substitution of an ion, usually at a specific site, in a crystalline lattice. This technique is applied in semiconductor materials, where it modifies the density of states around the Fermi level. Figure 1.7 illustrates the changes that can occur when the group 15 cation Bi is replaced by a group 14 cation, such as Pb, in $BaBi_{1-x}Pb_xO_3$. As depicted in (*a*), the undoped material exhibits a wide band gap and disproportionation of the Bi charges into Bi^{3+} and Bi^{5+} occurs. This disproportionation diminishes as the concentration of the doping Pb cation and the gap between the higher energy (Bi^{5+}) and lower energy (Bi^{3+}) states decreases. (*c*) illustrates an emergence of the $(ns)^2(np)^2$ configuration, it indicates that the valence state of the *B* metal ions tends toward 4^+ and changes Fermi level. Hashimoto's experimental hypothesis mentions that the charge disproportionation of the valence skipping metal ions Bi^{3+} and Bi^{5+} will be impacted as the lead content increases , which will be validate within this dissertation.[49]

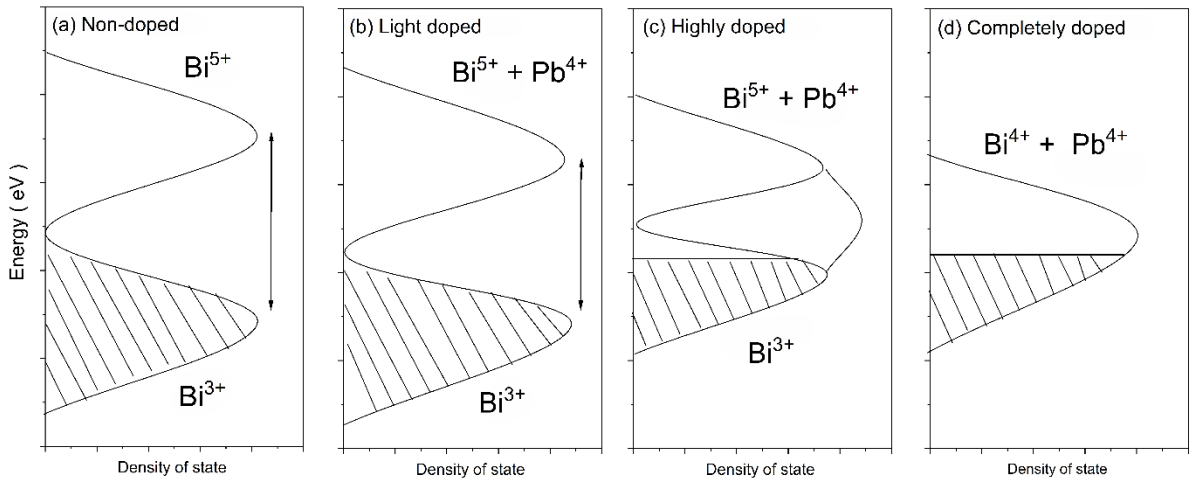

Figure 1.7: Schematic diagram showing the evolution of the band structure with increasing Pb content in $BaBi_{1-x}Pb_xO_3$ as proposed by Hashimoto *et al*.[49]

1.5 Condensed Matter Science

Condensed matter science is a branch of material science and physics and focusses on the properties and behaviours of materials. The study of superconductivity and nanostructures represents the most prominent research within this field. Solid-state chemistry is framed by crystallography and physical properties of solid-state materials and developing novel materials. Although there is a subtle difference between condensed matter science and solid-state chemistry, the theoretical framework provided by condensed matter science serves as a foundation for advancing solid-state chemistry in the development of various new materials. Consequently, the condensed matter theories pertaining to superconducting materials discussed in this thesis are crucial for understanding how atomic-scale variations influence material behaviour.

1.5.1 Charge Density Wave and Breathing Mode

Charge density wave (CDW) refers to a phenomenon in which under low-temperature conditions, a crystal structure undergoes distortion, that results in periodic fluctuations of internal charge density. This behaviour manifest with a wave vector **q** equal to twice the Fermi wave vector and leads to the formation of an energy gap where the change in energy exceeds the elastic energy of lattice distortion.[50] The transformation drives the material from a semiconductor or conductor to an insulator and it is known as a Peierls phase transition.[51, 52] In materials exhibiting both CDW and superconducting states, the Peierls phase transition temperature is generally observed to be higher than the superconducting critical temperature T_c. Most experimental results support the existence of a competitive mechanism between CDW and superconducting states at low-temperatures.[53]

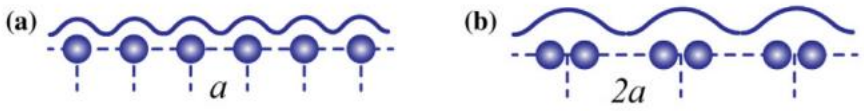

Figure 1.8: The schematic diagram illustrates the (a) one-dimensional chain and (b) two-dimensional lattice chain with dimerization. The change represents Peierls phase transition affect in atomic scale.[50]

Although both charge density wave (CDW) and charge ordering are associated with electron-phonon coupling, there are fundamental distinctions. Charge ordering specifically refers to the insulating ground state with hole doping, which is observed in the charge-ordered insulating phase of lanthanide oxides, it is correlated with Jahn-Teller effect and crystal field.[54, 55] In contrast, the formation of CDW necessitates the presence of well-defined Fermi surfaces.

A breathing mode is a vibrational mode within a crystal lattice, typically involving the symmetric in-phase movement of oxygen atoms toward and away from a central cation. In transition metal oxides, this mode corresponds to alternating expansion and contraction of the metal–oxygen octahedra (BO_6), analogous to a 'breathing' motion, as illustrated in Figure 1.9. The longer *B*–O bond length indicates an expanded octahedron, while the shorter *B*–O bond corresponds to a contracted one. These structural motifs alternate throughout the lattice in charge-ordered oxides, reflecting localized charge disproportionation (e.g., B^{3+}/B^{5+}). Unlike charge density waves (CDWs), which arise from Fermi surface instabilities, breathing modes in these systems typically result from strong electron–lattice coupling and static charge localization.[56, 57]

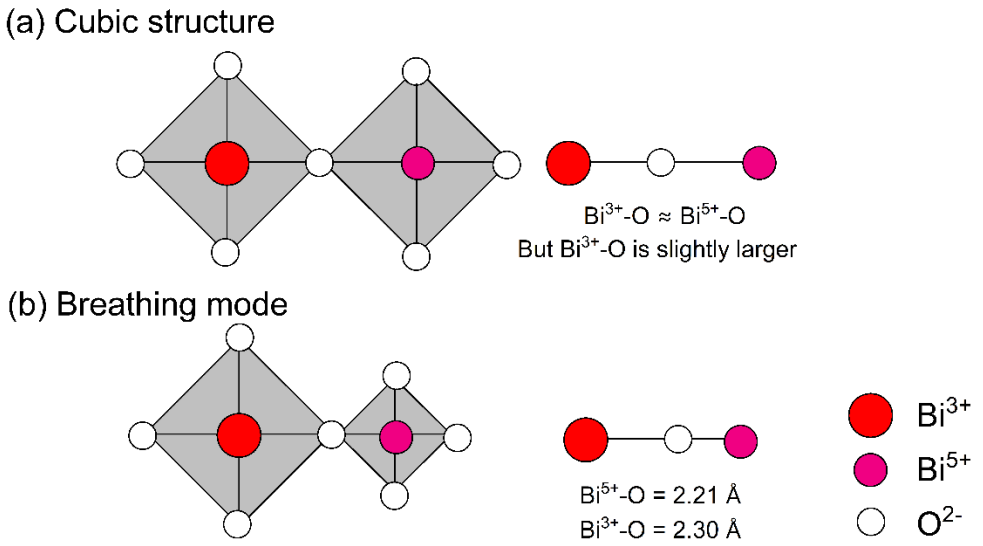

Figure 1.9: Illustration of the breathing mode model for $BaBiO_3$. (a) Undistorted oxygen octahedra exists in the cubic phase. (b) the larger octahedron is a result of the longer by Bi^{3+}-O bond (2.30 Å) and neighbouring small octahedron with the Bi^{5+}-O (2.21 Å) bond. Displacement of the oxygen atom occurs in the breathing mode.

1.5.2 Charge Disproportionation and Valence Skipping Elements

Charge disproportionation (CD) is a phenomenon where one element exists in two different oxidation states in the same material. Taking $CaFeO_3$ as an example the Fe^{4+} shows charge disproportionation as $2Fe^{4+} \rightarrow Fe^{3+} + Fe^{5+}$. The core reason for CD is the instability of intermediate oxidation state in the structure, with the mixed oxidation state energetically favoured compared to the intermediate state.[58] Charge disproportionation involves the redistribution of ions into a more ordered charge arrangement through re-equalization. This phenomenon is sensitive to changes at either the *A* or *B*-sites in perovskites. Charge disproportionation influences the magnetic, electric and optical properties of the material.[59-62].[63, 64] In $CaFeO_3$ the charge disproportionation occurs at a critical temperature ~ 290 K and is accompanied by a metal-insulator transition. Charge ordering in $CaFeO_3$ results in a phase transition from orthorhombic to monoclinic with the ordered Fe^{3+}/Fe^{5+} cations having a rock-salt type perovskite arrangement whilst retaining the same Glazer tilt pattern.[65, 66] CD is sensitive to chemical doping and, for example, Sun showed that this can be supressed by Co

doping in $CaFeO_3$. This observation is similar to the changes in Pb-doped $BaBiO_3$ studied in in this thesis.

The question of charge disproportionation in $BaBi_{1-x}Pb_xO_3$ is fascinating as the apparent disappearance of charge ordering as the Pb content increases implies the formation of Bi^{4+}. Valence skipping can be observed in elements that can exist in different valence, however one of the intermediate valences is not observed. This occurs for bismuth. Figure 1.10 (*a*) indicates valence states Bi^{3+} and Bi^{5+}, but not Bi^{4+}, occur. This reflects the stability of filled atomic shells in atoms.[67] The electronic configuration of Bi is [Xe]$4f^{14}$ $5d_{10}$ $6s^2 6p^3$. Removal of three electrons gives Bi^{3+} with two electrons (a lone pair) in the 6s orbital. Loss of a further electron to give a partially filled 6*s* shell that is unfavoured compared to the closed shell configuration of Bi^{5+} ($6s^0$) Valence skipping element supports charge disproportionation to maintain structural stability. Combined with Figure 1.6, valence skipping element within shadow area shows a tendency to correlate to superconductive materials. This arises from the formation of negative-*U* centres induced by valence skipping ions, it facilitates unimpeded mutual attraction between internally generated electrons. The resulting intense charge fluctuations give rise to unconventional superconducting properties.[67-70]

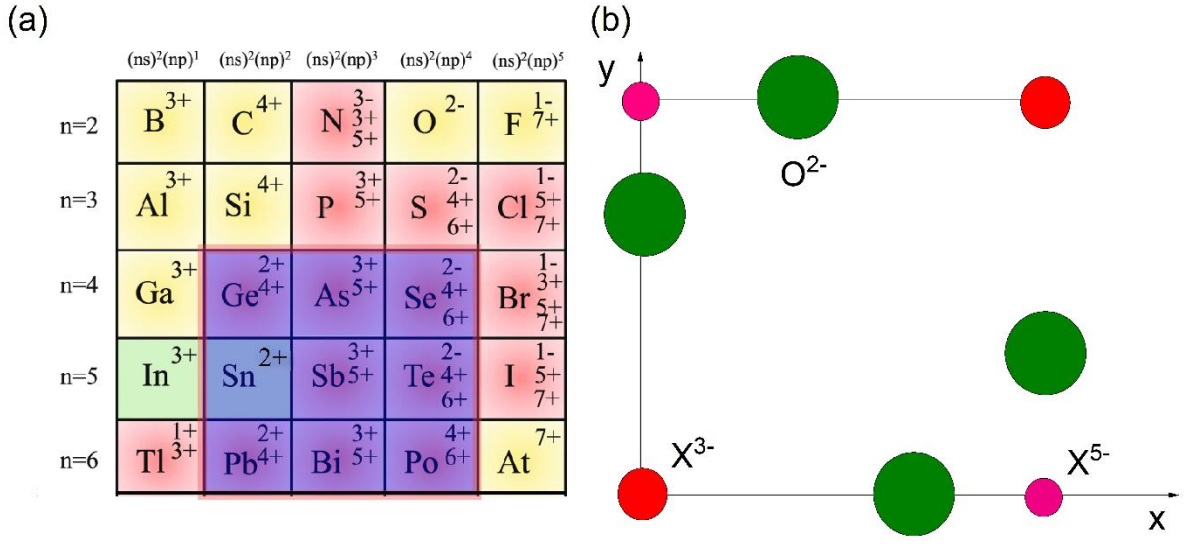

Figure 1.10: (*a*) The valence skipping element periodic table, red gradation elements are indicated as valence skippers, yellow gradation elements are defined as single valence states element and green gradation elements are recently to be determined. The cubic shadow area is included potential elements in superconductor material development.[67, 71] (*b*) The position of valence shipper exists in its metal

oxide BO_6 octahedra (diagram use group 15 valence shipping element as example which displays as X^{3+} and X^{5+}), the schematic diagram ignores the tilting in Glazer notation.

1.5.3 Spin–Orbit Coupling

Spin–orbit coupling (SOC) is a quantum mechanical phenomenon arising from the interaction between a particle's intrinsic spin and its orbital angular momentum. In crystalline materials, SOC can influence the electronic band structure, often appearing as a weak effect in light elements but becoming significant in heavier atoms. While generally subtle, SOC can have a pronounced impact on bands near the Fermi level, especially in materials containing heavy elements. The strength of SOC increases with atomic number and the extent of orbital angular momentum, making it particularly important in 5*d* transition metal compounds, where it contributes to strong spin–orbit-driven effects such as band splitting, anisotropy, and complex magnetic behaviour. The Bardeen–Cooper–Schrieffer (BCS) theory describes superconductivity as arising from the formation of Cooper pairs which are bound states of two electrons with opposite momenta and spin. These form below a critical temperature T_c. Cooper pairs are mediated by electron–phonon interactions and move coherently through the lattice without scattering, giving rise to zero electrical resistance.

In recent years, the interplay between SOC and superconductivity has attracted significant interest. SOC entangles an electron's spin and orbital motion, enabling the possibility of mixed spin-singlet and spin-triplet pairing states in certain materials. This contrasts with conventional BCS superconductors, which host only spin-singlet pairs. Such unconventional pairing symmetries may enhance or stabilize superconductivity in systems with strong SOC.

Bismuth (Bi), a heavy element with strong SOC due to its high atomic number and unique electron configuration, exhibits Type I superconductivity at low temperatures. Its SOC-driven properties make it a model system for exploring the role of relativistic effects in superconductivity.[72, 73]

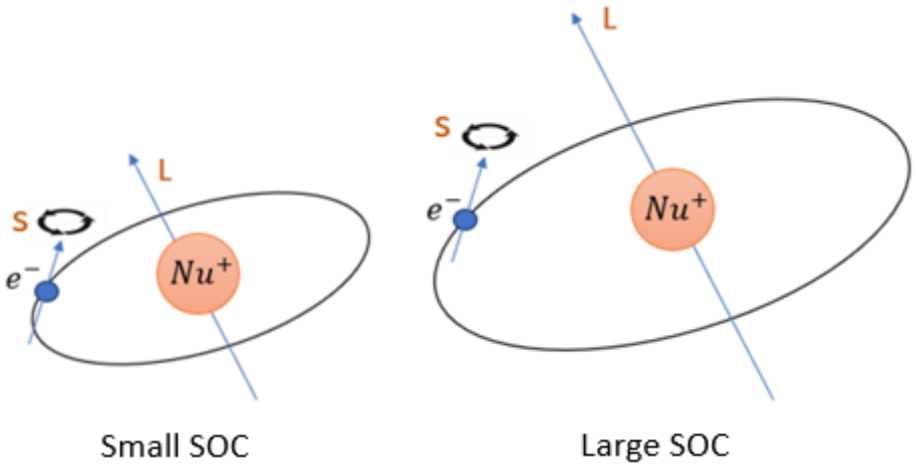

Figure 1.11: The schematic representation of spin-orbit coupling effect. The larger electron orbit leads the greater orbital momentum contribution and reduces the magnetic moment in high-orbital metal ions. Left panel stand for lower orbital metal compared with right panel.

1.6 Applications of ABO_3 and $A_2BB'X_6$

Both ABO_3 and $A_2BB'X_6$ type perovskite have been developed for a broad range of practical applications. Perovskites can be used in the development of high-efficiency solar cells and photocatalyst, and perovskite with high luminescent quantum efficiency apply for LED fabrication.[74-76] The high sensitivity of fluorescent perovskites is employed in sensor production, and the unique physical properties of perovskites enable the application of laser fabrication.[77-79] Alternatively, perovskite like $BaTiO_3$ that are characterized by their high dielectric constant are used as ceramic capacitors.[80] The following section provides an overview of the materials involved in the project, which detailing the applications of project material and elucidating the objectives of the study.

1.6.1 Oxide Topological Insulators $BaBiO_3$

Topological insulators (TI) is a material characterized by insulating bulk properties and conductive surface states, it results as a phenomenon from the twisted band gap between the valence and conduction bands and facilitates electron movement exclusively along the surface. This fundamental distinction sets topological insulator apart from conventional insulators. The conceptual framework of topological insulators was initially proposed by Pankratov and Volkov in the last century. These materials have been successfully implemented in the quantum Hall effect, emerging as one of the promising candidates in quantum computing.[81] Furthermore, bismuth-based topological insulators carry an exceptionally carrier mobility and low lattice thermal conductivity to achieve high thermoelectric convention efficiency, it results in offering viable material substitution for thermoelectric generator technologies.[82]

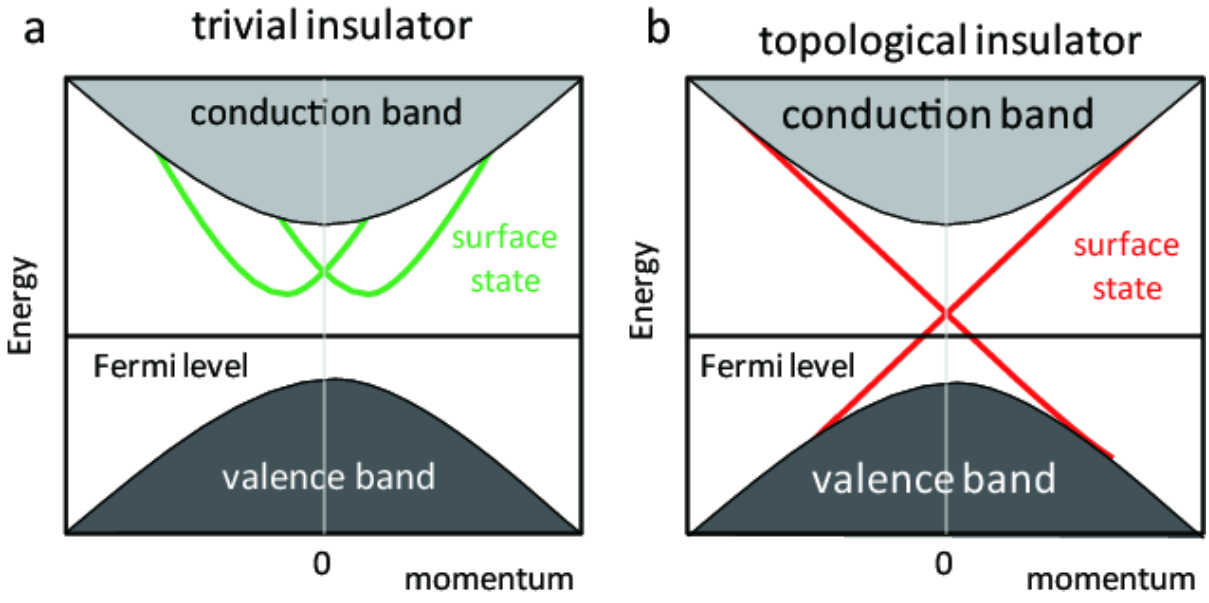

Figure 1.12: The schematic representation of the bond gap from 2D and 3D material. (a) is conventional insulator and (b) displays topological insulator. The shaded region shows the bulk continuum states, and the lines show discrete surface (or edge) bands localized near one of the surfaces. *b* occurs in topological insulators and guarantees that the surface bands cross any Fermi level inside the bulk gap.[83]

The operational principle of topological insulator materials in the thermoelectric devices relies on the conversion of temperature gradients into voltage. Topological insulator materials centred on Bi, like Bi_2Te_3, can achieve thermoelectric effect by spin-momentum-locked surface states and inherently low lattice thermal conductivity.[84]

This dissertation is focusing on the characterization of $BaBiO_3$ and its doped derivatives. $BaBiO_3$ was first synthesized and reported in 1963, it is a structural analogue of $LiBiO_3$. Scholder provided a hypothesis that Bi ion displays two valence states within one crystalline, Bi^{3+} and Bi^{5+}, it resulted by similar structure compared with Ba_2LaBiO_6, which is a phenomenon known as " charge disproportionation".[85] $BaBiO_3$ has been investigated as a semiconductor material for over half century. However, $BaBiO_3$ has been redefined as the topological insulator material as the growing interest in Density Functional Theory (DFT) and theorical application of TI material. TI was initially classified as materials which have nontrivial band structure displaying a gapless surface, if it reaches a trivial insulator.[57] $BaBiO_3$ obtained strong spin-orbit coupling (SOC) and dual valence states of Bi ions, it supports a maximum bulk band gap about 0.7 eV which is the largest value within TI materials.[86] Therefore, $BaBiO_3$ can easily facilitating the excitation of energy levels. Some condensed matter physics points are indicated in Selection 1.5.

1.6.2 High-Temperature Superconductors $BaBi_{1-x}Pb_xO_3$ and $Ba_xK_{(1-x)}BiO_3$

The enthusiasm of $BaBiO_3$ research stems from the theoretical breakthroughs based on quantum physics, but the superconducting properties of its derivatives are more attractive. Currently, scientists discovered superconducting material across a range from 4.2 K to 134 K, and some materials with critical temperature higher than 30 K are defined as high-temperature superconductor (HTS).[87, 88] However, the research about superconductive materials is in a bottleneck stage. Although the potential application of superconductor is unexpected, it requires intensive energy to refrigerate HTS remain as superconductive state and extra cost during manufacturing material into a usable form. Undoubtedly, the significance of superconducting materials is not only the exploration of physic, but also the realization of zero-

consumption superconducting magnetic energy storage or the utilization of superconducting materials to simulate the sun burning and employed as fusion energy.[89] Most high-temperature superconductive materials are ceramic materials composed of copper oxide, doped $BaBiO_3$ can active superconductive state as HTS, which establish a connection between superconductor and topological insulators within same parent materials, it can provide the correlation between Bismuth element and superconductive property.

1.6.3 Functional Energy Materials Cs_2AgBiX_6 (X = Cl, Br)

Lead halide perovskites have been used in the fabrication of photovoltaic devices, photodetectors and LEDs due to their superior optoelectronic properties, it demonstrates significant application potential.[90, 91] However, the practical implementation of those materials is constrained by toxicity of lead and poor sustainability. Bismuth ions possessing electronic structures analogous to lead and obtains less toxicity, it can serve as *B*-site substituents for Pb^{2+} ion and forming lead-free halide double perovskite – Cs_2AgBiX_6.

$Cs_2AgBiBr_6$ as most popular composition in this series exhibits advantages including extended carrier lifetime and a relatively large indirect bandgap. Nevertheless, experimental results indicate that theoretical power convention efficiency (PCE) of $Cs_2AgBiBr_6$ remains limited to ~ 7 to 8%, and despite achieving and open-circuit voltage to 1 V in perovskite solar cell configuration, whilst the PCE of $CH_3NH_3PbI_3$ is approach to 30%.[92, 93] In photodetector field, $Cs_2AgBiBr_6$ exhibits exceptional performance with a theoretical defectivity reaching 3.29×10^{12} Jones, which obtains highest defectivity in lead-free perovskites.[94, 95] As the ionic radii of *X*-site decrease to Cl^-, $Cs_2AgBiCl_6$ have been investigated with LEDs and photodetector due to similar band structure with $Cs_2AgBiBr_6$. Additionally, $Cs_2AgBiCl_6$ is well-known as an efficient visible light photocatalyst for organic dye degradation, where its reduced particle size enhances catalytic performance through increasing surface and shortening charge carrier migration pathways.[96]

The structural-property relationship studies in this dissertation exhibits $Cs_2AgBiBr_6$ undergoes a cubic-tetragonal phase transition accompanied by alteration in optical properties, which are attributed to the distortion of $AgBi_6$ and $AgBr_6$ octahedra within crystal structure, whilst $Cs_2AgBiCl_6$ does not show a phase transition with temperature dependence.

Bibliography

(1) Rao, C. N. R.; Winter School in Solid State, C. *Solid state chemistry*; M. Dekker, 1974.

(2) Martin, J. D. What's in a Name Change?: Solid State Physics, Condensed Matter Physics, and Materials Science. *Physics in perspective* **2015**, *17* (1), 3-32. DOI: 10.1007/s00016-014-0151-7.

(3) Li, Y.; Zhang, Y.; Qian, K.; Huang, W. Metal–Support Interactions in Metal/Oxide Catalysts and Oxide–Metal Interactions in Oxide/Metal Inverse Catalysts. *ACS Catalysis* **2022**, *12* (2), 1268-1287. DOI: 10.1021/acscatal.1c04854.

(4) Ferrel-Alvarez, A. C.; Regmi, G.; Velumani, S.; Castaneda, H. Chapter 6 - Functionally integrated metal oxides for corrosion protection. In *Inorganic Anticorrosive Materials*, Verma, C., Aslam, J., Hussain, C. M. Eds.; Elsevier, 2022; pp 113-138.

(5) Metal Oxide Semiconductors for Solar Cells. In *Metal Oxide Semiconductors*, 2024; pp 171-210.

(6) Kaluza, S.; Muhler, M. A novel continuous approach for the synthesis and characterization of pure and mixed metal oxide systems applied in heterogeneous catalysis. In *Studies in Surface Science and Catalysis*, Gaigneaux, E. M., Devillers, M., Hermans, S., Jacobs, P. A., Martens, J. A., Ruiz, P. Eds.; Vol. 175; Elsevier, 2010; pp 217-220.

(7) Bednorz, J. G.; Müller, K. A. Possible highTc superconductivity in the Ba−La−Cu−O system. *Zeitschrift für Physik B Condensed Matter* **1986**, *64* (2), 189-193. DOI: 10.1007/BF01303701.

(8) Trabaldo, E.; Kalaboukhov, A.; Arpaia, R.; Wahlberg, E.; Lombardi, F.; Bauch, T. Mapping the Phase Diagram of a $YBa_2Cu_3O_{7-\delta}$ Nanowire Through Electromigration. *Physical Review Applied* **2022**, *17* (2), 024021. DOI: 10.1103/PhysRevApplied.17.024021.

(9) Alcalà, J.; Fernández-Rodríguez, A.; Günkel, T.; Barrera, A.; Cabero, M.; Gazquez, J.; Balcells, L.; Mestres, N.; Palau, A. Tuning the superconducting performance of $YBa_2Cu_3O_{7-\delta}$

films through field-induced oxygen doping. *Scientific Reports* **2024**, *14* (1), 1939. DOI: 10.1038/s41598-024-52051-1.

(10) Jonker, G. H.; Van Santen, J. H. Ferromagnetic compounds of manganese with perovskite structure. *Physica* **1950**, *16* (3), 337-349. DOI: 10.1016/0031-8914(50)90033-4.

(11) Baibich, M. N.; Broto, J. M.; Fert, A.; Van Dau, F. N.; Petroff, F.; Etienne, P.; Creuzet, G.; Friederich, A.; Chazelas, J. Giant Magnetoresistance of (001)Fe/(001)Cr Magnetic Superlattices. *Physical Review Letters* **1988**, *61* (21), 2472-2475. DOI: 10.1103/PhysRevLett.61.2472.

(12) Tafra, E.; Novosel, N.; Skoko, Ž.; Ivek, T.; Basletić, M.; Mihaljević, B.; Jagličić, Z.; Góngora, D. R.; Tomić, S.; Hamzić, A.; et al. Colossal magnetoresistance effect and spin-dependent variable-range hopping in the charge ordered phase of overdoped (La,Ca)MnO_3 manganites. *Physical Review B* **2025**, *111* (11), 115107. DOI: 10.1103/PhysRevB.111.115107.

(13) Boora, N.; Ahmad, R.; Rahman, S.; Dung, N. Q.; Ahmad, A.; Alshammari, M. B.; Lee, B. Recent Advances of Colossal Magnetoresistance in Versatile La-Ca-Mn-O Material-Based Films. *Magnetochemistry* **2025**, *11* (1), 5.

(14) Bati, A. S. R.; Zhong, Y. L.; Burn, P. L.; Nazeeruddin, M. K.; Shaw, P. E.; Batmunkh, M. Next-generation applications for integrated perovskite solar cells. *Communications Materials* **2023**, *4* (1), 2. DOI: 10.1038/s43246-022-00325-4.

(15) Kojima, A.; Teshima, K.; Shirai, Y.; Miyasaka, T. Organometal Halide Perovskites as Visible-Light Sensitizers for Photovoltaic Cells. *Journal of the American Chemical Society* **2009**, *131* (17), 6050-6051. DOI: 10.1021/ja809598r.

(16) Lee, M. M.; Teuscher, J.; Miyasaka, T.; Murakami, T. N.; Snaith, H. J. Efficient Hybrid Solar Cells Based on Meso-Superstructured Organometal Halide Perovskites. *Science* **2012**, *338* (6107), 643-647. DOI: doi:10.1126/science.1228604.

(17) Liu, J.; Aydin, E.; Yin, J.; De Bastiani, M.; Isikgor, F. H.; Rehman, A. U.; Yengel, E.; Ugur, E.; Harrison, G. T.; Wang, M.; et al. 28.2%-efficient, outdoor-stable perovskite/silicon tandem solar cell. *Joule* **2021**, *5* (12), 3169-3186. DOI: 10.1016/j.joule.2021.11.003 (acccessed 2025/06/26).

(18) Glazer, A. The classification of tilted octahedra in perovskites. *Acta Crystallographica Section B* **1972**, *28* (11), 3384-3392. DOI: doi:10.1107/S0567740872007976.

(19) Howard, C. J.; Stokes, H. T. Group-Theoretical Analysis of Octahedral Tilting in Perovskites. *Acta Crystallographica Section B* **1998**, *54* (6), 782-789. DOI: doi:10.1107/S0108768198004200.

(20) Sa, R.; Zhang, Q.; Luo, B.; Liu, D. Exploring the electronic and optical properties of vacancy-ordered double perovskites Cs_2PtX_6 (X = Cl, Br, I). *Journal of Solid State Chemistry* **2021**, *304*, 122602. DOI: https://doi.org/10.1016/j.jssc.2021.122602.

(21) Faizan, M.; Bhamu, K. C.; Murtaza, G.; He, X.; Kulhari, N.; Al-Anazy, M. M.; Khan, S. H. Electronic and optical properties of vacancy ordered double perovskites A_2BX_6 (A = Rb, Cs; B = Sn, Pd, Pt; and X = Cl, Br, I): a first principles study. *Scientific Reports* **2021**, *11* (1), 6965. DOI: 10.1038/s41598-021-86145-x.

(22) Howard, C. J.; Kennedy, B. J.; Woodward, P. M. Ordered double perovskites -- a group-theoretical analysis. *Acta Crystallogr B* **2003**, *59* (Pt 4), 463-471. DOI: 10.1107/s0108768103010073 From NLM.

(23) Kojima, A.; Teshima, K.; Shirai, Y.; Miyasaka, T. Organometal Halide Perovskites as Visible-Light Sensitizers for Photovoltaic Cells. *Journal of the American Chemical Society* **2009**, *131* (17), 6050-+. DOI: 10.1021/ja809598r.

(24) Han, J.; Park, K.; Tan, S.; Vaynzof, Y.; Xue, J.; Diau, E. W.-G.; Bawendi, M. G.; Lee, J.-W.; Jeon, I. Perovskite solar cells. *Nature Reviews Methods Primers* **2025**, *5* (1), 3. DOI: 10.1038/s43586-024-00373-9.

(25) Muscarella, L. A.; Hutter, E. M. Halide Double-Perovskite Semiconductors beyond Photovoltaics. *Acs Energy Letters* **2022**, *7* (6), 2128-2135. DOI: 10.1021/acsenergylett.2c00811.

(26) Snaith, H. J. Perovskites: the emergence of a new era for low-cost, high-efficiency solar cells. *The journal of physical chemistry letters* **2013**, *4* (21), 3623-3630.

(27) https://www.nrel.gov/pv/cell-efficiency.html. (accessed.

(28) Abtew, M.; Selvaduray, G. Lead-free solders in microelectronics. *Materials Science & Engineering R-Reports* **2000**, *27* (5-6), 95-141. DOI: 10.1016/s0927-796x(00)00010-3.

(29) Takenaka, T.; Kei-ichi Maruyama, K.-i. M.; Koichiro Sakata, K. S. $(Bi_{1/2}Na_{1/2})TiO_3$-$BaTiO_3$ System for Lead-Free Piezoelectric Ceramics. *Japanese Journal of Applied Physics* **1991**, *30* (9S), 2236. DOI: 10.1143/JJAP.30.2236.

(30) Song, T. B.; Yokoyama, T.; Stoumpos, C. C.; Logsdon, J.; Cao, D. H.; Wasielewski, M. R.; Aramaki, S.; Kanatzidis, M. G. Importance of Reducing Vapor Atmosphere in the Fabrication of Tin-Based Perovskite Solar Cells. *Journal of the American Chemical Society* **2017**, *139* (2), 836-842. DOI: 10.1021/jacs.6b10734.

(31) Li, B.; Di, H. X.; Chang, B. H.; Yin, R. Y.; Fu, L.; Zhang, Y. N.; Yin, L. W. Efficient Passivation Strategy on Sn Related Defects for High Performance All-Inorganic $CsSnI_3$ Perovskite Solar Cells. *Advanced Functional Materials* **2021**, *31* (11). DOI: 10.1002/adfm.202007447.

(32) Sun, H.; Zhou, J.; Qiu, J. Recent advances in bismuth activated photonic materials. *Progress in Materials Science* **2014**, *64*, 1-72. DOI: https://doi.org/10.1016/j.pmatsci.2014.02.002.

(33) Gao, J.; Zeng, W.; Tang, B.; Zhong, M.; Liu, Q.-J. Optical, electronic, and mechanical properties of p-type conductive oxide BaBiO3: A density functional theory study. *Chemical Physics Letters* **2020**, *761*, 138054. DOI: https://doi.org/10.1016/j.cplett.2020.138054.

(34) Bhatia, A.; Hautier, G.; Nilgianskul, T.; Miglio, A.; Sun, J.; Kim, H. J.; Kim, K. H.; Chen, S.; Rignanese, G.-M.; Gonze, X.; et al. High-Mobility Bismuth-based Transparent p-Type Oxide from High-Throughput Material Screening. *Chemistry of Materials* **2016**, *28* (1), 30-34. DOI: 10.1021/acs.chemmater.5b03794.

(35) Tayebi, M.; Lee, B.-K. Recent advances in BiVO4 semiconductor materials for hydrogen production using photoelectrochemical water splitting. *Renewable and Sustainable Energy Reviews* **2019**, *111*, 332-343. DOI: https://doi.org/10.1016/j.rser.2019.05.030.

(36) Brito, J. F. d.; Corradini, P. G.; Zanoni, M. V. B.; Marken, F.; Mascaro, L. H. The influence of metallic Bi in BiVO4 semiconductor for artificial photosynthesis. *Journal of Alloys and Compounds* **2021**, *851*, 156912. DOI: https://doi.org/10.1016/j.jallcom.2020.156912.

(37) Mullens, B. G.; Marlton, F. P.; Brand, H. E. A.; Maynard-Casely, H. E.; Everett, M.; Tucker, M. G.; Van Auken, E. R.; Manjon-Sanz, A. M.; Baldinozzi, G.; Vornholt, S. M.; et al. The Local-Scale Origin of Ferroic Properties in BiVO4. *Journal of the American Chemical Society* **2025**, *147* (9), 7840-7848. DOI: 10.1021/jacs.4c18032.

(38) Kittel, C. *Introduction to solid state physics*; Wiley, 2005.

(39) Cutler, M.; Mott, N. F. Observation of Anderson Localization in an Electron Gas. *Physical review* **1969**, *181* (3), 1336-1340. DOI: 10.1103/PhysRev.181.1336.

(40) Kittel, C.; Masi, J. F. Introduction to Solid State Physics. *Physics today* **1954**, *7* (8), 18-19. DOI: 10.1063/1.3061720.

(41) Kumar, R. Metal Oxides-Based Nano/Microstructures for Photodegradation of Microplastics. *Advanced Sustainable Systems* **2023**, *7* (6), 2300033. DOI: https://doi.org/10.1002/adsu.202300033.

(42) Kim, M.; Kwon, B.; Joo, C. W.; Cho, M. S.; Jang, H.; Kim, Y. j.; Cho, H.; Jeon, D. Y.; Cho, E. N.; Jung, Y. S. Metal oxide charge transfer complex for effective energy band tailoring in multilayer optoelectronics. *Nature Communications* **2022**, *13* (1), 75. DOI: 10.1038/s41467-021-27652-3.

(43) Sayyad, P. W.; Park, S. J.; Ha, T. J. Recent advances in biosensors based on metal-oxide semiconductors system-integrated into bioelectronics. *Biosens Bioelectron* **2024**, *259*, 116407. DOI: 10.1016/j.bios.2024.116407 From NLM.

(44) Dong, W.; Tong, Y.; Zhu, B.; Xiao, H.; Wei, L.; Huang, C.; Wang, B.; Wang, X.; Kim, J.-S.; Wang, H. Semiconductor TiO_2 thin film as an electrolyte for fuel cells. *Journal of Materials Chemistry A* **2019**, *7* (28), 16728-16734, 10.1039/C9TA01941C. DOI: 10.1039/C9TA01941C.

(45) Ray, P. J. Structural investigation of $La_{(2-x)}Sr_{(x)}CuO_{(4+y)}$. 2016.

(46) Bardeen, J.; Cooper, L. N.; Schrieffer, J. R. Theory of Superconductivity. *Physical Review* **1957**, *108* (5), 1175-1204. DOI: 10.1103/PhysRev.108.1175.

(47) Encyclopedia of Materials: Technical Ceramics and Glasses - ResearchAndMarkets.com. *Journal of Engineering* **2021**, 548.

(48) Onnes, H. K. Further Experiments with Liquid Helium. D. On the Change of the Electrical Resistance of Pure Metals at very low Temperatures, etc. V. The Disappearance of the resistance of mercury. In *Through Measurement to Knowledge: The Selected Papers of Heike Kamerlingh Onnes 1853–1926*, Onnes, H. K., Gavroglu, K., Goudaroulis, Y. Eds.; Springer Netherlands, 1991; pp 264-266.

(49) Hashimoto, T.; Kawazoe, H.; Shimamura, H. Effects of substitution of Bi with Pb in $BaBi_{1-x}Pb_xO_3$ on crystal structure and conduction behavior. *Physica. C, Superconductivity* **1994**, *223* (1-2), 131-139. DOI: 10.1016/0921-4534(94)90705-6.

(50) Zhu, H.; Han, H. Charge density wave in low dimensional materials. *Journal of physics. Conference series* **2022**, *2338* (1), 12028. DOI: 10.1088/1742-6596/2338/1/012028.

(51) Peierls, R. E. *Quantum theory of solids*; Clarendon, 1955.

(52) Thorne, R. E. Charge-Density-Wave Conductors. *Physics today* **1996**, *49* (5), 42-47. DOI: 10.1063/1.881498.

(53) Luo, H.; Xie, W.; Tao, J.; Inoue, H.; Gyenis, A.; Krizan, J. W.; Yazdani, A.; Zhu, Y.; Cava, R. J. Polytypism, polymorphism, and superconductivity in $TaSe_{2-x}Te_x$. *Proceedings of the National Academy of Sciences - PNAS* **2015**, *112* (11), E1174-E1180. DOI: 10.1073/pnas.1502460112.

(54) Ma, D.-L.; Bag, P.; Kuo, Y.-K.; Kuo, C.-N.; Lue, C. S. Thermoelectric and specific heat characteristics of the charge density wave compounds RTe_3 = (*R* = Gd, Tb, Dy, Ho, and Er). *Physical Review B* **2025**, *111* (16), 165420. DOI: 10.1103/PhysRevB.111.165420.

(55) Saint-Paul, M.; Remenyi, G.; Guttin, C.; Lejay, P.; Monceau, P. Thermodynamic and critical properties of the charge density wave system $ErTe_3$. *Physica B: Condensed Matter* **2017**, *504*, 39-46. DOI: https://doi.org/10.1016/j.physb.2016.10.009.

(56) Schwarz, K.; Blaha, P.; Woike, T.; Schaniel, D. DFT calculations of solids in the ground state. Walter de Gruyter GmbH, 2018; pp 67-100.

(57) Bouwmeester, R. L.; Brinkman, A. $BaBiO_3$—From single crystals towards oxide topological insulators. *Reviews in Physics* **2021**, *6*, 100056. DOI: https://doi.org/10.1016/j.revip.2021.100056.

(58) Holleman, A. F.; Wiberg, E. *Holleman-Wiberg's Inorganic Chemistry*; Academic Press 2001.

(59) Long, Y.; Saito, T.; Tohyama, T.; Oka, K.; Azuma, M.; Shimakawa, Y. Intermetallic charge transfer in *A*-site-ordered double perovskite $BiCu_3Fe_4O_{12}$. *Inorganic chemistry* **2009**, *48* (17), 8489-8492.

(60) Yamada, I.; Takata, K.; Hayashi, N.; Shinohara, S.; Azuma, M.; Mori, S.; Muranaka, S.; Shimakawa, Y.; Takano, M. A perovskite containing quadrivalent iron as a charge-disproportionated ferrimagnet. *Angewandte Chemie* **2008**, *120* (37), 7140-7143.

(61) Wang, X.; Chai, Y.; Zhou, L.; Cao, H.; Cruz, C.; Yang, J.; Dai, J.; Yin, Y.; Yuan, Z.; Zhang, S. Observation of magnetoelectric multiferroicity in a cubic perovskite system: $LaMn_3Cr_4O_{12}$. *Physical review letters* **2015**, *115* (8), 087601.

(62) da Silva, E. A.; de Candido, S. D.; Abbate, M. Electronic, magnetic and optical properties of the charge-disproportionated $YNiO_3$ compound calculated using the GGA+U method. *RSC Advances* **2024**, *14* (26), 18291-18295, 10.1039/D4RA01908C. DOI: 10.1039/D4RA01908C.

(63) Morrow, R.; Mishra, R.; Restrepo, O. D.; Ball, M. R.; Windl, W.; Wurmehl, S.; Stockert, U.; Büchner, B.; Woodward, P. M. Independent ordering of two interpenetrating magnetic sublattices in the double perovskite Sr_2CoOsO_6. *Journal of the American Chemical Society* **2013**, *135* (50), 18824-18830.

(64) Kanungo, S.; Yan, B.; Jansen, M.; Felser, C. Ab initio study of low-temperature magnetic properties of double perovskite Sr_2FeOsO_6. *Physical Review B* **2014**, *89* (21), 214414.

(65) Sun, Q.; Yang, Z. The charge disproportionation and electric properties of perovskite $CaFe_{1-x}Co_xO_3$. *Results in Physics* **2021**, *24*, 104198. DOI: https://doi.org/10.1016/j.rinp.2021.104198.

(66) Woodward, P. M.; Cox, D. E.; Moshopoulou, E.; Sleight, A. W.; Morimoto, S. Structural studies of charge disproportionation and magnetic order in CaFeO3. *Physical review. B, Condensed matter and materials physics* **2000**, *62* (2), 844-855. DOI: 10.1103/PhysRevB.62.844.

(67) Matsuura, H.; Mukuda, H.; Miyake, K. Valence skipping phenomena, charge Kondo effect, and superconductivity. *AAPPS Bulletin* **2022**, *32* (1), 30. DOI: 10.1007/s43673-022-00056-1.

(68) Patel, S.; Taraphder, A. Superconductivity, valence skipping, and topological crystalline metallic phase in $AgSnSe_2$. *Physical Review B* **2025**, *111* (2), 024508. DOI: 10.1103/PhysRevB.111.024508.

(69) Zhang, C.; Huang, J.; Zhai, K.; Akhtari, K.; Shen, Z.; Ao, L.; Li, Z.; Qin, F.; Chang, Y.; Zhou, L.; et al. Valence-skipping and quasi-two-dimensionality of superconductivity in a van der Waals insulator. *Nature Communications* **2022**, *13* (1), 6938. DOI: 10.1038/s41467-022-34726-3.

(70) Taraphder, A.; Coleman, P. Heavy-fermion behavior in a negative-*U* Anderson model. *Physical Review Letters* **1991**, *66* (21), 2814-2817. DOI: 10.1103/PhysRevLett.66.2814.

(71) Shannon, R. D. Revised effective ionic radii and systematic studies of interatomic distances in halides and chalcogenides. *Acta Crystallographica Section A* **1976**, *32* (5), 751-767. DOI: 10.1107/S0567739476001551.

(72) Lo, S.; Lin, S.; Wang, Y.; Lin, S.; Liang, C. T. Spin-orbit-coupled superconductivity. *Scientific Reports* **2014**, *4* (1), 5438. DOI: 10.1038/srep05438.

(73) Zeng, M.; Xu, D.; Wang, Z.; Hu, L.-H. Spin-orbit coupled superconductivity with spin-singlet nonunitary pairing. *Physical review. B* **2023**, *107* (9). DOI: 10.1103/PhysRevB.107.094507.

(74) Temerov, F.; Baghdadi, Y.; Rattner, E.; Eslava, S. A Review on Halide Perovskite-Based Photocatalysts: Key Factors and Challenges. *ACS Applied Energy Materials* **2022**, *5* (12), 14605-14637. DOI: 10.1021/acsaem.2c02680.

(75) Bibi, N.; Usman, M.; Ruyhan. A theoretical investigation of ABO_3 (*A*=Na and *B* = Ti, In) perovskites for solar cell and optoelectronic applications. *Materials Science in Semiconductor Processing* **2025**, *186*, 109047. DOI: https://doi.org/10.1016/j.mssp.2024.109047.

(76) Wang, H.; Kosasih, F. U.; Yu, H.; Zheng, G.; Zhang, J.; Pozina, G.; Liu, Y.; Bao, C.; Hu, Z.; Liu, X.; et al. Perovskite-molecule composite thin films for efficient and stable light-emitting diodes. *Nature Communications* **2020**, *11* (1), 891. DOI: 10.1038/s41467-020-14747-6.

(77) Huang, S.; Guo, M.; Tan, J.; Geng, Y.; Wu, J.; Tang, Y.; Su, C.; Lin, C. C.; Liang, Y. Novel Fluorescence Sensor Based on All-Inorganic Perovskite Quantum Dots Coated with Molecularly Imprinted Polymers for Highly Selective and Sensitive Detection of Omethoate. *ACS Applied Materials & Interfaces* **2018**, *10* (45), 39056-39063. DOI: 10.1021/acsami.8b14472.

(78) Zhang, Q.; Shang, Q.; Su, R.; Do, T. T. H.; Xiong, Q. Halide Perovskite Semiconductor Lasers: Materials, Cavity Design, and Low Threshold. *Nano Letters* **2021**, *21* (5), 1903-1914. DOI: 10.1021/acs.nanolett.0c03593.

(79) Tian, J.; Tan, Q. Y.; Wang, Y.; Yang, Y.; Yuan, G.; Adamo, G.; Soci, C. Perovskite quantum dot one-dimensional topological laser. *Nature Communications* **2023**, *14* (1), 1433. DOI: 10.1038/s41467-023-36963-6.

(80) Kong, X.; Yang, L.; Meng, F.; Zhang, T.; Zhang, H.; Lin, Y.; Huang, H.; Zhang, S.; Guo, J.; Nan, C. High-entropy engineered $BaTiO_3$-based ceramic capacitors with greatly enhanced high-temperature energy storage performance. *Nature Communications* **2025**, *16* (1), 885. DOI: 10.1038/s41467-025-56195-0.

(81) König, M.; Wiedmann, S.; Brüne, C.; Roth, A.; Buhmann, H.; Molenkamp, L. W.; Qi, X.; Zhang, S. Quantum Spin Hall Insulator State in HgTe Quantum Wells. *Science (American Association for the Advancement of Science)* **2007**, *318* (5851), 766-770. DOI: 10.1126/science.1148047.

(82) Witting, I. T.; Chasapis, T. C.; Ricci, F.; Peters, M.; Heinz, N. A.; Hautier, G.; Snyder, G. J. The Thermoelectric Properties of Bismuth Telluride. *Advanced Electronic Materials* **2019**, *5* (6), 1800904. DOI: https://doi.org/10.1002/aelm.201800904 (acccessed 2025/06/28).

(83) Topological insulators. *Scholarpedia* **2015**, *10*, 30275.

(84) Chen, X.; Ma, X.-C.; He, K.; Jia, J.-F.; Xue, Q.-K. Molecular Beam Epitaxial Growth of Topological Insulators. *Advanced Materials* **2011**, *23* (9), 1162-1165. DOI: https://doi.org/10.1002/adma.201003855 (acccessed 2025/06/28).

(85) Scholder, R.; Ganter, K. W.; Gläser, H.; Merz, G. Über Alkali- und Erdalkalioxobismutate(V). *ZAAC - Journal of Inorganic and General Chemistry* **1963**, *319* (5-6), 375-386, Article. DOI: 10.1002/zaac.19633190518 Scopus.

(86) Yan, B.; Jansen, M.; Felser, C. A large-energy-gap oxide topological insulator based on the superconductor $BaBiO_3$. *Nature Physics* **2013**, *9* (11), 709-711.

(87) Loret, B.; Forget, A.; Moussy, J.-B.; Poissonnet, S.; Bonnaillie, P.; Collin, G.; Thuéry, P.; Sacuto, A.; Colson, D. Crystal Growth and Characterization of $HgBa_2Ca_2Cu_3O_{8+\delta}$ Superconductors with the Highest Critical Temperature at Ambient Pressure. *Inorganic Chemistry* **2017**, *56* (16), 9396-9399. DOI: 10.1021/acs.inorgchem.7b01372.

(88) Grant, P. M. The great quantum conundrum. *Nature* **2011**, *476* (7358), 37-39. DOI: 10.1038/476037a.

(89) Breeze, P. Chapter 5 - Superconducting Magnetic Energy Storage. In *Power System Energy Storage Technologies*, Breeze, P. Ed.; Academic Press, 2018; pp 47-52.

(90) Zhou, L.; Guo, X.; Lin, Z.; Ma, J.; Su, J.; Hu, Z.; Zhang, C.; Liu, S. F.; Chang, J.; Hao, Y. Interface engineering of low temperature processed all-inorganic $CsPbI_2Br$ perovskite solar cells toward PCE exceeding 14%. *Nano Energy* **2019**, *60*, 583-590.

(91) Xing, G.; Mathews, N.; Sun, S.; Lim, S. S.; Lam, Y. M.; Grätzel, M.; Mhaisalkar, S.; Sum, T. C. Long-range balanced electron-and hole-transport lengths in organic-inorganic $CH_3NH_3PbI_3$. *Science* **2013**, *342* (6156), 344-347.

(92) Igbari, F.; Wang, Z. K.; Liao, L. S. Progress of lead-free halide double perovskites. *Advanced Energy Materials* **2019**, *9* (12), 1803150.

(93) Zhang, Z.; Sun, Q.; Lu, Y.; Lu, F.; Mu, X.; Wei, S.-H.; Sui, M. Hydrogenated $Cs_2AgBiBr_6$ for significantly improved efficiency of lead-free inorganic double perovskite solar cell. *Nature Communications* **2022**, *13* (1), 3397. DOI: 10.1038/s41467-022-31016-w.

(94) Lyu, M.; Yun, J. H.; Chen, P.; Hao, M.; Wang, L. Addressing toxicity of lead: progress and applications of low-toxic metal halide perovskites and their derivatives. *Advanced Energy Materials* **2017**, *7* (15), 1602512.

(95) Yang, J.; Bao, C.; Ning, W.; Wu, B.; Ji, F.; Yan, Z.; Tao, Y.; Liu, J. M.; Sum, T. C.; Bai, S. Stable, high-sensitivity and fast-response photodetectors based on lead-free $Cs_2AgBiBr_6$ double perovskite films. *Advanced Optical Materials* **2019**, *7* (13), 1801732.

(96) Guo, K.; Lin, P.; Wu, D.; Shi, Z.; Chen, X.; Han, Y.; Tian, Y.; Li, X. Cs2AgBiCl6: a Novel, High-Efficient and Stable Visible-Light Photocatalyst for Degradation of Organic Dyes. *Chemistry – A European Journal* **2023**, *29* (35), e202300400. DOI: https://doi.org/10.1002/chem.202300400 (acccessed 2025/08/21).

Chapter 2 Experiment Methods

2.1 Synthetic Methods

2.1.1 Solid State Synthetic Methods

The typical method of solid-state synthesis involves repeatedly mixing and heating stoichiometric reagents at a suitably high temperature. In general, the temperature is close to, but below, the reagents melting points. This method usually involves a mixture of dried metal oxides. The preparation of the mixture typically involves the repeated grinding of a stoichiometric ratio of the reactants in an agate mortar and pestle, often in the presence of milling media (in this thesis, acetone and ethanol were employed) to ensure maximum interparticle contact. In thermodynamic system, the synthesis heating temperature of crystalline materials, including even nanoscale metallic solid-phase materials, is determined by the melting points of the reactants. According to Tammann's rule, the ideal temperature -- a Tammann temperature, $T_{Tammann}$, is given by the simple relationship:

$$T_{Tammann} = \beta \times T_{mp} \quad (2.1)$$

The β value is a constant (normally considered as 0.5) which is generally independent of the material properties.[1]

When the reaction temperature exceeds the threshold of $T_{Tammann}$, atoms or ions become capable of migrating or diffusing within the bulk crystal lattice. Prolonged isothermal heating at elevated temperatures facilitates the completion of crystallization and sintering processes at a constant rate.

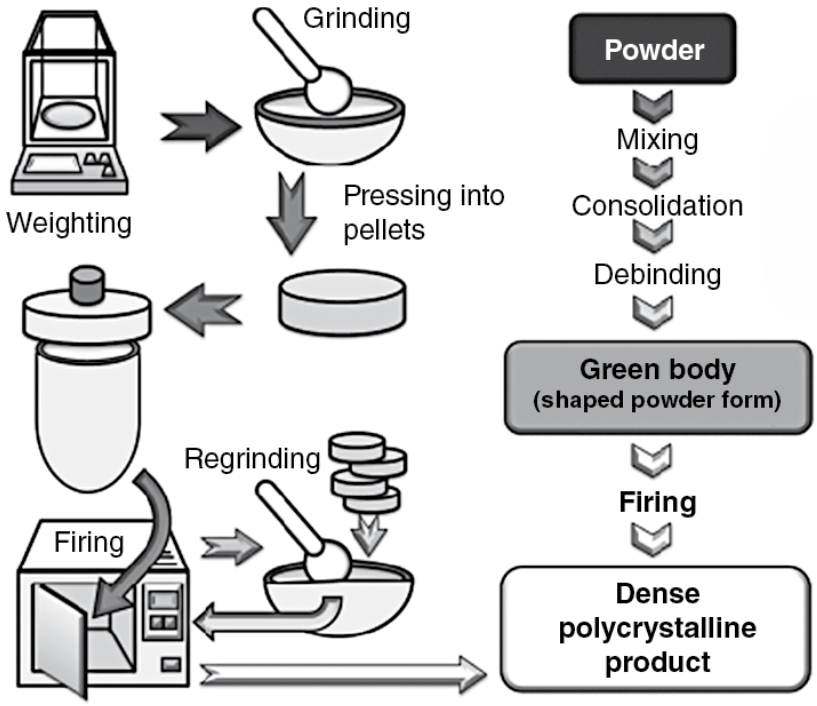

Figure 2.1: The representation of reaction scheme for solid state synthesis at standard atmospheric pressure. Typically synthesis requires regrinding and re-heat several times to phase pure crystalline products.[2]

The chemical reagents used in the synthesis for $BaBiO_3$, $Ba_{1-x}K_xBiO_3$ and $BaBi_{1-x}Pb_xO_{3-1/2x}$ were prepared with analytical grade (> 99.5 %; provided by Merck). The sample of $BaBiO_3$ was prepared by two-step heating solid state method with Bi_2O_3 and $BaCO_3$ in a stoichiometric ratio, heating to around 800 ◦C. The doped samples required additional element contained regents to replace specific reagents (e.g. PbO_2 replace Bi_2O_3, K_2CO_3 replace $BaCO_3$). The synthesis method for $BaBiO_3$, $Ba_{1-x}K_xBiO_3$ and $BaBi_{1-x}Pb_xO_{3-1/2x}$ are based on literature reports.[3, 4]

For example, to synthesize 3 g $BaBi_{0.7}Pb_{0.3}O_{2.85}$ (7.67 mmol). The sample requires 7.67 mmol of Ba^{2+}, 5.369 mmol of Bi^{3+} and 2.301 mmol of Pb^{4+}. These are obtained from 1.514 g of $BaCO_3$ (7.67 mmol), 1.251 g of Bi_2O_3 (2.6845 mmol Bi_2O_3, as it contains 2 mmol Bi^{3+} ions within 1 mmol Bi_2O_3) and 0.55 g of PbO_2 (2.301 mmol). The reaction processes as follows:

$$2\ BaCO_{3(s)} + 0.35\ Bi_2O_{3(s)} + 0.6\ PbO_{2(s)} \rightarrow 2\ BaBi_{0.7}Pb_{0.3}O_{2.85(s)} + CO_{2(g)} + n_{excess}O_{2(g)}$$

2.1.2 Hydrothermal Synthesis Methods

Most metals, binary metal oxides and even non-metal elements are insoluble in conventional solutions (e.g. water or ethanol). This behaviour is a result of a combination of strong ionic and/or covalent bonds.[5] Therefore, hydrothermal synthesis is used with a flux (e.g. polar solvent or hydroxide fluxes) or strong acid/base to reduce the energy required to decompose the crystal structure of their starting reagent, and achieve the crystallization at the temperature of the crystal growth zone (normally through high-temperature dissolution followed by crystallization at a lower temperature, which is named as the temperature-difference method).

Cs_2AgBX_6 (B = In, Bi; X = Cl, Br) were prepared by two different methods. All reagents were analytical grade (>99.9%; provided by Merck and Glenthan). Cs_2AgBiX_6 reacted by hydrothermal method: CsCl (or CsBr), $AgNO_3$ and $BiCl_3$ (or $BiBr_3$) in a stoichiometric ratio of 2:1:1 were dissolved in the corresponding acid (HCl or HBr) and heated to approximately 150 °C. Cs_2AgInX_6 was also prepared by a solid state method. A mixture of CsCl, AgCl and $InCl_3$ in a stoichiometric ratio of 2:1:1 was finely mixed and then heated at 210 °C for 72 hours three times, with intermediate grinding.[6]

The synthesis of $Cs_2AgBiBr_6$ required extra conditions. $BiBr_3$ has a melting point about 219 °C. This low melting point limits the temperature for solid-state synthesis as it is much lower than the Tammann temperature of the other reagents ($T_{Tammann}$ for CsBr ~ 318 °C, $T_{Tammann}$ for AgBr ~ 216 °C). This results in low efficiency of atom migration through the crystal lattice resulting in incomplete reaction. The feasibility of dissolving the silver salts in concentrated acid facilitates hydrothermal synthesis which becomes the preferred technique.[7] $Cs_2AgBiBr_6$ was prepared from a solution of AgBr (0.942 mmol) dissolved in 47% HBr (10 ml at 110°C), to which was sequentially added CsBr (1.884 mmol) and $BiBr_3$ (0.942 mmol). The solvent was partially evaporated at 110 °C for 4 hours to crystallise the product, then that was collected by filtration. The reaction process as:

$$2CsBr_{(aq)} + AgBr_{(aq)} + BiBr_{3\,(aq)} \xrightarrow{HBr_{(aq)}} Cs_2AgBiBr_{6\,(s)}$$

The reaction yielded approximately 0.712 g of orange-red crystal (71.2 %), but the product cannot be dried above 200 °C.

2.2 Long-Range Diffraction Determine Technique

Since the crystallographic arrangement of atoms in a solid determine its functionality, determining the structure is a critical step in solid-state chemistry. Therefore, it is important to use a technique that can investigate and locate atoms within a Bravais lattice without destroying the sample.

X-ray diffraction has demonstrated remarkable reliability and utility as a method for elucidating the structure of crystalline materials for over a century. *X*-ray diffraction traces its origins to the serendipitous discovery of *X*-rays by Wilhelm Röntgen in 1895. Approximately seventeen years later, the German crystallographers Paul Peter Ewald and Max von Laue introduced the foundational theory of *X*-ray diffraction by crystals, subsequently producing the earliest diffraction pattern of zinc blende.[8] The theoretical framework of this method was later formalized by the physicist William Lawrence Bragg and his father, William Henry Bragg, who were instrumental in the advancement and perfection of crystal diffraction techniques.[9]

Bragg diffraction can occur if the wavelength of an incident beam of photons is similar to the atomic spacing within a lattice. As illustrated in Figure 2.2 photons are scatted from periodically arranged atom within planes rather than scattered from random point atom. The atomic spacing and distance between emitted wave 1 and wave 2 and the atomic planes arranged particles is a function of the angle of incident wavelength λ as labelled in Figure 2.3. Consider incident, coherent, photons, designated as *A* and *B*, with wavevectors $\vec{k}_A$ and $\vec{k}_B$ respectively. An atom in the upper parallel atomic plane (referred to as particle *A*) elastically scatters photon *A*, while photon *B* is elastically scattered by a lower parallel atomic plane (referred to as particle *B*). The interplanar spacing between these atomic layers is denoted by

d. Both photons are scattered at an angle of 2θ, however photon *B* travels an additional path length of *dsin*θ compared to photon *A*. For constructive interference to occur between the scattered wavefronts of photons A and B, their phase difference must correspond to an integer multiple of the photon wavelength. This implies that the extra path length traversed by photon B must equal $n\lambda$, where *n* is a positive integer and λ is the photon wavelength.

This condition yields the Bragg's law equation:

$$2d\ sin(\theta) = n\lambda \tag{2.2}$$

In crystallography, the representation of the reciprocal space concept has a ground-breaking effect on the validation of Bragg's law. It is evident that the $n\lambda$ term in Bragg's law equation 2.2, that measures the number of wavelengths between two atomic layers, is valid as if the distance is inversely proportional to distance *d*. If the incident vector is denoted by $\vec{k}_i$, and the scattering resulting from the beam passing through the crystal is denoted as $\vec{k}_f$, then in the vector equation $\vec{Q} = \vec{k}_f - \vec{k}_i$, known as the Laue equation, $\vec{Q}$ represents the reciprocal lattice vector. Considering the diffraction process as a Fourier transform of the spatial crystal structure into reciprocal space, a Fourier transform under the condition of momentum transfer conservation through equation 2.2 establishes the relationship between the diffraction angle and *Q* space, which is elaborated on in Equation 2.3:

$$Q = \frac{4\pi\ sin(\theta_i)}{\lambda_i} \tag{2.3}$$

The Bragg condition $|\vec{k}_i| = |\vec{k}_f|$ and $\lambda_i = \lambda_f$, is only satisfied for elastic scattering within point-like conditions.

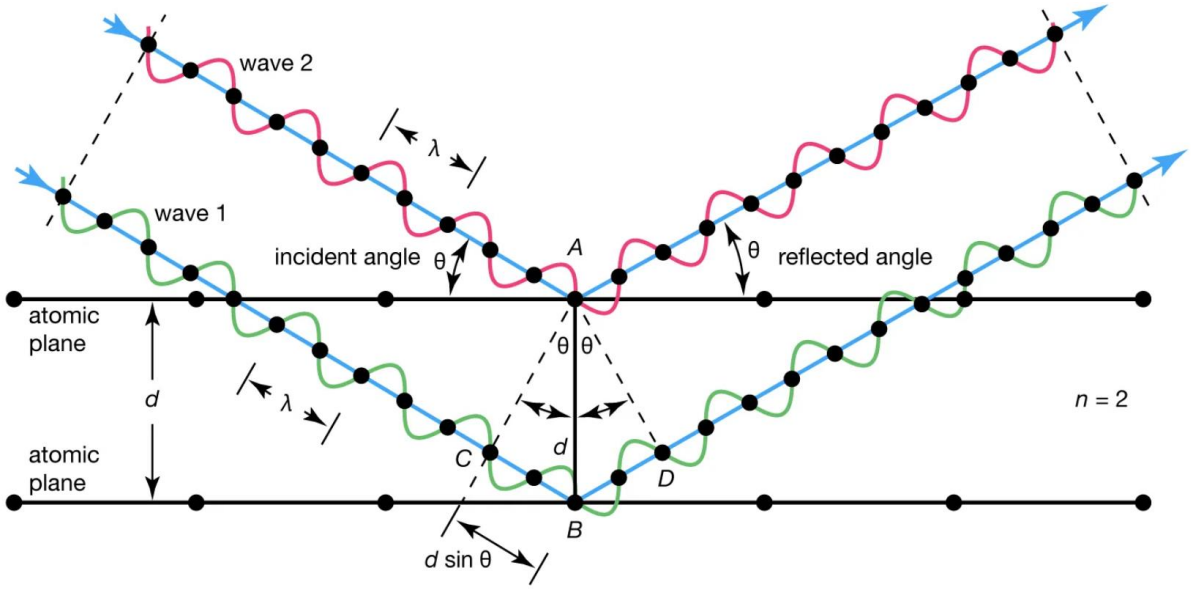

Figure 2.2: Schematic representation diagram of Bragg diffraction, the black dots represent atoms and black lines is lattice plane. The incident waves 1 (red) and 2 (green) represent photons scattering from atom *A* and atom *B* respectively. The distance between the waves is an integer multiple of the wavelength.

Upon satisfying the Bragg condition, Bragg diffraction is obtained. Prior to the 1960s, crystallographer determined interatomic distance and other lattice information through systematically comparing collected diffraction pattern. Even with current refinement techniques, the approach of analysing a two-dimensional diffraction pattern and extending to three-dimensional space remains a challenging. Referring to Bragg's Equation 2.2, diffraction is achieved by maintaining a constant wavelength while rotating the detector angle to collect intensity reflections from different planar layers, which are demonstrated as a diffraction pattern. Each of planes are known as Miller plane, as demonstrated in Figure 2.4, where three-dimensional planes are represented by three indicates, *h,k,l*.

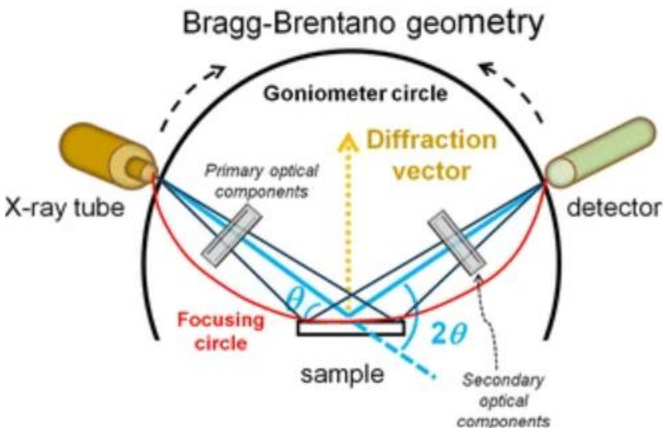

Figure 2.3: The representation of X-ray diffraction instrument with Bragg–Brentano geometry. The incident angle is modified by moving detector and X-ray tube.[10]

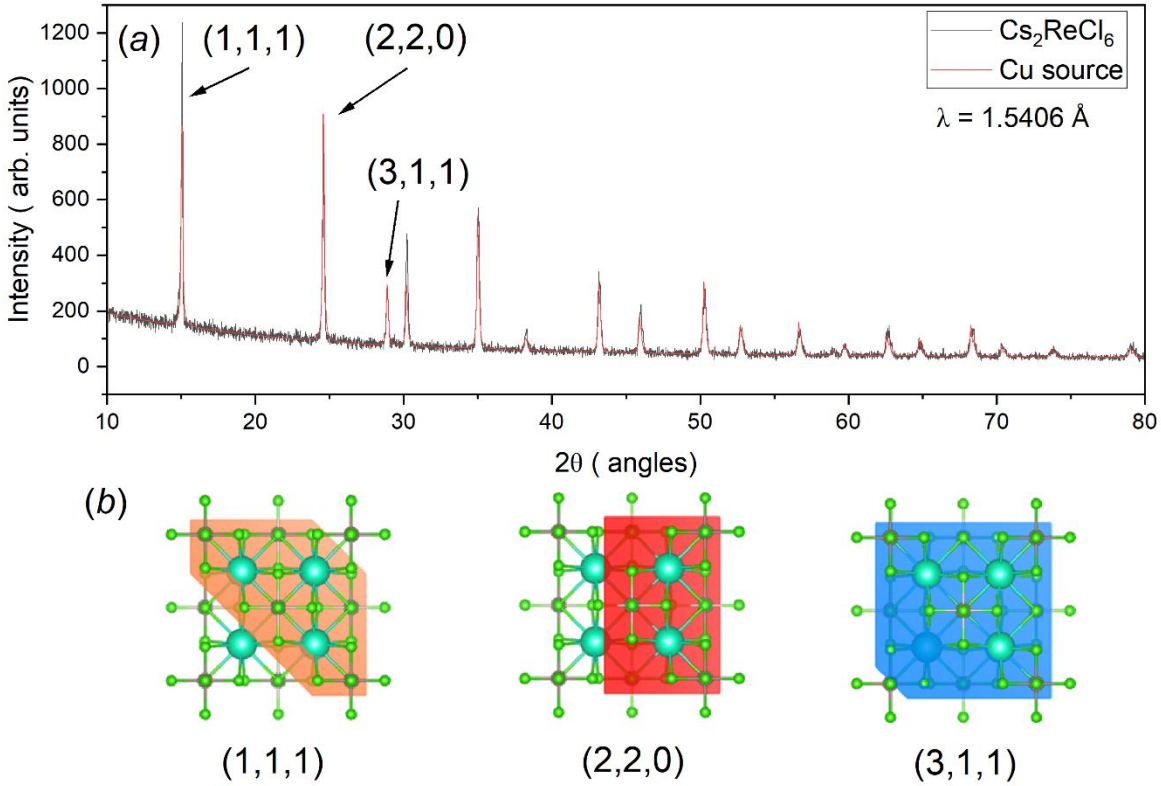

Figure 2.4: X-ray diffraction pattern of Cs_2ReCl_6 with crystal structure Fm-3m, as collected using (a) Panalytical X'Pert Pro copper source diffractometer, and (b) represented Miller indices (hkl) and obseved lattice planes in Cs_2ReCl_6.

Ewald indicated that the *hkl* planes exhibit absolute sensitivity to diffraction, with diffraction occurring exclusively when the sum of $h+k+l$ is equal to a particular value. This phenomenon is correlated through the Ewald sphere, which precisely corresponds to the specific arrangement of the reciprocal lattice.[11] The Ewald sphere theory postulates that as a crystal rotates in real space, its reciprocal space counterpart rotates around the reciprocal coordinate (0,0,0), with *hkl* values determined through the intersection of various lattice points with the sphere, see figure 2.5. The Miller planes derived from the different *hkl* values can be utilized to determine the peak profiles and intensities of Bragg reflections in various crystal structures, thereby facilitating the determination of lattice parameters. In the simplest case of a cubic structure the relationship is expressed as:

$$a = d_{hkl}\sqrt{h^2 + k^2 + l^2} \tag{2.4}$$

Where a determines the lattice spacing within a cubic crystal, it represents any h,k,l value exhibit reflection in simple cubic structures.

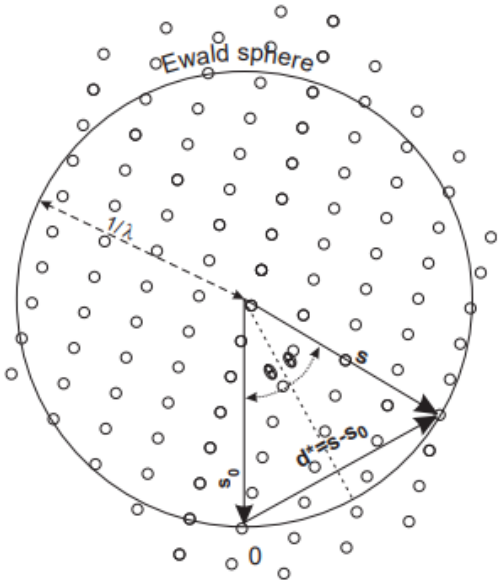

Figure 2.5: Schematic representation of the Ewald sphere within reciprocal space. The origin is at the reciprocal coordinate (0,0,0). The incident beam wavevector cross through origin coordinate and reflected to a detector. The small black circle interpret with Ewald sphere is resulting in appear to

diffraction spots, sample point arrangement represented as particular orientation within crystal. This figure is adopted from reference. [12]

2.2.1 Powder *X*-ray Diffraction

Laboratory powder X-ray diffraction (PXRD) serves as the most commonly used instrument for crystallographic analysis in laboratory settings, across various institutions and industries. Its fundamental functionalities encompass, but are not limited to, crystalline structure composition analysis (e.g. distinguishing between various organic and inorganic phase) and grain strain analysis. In the present thesis two diffractometers Rigaku SmartLab SE and STOE P were extensively used for powder X-ray diffraction measurements.

Normally, the principle of *X*-ray diffraction involved irradiating a crystal with *X*-rays and collecting the intensity of diffraction ray by continuously adjusting the angle (within a 2θ range) of the detector, thereby revealing the crystal structure. The generation of *X*-ray is achieved by heating a refractory metal to a high temperature, where thermal energy accelerated ions to the metal anode target (typically made of copper). Upon collision, high-energy electrons interact with the inner shell (*K*-shell) electrons of the target element – leading to the ejection of an electron and the creation of core holes. To fill these core holes, higher-energy electrons transition to *K*-shell. An energy lost in the transition process is emitted as *X*-rays.

The Rigaku SmartLab SE uses a Cu anode to produce *X*-ray (about wavelength $\lambda K\alpha 1$ = 1.5406 Å and $\lambda K\alpha 2$ = 1.5444 Å, respectively). The STOE-P diffractometer is equipped with a Mo anode (monochromated wavelength $\lambda K\alpha 1$ = 0.7093 Å). Diffraction characterization techniques derive data based on the wavelength of the anode target materials.

The Rigaku SmartLab was operated in a Bragg-Brentano, $\theta - 2\theta$, geometry with flat plate sample holder. It is equipped with a PhotonMax high-flux 9 kW rotating copper anode source that generates the *X*-rays. The diffracted X-rays are measured via a HyPix-3000 high-energy-resolution 2D multidimensional semiconductor detector that was rotated at a rate of 0.75 θ

min^{-1}. A large angular range ($0 < 2\theta \leq 155°$) was used to enable precise quantification of different phases and distribute accurate Bragg reflection within entire 2θ range.

The STOE Stadi P is configured in Debye-Scherrer diffraction geometry and has three Mythen strip detectors. Data collected over angular range from 0 - 56°. Although the Mythen detectors function similarly to detectors of Rigaku, the distance between these and the sample is shorter, resulting in broader peaks (lower peak shape resolution). Consequently, the STOE was primarily used to study temperature-dependent phase transitions rather than survey samples for the presence of minor impurities. In the Debye-Scherrer method the sample is contained in a narrow diameter thing walled glass or quartz capillary. In this work capillaries of 0.2-0.5 mm dia. were used. This reduced the amount of sample required compared with Rigaku diffractometer. Temperature control was achieved using either an Oxford cryostream, for low temperatures (80-400 K) or an FMB hit air blower for temperatures between 400 and 1300 K.

2.2.2 Synchrotron *X*-Ray Diffraction

The precision and uniqueness of S-XRD in analysing the atomic arrangement and molecular structure of materials has seen its widespread use across the globe. Compared with traditional laboratory XRD, S-XRD offers numerous advantages: S-XRD features a light source intensity far exceeding that of ordinary XRD (e.g. S-XRD can rapidly conduct *in-situ* measurements and acquire high-resolution data for a large number of sample). Additionally, the wavelength of the X-rays can be tuned and enabling radiation from ~2 keV to 100 keV. Therefore, synchrotron scientist can modify the radiation intensity based on anomalous scattering or maintain the radiation energy at the minimum level of fluorescence according to the material properties.

The principle of synchrotron radiation is based on electromagnetic radiation emitted through accelerated charged particle, thus synchrotron also named *Magnetobremsstrahlung*.[13] The charged particles imparting substantial acceleration with the influence of electromagnetic forces. When the velocity of these electrons approaches to the speed of light (when kinetic

energies far outweigh than $m_e c^2$), the application of magnetic field to alter trajectory enables the utilization of the electromagnetic radiation emitted by electrons for diffraction.

The S-XRD data described this dissertation were collected at the powder diffraction beamline BL-10 from Australian Synchrotron, Melbourne. BL-10 beamline can accumulate XRD data with energies ranging from 5 keV to 21 keV.[14] The samples were loaded into 0.2 mm ~ 0.3 mm capillaries. A bank of 16 1-D Mythen detectors were used to compile raw synchrotron data with an angular range from 0˚ to 80 ˚. The space between each strip of Mythen detectors is included by shifting all the detection by 0.5˚. Finally, the raw datasets were merged using the computer software PDviper.2.

2.2.3 Neutron Scattering Experiments

Neutron diffraction data in this for were collected from 300 K to 873 K using the *Nanoscale-Ordered Materials Diffractometer* (NOMAD) and, at 10 K, the *Powder Diffractometer BL-11A* (POWGEN) at the Spallation Neutron Source (ORNL). The samples will be loaded in 6 mm vanadium cans to a height of 20 mm, then heated in an ILL-type high-vacuum furnace fitted with niobium heating elements in a counting time of approximately 4hrs per dataset. It provides adequate signal-to-noise between both Bragg and diffuse scattering, enables an accurate local structural correlation.

2.2.4 Rietveld Refinement and Modelling

Rietveld refinement represents an exceptionally efficient method to refine the structures of crystalline material. Powder diffraction patterns are generated by collecting *X*-rays that have been scattered by randomly oriented crystals within a polycrystalline aggregate. Consequently, each *hkl* plane contributes a peak intensity in accordance with Bragg's law, thereby enabling the determination of interplanar spacings, unit cell parameters and atomic coordinates. However, the peak intensity in polycrystalline aggregates represents the superposition of

intensities from all crystallographic planes satisfying the *hkl* diffraction condition in a one-dimensional diffraction pattern. The intensity of individual peaks is influenced by microstructural factors such as atomic arrangement within the unit cell and crystallite size, which introduce uncertainties in determining the intensity from individual *hkl* reflections. Therefore, in the analysis of powder diffraction patterns, profile fitting techniques are used to enhance the accuracy of crystal structure determination. Initially, it is imperative to identify potential structural models for the material. The expected diffraction pattern of the model is compared to the observed pattern and iterative adjustment of variable parameters within the structure, including the lattice parameters, atomic coordinates, site occupancies and atomic displacements parameters is undertaken. Through continuous iteration of the variable parameters, the simulated diffraction pattern derived from the structural model is progressively optimised against the experimental diffraction pattern.

Rietveld refinement was initially introduced and applied in the refinement of structures from neutron diffraction data in the 1960s by Hugo Rietveld.[15] This refinement approach employs non-linear least squares method as the fitting methodology varying the assignment of intensities in overlapping *hkl* reflections and optimisation of these assignments are a key part of the structural refinement process. Mathematically, non-linear least squares utilize a continuous nonlinear regression model through iterative processes to achieve model fitting. In the context of Rietveld refinement, it comprises comparing the residuals between calculated intensities (Y_i^{cal}) and observed intensities (Y_i^{obs}), staring from an initial structure model.[16] The minimized function represents quantity *M* as:

$$M = \sum_{i=1}^{n} W_i \, (Y_i^{obs} - Y_i^{cal})^2 \qquad (2.5)$$

Where W_i is represented weight value and i is any point within the range of diffraction pattern.

Although visual comparison of the residual plot is a rapid qualitative method to judge the quality of a Rietveld fit the validity of the refined model is best achieved using a combination of a quantitative fit parameters and by examining the chemical validity of the model. R_{wp} is

the most commonly used fit factor used to assess the difference between the observed result and the structural models. In 1982, Young *et al.* proposed that the difference between each observed intensity at i point and the actual intensity be considered as a term with the weight ratio assumed to be n. If the sum of weighted squared differences between all observed values and the model estimated with p parameters equal to $n-p$, the goodness of fit is established. Therefore, the R_{wp} is expressed as:

$$R_{wp} = \left\{ \sum_{i=1}^{n} w_i \left[y_i - M_i(\hat{x}) \right]^2 / \sum_{i=1}^{n} w_i \, y_i^2 \right\}^{1/2} \tag{2.6}$$

R_e, named expected R index which represents the value at $n-p$ equal to expected value. To further examine the fit optimization, "goodness of fit" serves as a criterion for assessing the estimates of uncertainty, specifically through the ratio of R_{wp}/R_e. This aspect will be illustrated in the Appendix alongside with other R indexes.[17]

All diffraction patterns within this thesis were analysed by the Rietveld method using the computing software TOPAS6[15]. This employed the Thompson-Cox-Hastings pseudo-Voigt model in the analyse of the constant wavelength data to explain the axial divergence asymmetry. Gaussian and Lorentzian components were employed. The wavelength of SXRD data was determined through Rietveld refinement of a LaB_6 standard based on certified lattice dimensions. The appropriate Crystallographic Information Files (CIF) were obtained from the Inorganic Cystal Structure Database (ICSD), which specify accurately single crystal lattice parameter and structure information. Refined model parameters include unit cell parameters, atomic coordinated. The atomic displacements parameters (ADP) considered the symmetry constraints for each particular Wyckoff site in the structure. TOPAS calculation cited the data from Wills' table.[18] Finally, VESTA is applied for visualizing different space groups, including calculated bond distance and bond valance sums (BVS) (bond valence parameters refer from IUCr database).[19]

2.3 Short-Range Local Structure Determination

With the continuous exploration and development of an increasing number of materials, the unique properties of certain complex structural materials have hindered the application of conventional X-ray technique. These materials are composed of diverse elements and form unit cells, that may also have short-range aperiodic disorder. However, conventional X-ray diffraction cannot always accurately represent the real configuration at local range. As Bragg law combined with crystallographic symmetry can be inadequate for measuring such local structure distortions, it is vital to use an alternate approach that is capable of accurately representing local distortion.

2.3.1 Pair Distribution Function

Atomic pair distribution function (PDF) is a powerful method to analyse short-range local structure. From a materials chemistry perspective, crystals may contain defects and may incorporate impurities within their lattice interstices, which cannot be detected through conventional X-ray diffraction (XRD) or neutron diffraction techniques. This limitation arises because conventional XRD yields an average crystal structure, that may not account for local structural configurations. The pair distribution function technique is a method that was initially developed to study non-crystalline structures (solutions; glasses) that determines individual interatomic distances, thereby circumventing the interference caused by defects, impurities and even overlapping reflections. Over the past 20-years it has been extended to study local disorder in otherwise crystalline materials. PDF anlaysis applies the total scattering approach which considers both Bragg and diffuse scattering on an equal basis, it means that PDF measurement methods are similar to regular powder diffraction but with a critical difference in how the back-ground scattering is treated. Besides, pair distribution function data support other

valuable structural information about pair-correlation expect nearest-neighbour peak. PDFs can determine quantitatively structural information within range of tens of nanometres by high Q-range.[20]

The feasibility of the PDF analysis method is not limited to the theoretical knowledge of material chemistry or computational chemistry, but it is considered a break-through technique in crystallography analysis. Local structure analysis using PDF techniques enables the detection of atomic or nanoscale distortions and defects facilitating establishing the relationship between the structure and properties of amorphous materials and complex material. CdSe is one of the earliest nanomaterials that used PDF analysis to understand the correlation between particle size and performance. The crystal structure of CdSe is known, however conventional crystallography cannot establish the structure of nano-sized crystallites. PDF was used to successfully refined CdSe structure and to quantify structural compresses and strain resulted by static distortion, demonstrating that the Cd-Se bond distance decreased as particle size reduced.[21] PDF analysis provided the quantitative information on the size-dependent structure and strain in CdSe nanoparticles and provided insight into the feasibility for optimizing the performance of nanomaterials-based materials. In static structures the magnitude of atomic displacements is minimal, and it is considered that atoms maintain correct atomic arrangement from a macroscopic perspective. This is clearly not the case in CdSe nanoparticles, but it was also found to not be the case in the relaxor material $Sr_xBa_{1-x}Nb_2O_6$, the properties of which are influenced by subtle variation in bond lengths. The local structural in complex relaxor ferroelectric materials are often temperature-dependent and sensitive to octahedral tilting, which positively correlates with the ferroelectric properties of materials.[22]

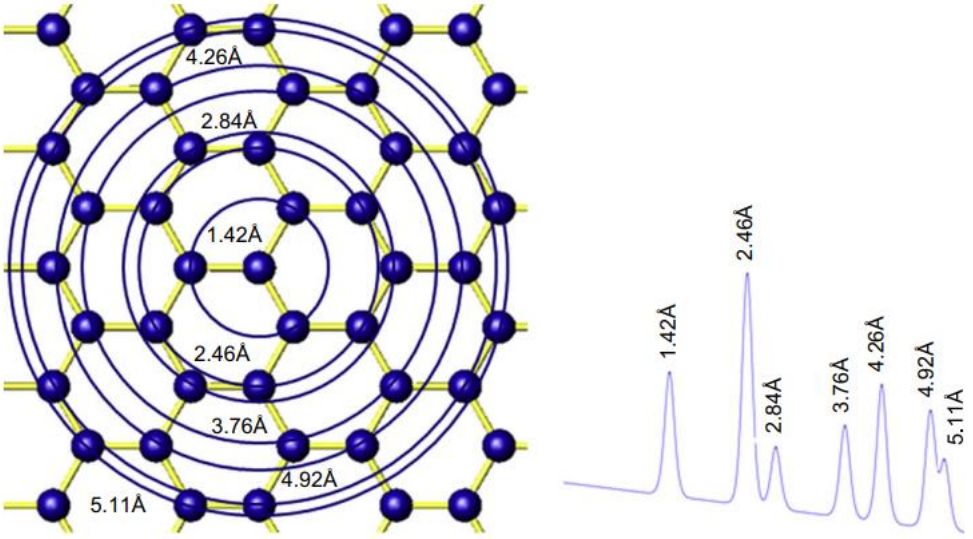

Figure 2.6: Left sketch represents hexagonal lattice of atom, right peaks corresponding to reduced PDF data G(*r*), each bond distances make contributions to peak intensity.[20]

In the total scattering method an explicit correction for external contributions to the experimental data, such as Compton scattering, fluorescence, background etc is required. It will reduce the influence factor $I_{coh}(Q)$. In general, a normalized version of the scattering intensity S(Q) will be considered with Bragg law equations, shown as:

$$S(Q) = \frac{I_{coh}(Q) - \langle f(Q)^2 \rangle + \langle f(Q) \rangle^2}{\langle f(Q) \rangle^2} \qquad (2.7)$$

Where $f(Q)$ is atomic form factor and the angle brackets represents is averaging overall atoms. $S(Q)$ is the total scattering structure function, and it stands for the intensity normalized by the incident flux per atom. The equation undergoes a FabereZiman definition to normalize $\langle S(Q) \rangle$ to 1. The reduced PDF data, G(r), is correlated with $S(Q)$ by a sine Fourier transform, derived as:

$$G(r) = \frac{2}{\pi} \int_{Q_{min}}^{Q_{max}} Q\,[S(Q) - 1] sin(Qr) dQ \qquad (2.8)$$

Equation 2.8 applies an integration to convolute with the broadened instrument resolution function at low Q range. Therefore, the probability density function will be attenuated by Fourier transformation, it results in a faster decay of PDFs with poorer Q resolution. This signal

amplitude decreases faster in samples with structural disorder, which can be an indicator of structural coherence in samples. The correlation is given as:

$$G(r) = 4\pi r(\rho(r) - \rho_0) = 4\pi r\rho_0(g(r) - 1) \qquad (2.9)$$

Where $g(r)$ is PDF, if r is approach to infinite, the $g(r)$ is close to 1. $\rho(r)$ is about the average number density of the material.[20] Normally the range is replaced by Q value set by the instrumentation, instead of infinite ∞. In this project, Q_{max} is limited with 30 Å^{-1} in NOMAD, and Q_{max} = ~ 32 Å^{-1} in POWGEN.

Figure 2.7 exhibits two of the most important parameters in PDF modelling. Beyond the physical limitations inherent in the detection instruments, the G(r) data determines the effective Q range after Fourier transformation. The Nyquist-Shannon sampling theorem indicates that the minimum effective interval is defined as $\Delta r = \pi/Q_{max}$. Consequently, a higher Q_{max} can minimize truncation effects and achieve optimal resolution. From Figure 2.7, the position of PDF peak directly indicates the average atomic distance, while the variation in PDF peak width (FWHM) is attributed to either static structural distortions or dynamic structural distortions. These two distinct types of distortions can be broadly categorized as: distortions arising from thermal atomic motion resulted by thermodynamic factor, disorder induced by doping, and disorder or amorphization caused by nanoscale dimensions. Distortions resulted by thermal atomic motion and doping will be considered in this dissertation. The average coordination properties of the atoms are determined by the integral intensity of the PDF peaks in *G(r)* pattern. The area of peak in governed through the coordination environment, therefore the variation in the height of the peaks in different crystalline phases within the same material demonstrate an inverse correlation with its peak widths. Proffen elucidated that in few high-performance oxide-contained perovskites materials with a ABO_3 structure, the peak height within the short range not only has a positive linear relationship with the thermal vibration amplitude, but the normalized height also diminishes with the increased chemical disorder achieved by doping the at *A*-site.[23] PDF peak cut-off is dominated by particle size effect, which is influenced by the sensitivity of PDF data to particle size and the potential inclusion of vectors exceeding the maximum particle diameter in long-range scale. However, nanoparticles are not considered in this work.

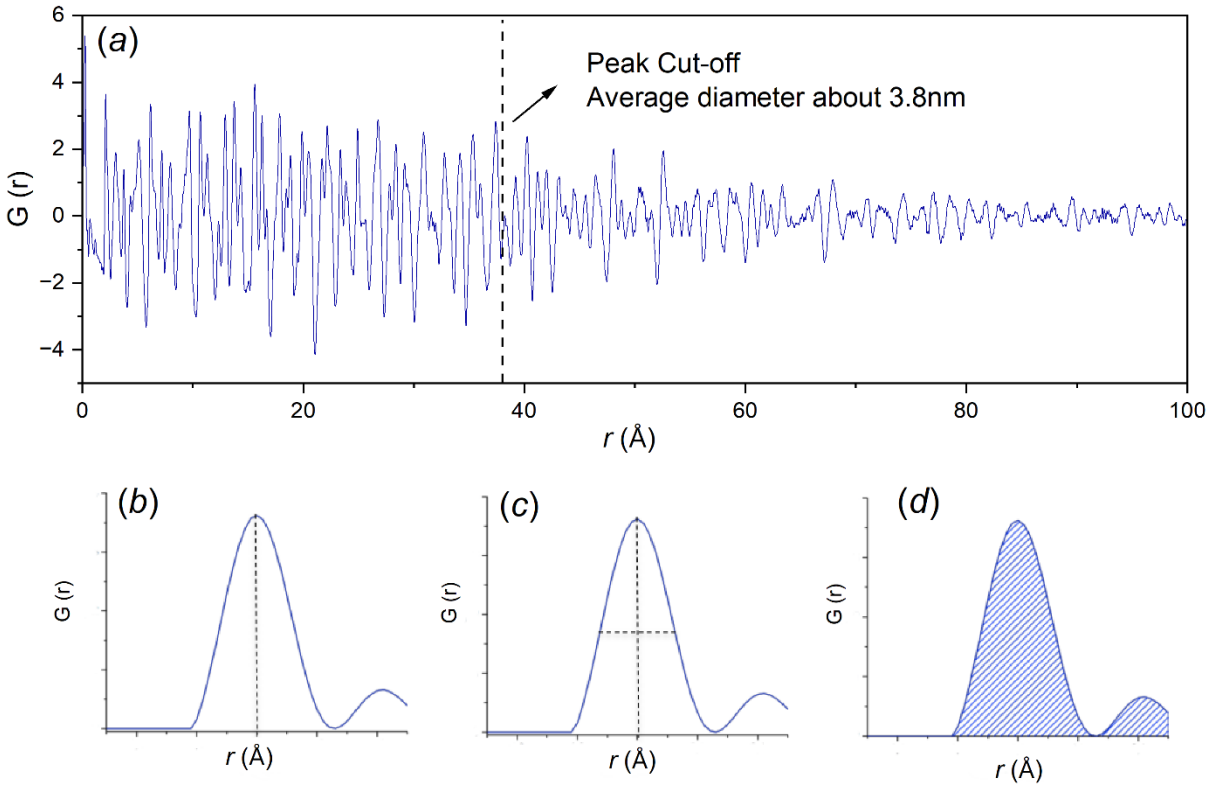

Figure 2.7: (*a*) The schematic representation diagram of normalized reduced function *G(r)* of sample PDF pattern, dot line represented peak cut-off and particle size. (*b*) exhibited peak position correlated with average atomic distance, (*c*) indicated peak width, and (*d*) reveal peak area.

PDF peak width can be expressed as a function of atomic pair separation, temperature and direction in the lattice through the Debye model, which describes atomic pair motion in crystals. This indicates that both static and dynamic disorder cause lattice vibrational effects that influence PDF peak broadening, with the extent that these correlations are modified through atomic interaction and crystal structure, and can have a pronounced effects on neighboring peaks.[24] Figure 2.8 (*b*) involved with *r-cut*, which is an approximation for the step-function-like sharpening behavior of rigid material like a perovskite. If the r-cutoff distance is beyond the ideal value, intermolecular interactions remain at the ideal position and, it results in the emergence of sharp peaks superimposed on the broad peaks and attributed to the extensive coexistence range of intra-molecular and inter-molecular atomic pairs.[25] Usually, the ***beq_rcut*** function can be applied in refinement script to restrict, with two constant parameters, the step

function, and exhibits a monotonically increasing behavior from small to large values at a predefined cutoff radius.[26]

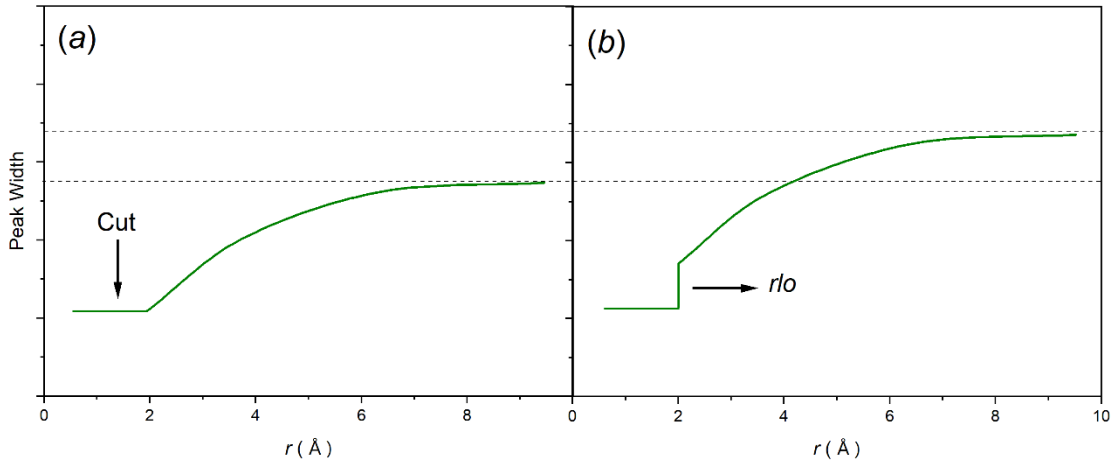

Figure 2.8: The representation of (*a*) Q-cutoff in G(*r*) and (*b*) r-cutoff in PDF data fit. Both (a) and (b) are the parameters applied in PDFs fit.

2.3.2 Modelling the PDF

There are two common methods for developing models from PDF data *G(r)*: "Big box" modelling and "Small box" modelling. The small box model uses space group symmetry and refines the crystallographic unit cell, with PDF resulting from the unit cell calculation convoluted with a Gaussian function to derive the distribution of atomic distance. Conversely, big box modelling does not exploit space group symmetry but rather treats each atom independently and simulates the model as a large box of atoms, which inherently increases computational complexity compared with the small box modelling. However, this methodology provides a clear distribution of atomic positions within the big box. Both methodologies will be applied in PDF modelling within this thesis, utilizing their distinct theory to elucidate atomic disordered structures.

2.3.2.1 Small Box Modelling

Rietveld refinement has a 30-year history as a small-box modelling technique in PDF data analysis. However, it exhibits both similarities and difference compared with traditional Bragg peak Rietveld refinement[27]. While both methods establish fractional coordinates through atomic position for fitting, local structure fitting incorporates crucial information about short-range atomic arrangement rather than deriving from the average structure. This "real space" refinement offers two distinct advantages in PDF crystalline materials analysis: it enables direct quantitative comparison between Bragg peak Rietveld refinement and PDF Rietveld refinement, thereby confirming the presence of local distortion beyond the average structure. Secondly, the real-space refinement demonstrates structural modelling simplicity, which permitting Rietveld refinement to accurately and rapidly acquire models specifically within ordered crystalline material.

PDFgui software is a sophisticated and comprehensive refinement tool for PDF data. PDFgui employs a muti-stage, holistic processing approach to datasets, it is characterized by operational flexibility that allows for tailored parameter adjustments based on diverse sample characteristics. THe PDFgui program addresses low-symmetry issues in local structures and through the use of constraints maintains space group symmetry for the desired parameters. It uses a least-squares minimization algorithm. The residual function within PDFfit is counterpart to R-values in Rietveld refinement, R_w function represented as:

$$R_w = \sqrt{\frac{\sum_{i=1}^{N} w(r_i)[G_{obs}(r_i) - G_{cal}(r_i)]^2}{\sum_{i=1}^{N} w(r_i)\, G_{obs}^2(r_i)}} \qquad (2.10)$$

Where G_{obs} represented as observed PDF data, G_{cal} is the calculated PDF data based on $G(r)$. r_i are the i^{th} data point from position r.

TOPAS-Academic v6 software is also applicable for PDF data fit, it uses a symmetric pattern refinement approach through script-based input for rapid optimization. Distinct from PDFgui, TOPAS adopts the $\boldsymbol{B_{iso}}$ parameter to model thermal motion. However, this constant value is an approximately correlated displacement, which potentially neglects its dynamics. Given PDF

analysis primarily probes interatomic distances, atoms in close proximity often exhibit highly correlated motion, leading to narrower peak widths at lower radial distances in G(r) data. Therefore, TOPAS requires the incorporation of an instrumental function to simulate the damping effect of reciprocal-space peak broadening. In this dissertation, *dQ_damping* parameter was used to model Gaussian peak sharp and the *convolute_Qmax_Sinc* function was used to account for termination ripples in PDF arising from finite Q_{max}.[26]

2.3.2.2 Reverse Monte-Carlo Modelling

Reverse Monte-Carlo Modelling (RMC) applies the simulation of tens of thousands of atoms within a large box to model. The model is compared with measured PDF data through reciprocal space analysis. In RMC modelling, PDF data is reproduced as thousands of instantaneous structures, it rapidly recorded akin as high-speed photography, where each snapshot represents the average value depicted through the PDF. This method allows the average PDF to simulate distortions under both static and dynamic disorder conditions, provided the big box model contains a sufficient number of atoms. The simulation of structure is achieved by fitting interatomic pair potentials, with RMC utilizing separation functions to compare the energies of atomic pairs, which are then incorporated into the big box model to construct the energy distribution. The Metropolis simulated annealing algorithm calculates potential energy changes by random variations atomic positions, with the underlying probability function derived as:

$$P = e^{-\Delta E/kT} \tag{2.11}$$

Where ΔE is the energy changes, k is the Boltzmann constant and T represented as initially setup temperature. Although the algorithm lacks a scientifically rigorous demonstration as to why the underlying probability adopts the Boltzmann distribution in simulated annealing. Fundamentally, simulated annealing represents the most promising approach for identifying structural solutions within disordered configuration.

Bond valence sum is introduced as a valuable method to estimate valence state and validation of structure, total bond valence sum contribution is represent for total bond valence of atom *j*, shown as $V_j = \sum_k s_{jk}$. The bond valence state s_{jk} between atom *j* and its neighboring atom *k* is evaluated through tabulated values of the empirical parameters R_0 and b (both parameters refer Brown) with $s_{jk} = \exp\left[\left(R_0 - r_{jk}\right)/b\right]$. RMCProfile program facilitating bond valence sum to calculate the agreement factor χ^2_{BVS}, as part of χ^2_{RMC} to determine the probability of generated atom movements being accepted or rejected, derived as:

$$\chi^2_{\mathrm{BVS}} = \frac{\sum_{j=1}^{N}\left(V_j - V_i\right)^2}{\sigma_i} \qquad (2.12)$$

Where V_j represents the calculated bond valence for atom *j* and V_i represents the expected bond valence for an atom of type *i* and σ_i is the weighting factor for an atom of type *i*. χ^2_{BVS} is a value combine total bond valence value of each atom within RMC configuration, while weighting factor σ_i can adjust the influence of individual atomic species. A r_{jk} range constrain for each pair of atoms defines the reasonable bond distances between *k* atoms and *j* atom and applied in the calculation of s_{jk}.[19, 28]

Bibliography

(1) Tammann, G. Die Temperatur des Beginns innerer Diffusion in Kristallen. *Zeitschrift für anorganische und allgemeine Chemie* **1926**, *157* (1), 321-325. DOI: https://doi.org/10.1002/zaac.19261570123.

(2) Ptacek, P. *Apatites and their Synthetic Analogues: Synthesis, Structure, Properties and Applications*; IntechOpen, 2016. DOI: 10.5772/59882.

(3) Kennedy, B. J.; Howard, C. J.; Knight, K. S.; Zhang, Z.; Zhou, Q. Structures and phase transitions in the ordered double perovskites $Ba_2Bi^{III}Bi^{V}O_6$ and $Ba_2Bi^{III}Sb^{V}O_6$. *Acta Crystallographica Section B* **2006**, *62* (4), 537-546. DOI: 10.1107/S0108768106018842.

(4) Sleight, A. W. Bismuthates: $BaBiO_3$ and related superconducting phases. *Physica C: Superconductivity and its Applications* **2015**, *514*, 152-165. DOI: https://doi.org/10.1016/j.physc.2015.02.012.

(5) Stein, A.; Keller, S. W.; Mallouk, T. E. Turning Down the Heat: Design and Mechanism in Solid-State Synthesis. *Science (American Association for the Advancement of Science)* **1993**, *259* (5101), 1558-1564. DOI: 10.1126/science.259.5101.1558.

(6) Liu, Y.; Nag, A.; Manna, L.; Xia, Z. Lead-Free Double Perovskite $Cs_2AgInCl_6$. *Angew Chem Int Ed Engl* **2021**, *60* (21), 11592-11603. DOI: 10.1002/anie.202011833 From NLM.

(7) Zelyanskii, A. V.; Zhukova, L. V.; Kitaev, G. A. Solubility of AgCl and AgBr in HCl and HBr. *Inorganic Materials* **2001**, *37* (5), 523-526. DOI: 10.1023/A:1017597321655.

(8) Ewald, P. P. *Fifty years of x-ray diffraction : dedicated to the International Union of Crystallographi on the occasion of the commemoration meeting in Munich July 1962*; N.V.A. Oosthoek, 1962. DOI: 10.1007/978-1-4615-9961-6.

(9) Bragg, W. L. The Specular Reflection of X-rays. *Nature* **1912**, *90* (2250), 410-410. DOI: 10.1038/090410b0.

(10) Doménech-Carbó, M. T.; Osete-Cortina, L. Another beauty of analytical chemistry: chemical analysis of inorganic pigments of art and archaeological objects. *ChemTexts (Cham)* **2016**, *2* (3), 1-50. DOI: 10.1007/s40828-016-0033-5.

(11) Ewald, P. P. Introduction to the dynamical theory of X-ray diffraction. *Acta Crystallographica Section A* **1969**, *25* (1), 103-108. DOI: 10.1107/S0567739469000155.

(12) Dinnebier, R. E.; Billinge, S. J. L. Chapter 1 - Principles of Powder Diffraction. *Powder diffraction : theory and practice* **2008**. DOI: 10.1039/9781847558237-00001.

(13) Condon, J. J.; Ransom, S. M. *Essential Radio Astronomy*; Princeton University Press, 2016. DOI: 10.23943/9781400881161.

(14) Wallwork, K. S.; Kennedy, B. J.; Wang, D. The High Resolution Powder Diffraction Beamline for the Australian Synchrotron. *AIP Conference Proceedings* **2007**, *879* (1), 879-882. DOI: 10.1063/1.2436201 (acccessed 4/25/2025).

(15) Rietveld, H. M. A profile refinement method for nuclear and magnetic structures. *Journal of applied crystallography* **1969**, *2* (2), 65-71. DOI: 10.1107/S0021889869006558.

(16) Pecharsky, V.; Zavalij, P. *Fundamentals of Powder Diffraction and Structural Characterization of Materials*; Springer Nature, 2005. DOI: 10.1007/978-0-387-09579-0.

(17) Young, R. A. *The Rietveld method*; International Union of Crystallograhy, 1993.

(18) Willis, B. T. M.; Pryor, A. W. Thermal vibrations in crystallography. Elsevier B.V: 1975; Vol. 32, pp 214-214.

(19) Brown, I. D.; Altermatt, D. Bond-valence parameters obtained from a systematic analysis of the Inorganic Crystal Structure Database. *Acta crystallographica. Section B, Structural science* **1985**, *41* (4), 244-247. DOI: 10.1107/S0108768185002063.

(20) Juhás, P.; Billinge, S. J. L.; Božin, E. S. Local Structure of Bulk and Nanocrystalline Semiconductors Using Total Scattering Methods. 2013; pp 229-257.

(21) Lyu, Y.; Hu, E.; Xiao, D.; Wang, Y.; Yu, X.; Xu, G.; Ehrlich, S. N.; Amine, K.; Gu, L.; Yang, X.-Q.; et al. Correlations between transition-metal chemistry, local structure, and global structure in $Li_2Ru_{0.5}Mn_{0.5}O_3$ investigated in a wide voltage window. *Chemistry of Materials* **2017**, *29* (21), 9053-9065. DOI: 10.1021/acs.chemmater.7b02299.

(22) Paściak, M.; Ondrejkovic, P.; Kulda, J.; Vaněk, P.; Drahokoupil, J.; Steciuk, G.; Palatinus, L.; Welberry, T. R.; Fischer, H.; Hlinka, J. Local structure of relaxor ferroelectric

$Sr_xBa_{1-x}Nb_2O_6$ from a pair distribution function analysis. *Physical Review B* **2019**, *99* (10), 104102.

(23) Proffen, T.; Billinge, S. J. L.; Egami, T.; Louca, D. Structural Analysis of Complex Materials Using the Atomic Pair Distribution Function — a Practical Guide. *Zeitschrift für Kristallographie. Crystalline materials* **2003**, *218* (2), 132-143. DOI: 10.1524/zkri.218.2.132.20664.

(24) Jeong, I. K.; Heffner, R. H.; Graf, M. J.; Billinge, S. J. L. Lattice dynamics and correlated atomic motion from the atomic pair distribution function. Ithaca, 2002.

(25) Terban, M. W.; Billinge, S. J. L. Structural Analysis of Molecular Materials Using the Pair Distribution Function. *Chemical reviews* **2022**, *122* (1), 1208-1272. DOI: 10.1021/acs.chemrev.1c00237.

(26) Bird, T. A.; Herlihy, A.; Senn, M. S. Symmetry-adapted pair distribution function analysis (SAPA): a novel approach to evaluating lattice dynamics and local distortions from total scattering data. *Journal of applied crystallography* **2021**, *54* (5), 1514-1520. DOI: 10.1107/S1600576721008499.

(27) Farrow, C. L.; Juhas, P.; Liu, J. W.; Bryndin, D.; Božin, E. S.; Bloch, J.; Proffen, T.; Billinge, S. J. L. PDFfit2 and PDFgui: computer programs for studying nanostructure in crystals. *Journal of physics. Condensed matter* **2007**, *19* (33), 335219-335219 (335217). DOI: 10.1088/0953-8984/19/33/335219.

(28) Norberg, S. T.; Tucker, M. G.; Hull, S. Bond valence sum: a new soft chemical constraint for RMCProfile. *Journal of applied crystallography* **2009**, *42* (2), 179-184. DOI: 10.1107/S0021889809004981.

Chapter 3 Local and Long-Range Structure of $BaBiO_3$

3.1 Introduction - $BaBiO_3$

$BaBiO_3$ undergoes three temperature induced structural phase transitions from a monoclinic structure in space group $P2_1/n$ to a second monoclinic, $I2/m$, structure near 140 K; a rhombohedral $R\bar{3}$ structure forms around 400 K and ultimately a cubic structure in $Fm\bar{3}m$ emerges above ~ 750 K.[1] These transitions are a result of changes in the tilting of the corner sharing BiO_6 octahedra. In the $P2_1/n$ structure, observed at the lowest studied temperature, the BiO_6 octahedra have a combination of in-phase (+) tilts about the c-axis and out-of-phase (-) tilts about the *ab* plane, described by the Glazer tilt notation $(a^-a^-c^+)$.[2] The in-phase tilts are lost on heating to 140 K with the $I2/m$ structure having a $a^-a^-c^0$ tilt pattern. In the rhombohedral $R\bar{3}$ structure the out of phase tilts are in the [111] direction or $(a^-a^-a^-)$. Finally the high temperature $Fm\bar{3}m$ cubic structure lacks any tilting with the tilt system described as $a^0a^0a^0$.[3] The corner sharing BiO_6 octahedra have alternating sizes as a consequence of charge disproportionation to Bi^{3+} and Bi^{5+}, leading to a doubling of the unit cell length compared to the equivalent $Pm\bar{3}m$ aristotype.[3] The larger Ba cation occupies the 12-coordinate BaO_{12} cuboctahedral site in the cubic structure and this site becomes progressively more distorted as the symmetry is lowered. In addition to changing the coordination geometry of the Ba cation, octahedral tilting can distort the BiO_6 octahedra. In both the cubic and rhombohedral structures there is a single Bi-O bond distances in each of the $Bi^{3+}O_6$ and $Bi^{5+}O_6$ octahedra, with the Bi-O distance being larger in the former in keeping with the larger ionic radii of Bi^{3+} compared with Bi^{5+}. In the $I2/m$ monoclinic structure there were two distinct Bi-O distances in each of the octahedra and this further increases to three crystallographically different Bi-O distances in the $P2_1/n$ structure. The four structures are illustrated in Figure 3.1.

The variation in bond distances for a particular polyhedra can be quantified by the "Distortion Index", given by:[4]

$$D = \frac{1}{n}\sum_{i=1}^{n}\frac{|l_i - l_\mu|}{l_\mu} \qquad (3.1)$$

Where n represents the number of bonds within a polyhedra, l_i is the bond length and l_μ is the average bond length. The distortion of the BiO_6 octahedra is approximately the same in the two monoclinic structures, considering the larger $Bi^{3+}O_6$ octahedra D increase slightly from 1.17×10^{-3} in the $P2_1/n$ structure to 1.98×10^{-3} in the $I2/m$ structure.[1] A similar small increase is seen for the smaller $Bi^{5+}O_6$ octahedra with D increasing from 4.1×10^{-4} to 4.7×10^{-4} in the $P2_1/n$ and $I2/m$ structures respectively. The distortion index is one for both Bi octahedra in the rhombohedral and cubic structures. For the BaO_{12} polyhedra, D decreases from 7.96×10^{-2} to 6.72×10^{-2} at the $P2_1/n$ - $I2/m$ phase transition and decreases further at the transition to rhombohedral to 4.32×10^{-2}. It is possible that the larger distortion observed in the $Bi^{3+}O_6$ octahedra is a result of the stereochemical influence of the $6s^2$ lone pair electrons of Bi^{3+}. It is known that lone pair electrons can distort polyhedra.[5]

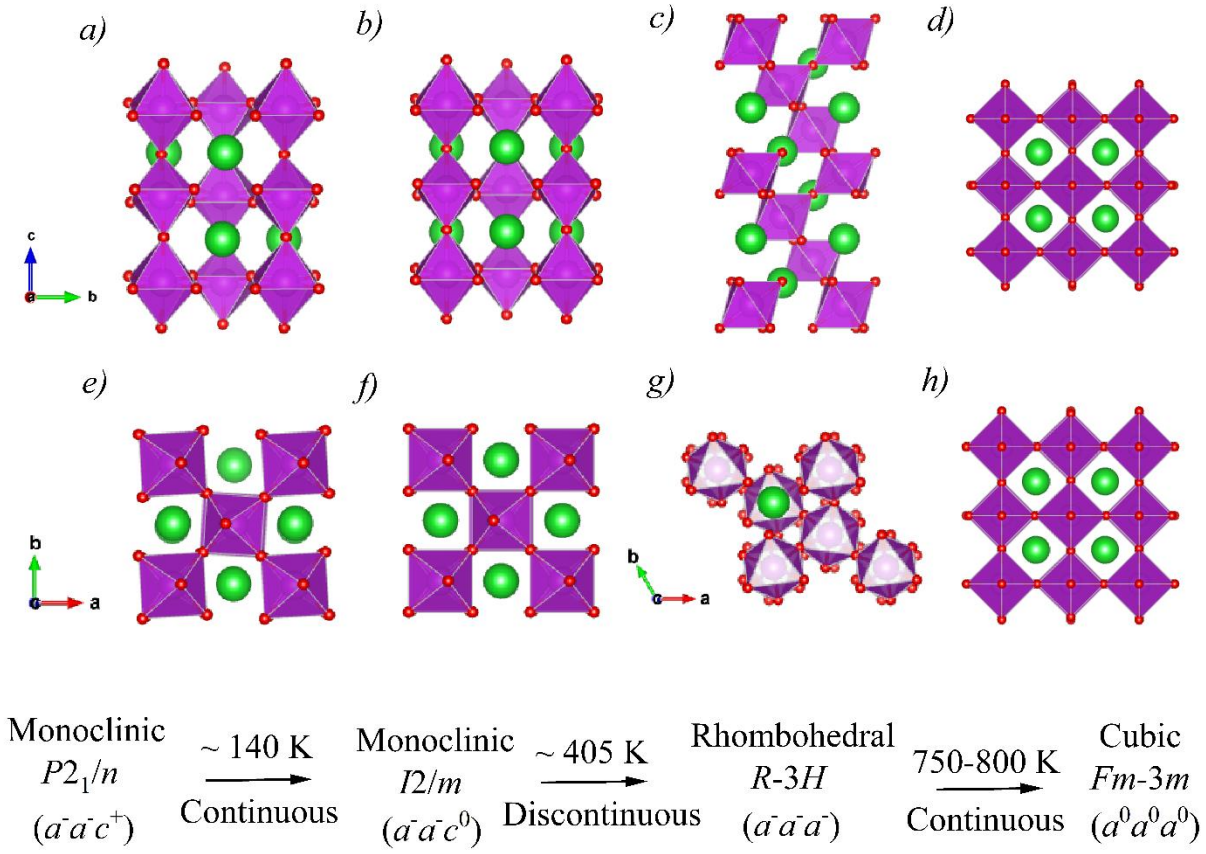

Figure 3.1: Representation of the four phases observed in $BaBiO_3$. (*a,e*) The monoclinic structure in space group $P2_1/n$, (*b,f*) the monoclinic structure in space group $I2/m$, (*c,g*) the rhombohedral structure

in space group $R\bar{3}$ and (*d.h*) the cubic structure in space group $Fm\bar{3}m$. (*a*) to (*d*) are shown along the *a*-axis and (*e*) to (*h*) along the *c*-axis. The BiO_6 polyhedra are displayed in purple, oxygen is represented by the small red spheres and barium by the large green spheres. The observed sequence of transitions, that is associated with progressive changes in the tilting of the octahedra has been elaborated using group theory. [1, 6]

The stereochemical lone pair effect has been observed in other Bi- or Pb-based compounds including in scheelite-type oxides such as $BiVO_4$ and $Bi_3FeMo_2O_{12}$ and in perovskites including $PbTiO_3$ and $CsSnBr_3$.[5, 7 8] The stereochemically active lone pair electrons exert a significant influence on the polyhedral structure, which correlates with distinctive physical properties such as ferroelectricity and photoelectricity. There are examples of oxides such as $PbWO_4$ where the lone pair electrons do not result in long-range structural distortions.[9] Likewise, as discussed in Chapter 5, there is no long-range distortion of the structure of $Cs_2AgBiBr_6$, that has cubic symmetry at room temperature. In $BaBiO_3$, the $6s^2$ orbital in Bi^{3+} can hybridize with the O 2*p* orbital and shift the valence band maximum, which may enhance the electron mobility and facilitate *p*-type semiconductor characteristics according to DFT modelling.[10]

3.2 Variable Temperature Neutron Powder Diffraction Data

A black, polycrystalline sample of $BaBiO_3$ was synthesized by a solid-state method and powder X-ray diffraction was used to confirm the structure and purity of the sample. Neutron diffraction data for were collected from 300 K to 873 K using the *Nanoscale-Ordered Materials Diffractometer* (NOMAD) and, at 10 K, the *Powder Diffractometer BL-11A* (POWGEN) at the Spallation Neutron Source (SNS) at Oak Ridge National Laboratory (ORNL). The temperature dependent symmetry lowering in $BaBiO_3$ is a result of displacement of the O atoms from the equivalent high symmetry site associated with the cooperative tilting of the BiO_6 octahedra, that can exist together with a breathing mode-like displacement. Neutron diffraction provides

sufficient sensitivity to the oxygen sublattice in $BaBiO_3$ to quantify the positions of the light oxygen atoms in the presence of the very heavy Ba and Bi cations. Whilst NOMAD has lower peak-shape resolution than POWGEN, the detectors are arranged to provide data over a wide Q-range making this more suitable for total scattering experiments.[11] Figure 3.2 illustrates the differences between data measured on the two diffractometers.

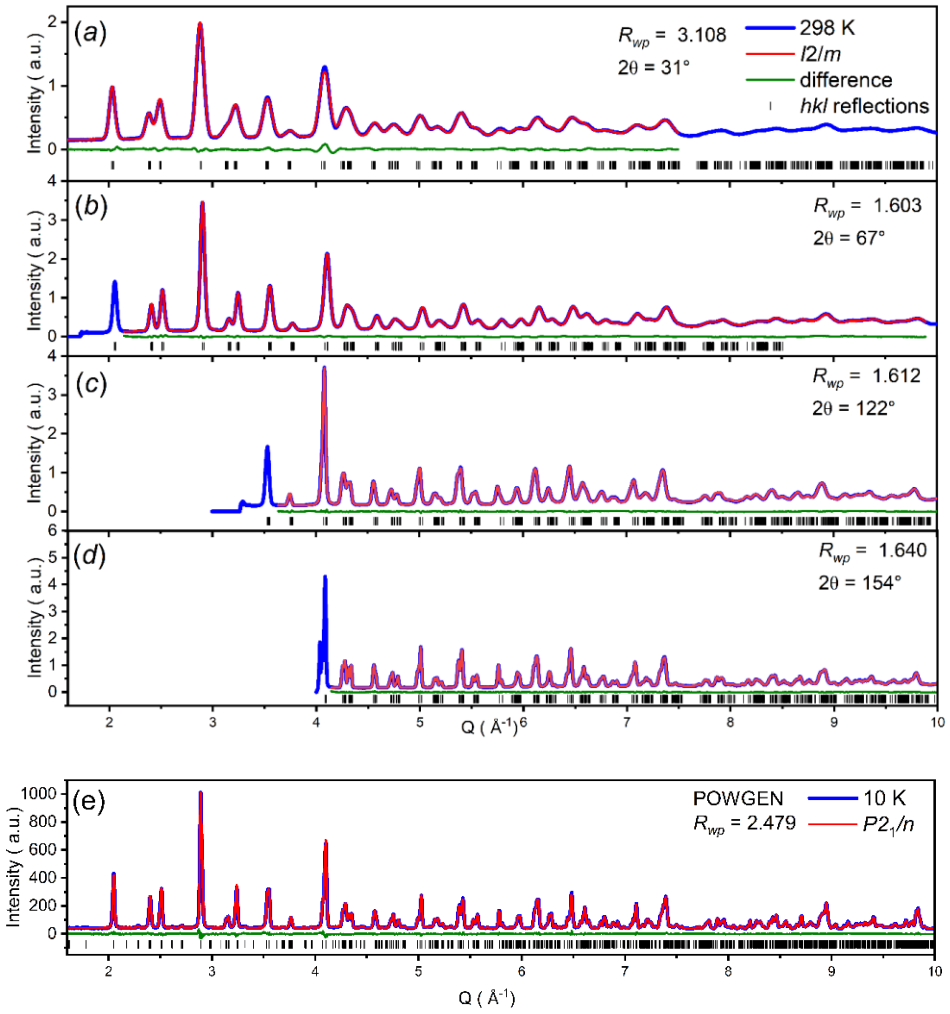

Figure 3.2: Comparison for neutron powder diffraction data of $BaBiO_3$ collected using NOMAD and POWGEN. (a) to (d) are for data measured at room temperature using the four detector banks (a) 31°, (b) 67°, (c) 122° and (d) 154° on NOMAD and the corresponding Rietveld fits. (e) is data measured at 10 K from POWGEN with wavelength 0.8 Å. The blue line represents the data, the red line represents the calculated fit to the data, and the green line represents the difference between the two. The black vertical tick shows the positions of the space group allowed *hkl* reflections.

At room temperature, the structure of $BaBiO_3$ was identified as being monoclinic in space group *I*2/*m*, which is an alternate setting of space group *C*2/*m* (#12), in agreement with previous studies.[1, 12, 13] The Rietveld refinement indicates the presence of alternating large and small BiO_6 polyhedra indicative of charge disproportionation of the type $2Bi^{4+} \rightarrow Bi^{3+} + Bi^{5+}$, as illustrated in Figure 3.3. Details of the Rietveld refinement are given in Table 3.1 Rietveld refinements of the structure against the NOMAD data, showed the larger $Bi^{3+}O_6$ octahedra has three pairs of crystallographically distinct Bi-O bond lengths at 2.294(17) Å, 2.298(19) Å and 2.300(19) Å. The corresponding bond lengths in the smaller $Bi^{5+}O_6$ octahedra are 2.102(19), 2.112(17) Å and 2.115(19) Å. There are seven Ba-O bonds in in the range 2.722(16) Å to 3.464 (16) Å in the *I*2/*m* structure, with five longer Ba-O, see Table 3.2.[1]

Upon cooling below 140 K the monoclinic structure in $BaBiO_3$ is described by space group $P2_1/n$ (#14) as a consequence of the presence of in-phase tilting around the [001] direction in addition to the out-of-phase tilts seen in the *I*2/*m* structure. This low temperature structure, refined against data measured at 10 K using POWGEN, has three distinct long Bi^{3+}-O bond lengths of 2.294(17) Å, 2.298(19) Å and 2.300(19) Å, and three shorter Bi^{5+}-O bond lengths of 2.102(19), 2.112(17) Å and 2.115(19) Å. The twelve Ba-O bond length are in the range 2.704 (2) Å to 3.482(2) Å.

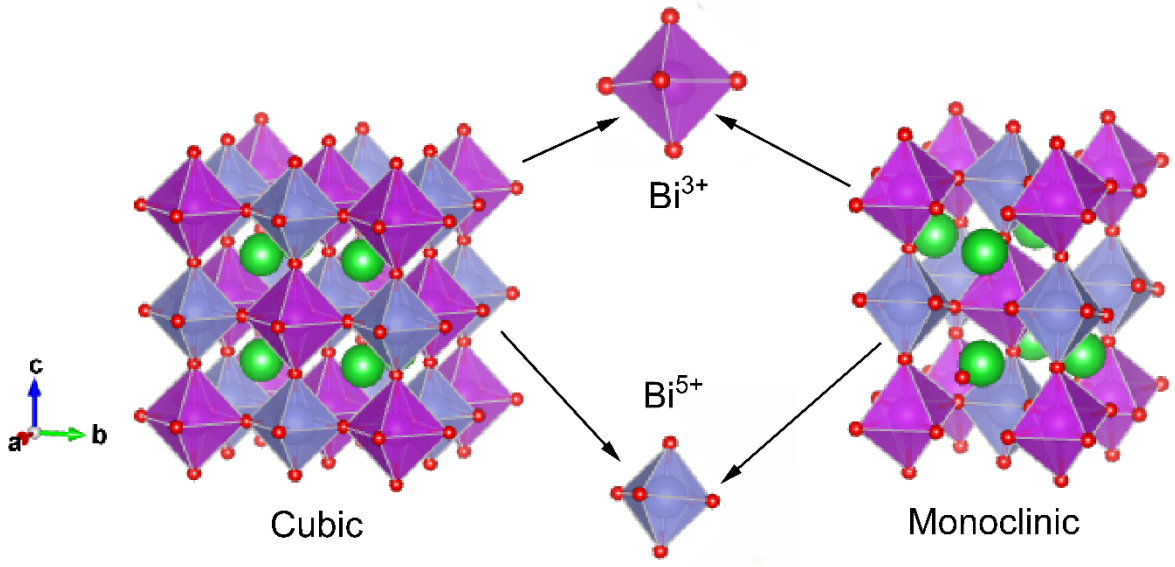

Figure 3.3: The representation of charge disproportion Bi ion located in cubic structure (right) and monoclinic structure (left) of $BaBiO_3$. The purple octahedral represents Bi^{3+} and the blue octahedral Bi^{5+}.

Comparison of the NPD patterns measured at 373 and 423 K, shown in Figure 3.4, reveals a number of significant differences, most obvious between Q = 4.5 – 5.5 $Å^{-1}$ consistent with a change in symmetry from monoclinic to rhombohedral as first described by Cox & Sleight. This phase transition involves a reorientation of the tilts, from having out-of-phase tilts about the [110] direction to about the [111] direction. Howard *et al.* showed that such a rearrangement must be first order.[3] The Bi^{3+}-O and Bi^{5+}-O bond distances in the rhombohedral structure are 2.228(6) Å and 2.172(6) Å respectively. The difference between these is less than expected based on the relative difference in the ionic radii of Bi^{5+} and Bi^{3+}, 0.76 and 1.03 Å respectively.[14] It was noted by Kennedy *et al*. that structural refinements in the rhombohedral phase were susceptible to underestimating the difference, presumably because of a correlation between the atomic displacement parameters (ADPs) and the positional parameters. Indeed, in the current work it was observed that the use of anisotropic atomic displacement parameters was critical to refining a chemically sensible value the oxygen position parameter.[1] Even using anisotropic ADPs the refined Bi-O distance in the rhombohedral structure is anomalous as clearly evident in Figure 3.5.

Further heating of the sample to above 800 K resulted in additional changes to the diffraction patterns that were consistent with a transition to a cubic structure in $Fm\bar{3}m$. Successful refinements of the structure required the use of anisotropic atomic displacement parameters of the oxide anions. Again, two distinct BiO_6 octahedra are evident with Bi-O bond distances of: 2.105(13) Å and 2.284(13) Å corresponding to the Bi^{5+} and Bi^{3+} sites respectively.

As noted above, the use of anisotropic ADPs for the anions was critical in obtaining accurate structures. The ellipsoids for the anions were all highly anisotropic and in all four structures the greatest displacement was perpendicular to the Bi-O-Bi bonding chain, see Figure 3.6. This indicates that the oxygen atoms undergo dynamic motion in direction perpendicular to the

bonding axis. This behavior is consistent with soft mode displacements of the anions. The average Ba-O bond distances show a linear increase with temperature.

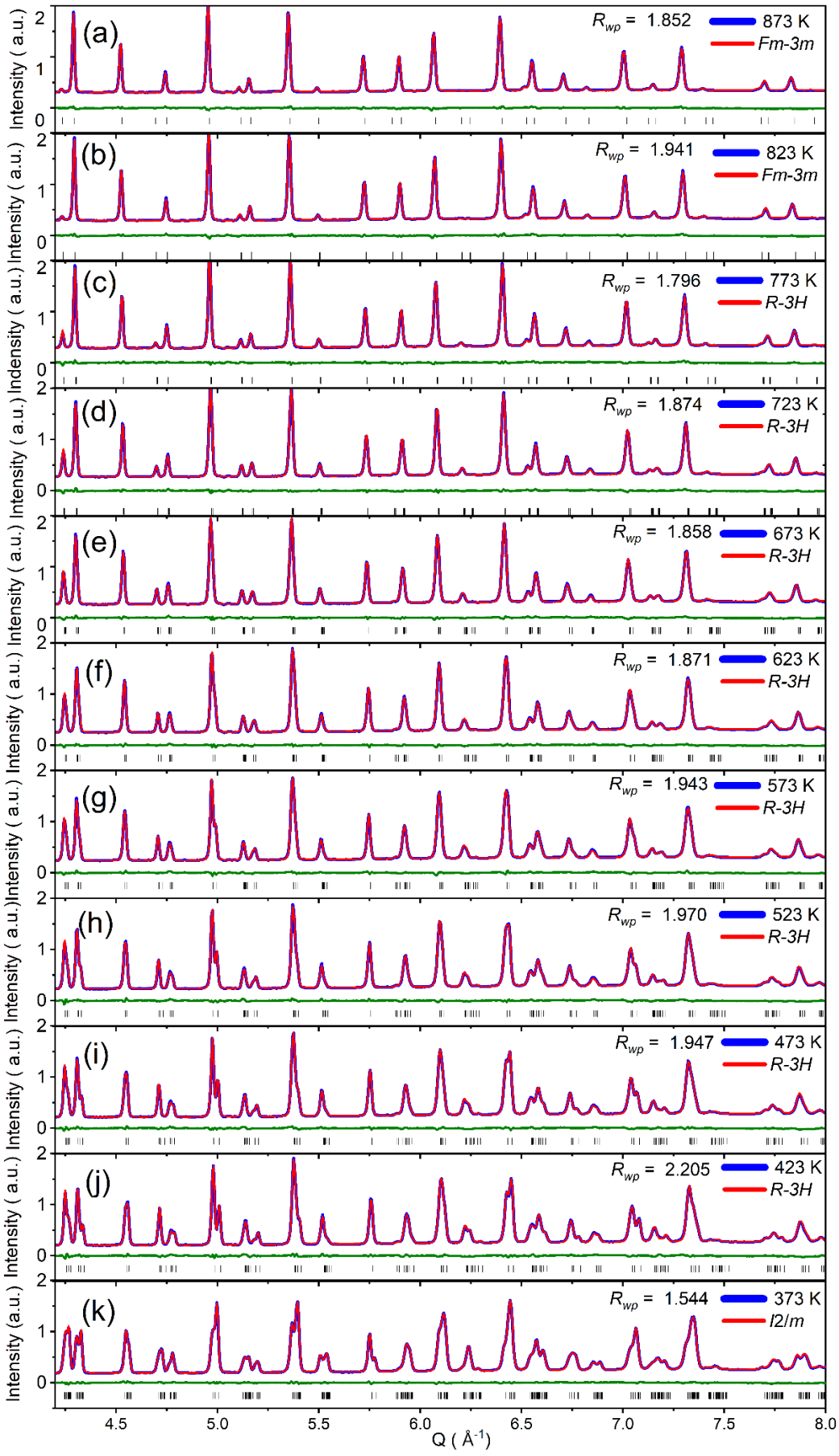

Figure 3.4: Variable temperature neutron powder diffraction data of $BaBiO_3$. (a) to (k) 373 K to 873 K Bragg peak fit for $BaBiO_3$ from Q range 4.2 to 8 Å^{-1} with diffraction angle 154°. The blue line represents the data, the red line represents the calculated fit to the data and the green line represents the difference between the two. The black tick represents the allowed *hkl* position, R_{wp} above shows the good of fit.

The temperature dependence of the refined unit cell parameters of $BaBiO_3$ are shown in Figure 3.5. This figure highlights the discontinuous changes around 400 K in the lattice parameters associated with the $I2/m \rightarrow R\bar{3}$ phase transition.[1, 12, 13] The unit cell parameters exhibit an approximately linearly increase in both the rhombohedral and cubic structure. The rate of increase in the *c*-parameter is notably greater than that of the *a*-parameter across the rhombohedral phase with the *a* and *c* parameters of the rhombohedral phase merging at the transition to cubic symmetry near 800 K. The anisotropy in the unit cell parameters is a consequence of the octahedral tilting, with the different rates of thermal expansion a result of the continuous expansion in the cell volume.

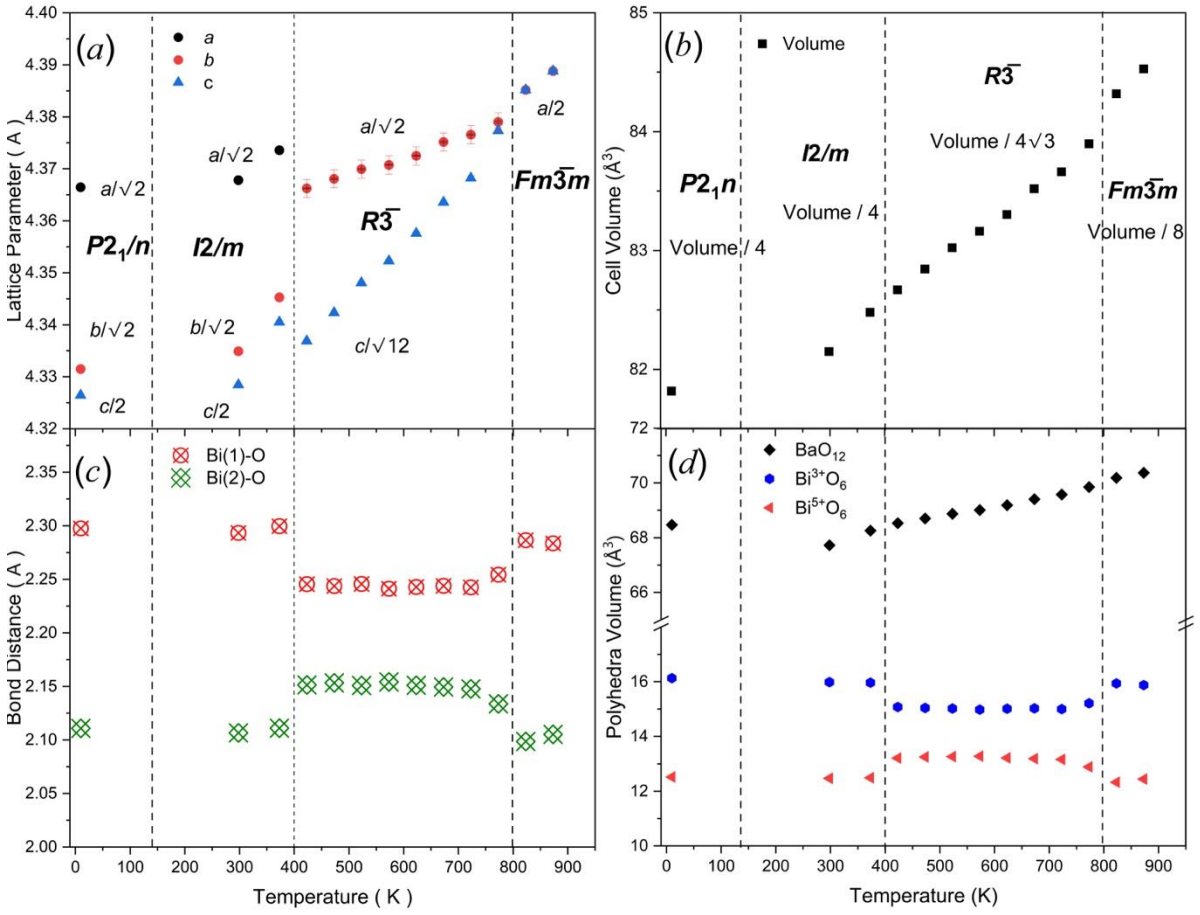

Figure 3.5: Temperature dependence of (a) the equivalent primitive unit cell parameters and (b) the unit cell volume for $BaBiO_3$ upon heating from 10 K to 873 K as determined by Rietveld refinements against powder neutron diffraction data. The average Bi-O bond distance is shown in (c) where Bi (1) represents Bi^{3+} and Bi (2) represents Bi^{5+}, and (d) shows the volume

of each cation-oxygen polyhedra.

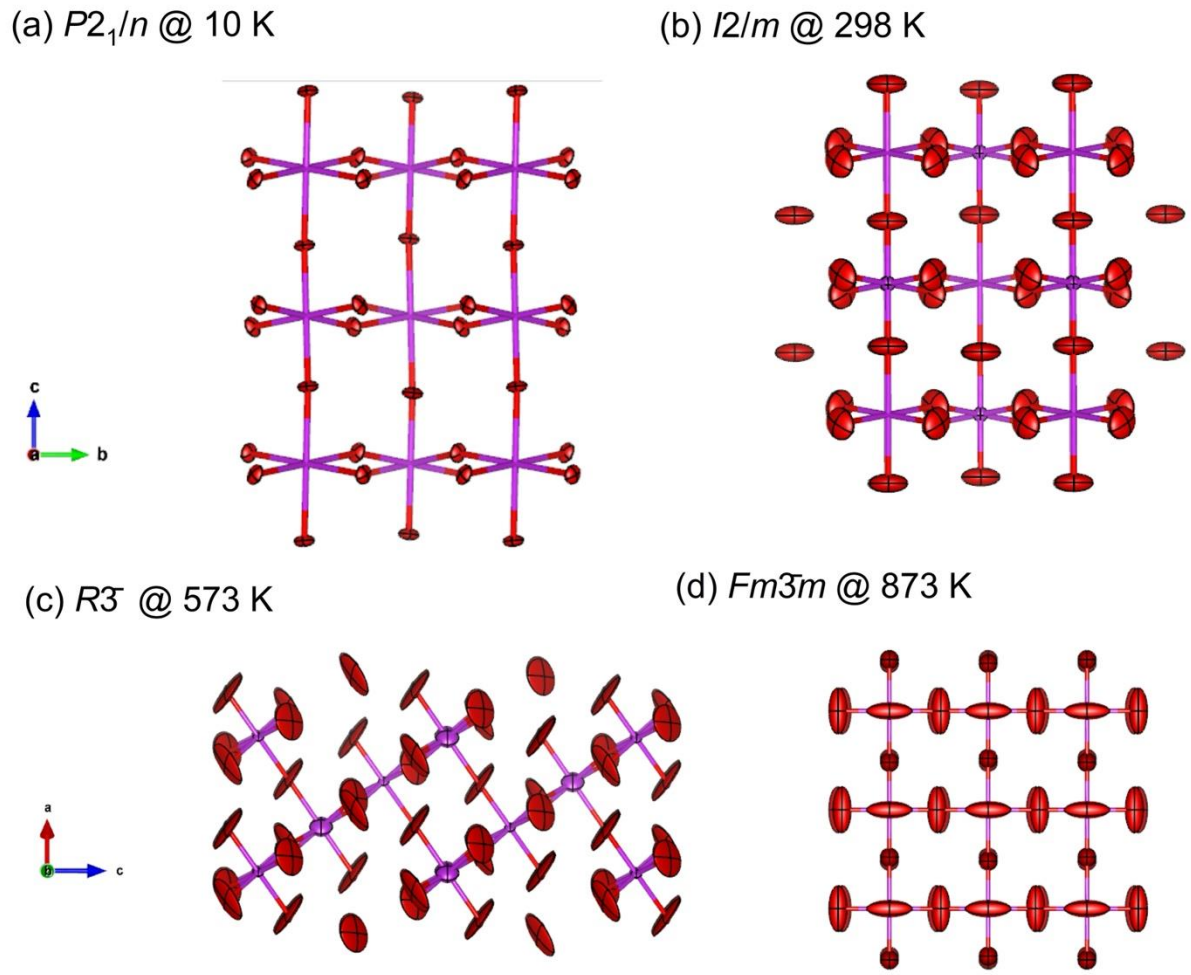

Figure 3.6: Representation of atomic displacements for oxygen atom in four space groups of $BaBiO_3$, oxygen atom is represented as ellipsoid and connect with violet sphere (Bi atom).

Table 3.1: Rietveld refinement results for the four observed phases of $BaBiO_3$ obtained against neutron powder diffraction data.

	$BaBiO_3$			
Temperature (K)	10	298	573	873
Space group	$P2_1/n$	$I2/m$	$R\bar{3}$	$Fm\bar{3}m$
a (Å)	6.178 (5)	6.180 (5)	6.181 (4)	8.778 (5)
b (Å)	6.128 (5)	6.135 (5)	6.181 (4)	8.778 (5)
c (Å)	8.656 (6)	8.664 (4)	15.076 (5)	8.778 (5)
β (°)	90.265 (1)	90.179 (1)	90	90
Vol. (Å^3)	327.69 (4)	328.931(8)	498.821 (8)	676.23 (6)
Ba *x*	0.5047 (2)	0.5032 (10)	0	0.25
Ba *y*	-0.0120 (2)	0	0	0
Ba *z*	0.2491 (1)	0.2483 (10)	0.2501 (8)	0.25
Bi(2) *z* *	0.5	0.5	0.5	0.25
O (1) *x*	0.0679 (2)	0.0630 (10)	0.5407 (5)	0.2602 (6)
O (1) *y*	0.0086 (3)	0	0	0
O (1) *z*	0.2612 (1)	0.2613 (11)	0.2552 (9)	0
O (2) *x*	0.2469 (2)	0.2627 (10)	/	/
O (2) *y*	0.2742 (2)	0.2579 (10)	/	/
O (2) *z*	-0.0363 (2)	-0.0336 (10)	/	/
O (3) *x*	0.2774 (2)	/	/	/
O (3) *y*	0.7561 (2)	/	/	/
O (3) *z*	-0.0370 (2)	/	/	/
Ba U_{11} (Å^2)	0.0014 (2)	0.0074 (1)	0.0098 (5)	0.0235 (5)
Ba U_{22} (Å^2)	0.0013 (2)	= U_{11}	= U_{11}	= U_{11}
Ba U_{33} (Å^2)	0.0012 (2)	= U_{11}	0.0191 (6)	= U_{11}
Bi (1) U_{11} (Å^2)	0.0007 (3)	0.0069 (2)	0.0037 (5)	0.0144 (5)
Bi (1) U_{22} (Å^2)	0.0012 (3)	= U_{11}	= U_{11}	= U_{11}
Bi (1) U_{33} (Å^2)	0.0011 (2)	= U_{11}	0.0038 (6)	= U_{11}
Bi (2) U_{11} (Å^2)	0.0004 (3)	0.0051 (5)	0.0142 (6)	0.0000 (5)
Bi (2) U_{22} (Å^2)	0.0009 (3)	0.0047 (2)	= U_{11}	= U_{11}
Bi (2) U_{33} (Å^2)	0.0006 (2)	0.0050 (4)	0.0182 (6)	= U_{11}
O (1) U_{11} (Å^2)	0.0056 (2)	0.1251 (19)	0.0468 (5)	0.01357 (5)
O (1) U_{22} (Å^2)	0.0077 (3)	0.01 (20)	0.0542 (5)	0.09019 (5)
O (1) U_{33} (Å^2)	0.0021 (2)	= U_{22}	0.0268 (6)	0.01357 (5)
O (2) U_{11} (Å^2)	0.0048 (3)	0.1251 (19)	/	/
O (2) U_{22} (Å^2)	0.0050 (3)	0.01 (20)	/	/
O (2) U_{33} (Å^2)	0.0063 (4)	= U_{22}	/	/
O (3) U_{11} (Å^2)	0.0047 (3)	/	/	/
O (3) U_{22} (Å^2)	0.0049 (4)	/	/	/
O (3) U_{33} (Å^2)	0.0069 (4)	/	/	/

* Bi^{3+} occupies a *B*-site with Wyckoff position (0,0,0) and Bi^{5+} occupies a *B*-site with Wyckoff position (0,0,0.5).

Table 3.2: Bond distances, Bond Valence Sums (BVS) [15] and Distortion Index (*D*) values for the four $BaBiO_3$ structures as deduced from Rietveld refinements observed against neutron powder diffraction data.

	$BaBiO_3$			
Temperature (K)	10	298	573	873
Space group	$P2_1/n$	$I2/m$	$R\bar{3}$	$Fm\bar{3}m$
Bi(1)-O (1) (Bi^{3+}) (Å)	2.2985(9)	2.2973(15)	2.2860 (3)	2.2835 (13)
Bi(1)-O (2) (Bi^{3+}) (Å)	2.2926(12)	2.2871(16)	/	/
Bi(1)-O (3) (Bi^{3+}) (Å)	2.2987(12)	/	/	/
Bi(2)-O (1) (Bi^{5+}) (Å)	2.1115(9)	2.1051(15)	2.1085 (10)	2.1052 (13)
Bi(2)-O (2) (Bi^{5+}) (Å)	2.1102(12)	2.1073(16)	/	/
Bi(2)-O (3) (Bi^{5+}) (Å)	2.1090(12)	/	/	/
Ba-O (1) (Å)	2.7044(16)	2.7237(16)	2.840(3)	3.10456 (7)
Ba-O (1) (Å)	2.9732(16)	3.0970(3)	3.079(7)	3.10456 (7)
Ba-O (1) (Å)	3.2229(16)	3.4623(16)	3.109(7)	3.10456 (7)
Ba-O (1) (Å)	3.4819(16)	/	3.345(2)	3.10456 (7)
Ba-O (2) (Å)	2.7894(18)	2.849(3)	/	/
Ba-O (2) (Å)	2.8887(18)	2.878(3)	/	/
Ba-O (2) (Å)	3.2190(19)	3.275(3)	/	/
Ba-O (2) (Å)	3.4187(19)	3.315(3)	/	/
Ba-O (3) (Å)	2.7674(19)	/	/	/
Ba-O (3) (Å)	2.9119(18)	/	/	/
Ba-O (3) (Å)	3.1762(19)	/	/	/
Ba-O (3) (Å)	3.4635(19)	/	/	/
BiO_6 (Bi^{3+}) ($Å^3$)	16.13	15.99	14.98	15.88
BiO_6 (Bi^{5+}) ($Å^3$)	12.52	12.47	13.28	12.44
BaO_{12} ($Å^3$)	68.47	67.92	69.01	70.37
D Index BiO_6 (Bi^{3+})	0.00117	0.00198	0	0
D Index BiO_6 (Bi^{5+})	0.00041	0.00047	0	0
D Index BaO_{12}	0.07961	0.06728	0.04323	0
R_{wp} (%)	2.291	2.155	2.320	2.974
BVS (BiO_6 / Bi^{3+})	3.46	3.54	4.04	3.60
BVS (BiO_6 / Bi^{5+})	5.24	5.29	4.65	5.31

3.3 Neutron Total Scattering

3.3.1 Variable Temperature Neutron Powder Diffraction

The results of the Rietveld analysis of the structures of $BaBiO_3$ described above are in good agreement with the earlier independent powder neutron diffraction studies of Pei *et al.*[13] and Kennedy *et al*.[1] Next the possibility that the local structure was impacted by the Bi $6s^2$ lone pairs was considered using Neutron Pair Distribution Function (NPDF) analysis. Since it was not possible to schedule the measurement of data for the low temperature $P2_1/n$ phase using the NOMAD diffractometer it was necessary to collect such data on POWGEN. Although POWGEN provides higher peak-shape resolution in reciprocal space than NOMAD data collection times are appreciably longer. Examples of the NPDF plots are illustrated in Figure 3.7. The obvious changes between the NPDF measured at 10 and 298 K are a result of the use of different instruments and temperatures. There are no obvious features in the NPDF that could be used to establish the appropriate space group, and consequently the data were fit assuming the sequence of structures established from the Rietveld analysis. As illustrated by the partial PDFs shown in Figure 3.8(b) the first peak in the PDF at ~ 2.1 Å corresponds to Bi-O bonds. The Ba-O and O-O distances are around 3.0 Å and the cation-cation distances are around 3.5-4.5 Å. The presence of two distinct Bi-O distances, from the $Bi^{3+}O_6$ and $Bi^{5+}O_6$ octahedra, is apparent in the low temperature NPDF. The broadening of this, and other features at low *r*-values, as the temperature increases is a consequence of the increased thermal motion of the atoms. This broadening of the features at low *r*-values makes it difficult to discern local structure changes in the Bi-O, Ba-O and O-O distances associated with changes in the tilting of the octahedra.

At this stage several observations can be made. Firstly, although the fits to the NPDF shown in Figure 3.7 appear reasonable. They are clearly not optimal with the exception of that

measured at 10 K. This is most obvious over the region 2.5-4.0 Å indicating that the long-range average structure does not account for subtle changes in the O-O and Ba-O distances. The latter are especially susceptible to changes in the tilting of the BiO_6 octahedra.[16] Secondly NPDF analysis using TOPAS only allowed isotropic atomic displacement parameters, Biso, to be used. In the Bragg fitting it was observed that the ADPs, especially of the oxygen atoms, were highly anisotropic. An alternate program, PDFGui, allows for anisotropic atomic displacement parameters.[17] Fits using PDFGui revealed similar discrepancies to that found using TOPAS, demonstrating the misfitting was not a result of the neglect of anisotropic atomic displacement.

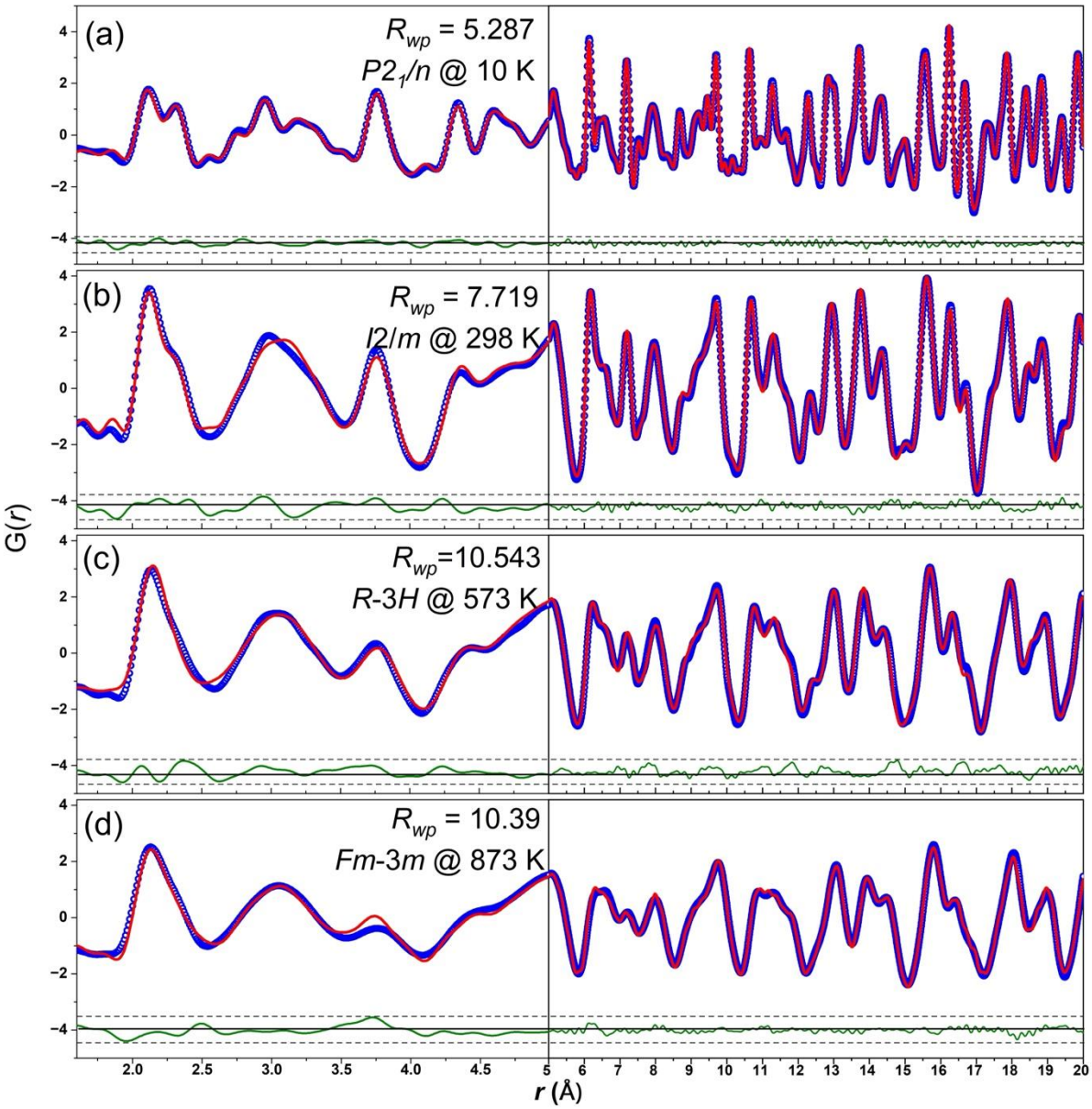

Figure 3.7: Neutron pair distribution function data fit for $BaBiO_3$ from 1.6-20 Å assuming the long-range structural model. (*a*) Monoclinic structure $P2_1/n$, (*b*) monoclinic structure $I2/m$, (*c*) rhombohedral structure $R\bar{3}$ and (*d*) cubic structure $Fm\bar{3}m$. The blue circles represent the normalized data, the red line represents the calculated data, and the green line indicates the difference between these. The NPDF results were obtained using PDFgui.

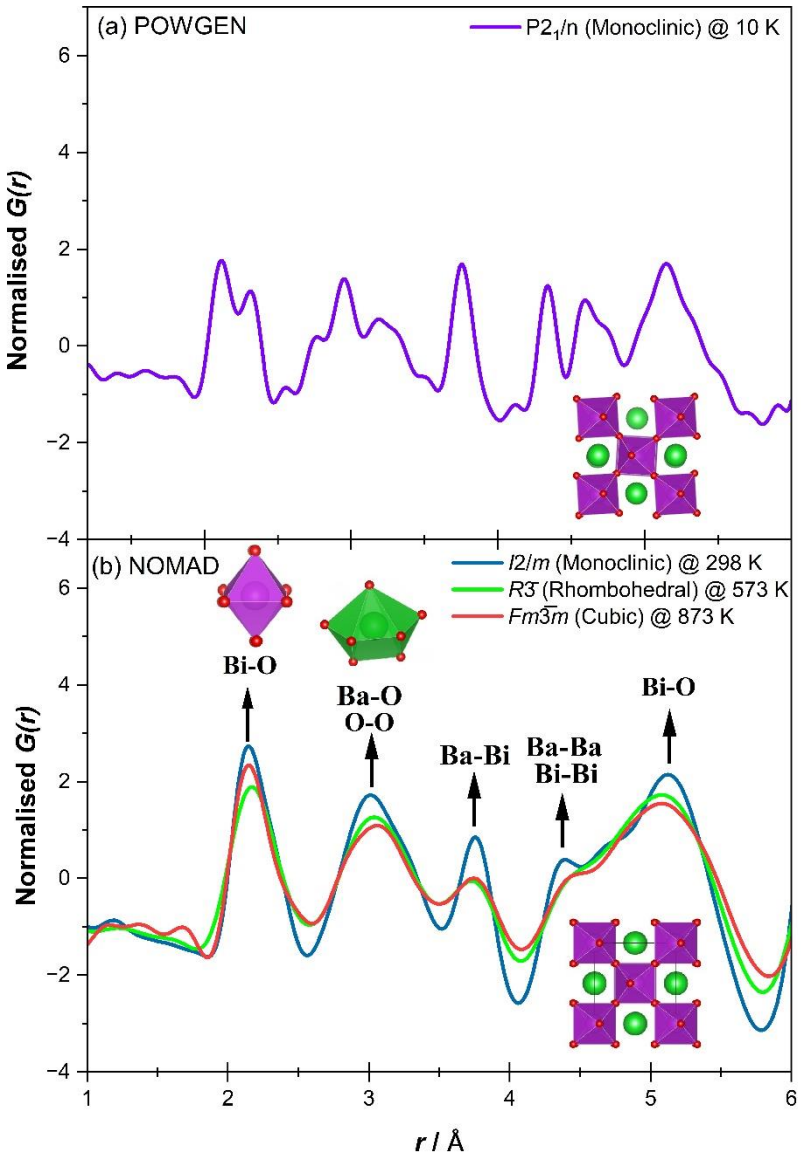

Figure 3.8: Portions of the Neutron Pair Distribution Function (NPDF) data for $BaBiO_3$. (a) Shows the NPDF measured at 10 K using POWGEN where the long-range structure is monoclinic in $P2_1/n$. (b) Shows the data measured using NOMAD at 298 K (blue line), 573 K (Green line) and 873 K (Red line)

corresponding to the monoclinic structure *I*2/*m*, rhombohedral structure R$\bar{3}$ and cubic structure Fm$\bar{3}$m long range structures respectively. More details on the partial PDF are given in Figure 3.9.

The NPDF refinement of the structure of $BaBiO_3$ measured at 10 K yielded an excellent fitting result, with R_{wp} ~5.287. As illustrated in Figure 3.10a, the $P2_1/n$ model reproduces both the short-range local scale and long-range average structures. In this context the local structure is considered to be the r-range 1.6 to 5.0 Å as illustrated in the left panel of Figure 3.7. The splitting of the first peak into two distinct features confirms the presence of two Bi -O distances as expected if charge disproportion has occurred. The Bi^{3+}-O bond is observed at approximately 2.29 Å, while the Bi^{5+}-O bond is located around 2.10 Å. These distances are in good agreement with the values obtained from the Rietveld refinements described above. The next group of peaks belongs to the Ba-O and O-O distances. Due to the octahedral tilting in the $P2_1/n$ structure, the twelve Ba-O bonds split have seven different lengths.[18] The shortest Ba-O peaks are at approximately 2.70 - 2.92 Å, corresponding to the edge adjacent to another BaO_{12} cuboctahedra. There are additional longer Ba-O lengths with three Ba-O distances at ~ 3.2 Å, and three at ~ 3.45 Å. The first group of O-O peaks, at around 2.98 Å, is associated with the smaller $Bi^{5+}O_6$ octahedra. There is a second group of O-O peaks distributed around 3.3 Å to 3.4 Å from the larger $Bi^{3+}O_6$ octahedral. Comparing the distribution of the Ba-O and O-O distances in the $P2_1/n$ (Figure 3.9 a) and $Fm\bar{3}m$ (3.9d), highlights the impact of tilting on the environment of the A-site cation in perovskite materials.

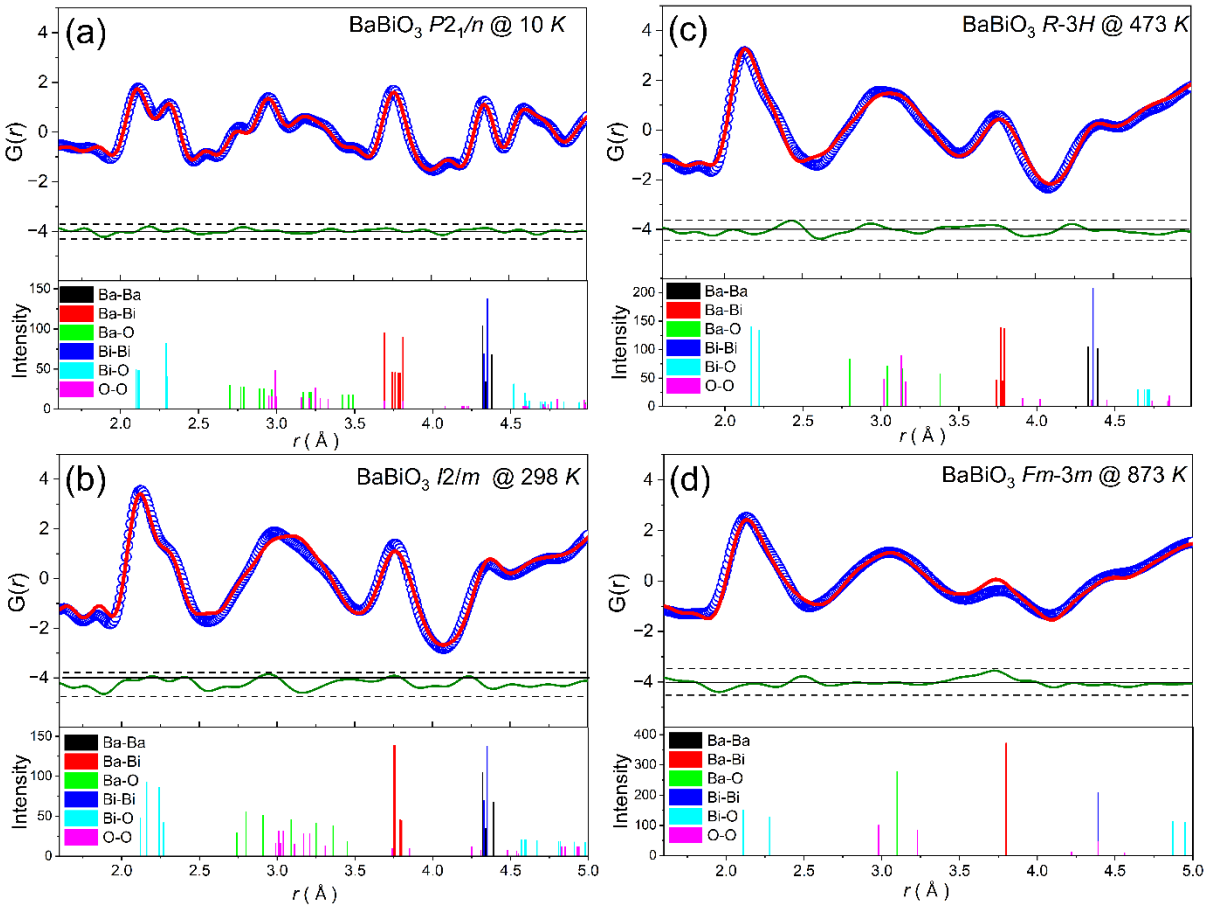

Figure 3.9: Partial neutron pair distribution function data indicates $BaBiO_3$ fitted with (a) monoclinic $P2_1/n$ space group at 10 K, (b) monoclinic space group $I2/m$ at 298 K, (c) rhombohedral space group $R\bar{3}$ at 473 K and cubic space group $Fm\bar{3}m$ at 873 K. Data was fitted across from 1.6-20 Å range through PDFgui. The blue circles represent the observed data, the red line represents the calculated profile, the green line represents the difference between the two.

The temperature dependence of the lattice parameters of $BaBiO_3$ estimated from the NPDF analysis is shown in Figure 3.10 and is in good agreement with the results from the Rietveld refinements illustrated in Figure 3.5. Again, it is observed that the difference in the average Bi-O distances for the Bi^{III} and Bi^{V} polyhedral in the rhombohedral structure is systematically smaller than that observed for the other three structures, although the detail is somewhat different.

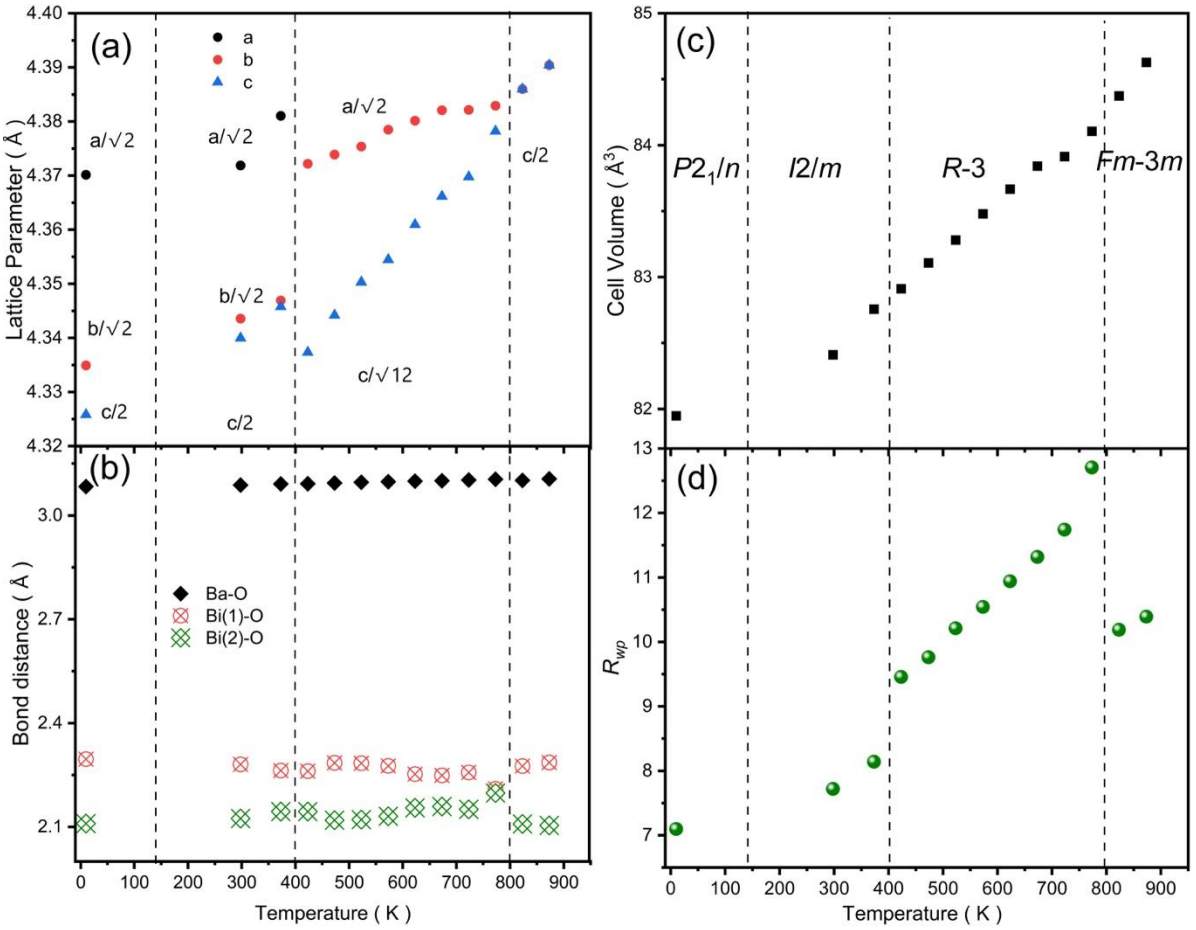

Figure 3.10: Temperature dependence of the lattice parameters of $BaBiO_3$. (a) lattice parameters calculated through NPDF, (b) bond distances, Bi (1) represents Bi^{3+} and Bi (2) represents Bi^{5+}, (c) cell volume and (d) R_{wp} indicates the good of fit.

3.3.2 Box-car Model

Several strategies were explored to improve the quality of the fit for the NPDF patterns measured at or above room temperature. Firstly, in PDF fitting, the peak width varies as a function of *r* due to changes in correlations between nearest and furthest interatomic neighbours, as outlined by Jeong *et al.*[19] The value of the isotropic displacement Biso is determined from the peak width in the PDF, but this single parameter cannot reproduce the displacements observed in the Rietveld analysis. Consequently, and as noted above, the use of both isotropic and anisotropic ADPs was explored, but irrespective of the approach poor fits were observed

for the PDFs measured at or above room temperature, that is in the $I2/m$, $R\bar{3}$ and $Fm\bar{3}m$ structures, below 5 Å. Secondly the possibility of oxygen non-stoichiometry was considered. Previous studies of $BaBiO_{3-\delta}$ ceramic membranes have shown that variations in oxygen vacancies directly influence the bandgap. and significantly impacts its phase transition behaviour. The literature suggests that $BaBiO_3$ only undergoes significant oxygen loss when heated between 873 K and 1300 K, which falls outside our experimental temperature range.[20-22] This coupled with the lack of evidence for appreciable oxygen non-stoichiometry in the Rietveld analysis suggests the relatively poor fits to the low r-region are not associated with oxygen vacancies. Finally, the possibility that there were local distortions present, that disappear at longer distances, was considered. This possibility was tested using a box-car fit in which the small-*r* fits are dominated by local atomic arrangements and large-*r* region reflects the longer-range, average structure. The box-car fitting method enables the fitting of distinct structural models and parameters to PDF data across varying *r* distances, and is important to addresses the structural information discrepancies observed in short-range, medium-range and long-range distances.[17, 23] Given the $P2_1/n$ model provided an acceptable fit over the full range for the data measured at 10 K it was hypothesised that local in-phase octahedral tilts persist at short distances over the entire temperature range.

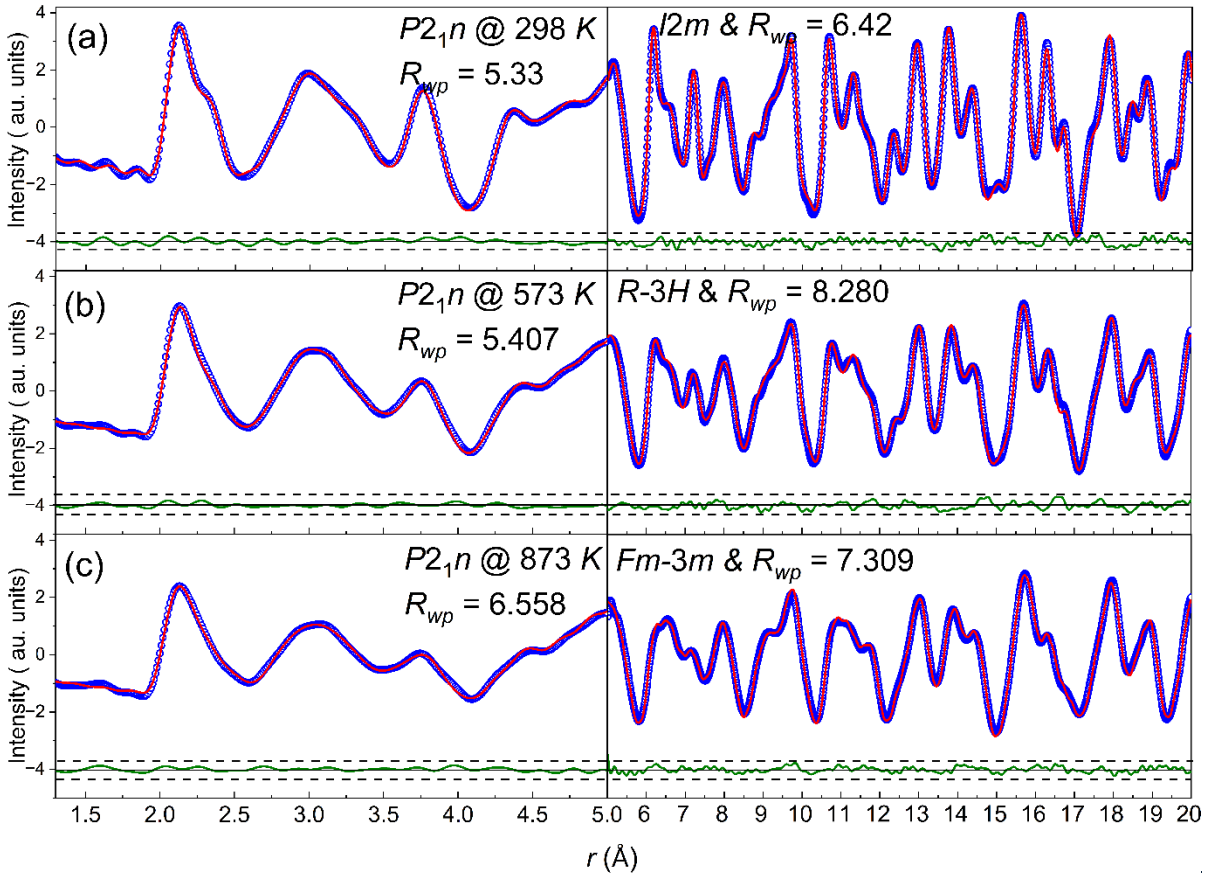

Figure 3.11: NPDF data for $BaBiO_3$ at (a) 298 K, (b) 573 K and (c) 873 K fitted over a range of 1.3 to 20 Å with a box-car model. Within range 1.3 to 5 Å fitted with low symmetry space group $P2_1/n$ and fitted high symmetry space group with long range. The blue circles represent the measured data, the red line represents the calculated profile, and the green line shows the difference between the two.

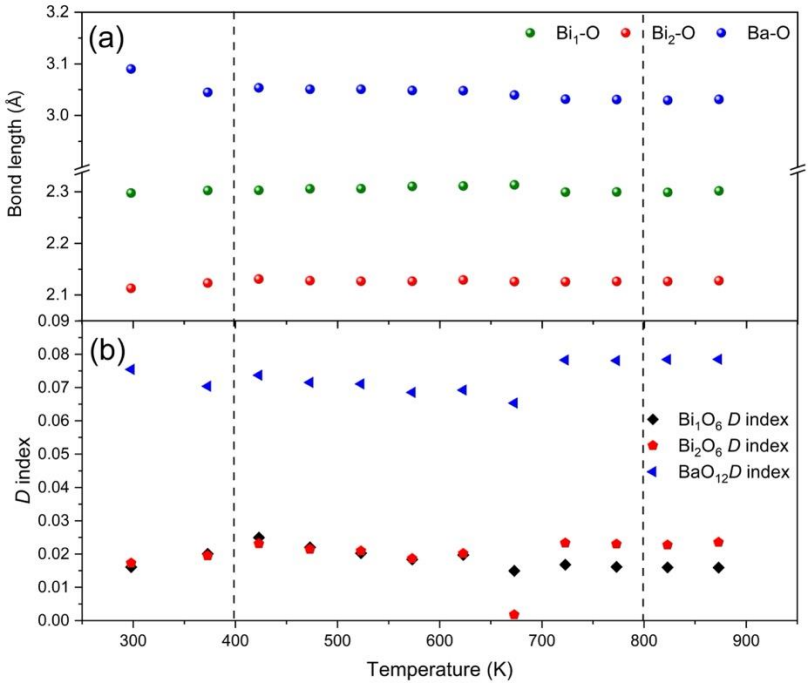

Figure 3.12: The short-range results from box-car model fitting with monoclinic structure $P2_1/n$ between 1.3 to 5 Å. (a) Cation-oxygen bond distance with temperature dependence in $P2_1/n$, and (b) The temperature dependence of distortion index in each oxygen polyhedra. The dash line indicates the phase transition temperature point for long-range average structure. The point 673 K is an experimental artefact.

Based on the fitting results presented in Figure 3.11, it is evident that between 300 and 873 K, the $P2_1/n$ structure provides a satisfactory fit to the local-scale features. This indicates that, despite the temperature induced changes in the long-range symmetry, locally in-phase tilting persists.[24] Maughan and co-workers observed a similar phenomenon in the vacancy ordered double perovskite, Rb_2SnI_6, where NPDF analyses revealed the local coordination environment was best described by a the monoclinic structure as a consequence of dynamic octahedral rotations. [25]

The NPDF analysis is consistent with Bi charge disproportionation in $BaBiO_3$ as previously suggested by Martoňák and co-workers.[24] Again the values in the rhombohedral phase were anomalous, and not typical of charge ordering. It is proposed that is a lack of local ordering and this is potentially related to the thermal decoupling between local and global structure.

Box-car fitting was also performed on the data measured at 573 K this could be fit assuming a long-range *I2/m* structure together with the short range $P2_1/n$ structure

Table 3.3: The distribution of oxygen-oxygen distance in the polyhedra for the four $BaBiO_3$ structures as determined by the box-car fit with NPDF within 1.6-5 Å range.

	$P2_1/n$	*I2/m*	$R\bar{3}$	$Fm\bar{3}m$
BiO_6 octahedra (Bi^{3+}) (Å)	3.1649 (18) X 2	3.0359 (14) X 2	2.9718 (14) X 2	2.9651 (16) X 2
	3.209 (2) X 2	3.1824 (13) X 2	3.2270 (3) X 2	3.1420 (20) X 2
	3.249 (3) X 2	3.2256 (3) X 2	3.2328 (14) X 2	3.1889 (17) X 2
	3.250 (3) X 2	3.2445 (16) X 2	3.3014 (17) X 2	3.3187 (3) X 2
	3.276 (3) X 2	3.3912 (14) X 2	3.3909 (14) X 2	3.4394 (17) X 2
	3.3297 (18) X 2	3.4040 (12) X 2	3.4640 (13) X 2	3.4523 (17) X 2
	4.585 (3)	4.4843 (16)	4.4938 (16)	4.4935 (15)
	4.588 (3)	4.6368 (17)	4.6333 (17)	4.607 (2)
	4.603 (3)	4.6643 (17)	4.7361 (18)	4.7090 (19)
BiO_6 octahedra (Bi^{5+}) (Å)	2.953(2) X 2	2.8512 (14) X 2	2.8056 (15) X 2	2.7985 (17) X 2
	2.990 (3) X 2	2.9581 (13) X 2	2.9260 (3) X 2	2.8538 (3) X 2
	2.9901 (18) X 2	2.9681 (3) X 2	2.9763 (13) X 2	3.031 (2) X 2
	2.9741 (18) X 2	3.0225 (13) X 2	3.0839 (14) X 2	3.0295 (17) X 2
	2.992 (3) X 2	3.0453 (12) X 2	3.1174 (13) X 2	3.1059 (7) X 2
	3.003 (3) X 2	3.0831 (16) X 2	3.1266 (17) X 2	3.2214 (17) X 2
	4.200 (3)	4.1199 (17)	4.1902 (17)	4.1620 (19)
	4.224 (3)	4.2229 (16)	4.1978 (18)	4.1993 (17)
	4.235 (3)	4.3357 (17)	4.3721 (18)	4.4056 (19)
BaO_{12} cuboctahedra (Å)	2.953(2) X 2	2.8512(14) X 2	2.8056(15) X 2	2.7985(17) X 2
	2.9741(18) X 2	2.9581(13)	2.9260(3) X 2	2.8538(3) X 2
	2.990(3) X 2	2.9681(3)	2.9718(14) X 2	2.9651(16) X 2
	2.9901(18) X 2	3.0225(13) X 2	2.9763(13) X 2	3.0295(17) X 2

	2.992(3) X 2	3.0359(14)	3.0839(14)	3.031(2)
	3.003(3) X 2	3.0453(12) X 2	3.1174(13)	3.1059(17)
	3.1649(18) X 2	3.0831(16) X 2	3.1266(17) X 2	3.142(2)
	3.209(2) X 2	3.1824(13) X 2	3.2270(3) X 2	3.1889(17) X 2
	3.249(3) X 2	3.2256(3) X 2	3.2328(14)	3.2214(17) X 2
	3.250(3) X 2	3.2446(16)	3.3014(17) X 2	3.3187(3) X 3
	3.276(3) X 2	3.7738(19) X 2	3.3909(14) X 2	3.4394(17) X 2
	3.3297(18) X 2	3.3912(14) X 2	3.4640(13)	3.4523(17)
	3.690(3) X 2	3.4040(12) X 2	3.7577(11) X 2	3.7633(19) X 2
	3.8105(14) X 2	3.82852(13) X 2	3.7795(19) X 2	3.8376(11)
	4.079(3)	4.2900(16)	4.1515(17)	3.8630(17)
	4.189(3)	4.6026(18)	4.2781(16)	4.2549(17)
	4.613(3)	4.6278(16)	4.6984(17)	4.627(3)
	4.7077(19)	4.7314(12)	4.7085(15)	4.6588(19)
	4.724(3)	4.756(3)	4.7191(15)	4.737(3) X 3
	4.7439(19)	4.7576(12)	4.7628(19) X 2	3.8376(11)
	4.797(3)	4.7724(19)	4.989(3)	4.7500(19) X 2
	4.800(3)	4.9854(12)		4.9091(12)
	4.9651(19)			4.9678(17)
	4.970(3) X 2			4.9697(11)
	4.9774(18) X 2			4.982(3)
	4.9954(19)			

3.4 Big-box RMC Modelling

To provide a more intuitive representation of the short-range 1.8-5 Å fitting, reverse Monte Carlo (RMC)[26, 27] big-box models were applied to local-scale range of $BaBiO_3$. For this analysis it was elected to focus on the data measured at 10 K as this will have the least thermal (dynamic) disorder. Figure 3.13 illustrates the G(r) data between cation-cation and cation-oxide pairs. The RMC profile employed an $8 * 8 * 6$ supercell structure to replicate the fine local structural features observed in the experiment. During the RMC simulation, there are no space group-imposed symmetry constraints. The RMC generated structural model provides an excellent fit to the observed data. As shown in Figure 3.13, calculated Bi-O and Ba-O bond lengths together with the O-O and cation-cation pair distances are derived from the model.

The RMC analysis indicates that there is a strong splitting of the Bi-O peak near 2.1–2.4 Å. It was then attempted to include Bond Valence Sum (BVS) constraints into the RMC analysis,[28] to confirm the assignment of the short and long Bi-O distances to Bi^{5+} and Bi^{3+} octahedra respectively. However, when BVS constraints are included in the simulations χ^2 increased compared to a model without BVS. It is counterintuitive that BVS constraints would result in a worse the fit, especially in a known charge-ordered system such as $BaBiO_3$.

In the RMC simulations the peaks from the Ba–O and O–O correlations are relatively broad, indicating a wide distribution of bond lengths consistent with local static disorder, as also seen in the Rietveld refinements. By comparison, the Bi–O peaks are relatively sharp, suggesting a narrower distribution of bond-lengths. As illustrated in Figure 3.13 the Bi-O peak is resolved into two sub-peaks that can be considered as Bi^{3+}–O and Bi^{5+}–O bonds. In the absence of BVS constraints the RMC simulations enable the Bi to occupy a Bi^{4+} like environment, that is intermediate between Bi^{3+} and Bi^{5+}, leading to a distribution of Bi–O environments. In contrast, the BVS-constrained simulation forces distinct Bi^{3+} and Bi^{5+} states, which produces clear separation of the two Bi–O sub-peaks. This enforced separation, whilst chemically

sensible, results in a worse fit. The reduced intensity of the Ba–O and O–O peaks in Figure 3.14 compared to Figure 3.13 implies improved structural order.

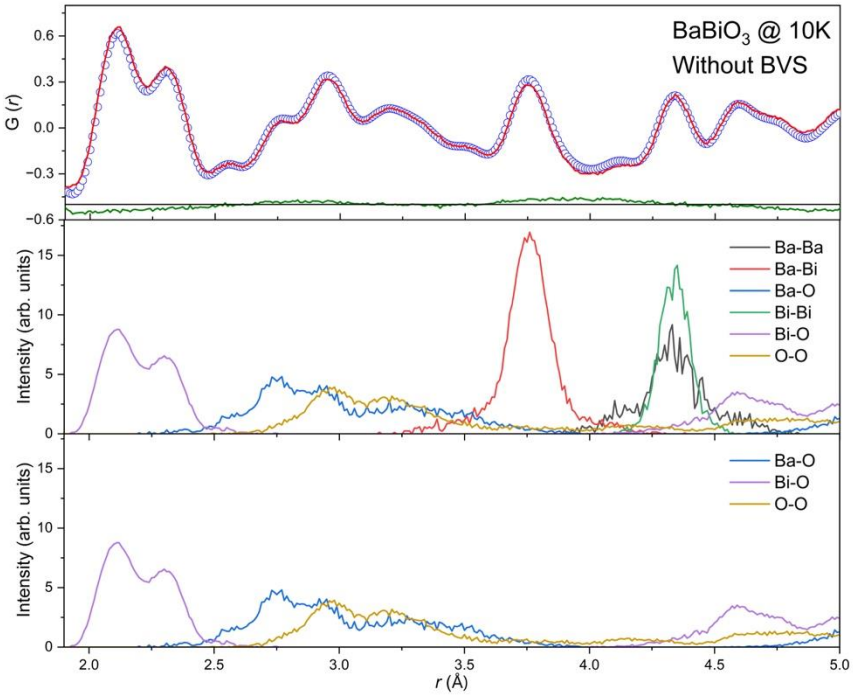

Figure 3.13: Partial PDF data of $BaBiO_3$ fit with reverse Monte Carlo (RMC) approach at 10 K. This fit does not include bond valence sum (BVS) constraints. The mid panel represent the simulation of bond distance over a range of 1.9 to 5 Å. The bottom panel shows only the contacts involving oxygen.

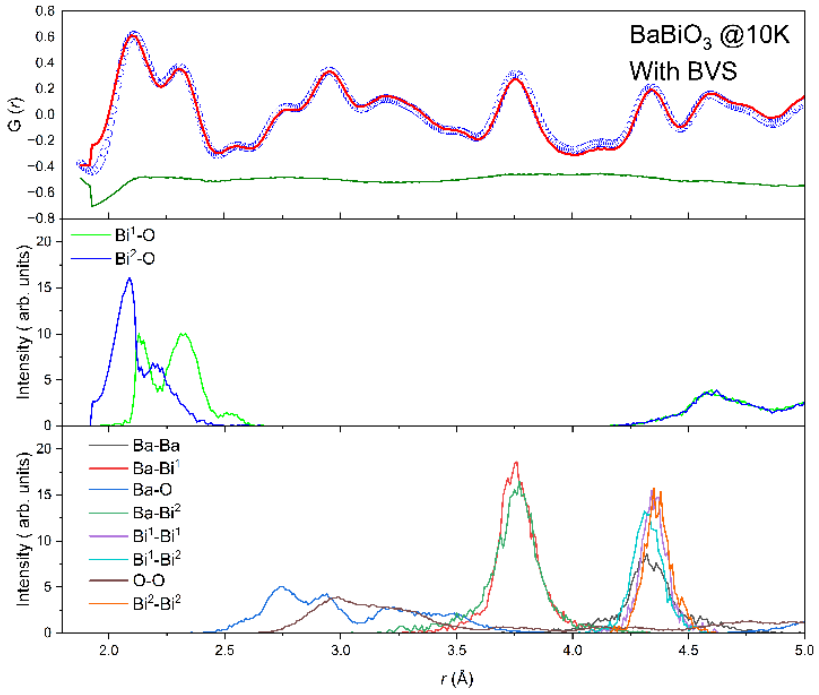

Figure 3.14: Partial PDF data of $BaBiO_3$ fit with reverse Monte Carlo (RMC) approach at 10 K. The fit result set Bi^{3+} as Bi^1 and Bi^{5+} as Bi^2 by bond valence sum (BVS). The mid panel represent the simulation of bond distance over a range of 1.5 to 5 Å. The bottle panel presents two different Bi-O bonds exhibited.

The 2-D density pattern analysis illustrates the displacement of the atoms located at the *A, B* and O sites. Figure 3.15 (a) shows that in the absence of BVS constraints the Ba and Bi cations are distributed isotropically. The inclusion of BVS constraints in the RMC simulations has little impact on this distribution. By comparison the O atoms are not centred but rather display a wide distribution of sites suggestive of an ordered displacement along the (1,1,1) direction. The inclusion of BVS constraints, Figure 3.15(b), has little impact on the displacements of the Ba and Bi cations as would occur if these occupied a single position in a rigid lattice. There are however changes in the oxygen displacements. It is perhaps not unsurprising that displacements of the O-site atoms are favoured as these would correspond to tilting of the octahedra. Further analysis of these results, including comparing the distribution in both the low symmetry and high symmetry structures is required to understand these changes.

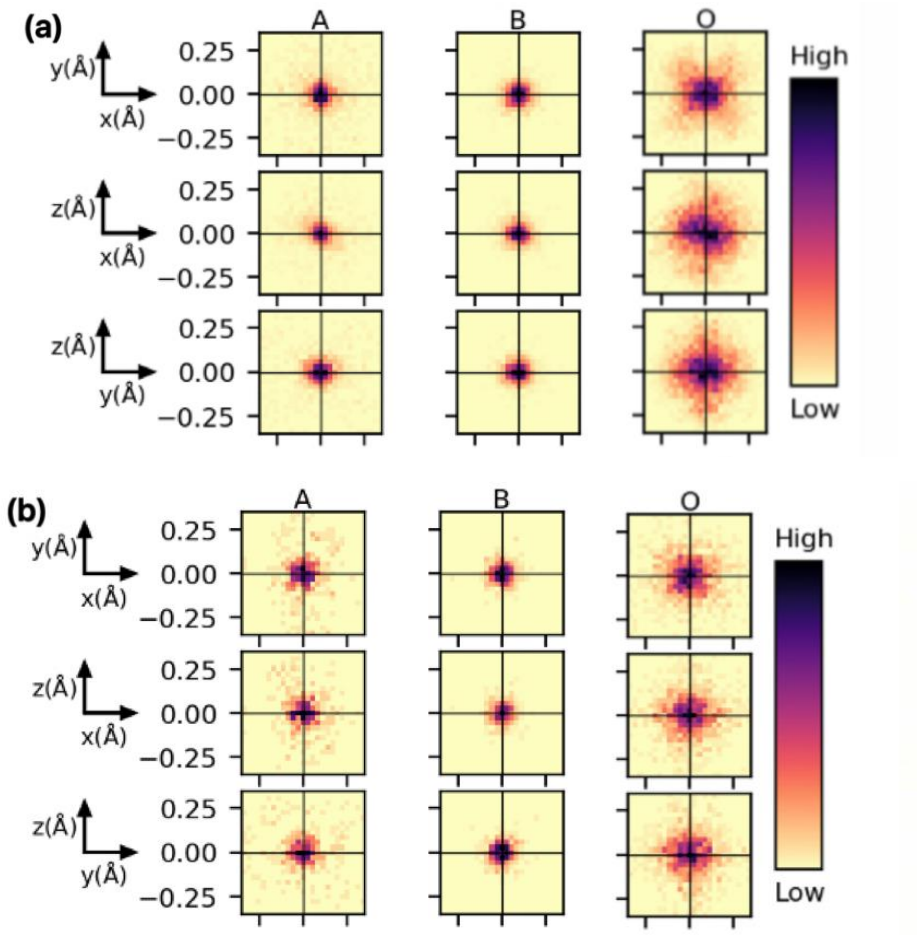

Figure 3.15: The 2D-density pattern derived by RMCprofile. (a) $BaBiO_3$ atom displacement without BVS and (b) $BaBiO_3$ atom displacement with BVS. *A* represents *A*-site atom Ba, *B* and Bi represents *B*-site and *B'*-site atom Bi^{3+} and Bi^{5+} (in BVS plot), *B* in without BVS plot represent to average Bi atom. *O* represents to oxygen atom. Three rows visualize the displacement from different axis.

3.5 Conclusions

This chapter describes a variable temperature neutron diffraction study of the local and long-range structure in the charge ordered perovskite oxide $BaBiO_3$. Bi^{3+} has a $6s^2$ lone pair of electrons and the stereochemical activity of this is incompatible with the high symmetry of the octahedral site in the perovskite-type structures. The structure of $BaBiO_3$ at room temperature

was refined in the monoclinic space group $I2/m$ that contains only out-of-phase tilts of the corner sharing BiO_6 octahedra. In this structure there are alternating large and small BiO_6 polyhedra indicative of charge disproportionation of the type $2Bi^{4+} \rightarrow Bi^{3+} + Bi^{5+}$. Heating the sample changes the orientation of the out-of-phase tilts leading firstly to a rhombohedral structure in $R\bar{3}$ and ultimately to a cubic structure in $Fm\bar{3}m$. Cooling to 10 K introduces additional in-phase tilts to the structure that is described in space group $P2_1/n$. The temperature dependence of the Bi-O bond distances is unusual with the difference between the long Bi^{3+}-O and short Bi^{5+}-O bond distances being appreciably smaller in the rhombohedral structure than in the other three phases. The phase transitions in $BaBiO_3$ are different to those seen in $CaFeO_3$ that where the charge disproportionation is temperature dependent resulting in the series of structures as $P2_1/n \rightarrow Pnma \rightarrow Pm\bar{3}m$.[29]

NPDF studies were undertaken to establish local structural changes. These studies revealed a greater range of Ba-O and O-O contracts in the range 2.5 – 3.5 Å than allowed by the long-range average structural model. Tilting of the octahedra results in distortion of the BaO_{12} polyhedra leading to a broad range of O-O contacts. It was found that the local structure as consistent with the presence of in-phase tilts at all studied temperatures. The NPDF studies did not, however, reveal any evidence for additional symmetry breaking associated with stereochemical activity of the Bi^{3+} lone pair electrons.

NPD studies establish the distortion index (D) of BiO_6 octahedra is similar in the monoclinic structures $P2_1/n$ and $I2/m$, whilst D in the $R\bar{3}$ phase is equal to 0. The bond distance distributions in NPDF shows the behaviour aligns with the breathing mode model of the BiO_6 octahedra modulating the Bi-O bond lengths. It represents the adjustments in Bi-O-Bi tilt angles to accommodate the NPDF observations.[1].

The investigations about structural characteristics of $BaBiO_3$ from NPDF studies are pivotal for validating the findings of Cox and Sleight regarding the distortion leads through octahedral tilting and oxygen octahedral breathing mode.[12] NPDF observed distinctively features including distortions in the $I2/m$ structure with BaO_{12} cuboctahedra, $R\bar{3}$ structure with BiO_6 octahedra and merging of different Ba-Bi bond distances in cubic $Fm\bar{3}m$ structure. These distortions facilitated the identification of local scale in-phase tilting with a box-car model. To

explore the question of whether the local distortions are affected by the Bi^{3+} $6s^2$ lone pair electrons, the reverse Monte Carlo (RMC) method was used to establish if there was any evidence of Bi atom off-centering. However, Bi atom remained unchanged regardless of the use of bond valence sum constraints, it indicates the behaviors of Bi^{3+} lone pair electrons across temperature dependence configuration have not been found in $BaBiO_3$ through RMC.

Bibliography

(1) Kennedy, B. J.; Howard, C. J.; Knight, K. S.; Zhang, Z.; Zhou, Q. Structures and phase transitions in the ordered double perovskites $Ba_2Bi^{III}Bi^{V}O_6$ and $Ba_2Bi^{III}Sb^{V}O_6$. *Acta Crystallographica Section B* **2006**, *62* (4), 537-546. DOI: 10.1107/S0108768106018842.

(2) Glazer, A. M. The classification of tilted octahedra in perovskites. *Acta Crystallographica Section B* **1972**, *28* (11), 3384-3392. DOI: https://doi.org/10.1107/S0567740872007976.

(3) Howard, C. J.; Kennedy, B. J.; Woodward, P. M. Ordered double perovskites - a group-theoretical analysis. *Acta Crystallographica Section B* **2003**, *59* (4), 463-471. DOI: doi:10.1107/S0108768103010073.

(4) Baur, W. H. The geometry of polyhedral distortions. Predictive relationships for the phosphate group. *Acta Crystallographica Section B* **1974**, *30* (5), 1195-1215. DOI: 10.1107/S0567740874004560.

(5) Saura-Múzquiz, M.; Marlton, F. P.; Mullens, B. G.; Liu, J.; Vogt, T.; Maynard-Casely, H. E.; Avdeev, M.; Blom, D. A.; Kennedy, B. J. Cation and Lone Pair Order–Disorder in the Polymorphic Mixed Metal Bismuth Scheelite $Bi_3FeMo_2O_{12}$. *Chemistry of Materials* **2023**, *35* (1), 123-135. DOI: 10.1021/acs.chemmater.2c02740.

(6) Howard, C. J.; Stokes, H. T. Group-Theoretical Analysis of Octahedral Tilting in Perovskites. *Acta Crystallographica Section B* **1998**, *54* (6), 782-789. DOI: doi:10.1107/S0108768198004200.

(7) Fabini, D. H.; Laurita, G.; Bechtel, J. S.; Stoumpos, C. C.; Evans, H. A.; Kontos, A. G.; Raptis, Y. S.; Falaras, P.; Van der Ven, A.; Kanatzidis, M. G.; et al. Dynamic Stereochemical Activity of the Sn^{2+} Lone Pair in Perovskite $CsSnBr_3$. *Journal of the American Chemical Society* **2016**, *138* (36), 11820-11832. DOI: 10.1021/jacs.6b06287.

(8) Laurita, G.; Seshadri, R. Chemistry, Structure, and Function of Lone Pairs in Extended Solids. *Accounts of Chemical Research* **2022**, *55* (7), 1004-1014. DOI: 10.1021/acs.accounts.1c00741.

(9) Mullens, B. G.; Marlton, F. P.; Nicholas, M. K.; Permana, A. J.; Avdeev, M.; Mukherjee, S.; Vaitheeswaran, G.; Li, C.; Liu, J.; Chater, P. A.; et al. Seeing the Unseen: The Structural Influence of the Lone Pair Electrons in $PbWO_4$. *Inorganic Chemistry* **2024**, *63* (24), 11176-11186. DOI: 10.1021/acs.inorgchem.4c00866.

(10) Shi, J.; Rubinstein, E. A.; Li, W.; Zhang, J.; Yang, Y.; Lee, T.-L.; Qin, C.; Yan, P.; MacManus-Driscoll, J. L.; Scanlon, D. O.; et al. Modulation of the Bi^{3+} $6s^2$ Lone Pair State in Perovskites for High-Mobility p-Type Oxide Semiconductors. *Advanced Science* **2022**, *9* (6), 2104141. DOI: https://doi.org/10.1002/advs.202104141 (acccessed 2025/07/06).

(11) Neuefeind, J.; Feygenson, M.; Carruth, J.; Hoffmann, R.; Chipley, K. K. The Nanoscale Ordered MAterials Diffractometer NOMAD at the Spallation Neutron Source SNS. *Nuclear Instruments and Methods in Physics Research Section B: Beam Interactions with Materials and Atoms* **2012**, *287*, 68-75. DOI: https://doi.org/10.1016/j.nimb.2012.05.037.

(12) Cox, D. E.; Sleight, A. W. Crystal structure of $Ba_2Bi^{3+}Bi^{5+}O_6$. *Solid State Communications* **1976**, *19* (10), 969-973. DOI: https://doi.org/10.1016/0038-1098(76)90632-3.

(13) Pei, S.; Jorgensen, J.; Dabrowski, B.; Hinks, D.; Richards, D.; Mitchell, A.; Newsam, J.; Sinha, S.; Vaknin, D.; Jacobson, A. Structural phase diagram of the $Ba_{1-x}K_xBiO_3$ system. *Physical Review B* **1990**, *41* (7), 4126.

(14) Shannon, R. D. Revised effective ionic-radii and systematic studies of interatomic distances in halides and chalcogenides. *Acta Crystallographica Section A* **1976**, *32*, 751-767. DOI: 10.1107/s0567739476001551.

(15) Brown, I. D.; Altermatt, D. Bond-valence parameters obtained from a systematic analysis of the Inorganic Crystal Structure Database. *Acta crystallographica. Section B, Structural science* **1985**, *41* (4), 244-247. DOI: 10.1107/S0108768185002063.

(16) Ye, Z. Relaxor ferroelectric complex perovskites: structure, properties and phase transitions. *Key Engineering Materials* **1998**, *155*, 81-122.

(17) Proffen, T.; Billinge, S. J. L.; Egami, T.; Louca, D. Structural Analysis of Complex Materials Using the Atomic Pair Distribution Function — a Practical Guide. *Zeitschrift für Kristallographie. Crystalline materials* **2003**, *218* (2), 132-143. DOI: 10.1524/zkri.218.2.132.20664.

(18) Woodward, P. M. Octahedral Tilting in Perovskites. I. Geometrical Considerations. *Acta Crystallographica Section B* **1997**, *53* (1), 32-43. DOI: https://doi.org/10.1107/S0108768196010713.

(19) Jeong, I. K.; Heffner, R. H.; Graf, M. J.; Billinge, S. J. L. Lattice dynamics and correlated atomic motion from the atomic pair distribution function. Cornell University Library, arXiv.org: Ithaca, 2002.

(20) Hashimoto, T.; Kobayashi, T.; Tanaka, H.; Hirasawa, R.; Hirai, H.; Tagawa, H. Oxygen nonstoichiometry of $BaBiO_{3-\delta}$. *Solid State Ionics* **1998**, *108* (1), 371-376. DOI: https://doi.org/10.1016/S0167-2738(98)00065-4.

(21) Klinkova, L. A.; Nikolaichik, V. I.; Barkovskii, N. V.; Fedotov, V. K. Thermal Stability of the Perovskite $BaBiO_3$. *Journal of Solid State Chemistry* **1999**, *146* (2), 439-447. DOI: https://doi.org/10.1006/jssc.1999.8390.

(22) Saito, Y.; Maruyama, T.; Yamanaka, A. Thermoanalytical investigation of the phase relation in $BaBiO_{3-x}$. *Thermochimica Acta* **1987**, *115*, 199-205. DOI: https://doi.org/10.1016/0040-6031(87)88366-1.

(23) Hou, D.; Zhao, C.; Paterson, A. R.; Li, S.; Jones, J. L. Local structures of perovskite dielectrics and ferroelectrics via pair distribution function analyses. *Journal of the European Ceramic Society* **2018**, *38* (4), 971-987. DOI: https://doi.org/10.1016/j.jeurceramsoc.2017.12.003.

(24) Martoňák, R.; Ceresoli, D.; Kagayama, T.; Matsuda, Y.; Yamada, Y.; Tosatti, E. High-pressure phase diagram, structural transitions, and persistent non-metallicity of $BaBiO_3$: theory and experiment. Cornell University Library, arXiv.org: Ithaca, 2017.

(25) Maughan, A. E.; Ganose, A. M.; Almaker, M. A.; Scanlon, D. O.; Neilson, J. R. Tolerance Factor and Cooperative Tilting Effects in Vacancy-Ordered Double Perovskite Halides. *Chemistry of Materials* **2018**, *30* (11), 3909-3919. DOI: 10.1021/acs.chemmater.8b01549.

(26) McGreevy, R. L.; Pusztai, L. Reverse Monte Carlo Simulation: A New Technique for the Determination of Disordered Structures. *Molecular Simulation* **1988**, *1* (6), 359-367. DOI: 10.1080/08927028808080958.

(27) Tucker, M. G.; Keen, D. A.; Dove, M. T.; Goodwin, A. L.; Hui, Q. RMCProfile: reverse Monte Carlo for polycrystalline materials. *Journal of Physics: Condensed Matter* **2007**, *19* (33), 335218. DOI: 10.1088/0953-8984/19/33/335218.

(28) Norberg, S. T.; Tucker, M. G.; Hull, S. Bond valence sum: a new soft chemical constraint for RMCProfile. *Journal of Applied Crystallography* **2009**, *42* (2), 179-184. DOI: doi:10.1107/S0021889809004981.

(29) Woodward, P. M.; Cox, D. E.; Moshopoulou, E.; Sleight, A. W.; Morimoto, S. Structural studies of charge disproportionation and magnetic order in $CaFeO_3$. *Physical review. B, Condensed matter and materials physics* **2000**, *62* (2), 844-855. DOI: 10.1103/PhysRevB.62.844.

Chapter 4 Charge Order Melting in Pb doped $BaBiO_3$

$BaBiO_3$ is the earliest discovered oxide exhibiting topological insulator properties, that are a result of the non-metallic characteristics of $BaBiO_3$ and sparked increasing interest in whether altering the oxygen sites can modify the metallic properties.[1] In 1975, a study focused on hydrothermally synthesised oxygen-rich $BaBiO_{3+x,}$ prepared under high-temperature and high-pressure O_2 conditions, demonstrated the potential for superconductivity, which was subsequently confirmed in $BaBi_{(1-x)}Pb_xO_3$ materials.[2]

$BaBi_{(1-x)}Pb_xO_3$ maintains a perovskite-type structure across all doping ratios. However, the tolerance factor increases with higher lead doping. This arises from Pb^{4+} sharing octahedral sites with Bi^{3+} and Bi^{5+} ions. The average ionic radii of Bi^{3+} (1.03 Å) and Bi^{5+} (0.76 Å) is approximately 0.895 Å, compared with 0.775 Å for 6-coordinate Pb^{4+}. As illustrated in Figure 4.1 it requires over 750 K for $BaBi_{(1-x)}Pb_xO_3$ to achieve cubic symmetry at low Pb contents ($0 < x < 0.2$). By contrast, the crystal structure tends towards cubic symmetry at approximately 570 K at higher lead doping with the minimum around $x = 0.8$ for $BaBi_{(1-x)}Pb_xO_3$.[3, 4] This unique phenomena results in two t phase transition pathways in $BaBi_{(1-x)}Pb_xO_3$: if $0 < x < \sim 0.2$, $P2_1/n \rightarrow I2/m \rightarrow R\bar{3}m \rightarrow Fm\bar{3}m$ and if $\sim 0.2 < x < 1$, $Ibmm \rightarrow I4/mcm \rightarrow Pm\bar{3}m$. The investigation of the superconducting state remains a paramount research focus, the primary factors governing its emergence continue to elude scientific understanding. In the tetragonal phase the structure was identified as the most essential prerequisites for the superconductivity in bismuth-based materials. To validate the hypothesis, it was imperative to eliminate influencing factors associated with the *A*-site cation. Experiments involving different cations, but maintaining the tetragonal structure, excluded the possibility of cation dominance in superconductivity, as the substitution of Ba with Rb and K at the A-site cation still exhibited favourable superconducting properties at low-temperature.[2] The presence of a charge density wave (CDW) region that allows the tetragonal phase to exist in a metastable state from $0.1 < x < 0.3$, suggests the possibility of a direct correlation between the tetragonal phase and the superconducting state. A systematic analysis of the structures with varying doping ratios is crucial. The co-existence of the tetragonal and orthorhombic structures was observed at room temperature, within the CDW boundary. At room temperature co-existence behaviour re-emerges when the lead-doped ratio is from 0.7 to 0.95, with the superconducting critical temperature T_c exhibiting a positive correlation with the tetragonal phase proportion in two-phase composition.[2, 5, 6] This study

focuses on investigating whether the first order phase transition represents charge ordering melting occurs and to probe the possible correlation between charge ordering melting and the charge density wave state.

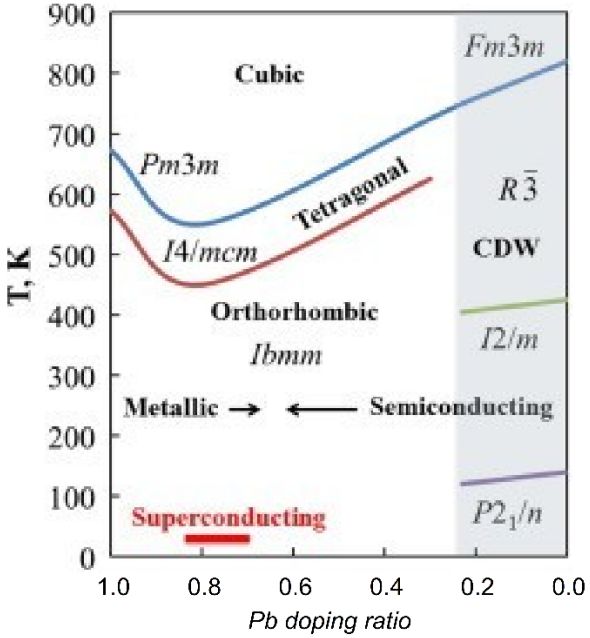

Figure 4.1: The phase diagram of $BaBi_{(1-x)}Pb_xO_3$ system with space group labelled above. The shadow area represents a charge density wave region exist between $0 > x > \sim 0.2$.[3]

4.1 Room Temperature Structures in the Series $BaBi_{1-x}Pb_xO_3$

4.1.1 Synchrotron X-ray Diffraction

The synchrotron X-ray diffraction (SXRD) data were collected at the Powder Diffraction beamline BL-10 at Australian Synchrotron.[7] The SXRD patterns for $BaBiO_3$ and $BaBi_{0.7}Pb_{0.3}O_3$ were indexed to monoclinic *I2/m* and orthorhombic *Ibmm* structures respectively Rietveld refinements were performed starting with the models described by Foyevtsov and Marx *et al.*[8, 9] As described in chapter 3 $BaBiO_3$ contains a 1:1 mixture of rock-salt like ordered Bi^{3+} and Bi^{5+}. The *Ibmm* model does not allow for ordering of the *B*-site cations. Further the X-ray form factor for Bi^{4+} is not available in TOPAS. Consequently, the

structural model contained a mixture of Bi^{3+} and Pb^{4+} on the octahedral site. Examination of Figure 4.2 suggests that, if the monoclinic angle is close to 90°, or if the diffraction data lacks the peak shape resolution to unequivocally observe diagnostic peak splitting it may be difficult to distinguish between the *I*2/*m* and two-phase structures. The refined lattice parameters and atomic coordinates of the two compositions studied here by SXRD are in good agreement with previous studies.

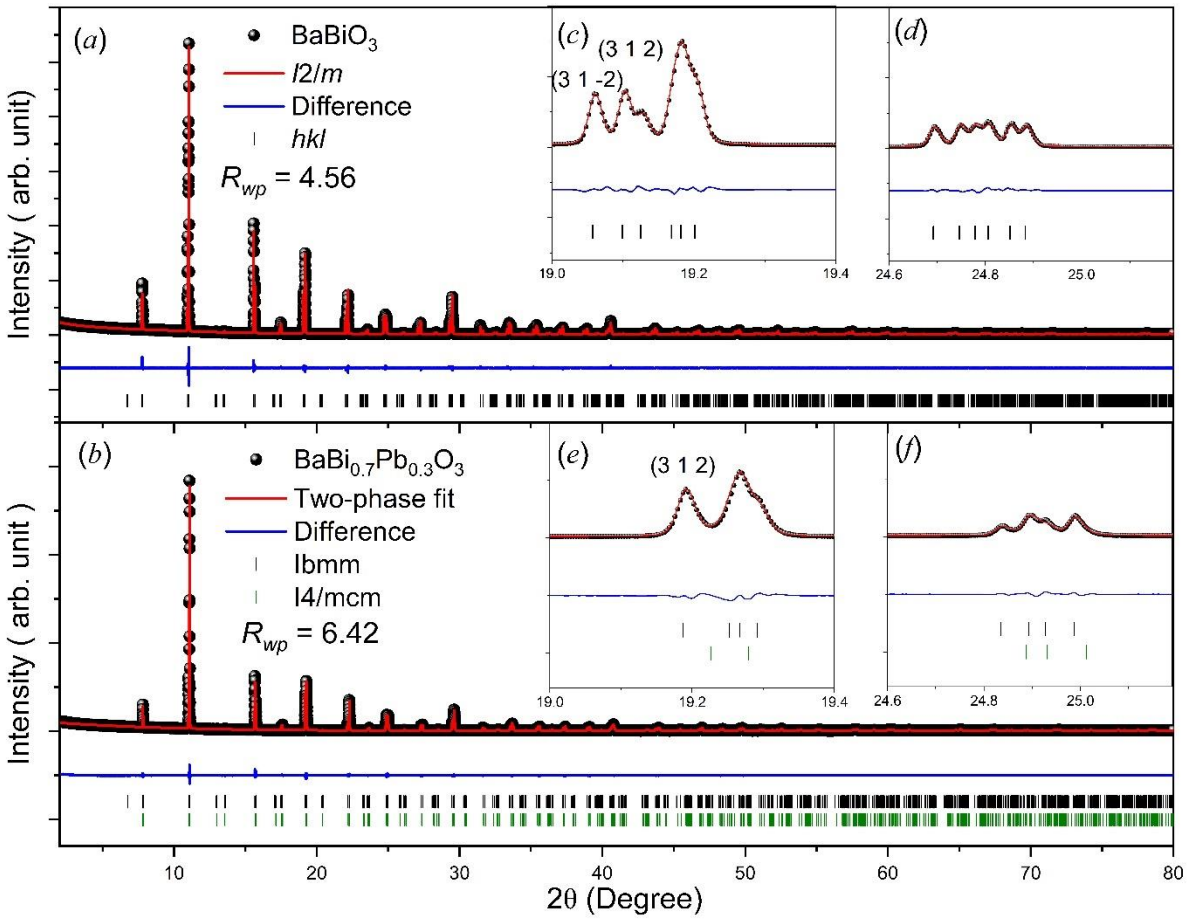

Figure 4.2: Rietveld refinement profiles of SXRD data collected for (*a*) $BaBiO_3$ and (*b*) $BaBi_{0.7}Pb_{0.3}O_3$ with wavelength 0.561545 Å. Black crosses represent the observed data; red lines indicate the calculated pattern, and the difference plot is shown in blue. Black vertical tick marks show the positions of the space group allowed *hkl* reflections. The insert (*c*) to (*f*) highlight the subtle differences between the monoclinic *I*2/*m* and orthorhombic-tetragonal co-existence (*Ibmm* and *I*4/*mcm*).

Table 4.1: Rietveld refinement parameters of $BaBiO_3$ and $BaBi_{0.7}Pb_{0.3}O3$ at 298 K from Synchrotron X-ray diffraction data.

	$BaBiO_3$	$BaBi_{0.7}Pb_{0.3}O_3$	
Space group	*I*2/*m*	*Ibmm*	*I*4/*mcm*
a (Å)	6.1838 (1)	6.1468 (3)	6.1321 (2)
b (Å)	6.13730 (2)	6.1090 (1)	6.1052 (6)
c (Å)	8.66699 (2)	8.6263 (1)	8.6183 (5)
β (°)	90.175(1)	90	90
Vol. (Å^3)	328.93 (1)	323.94 (1)	322.65 (4)
Ba *x*	0.5031 (3)	0.5036 (5)	0
Ba *z*	0.2493 (3)	0.25	0.25
Bi (2) *z* *	0.5	/	/
O (1) x	0.0454 (9)	0.0512 (14)	0
O (1) z	0.2591 (15)	0.25	0.25
O (2) x	0.2523 (10)	0.25	0.2138 (12)
O (2) y	0.2669 (12)	0.250	0.7088 (13)
O (2) z	-0.0407 (6)	0.9768 (11)	0
Ba U_{11} (Å^2)	0.0069 (2)	0.0053 (3)	0.056 (6)
Ba U_{22} (Å^2)	0.0105 (2)	0.0044 (4)	= U_{11}
Ba U_{33} (Å^2)	0.0073 (2)	0.0059 (4)	0.024 (5)
Bi (1) U_{11} (Å^2)	0.0019 (7)	0.0005 (59)	0.065 (6)
Bi (1) U_{22} (Å^2)	0.0015 (10)	0.000 (14)	= U_{11}
Bi (1) U_{33} (Å^2)	0.0029 (9)	0.000 (8)	0.002 (7)
Pb U_{11} (Å^2)	/	0.000 (14)	0.000 (5)
Pb U_{22} (Å^2)	/	0.000 (32)	= U_{11}
Pb U_{33} (Å^2)	/	0.000 (19)	0.000 (12)
Bi (2) U_{11} (Å^2)	0.0010 (7)	/	/
Bi (2) U_{22} (Å^2)	0.0015 (10)	/	/
Bi (2) U_{33} (Å^2)	0.0009 (8)	/	/

O (1) U_{11} (Å^2)	0.000 (3)	0.000 (4)	0.000 (23)
O (1) U_{22} (Å^2)	0.0051 (3)	0.000 (6)	= U_{11}
O (1) U_{33} (Å^2)	0.0009 (8)	0.031 (7)	0.111 (7)
O (2) U_{11} (Å^2)	0.0079 (20)	0.0305 (5)	0.082 (11)
O (2) U_{22} (Å^2)	0.000 (3)	0.0595 (8)	0.098 (11)
O (2) U_{33} (Å^2)	0.033 (3)	0.000 (4)	0.822 (12)
Bi-O (2) (Bi^{3+}/Å)	2.292 (7)	2.179 (1)	2.200 (8)
Bi-O (2) (Bi^{5+}/Å)	2.114 (1)	/	/
Ba-O (2) (Å)	3.084 (1)	3.073 (1)	3.066 (1)
BiO_6 (Bi^{3+}) (Å^3)	15.71	13.24	13.79
BiO_6 (Bi^{5+}) (Å^3)	12.60	/	/
BaO_{12} (Å^3)	68.08	67.74	66.87
R_{wp} (%)	4.502	6.420	
BVS (BiO_6 / Bi^{3+})	3.64	3.356	3.34
BVS (BiO_6 / Bi^{5+})	5.10	/	/

* Bi^{3+} occupies a *B*-site with Wyckoff position (0,0,0) and Bi^{5+} occupies a *B*-site with Wyckoff position (0,0,0.5).

* BVS for *Ibmm* space group Bi^{5+} BiO_6 octahedral calculated based on bond valence parameter of Bi^{5+} and Pb^{4+} within shared BiO_6 octahedral

4.1.2 Neutron Powder Diffraction

Neutron scattering data for seven members of the $BaBi_{1-x}Pb_xO_3$ series were measured using NOMAD, as illustrated in Figure 4.3. The diffraction patterns are all very similar and initially the structures were all refined, against the data measured on the highest resolution 154 ° bank, assuming monoclinic *I*2/*m* symmetry. At $x = 0.25$ the refined value of the monoclinic angle, was within error equal to 90 degrees indicating the structure was orthorhombic. This corresponds to the *I*2/*m* to *Ibmm* transformation as identified by earlier researchers. With the

exception of the pattern for$BaBi_{0.7}Pb_{0.3}O_3$ ($x = 0.3$) high quality fits were obtained, as illustrated in Figure 4.3. The results of the Rietveld refinements are summarised in Table 4.2.

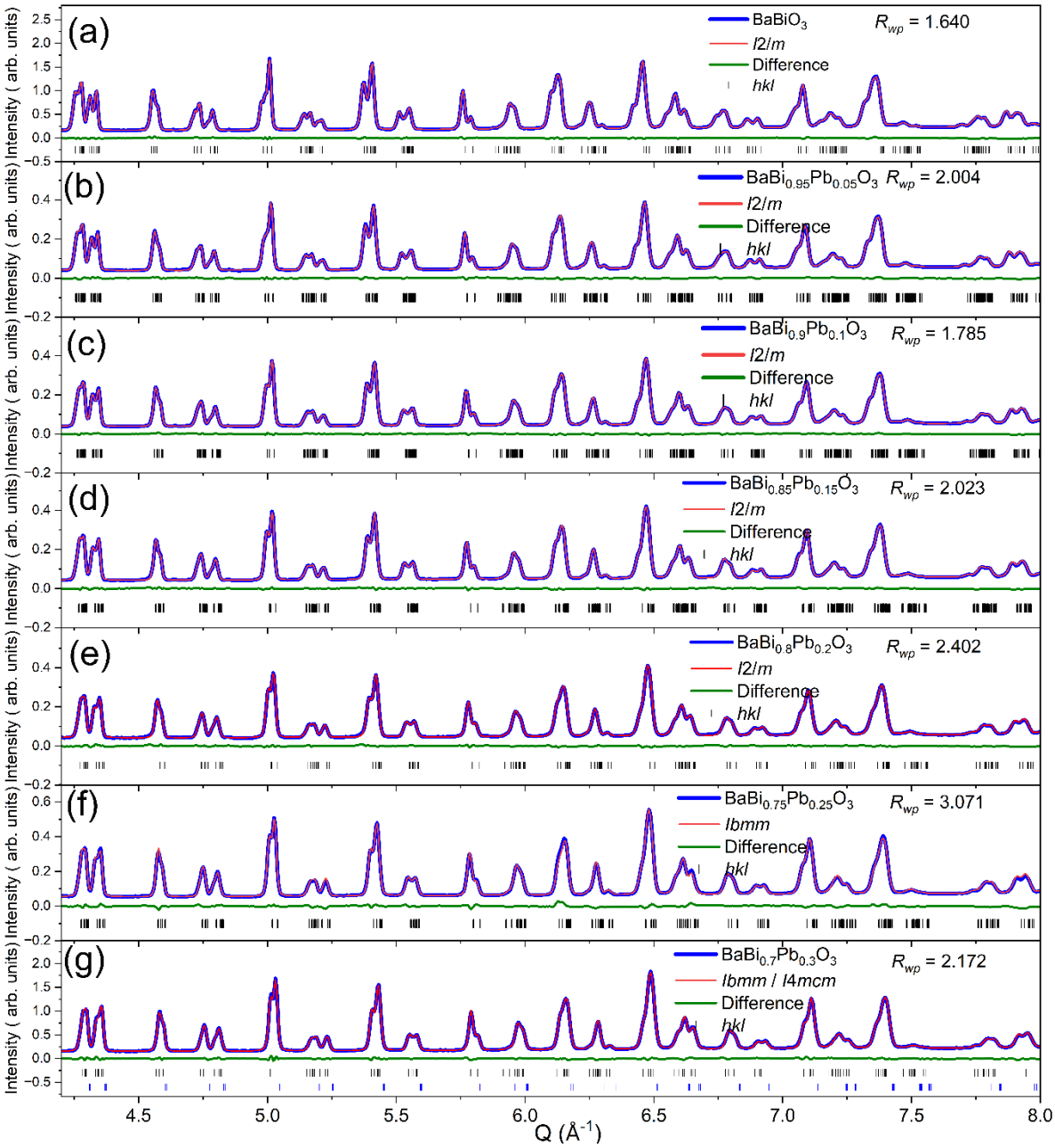

Figure 4.3: Neutron powder diffraction data of $BaBi_{(1-x)}Pb_xO_3$ ($0 \leq x \leq 0.3$). (a) to (g) Bragg peak fit for $BaBi_{(1-x)}Pb_xO_3$ from Q range 4.2 to 8 $Å^{-1}$ with diffraction angle 154°. The blue line represents the data, the red line represents the calculated fit to the data, and the green line represents the difference between the two. The black tick represents the allowed *hkl* position, R_{wp} above shows the good of fit for 154° bank reuslt.

Table 4.2: Rietveld refinement parameters of $BaBi_{(1-x)}Pb_xO_3$ neutron powder diffraction data at 298 K from NPD.[1]

	$BaBi_{(1-x)}Pb_xO_3$							
x Value	0	0.05	0.1	0.15	0.2	0.25	0.3	
Space group	*I2m*	*I2m*	*I2m*	*I2m*	*I2m*	*Ibmm*	*Ibmm*	*I4/mcm*
a (Å)	6.182(5)	6.175 (5)	6.170 (5)	6.156(3)	6.157(4)	6.148 (2)	6.156(1)	6.100 (1)
b (Å)	6.135(5)	6.1307 (5)	6.1278 (5)	6.117(3)	6.118(5)	6.111 (2)	6.120(1)	6.100 (1)
c (Å)	8.664(6)	8.6567 (4)	8.6525 (4)	8.637(4)	8.639(7)	8.629 (3)	8.641(4)	8.615 (2)
β (°)	90.179(5)	90.15(1)	90.11(1)	90.06(1)	90.04(1)	90	90	90
Vol. (Å^3)	328.60(6)	327.72 (6)	327.15 (6)	326.14(6)	325.41(7)	324.21(15)	325.02(6)	320.58 (10)
Ba *x*	0.5032 (2)	0.5033 (3)	0.5028 (1)	0.5021 (2)	0.5018 (1)	0.5016 (3)	0.5018 (2)	0
Ba *z*	0.2483 (1)	0.2498 (2)	0.2495	0.2487 (3)	0.2498 (2)	0.25	0.25	0.25
O (1) *x*	0.0633 (3)	0.0626 (9)	0.0609	0.0591 (2)	0.0587 (1)	0.0574 (2)	0.0552 (11)	0
O (1) *z*	0.2613 (2)	0.2606 (3)	0.2597	0.2434 (2)	0.2418 (1)	0.25	0.25	0.25
O (2) *x*	0.2627 (2)	0.2614 (4)	0.2605	0.2449 (1)	0.2435 (3)	0.25	0.25	0.2209
O (2) *y*	0.2579 (2)	0.2563 (1)	0.2557	0.2448 (3)	0.2476 (1)	0.25	0.25	0.7209
O (2) *z*	-0.0336 (3)	-0.0324 (4)	-0.0314 (3)	-0.0290 (1)	-0.0293 (4)	0.9713 (3)	0.9709 (2)	0
Ba U_{11} (Å^2)	0.0093 (5)	0.032(2)	0.0076 (6)	0.0124 (9)	0.0073 (6)	0.0088 (6)	0.088 (6)	0.30 (4)
Ba U_{22} (Å^2)	0.0127 (5)	0.018 (3)	0.0148 (7)	0.0125 (6)	0.0117 (7)	0.0128 (8)	0.024 (1)	0.30 (4)
Ba U_{33} (Å^2)	0.0117 (5)	0.000 (6)	0.0000 (5)	0.0104 (7)	0.0083 (7)	0.0094 (7)	0.048 (6)	0.027 (15)
Bi (1) U_{11} (Å^2)	0.0075 (5)	0.0034 (12)	0.02 (10)	0.0005 (14)	0.0032 (10)	0.0002 (6)	0.002 (1)	0.05 (2)
Bi (1) U_{22} (Å^2)	0.0100 (4)	0.007 (7)	0.00 (12)	0.0064 (20)	0.0104 (6)	0.0046 (16)	0.0006 (6)	0.05 (2)
Bi (1) U_{33} (Å^2)	0.0000 (6)	0.000 (4)	0.00 (5)	0.0093 (21)	0.0080 (8)	0.0020 (13)	0.000 (1)	0.000 (9)
Bi (2) U_{11} (Å^2)	0.0051 (5)	0.0015 (1)	0.00 (13)	0.0027 (22)	0.0107 (5)	/	/	/
Bi (2) U_{22} (Å^2)	0.0047 (5)	0.0028 (13)	0.00 (9)	0.0006 (17)	0.0030 (10)	/	/	/
Bi (2) U_{33} (Å^2)	0.0050 (5)	0.0029 (14)	0.00 (15)	0.0032 (20)	0.0000 (6)	/	/	/
O (1) U_{11} (Å^2)	0.0174 (5)	0.0168 (10)	0.0157 (8)	0.0184 (10)	0.0162 (10)	0.0127 (7)	0.042 (3)	0.038 (1)
O (1) U_{22} (Å^2)	0.0341 (5)	0.026 (3)	0.0344 (12)	0.0354 (15)	0.0335 (16)	0.0326 (12)	0.047 (3)	0.038 (1)
O (1) U_{33} (Å^2)	0.0070 (5)	0.020 (3)	0.0058 (10)	0.0027 (11)	0.0018 (12)	0.0110 (8)	0.075 (7)	0.003 (11)
O (2) U_{11} (Å^2)	0.0200 (5)	0.046 (3)	0.0183 (7)	0.0234 (8)	0.0227 (10)	0.0189 (6)	0.0254 (3)	0.11 (2)
O (2) U_{22} (Å^2)	0.0180 (5)	0.002 (2)	0.0187 (7)	0.0154 (8)	0.0133 (9)	0.0155 (7)	0.011 (1)	0.11 (2)
O (2) U_{33} (Å^2)	0.0242 (5)	0.0345 (19)	0.0233 (6)	0.0225 (7)	0.0218 (8)	0.0212 (6)	0.0335 (10)	0.23 (3)
Bi-O (2) (Bi^{3+}/Å)	2.296(15)	2.288(3)	2.278(4)	2.234(4)	2.259(6)	2.186(3)	2.1833 (1)	2.1856 (15)
Bi-O (2) (Bi^{5+}/Å)	2.106(15)	2.109(3)	2.114(4)	2.138(4)	2.120(6)	/	/	/
Ba-O (2) (Å)	3.096(3)	3.094(4)	3.090(4)	3.082(5)	3.0824(4)	3.077(3)	3.079(3)	3.048 (1)
BiO_6 (Bi^{3+}) (Å^3)	15.992(4)	15.713(3)	15.517(3)	15.224(4)	14.882(4)	13.865(3)	13.890(3)	13.742 (1)
BiO_6 (Bi^{5+}) (Å^3)	12.470(4)	12.598(4)	12.673(4)	12.828 (4)	13.019(3)	/	/	/
BaO_{12} (Å^3)	67.92 (4)	67.78 (4)	67.69 (4)	67.569 (4)	67.40 (5)	67.19 (5)	67.36 (4)	66.40 (3)
D Index BiO_6 (Bi^{3+})	0.00198	0.00336	0.00317	0.00549	0.00719	0.00093	0.00054	0.00573
D Index BiO_6 (Bi^{5+})	0.00047	0.00154	0.00148	0.00380	0.00539	/	/	

[1] Two phases fit at $x = 0.3$ will be illustrated in Selection 4.2.

D Index BaO_{12}	0.06728	0.06547	0.06330	0.06110	0.05943	0.05826	0.05702	0.05708
R_{wp} (%)*	2.155	2.554	2.613	2.422	2.549	2.767	2.172	
BVS (BiO_6 / Bi^{3+})	3.54	3.28	3.39	3.22	3.39	3.42	3.16	3.23
BVS (BiO_6 / Bi^{5+}) *	5.29	4.66	4.61	3.86	4.10	3.19	2.96	3.03

* Bi^{3+} occupies a *B*-site with Wyckoff position (0,0,0) and Bi^{5+} occupies a *B*-site with Wyckoff position (0,0,0.5).

* BVS for *Ibmm* space group Bi^{5+} BiO_6 octahedral calculated based on bond valence parameter of Bi^{5+} and Pb^{4+} within shared BiO_6 octahedral

* R_{wp} in Table 4.2 indicates average good of fit for four banks from 31 to 154°.

The unit cell volume in the series $BaBi_{1-x}Pb_xO_3$ ($0 \leq x \leq 0.3$) is observed to decrease as the Pb concentration increases. This is not unexpected as the ionic radii of six-coordinate Pb^{4+} (0.775 Å) is smaller than the average value (0.895 Å) for a 1:1 mixture of Bi^{3+} (1.03 Å) and Bi^{5+} (0.76 Å).[10, 11]

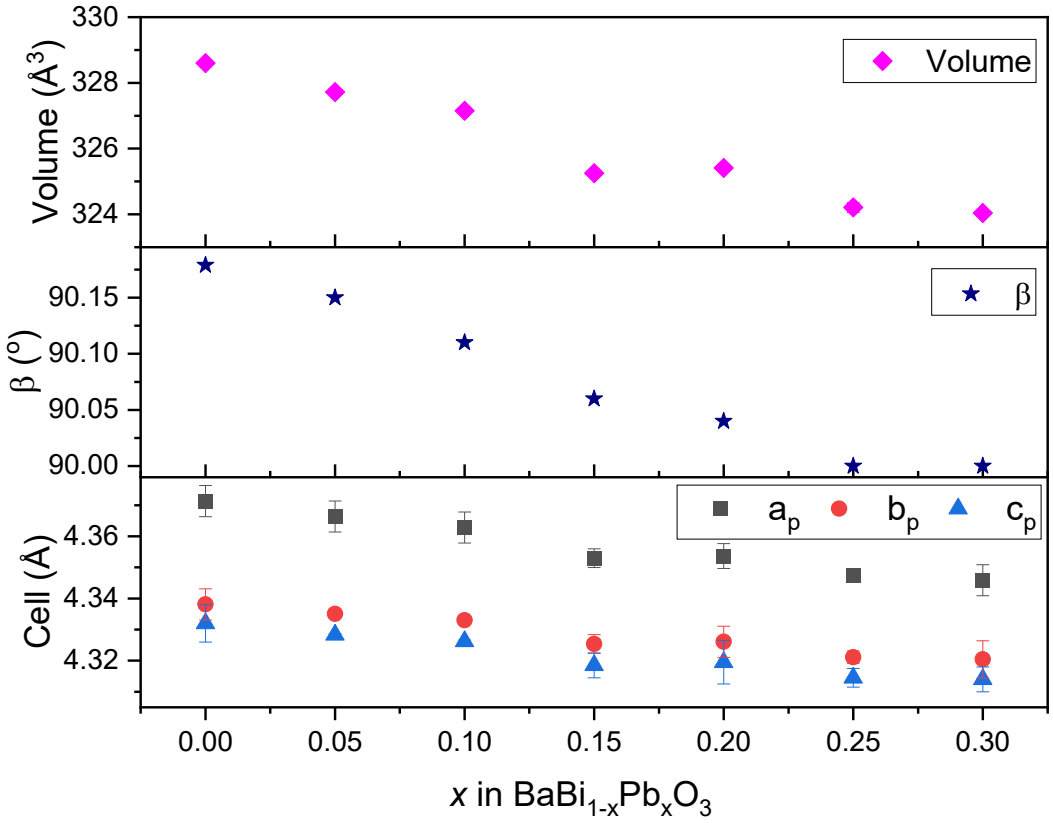

Figure 4.4: Rietveld refinements for the neutron powder diffraction for $BaBi_{1-x}Pb_xO_3$ ($0 \leqslant x \leqslant 0.3$) series of compounds at room temperature. Top panel shows volume across the series, mid plane shows the change for β angle from $I2/m \rightarrow Ibmm$, and bottle panel shows lattice parameters.

Assuming the observed ordering of the large and small octahedra in $BaBiO_3$ is a result of charge ordering there is no a priori reason that the Pb^{4+} should be distributed equally over the two sites in the monoclinic structure. Indeed, based on the size of the cations the local strain in the structure, caused by having two cations of different sizes disordered onto the same site, would be minimised if the Pb^{4+} cations preferentially occupied the same site as the smaller Bi^{5+} cations. If this occurred, it is expected that the size of the larger $Bi^{3+}O_6$ octahedra should be only weakly dependent on the total Pb content, as it would contain little, if any, Pb. That this is not observed (see the figure 4.5) suggests the lead statistically occupies the two sites. Another explanation for the alternating presence of large and small octahedra is that a lattice instability results in a breathing distortion, where alternate BiO_6 octahedra expand and contract without formal charge transfer. In this case a random distribution of the Pb cations might be expected. The Rietveld refinement results cannot distinguish between these possibilities.

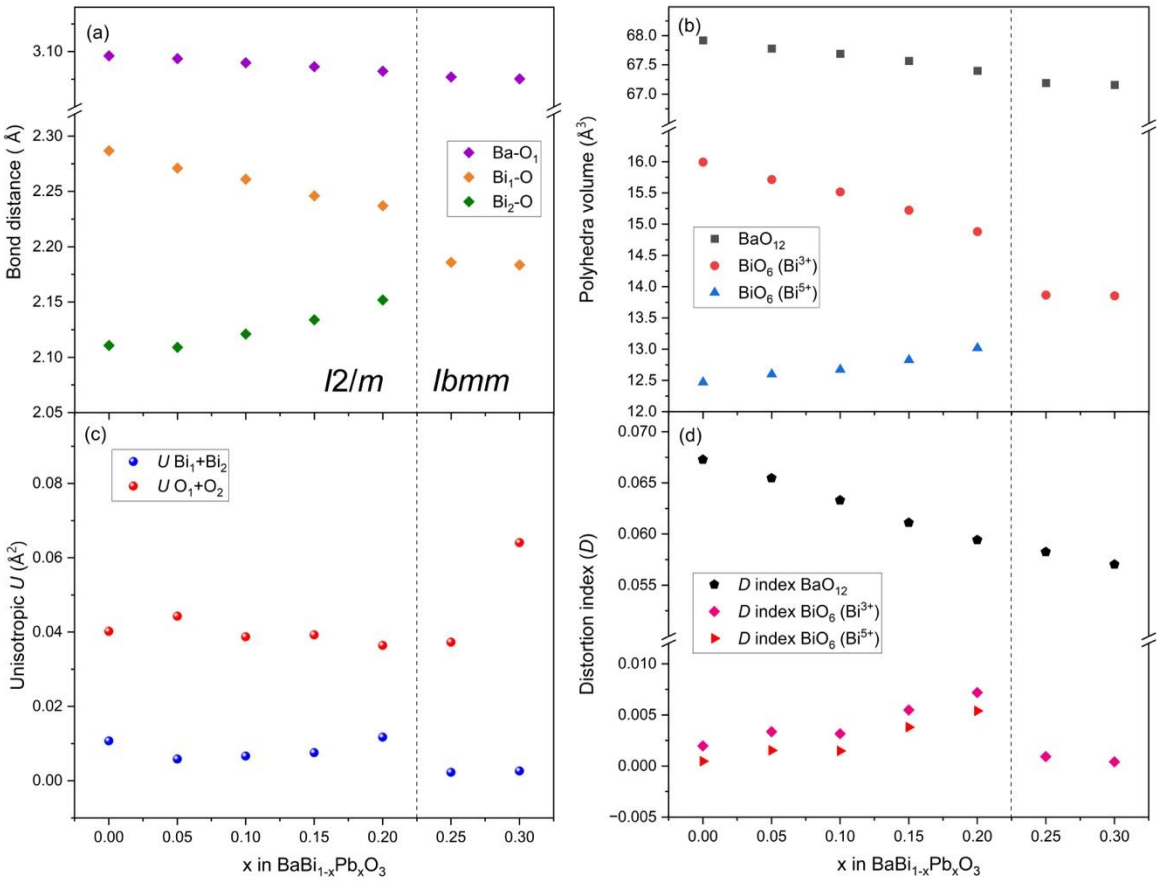

Figure 4.5: Rietveld refinements for the neutron powder diffraction for $BaBi_{1-x}Pb_xO_3$ ($0 \leq x \leq 0.3$) series of compounds at room temperature. With (a) the bond distances for cation-oxygen pair, (b) the polyhedral volume, (c) the atomic displacement parameters of Bi^{3+}+Bi^{5+} and as well as of the O atoms, and(d) distortion index *D* in each polyhedra. Dash line represents the I2/*m* → *Ibmm* boundary.

In addition to the anticipated orderly reduction in the unit cell volume, the observed changes in the space group align with the literature. The most significant aspect is the evolution of Bi-O bond lengths. For $0 \leq x \leq 0.3$, the distance between Bi and O with different valence states approach each other as the doping ratio nears the threshold. The difference between them decreases from approximately 0.2 Å to 0.1 Å. Interestingly, this change exhibits a fluctuation near $x \sim 0.2$, which we suspect to be within the range where charge ordering melting occurs under ambient conditions. $BaBi_{0.8}Pb_{0.2}O_3$ cannot provide convincing evidence of orthorhombic *Ibmm* structure or monoclinic *I2/m* structure (Figure 4.6). Both *hkl* reflection tick can match the peak towards to each space group and similar R_{wp} value (*I2/m* fit model has longer refinement range and β angle constraint, it will result high R_{wp}), but few small peaks observed

in NPD data at Q = ~ 4.35, 4.57 and bad fitted backgrounds in *Ibmm* model fit support 0.2 composition sample exist as a monoclinic phase.

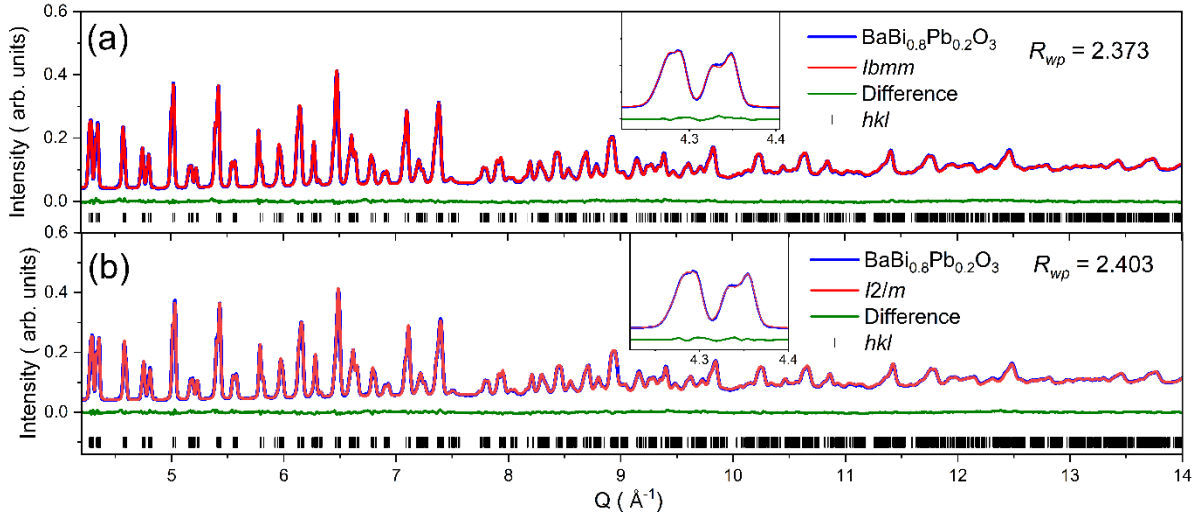

Figure 4.6: Room temperature neutron powder diffraction data of $BaBi_{0.8}Pb_{0.2}O_3$ collected from NOMAD beamline fitted with space group (a) *Ibmm* and (b) *I*2/*m*. The blue line represents the observed data and the red line represents the Rietveld refinement result and green line represent the difference between the two. Black ticks represent the space group allowed *hkl* reflection.

For x = 0.25 – 0.3, the monoclinic structure *I*2/*m* no longer fit the NPD Bragg peaks of the doped samples. The *Ibmm* fit is also not perfect, and it is hypothesized that a two phases region occurs near the CDW boundary. The average Bi-O bond length in the *Ibmm* structure is approximately ~2.18 Å. The ADPs for the *I*2/*m* and *Ibmm* structures are listed in Table 4.2. The orthorhombic and monoclinic structures show strong structural similarity, and in both the oxygen atom ADPs exhibit stronger displacements perpendicular to the Bi-O bond. ADPs for four equatorial oxygen atoms are more isotropic in the lead-doped samples.

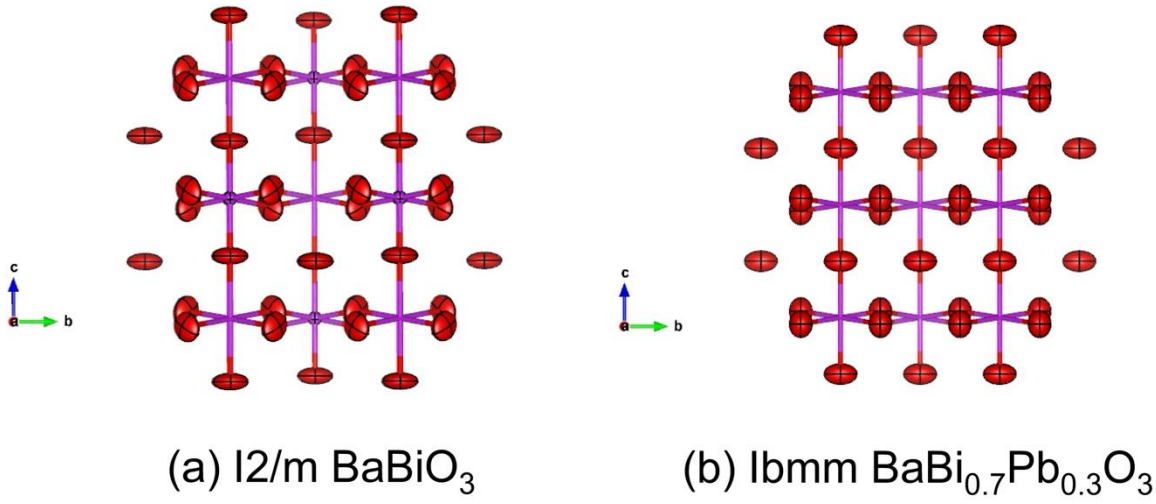

Figure 4.7: Comparision of the anisotropic atomic displacements of the oxygen atoms in undoped BaBiO3 (*I*2/*m*) and in $BaBi_{0.7}Pb_{0.3}O_3$ (*Ibmm*). The oxygen atoms are represented as ellipsoids and connect with violet sphere (Bi atom).

Finally, a BVS analysis on the Pb-doped samples was conducted. The BVS formula is $V_i = \sum_j \exp\left(\frac{R_0 - R_{ij}}{b}\right)$.[12] However, considering the disorder of the cations in the BiO_6 octahedra, the BVS calculation was weighted as $V_{total} = nV_{Bi} + mV_{Pb}$, where *n* and *m* represents the doping ratio. The incorporation of Pb^{4+}, reduces the BVS of the two *B*-sites, see Table 4.2. The BVS formula illustrates high sensitivity to bond length variations in its computational outcomes. Lead substitution induces local distortion in the BiO_6 octahedra and alters the average bond distances. In the Rietveld refinement, a crystallographic model where the Pb-Bi share the*B*-sitewas applied to calculate average BiO_6 octahedral environment. However, at the I2/*m* → *Ibmm* transition there is a discontinuous jump in the BVS which is potentially attributed to unmodeled static disorder. For *x* = 0.2 – 0.25, the Bi oxidation state behaves similarly to 4+, which corresponds to previously reports about charge order (CO) melting.[9, 13] The continuous decrease in the *Ibmm* structure may correlate with insufficient bonding caused by increased structure symmetry. Notably, the O-site coordinates are all next to the ideal Wyckoff positions, positions (*x, y, z*) approximately ~ 0.25 or ~0.5.

4.2 Temperature Dependent Structure of $BaBi_{0.7}Pb_{0.3}O_3$

The temperature dependence of the structure of $BaBi_{0.7}Pb_{0.3}O_3$ has been described previously.[9, 14] The phase transition pathway was identified as *Ibmm*→*I*4/*mcm*→*Pm* $\bar{3}$ *m*. The room temperature structure of $BaBi_{0.7}Pb_{0.3}O_3$ was well described by space group *Ibmm* and has a single octahedral site with an average Bi/Pb-O bond length of about 2.18 Å. The orthorhombic structure is reported to persist to around 573 K displays, [9, 15] and initial Rietveld refinements against the NPD (Figure 4.8) appeared to confirm this. However careful scrutiny of the profile measured between 298 K and 573 K revealed several changes that are not reproduced by the *Ibmm* model. The peaks at Q = 4.28, 4.35 and 5.02 were observed to change relative intensity during heating, with one peak progressively growing whilst another peak diminished, finally merging into a single peak. This behaviour is similar to the changes described for the first order phase transition in K_2ReI_6, where the two phases co-existed over a finite temperature range.[16] In the present case it was not possible to fit the profile measured at 373 K to single phase models of either *Ibmm* or *Pm*$\bar{3}$*m*. Nor was it possible to fit it to a two-phase mixture of the two. Likewise, a single-phase tetragonal *I*4/*mcm* model also proved unsatisfactory. A two phase *Ibmm* + *I*4/*mcm* model, did however provide a satisfactory fit, Figure 4.9-4.10. Evidently a two-phase region associated with a first order phase transition occurs in $BaBi_{0.7}Pb_{0.3}O_3$ (Figure 4.9), the reflections began to emerge in different Q range were observed for *Ibmm* space group, and the additional reflections for increasing peak were fitting with the space group *I*4/*mcm*. The two-phases region was fined until 573 K. The phase fraction of the *Ibmm* and *I*4/*mcm* phases is plotted in Figure 4.11.

Upon heating, conventional thermal expansion of the lattice occurs for both the orthorhombic *Ibmm* and tetragonal *I*4/*mcm* phases. The temperature dependence of the *B*–O bond distances, from the Rietveld refinements is displayed in Figure 4.11. The NPD study, that provides the greatest accuracy of oxygen position and hence Ba-O and Bi-O distances, that increase approximately linearly with temperature. In both the orthorhombic and tetragonal

phases, the BiO_6 octahedra are slightly distorted that may reflect the presence of a breathing mode.

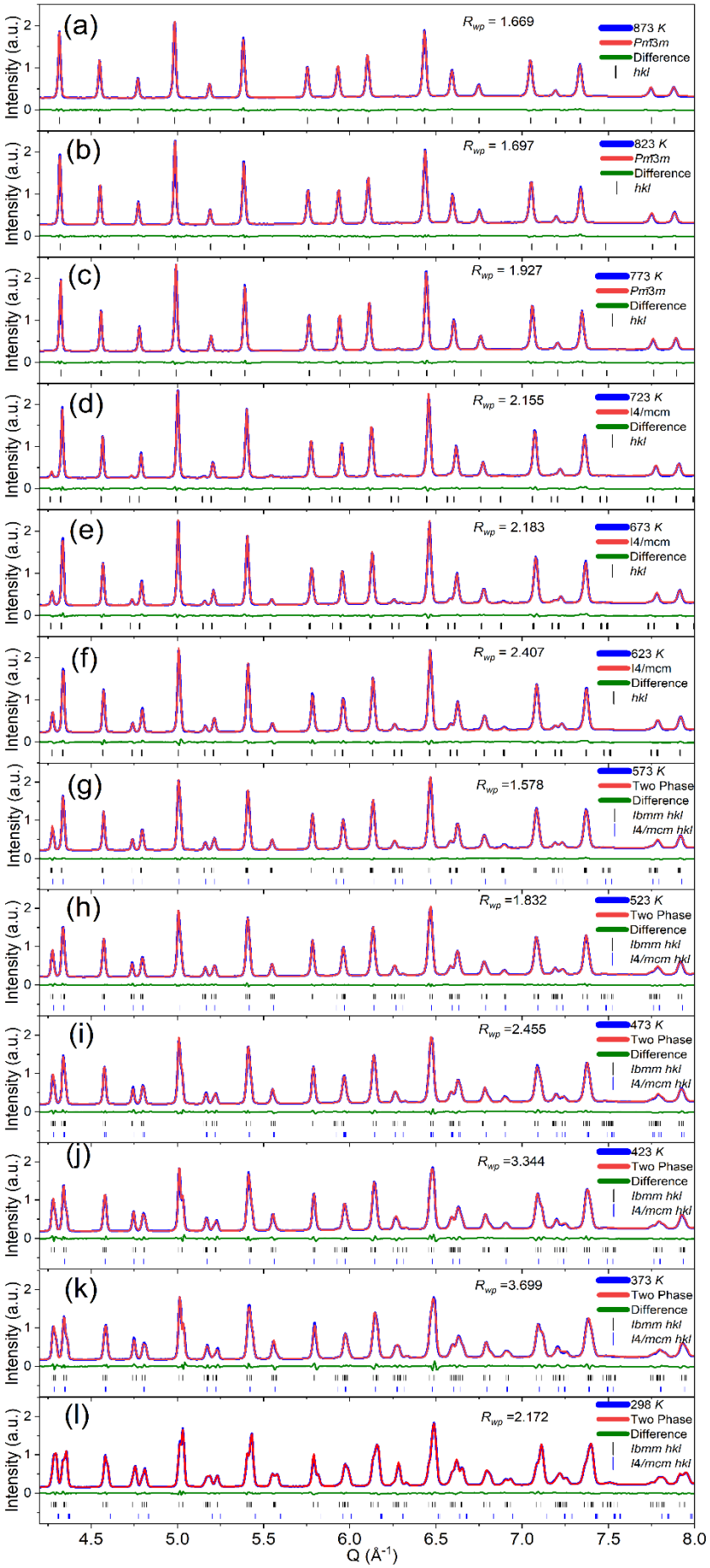

Figure 4.8: Variable temperature neutron powder diffraction data of $BaBi_{0.7}Pb_{0.3}O_3$ with 2 theta angle 154°. (a) to (f) 873 K to 623 K Bragg peak fit for $BaBi_{0.7}Pb_{0.3}O_3$ with a *I4/mcm* -*Pm*$\bar{3}$*m* phase transition. (g) to (l) $BaBi_{0.7}Pb_{0.3}O_3$ fit from Q range 4.2 to 8 Å^{-1} with space group *Ibmm* and *I4/mcm* co-exist. The blue line represents the data, the red line represents the calculated fit to the data, and the green line represents the difference between the two. The black tick represents the allowed *hkl* position, R_{wp} above shows the good of fit.

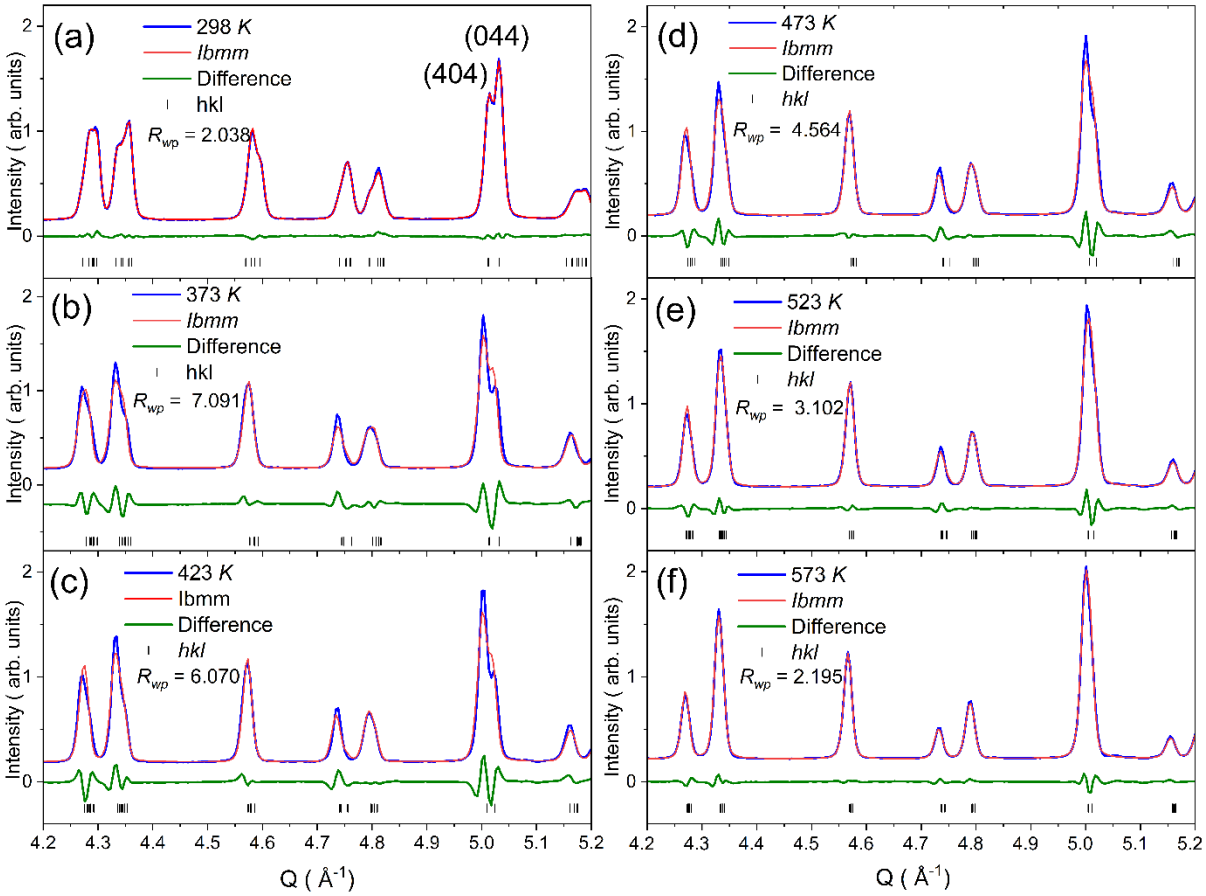

Figure 4.9: Variable temperature neutron powder diffraction data of $BaBi_{0.7}Pb_{0.3}O_3$ collected from NOMAD beamline fitted with space group *Ibmm*. The blue line represents the observed data, the red line represents the Rietveld refinement result and green line represent the difference between the two. Black ticks represent the space group allowed *hkl* reflection.

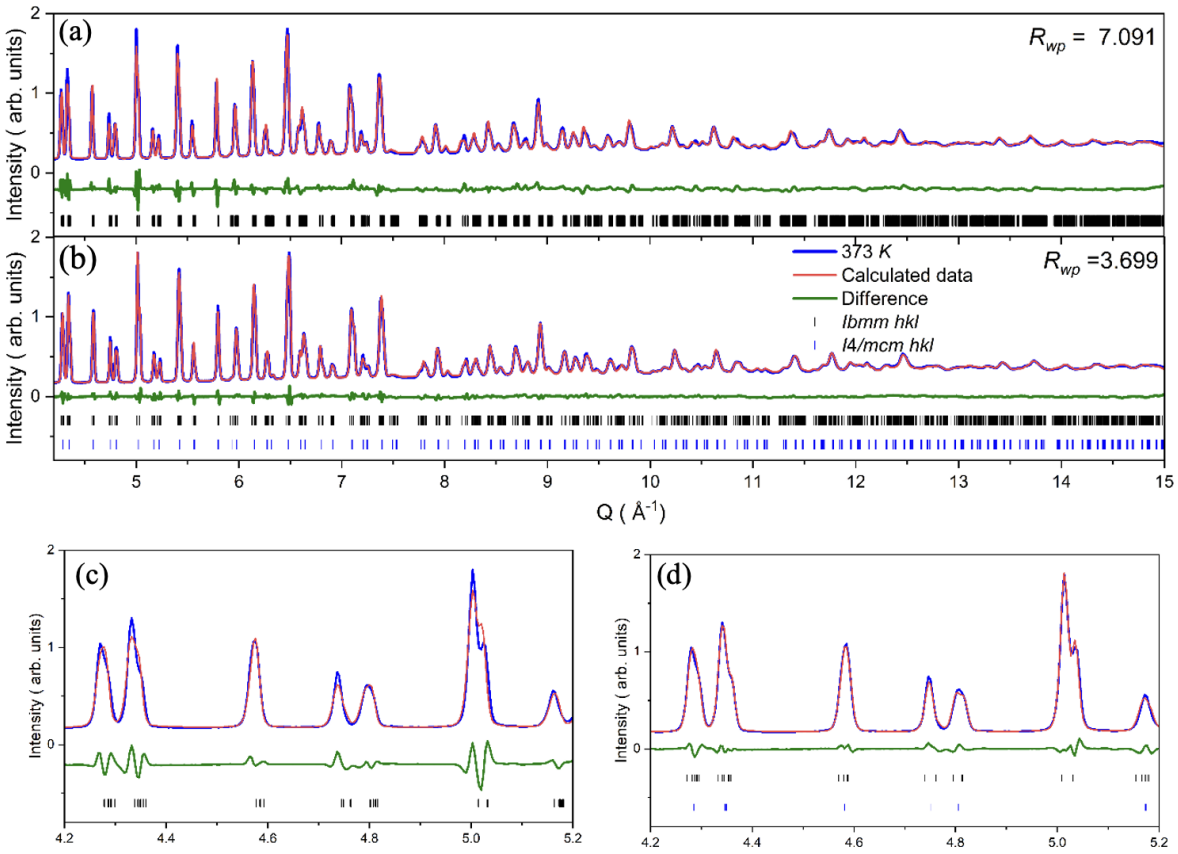

Figure 4.10: The Neutron powder diffraction pattern for $BaBi_{0.7}Pb_{0.3}O_3$ at 373 K with $\theta \sim 154$ °. (a) refine with space group *Ibmm*, (b) refine with two phases model *Ibmm* and *I*4/*mcm* labelled with *hkl* reflection. (c) and (d) are the inert area at $Q \sim 4.2$ to 5.2 for (a) and (b), respectively.

Table 4.3 provides a comprehensive summary of the temperature-induced phase transition process in $BaBi_{0.7}Pb_{0.3}O_3$. At the low-temperature state, the orthorhombic phase *Ibmm*, requires the Bi and Pb ions to be disordered on the same site. The co-existence of the two-phases observed under ambient temperature conditions suggests the retention of local octahedral tilting, while the increased proportion of the tetragonal phase signifies a tendency toward high-temperature pre-transitional disorder. Across all phases, the Bi-O bond length remains relatively stable (2.18-2.19 Å), with thermal variations within 0.005 Å^3. As seen for undoped $BaBiO_3$ strongly anisotropic atomic displacements of the oxygen atoms are observed, with anisotropy in the tetragonal phase, significantly higher than in the orthorhombic phase. Bi^{3+} maintains minimal ADPs across all phases, consistently below 0.001 Å^3, except during biphasic refinement, demonstrating its high degree of ordering. In accordance with the thermal

vibration-dominated disorder, Ba, Bi, and O all conform to the ADP variations induced by increased thermal vibrations. The distortion index (*D*) for the BiO_6 octahedra in $BaBi_{0.7}Pb_{0.3}O_3$ shows an unusual temperature dependence, although the values across the biphasic region are thought to be relatively inaccurate. Considering just the changes for the refinements where only a single phase *Ibmm* or *I*4/*mcm* was present then unexpectedly the distortion in the tetragonal phase $D = 1.77 \times 10^{-3}$ at 673 K is larger than that observed in the lower symmetry orthorhombic *Ibmm* structure at room temperature $Di \sim 2 \times 10^{-4}$. The BiO_6 octahedra is regular with D = 0 in the high temperature cubic structure. As noted previously, the distortion of the BaO_{12} polyhedra is a result of tilting of the semi-rigid BO_6 octahedra. This decreases from D ~ 6.7 x 10^{-2} in the orthorhombic structure to around 2.8×10^{-2} in the tetragonal structure and becomes zero in the cubic structure. The valence state of the *B*-site cation was investigated using the mixed valence state weighting method. The contribution of Bi^{3+} or Bi^{5+} when they are disordered on the same site are different as evident form the different valence state parameter (r_o) used. The effective BVS for the B-site cation is, assuming occupancy by Bi^{3+}, 3.15 ~ 3.23. Treating the cation as Bi^{5+} gives a lower effective BVS of 2.96 ~ 3.03, which is much lower than expected BVS value of Bi^{5+} (~ 5.20). This suggests that Pb^{4+} doping, tends to stabilie an average valance of +3 for the Bi cation hinting at the possibility of supersession of the charge disproportion in $BaBi_{0.7}Pb_{0.3}O_3$.

Table 4.3: Bragg peak Rietveld refinement structural parameters, bond distances for four phases $BaBi_{0.7}Pb_{0.3}O_3$ against neutron powder diffraction data.[12]

	$BaBi_{0.7}Pb_{0.3}O_3$				
Temperature (K)	10	298		673	873
Space group	*Ibmm*	*Ibmm* *	*I4/mcm*	*I4/mcm*	*Pm$\bar{3}$m*
a (Å)	6.147 (1)	6.156 (1)	6.100 (1)	6.147 (1)	4.361 (1)
b (Å)	6.095 (1)	6.120 (1)	6.100 (1)	6.147 (1)	4.361 (1)
c (Å)	8.600 (1)	8.641 (2)	8.615 (2)	8.690 (1)	4.361 (1)
β (°)	90	90	90	90	90
Vol. (Å^3)	322.21 (1)	325.02 (1)	320.58 (10)	328.36 (2)	82.96 (1)
Ba *x*	0.4951 (2)	0.5018 (2)	0	0	0
Ba *y*	0	0	0.5	0.5	0
Ba *z*	0.25	0.25	0.25	0.25	0
Bi *x* *	0	0	0	0	0.5
O (1) *x*	-0.0617 (2)	0.0557 (2)	0	0	0
O (1) *y*	0	0	0	0	0.5
O (1) *z*	0.25	0.25	0.25	0.25	0.5
O (2) *x*	0.25	0.25	0.2209 (2)	0.2288 (2)	/
O (2) *y*	0.25	0.25	0.7209 (2)	0.7288 (2)	/
O (2) *z*	1.0333 (1)	0.9709 (1)	0.0000	0.0000	/
Ba U_{11} (Å^2)	0.0036 (2)	0.088 (6)	0.30 (4)	0.019 (19)	0.028 (6)
Ba U_{22} (Å^2)	0.0048 (2)	0.024 (1)	0.30 (4)	0.019 (19)	0.028 (6)
Ba U_{33} (Å^2)	0.0013 (2)	0.048 (6)	0.027 (15)	0.000 (11)	0.00
Bi (1) U_{11} (Å^2)	0.0015 (2)	0.002 (1)	0.05 (2)	0.003 (9)	0.0 (29)
Bi (1) U_{22} (Å^2)	0.0016 (2)	0.0006 (6)	0.05 (2)	0.003 (9)	0.0 (29)
Bi (1) U_{33} (Å^2)	0.0006 (2)	0.000 (1)	0.000 (9)	0.018 (19)	0.00
Pb U_{11} (Å^2)	0.0015 (2)	0.002 (1)	0.05 (2)	0.003 (9)	0.0 (57)
Pb U_{22} (Å^2)	0.0016 (2)	0.0006 (6)	0.05 (2)	0.003 (9)	0.0 (57)
Pb U_{33} (Å^2)	0.0006 (2)	0.000 (1)	0.000 (9)	0.018 (19)	0.00
O (1) U_{11} (Å^2)	0.0111 (3)	0.042 (3)	0.038 (1)	0.067 (11)	0.0138 (2)
O (1) U_{22} (Å^2)	0.0151 (4)	0.047 (3)	0.038 (1)	0.067 (11)	0.0688 (6)
O (1) U_{33} (Å^2)	0.0089 (3)	0.075 (7)	0.003 (11)	0.031 (10)	0.0138 (2)
O (2) U_{11} (Å^2)	0.0145 (2)	0.0254 (3)	0.11 (2)	0.035 (2)	/
O (2) U_{22} (Å^2)	0.0091 (2)	0.011 (1)	0.11 (2)	0.035 (2)	/
O (2) U_{33} (Å^2)	0.0114 (2)	0.0335 (10)	0.23 (3)	0.097 (4)	/
Bi_1-O (2) (Bi^{3+}) (Å)	2.1831 (2)	2.1833 (1)	2.1856 (15)	2.1811 (2)	2.1807 (1)
Ba-O (1) (Å)	3.0750 (3)	3.0788 (3)	3.0474 (5)	3.0735 (1)	3.0840 (1)
BiO_6 (Bi^{3+}) (Å^3)	13.87	13.89	13.74	13.78	13.83
BaO_{12} (Å^3)	66.69	67.36	66.40	68.31	69.14
D Index BiO_6 (Bi^{3+})	0.00002	0.00054	0.00573	0.00177	0.00000

D Index BaO_{12}	0.06677	0.05806	0.05708	0.02844	0.00000
R_{wp} (%)	3.121	2.172		2.183	1.669
BVS (BiO_6 / Bi^{3+})	3.17	3.16	3.23	3.21	3.19
BVS (BiO_6 / Bi^{5+})	2.97	2.96	3.03	3.01	2.99

* Room temperature $BaBi_{0.7}Pb_{0.3}O_3$ combined *Ibmm* and *I4/mcm* two phase structure with ratio approximately 85:15 in Bragg peak fit.

* Bi occupies a *B*-site with Wyckoff position (0,0,0) at *Ibmm* and *I4/mcm* space group. Bi occupies a *B*-site with Wyckoff position (0, 0.5, 0.5) at $Pm\bar{3}m$ space group.

The Rietveld refinements result for two-phases fit exhibits chaotic behavior, the refined lattice parameters with b > *c* at room temperature have been observed in both NPD and synchrotron diffraction data. However, the relationship in lattice parameter undergoes inversion to *c* > *b* at the tetragonal phase. This behavior also manifested in average bond length of the cation-oxygen pair.

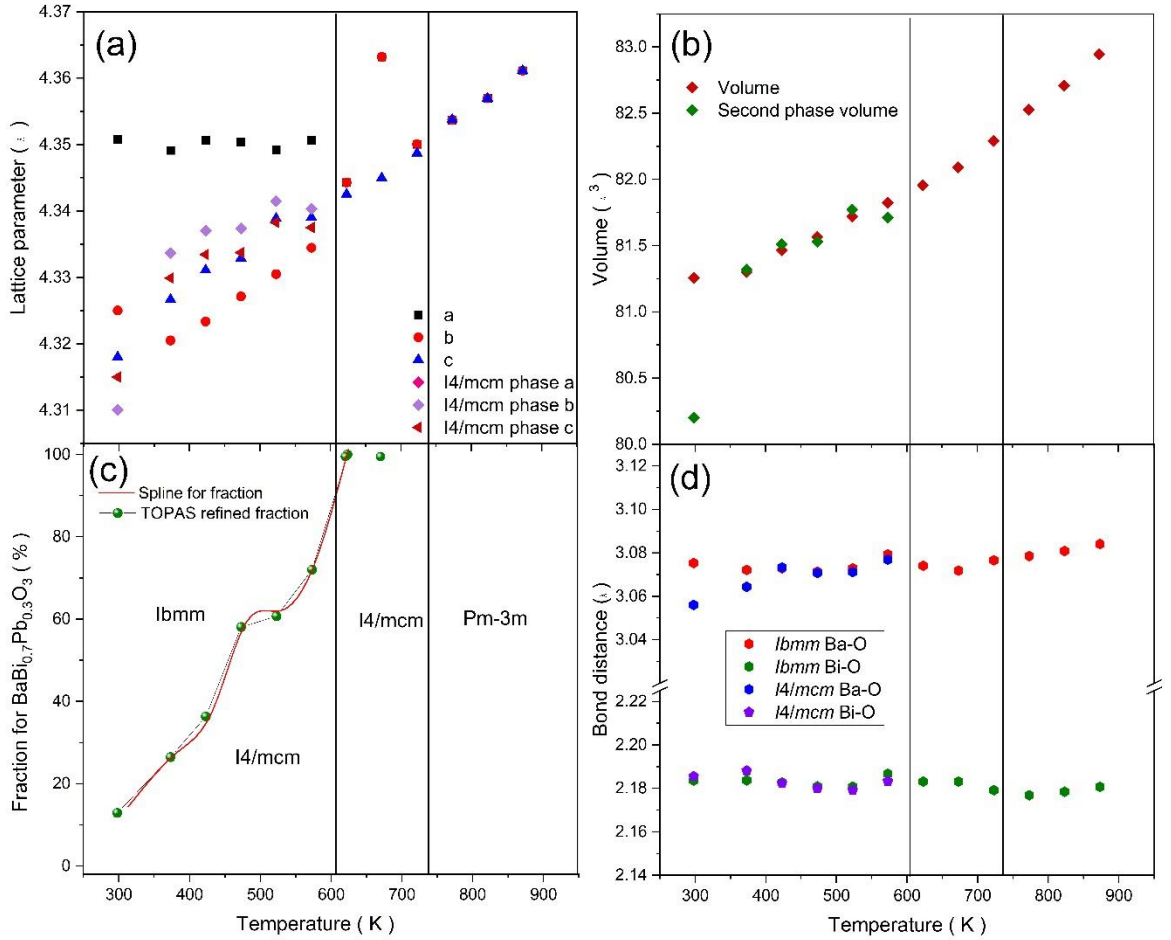

Figure 4.11: Temperature dependence of Rietveld refinements for the neutron powder diffraction for $BaBi_{0.7}Pb_{0.3}O_3$ from 298 K to 873 K. (a) shows lattice parameters, (b) shows cell volume, second phase is *I4/mcm*, (c) two phases ratio and (d) cation-oxygen bond distance.

Figure 4.12 (a) illustrates the overall anisotropy of oxygen ADPs decreasing with temperature, the coordination environment does not align with this behavior. The U_{iso}/U_{eq} value correlates with both static and dynamic disorder, it indicates that oxygen anisotropic displacement parameters show heightened sensitivity to anisotropic variations near the transition temperature. This explains the observed large drop in the values around 573 K, above which the values are approximately constant. The U_{iso} / U_{eq} value of O atom in $BaBi_{0.7}Pb_{0.3}O_3$ decreases from ~ 0.136 $Å^3$ at 298 K to ~ 0.001 $Å^3$at 873 K, whilst U_{iso} / U_{eq} value of Bi remains below 0.02 $Å^3$. It might be anticipated that the U_{iso} / U_{eq} value of Bi atom should increase as lead is added, reflecting the partial suppression of charge disproportionation of the Bi ion. Unfortunately, the oxygen atoms are more sensitive to this behavior, as the Bi-O bond distances changes. Therefore, the significant change in U_{iso} / U_{eq} of the O atom indicates its dominant position in phase transition and local distortion of the lead-bearing structure.

*I*4/*mcm* fit based on a two-phase model accompanying with *Ibmm* and obtain a higher symmetry. The U_{iso} / U_{eq} value of O atom in tetragonal structure remains around 0.175 $Å^3$ from 298 K to 573 K, whereas that value of Bi atom sharply increases from ~ 0.035 to ~ 0.21 $Å^3$. Compared with large *U* value of the O atom in the orthorhombic structure, possibly as a result polyhedral tilting, that in tetragonal structure. The positions of the oxygen atoms are constrained by symmetry leading to an abnormal large *U* value. Bi site exhibits a significant increase in *U* value with temperature dependence, indicating that a dynamic distortion exists.

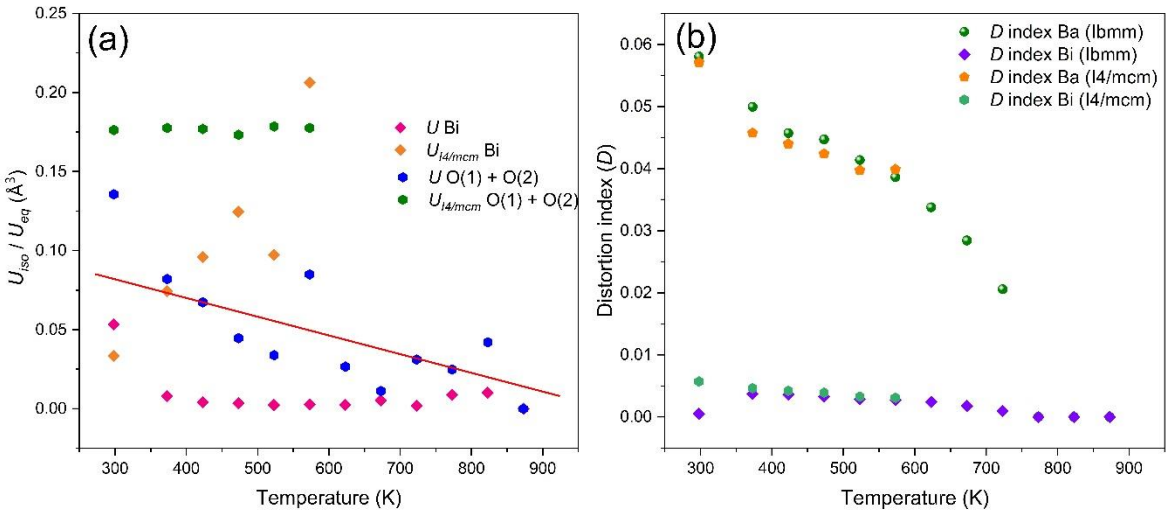

Figure 4.12: Rietveld refinements for the neutron powder diffraction for $BaBi_{0.7}Pb_{0.3}O_3$, shows (a) the U_{iso} / U_{eq} value of Bi atom and O (1) + O (2), (b) distortion index D in each polyhedra. The red line indicates the tendency of anisotropic O atom.

Figure 4.13 illustrates the anisotropic displacements of the oxygen atoms. Similar to the temperature dependent ADPs results of $BaBiO_3$, it has not been found a large oxygen ellipsoid or sphere were obtained in highest symmetry structure $Pm\bar{3}m$. The static distortion and oxygen coordination positions were averaged according to cubic symmetry during Rietveld refinement.

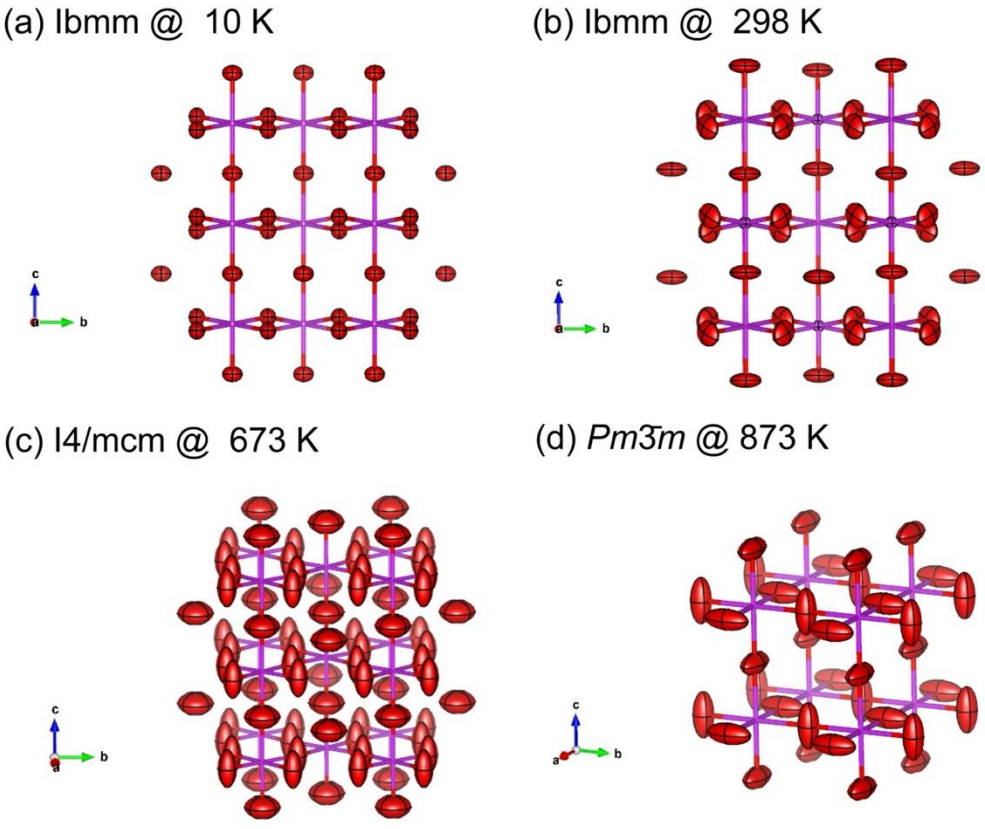

Figure 4.13: Representation of atomic displacements for oxygen atom in $BaBi_{0.7}Pb_{0.3}O_3$ with temperature dependence, oxygen atom is represented as ellipsoid and connect with violet sphere (Bi atom). (d) shows the standardization of $Pm\bar{3}m$.

4.3 NPDF Studies of the room temperature structures of $BaBi_{1-x}Pb_xO_3$

For x = 0.00 – 0.20, both Bragg peak of NPD and small box fit of NPDF can refine with monoclinic *I2/m* model (Figure 4.15 (a) to (e) and Appendix). For x = 0.25 – 0.30, the G (r) and NPDF exhibit good fit with orthorhombic *Ibmm* model.

In neutron pair distribution function, the distribution of G(r) is dominated by the atom-atom pair distance, whilst the strength of the peak is correlated with scattering length b that is an efficient parameter describing neutron-nucleus interaction. The neutron scattering lengths of Bi and Pb are 8.532 fm and 9.405 fm, respectively.[17] Although the scattering lengths of Bi and Pb are close, it still remains subtle difference within PDFs.

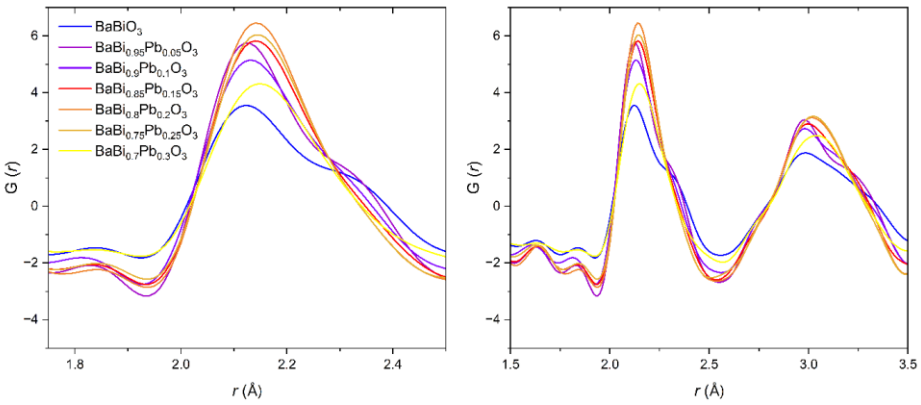

Figure 4.14: Neutron pair distribution function data of $BaBi_{(1-x)}Pb_xO_3$ ($0 \leqslant x \leqslant 0.3$) at 298 K over a range of 1.5-3.5 Å highlighting changes in both the Bi/Pb-O contacts near 2.2 Å and various O-O contacts around 3.0 Å. The latter are sensitive to changes in the BaO12 polyhedra.

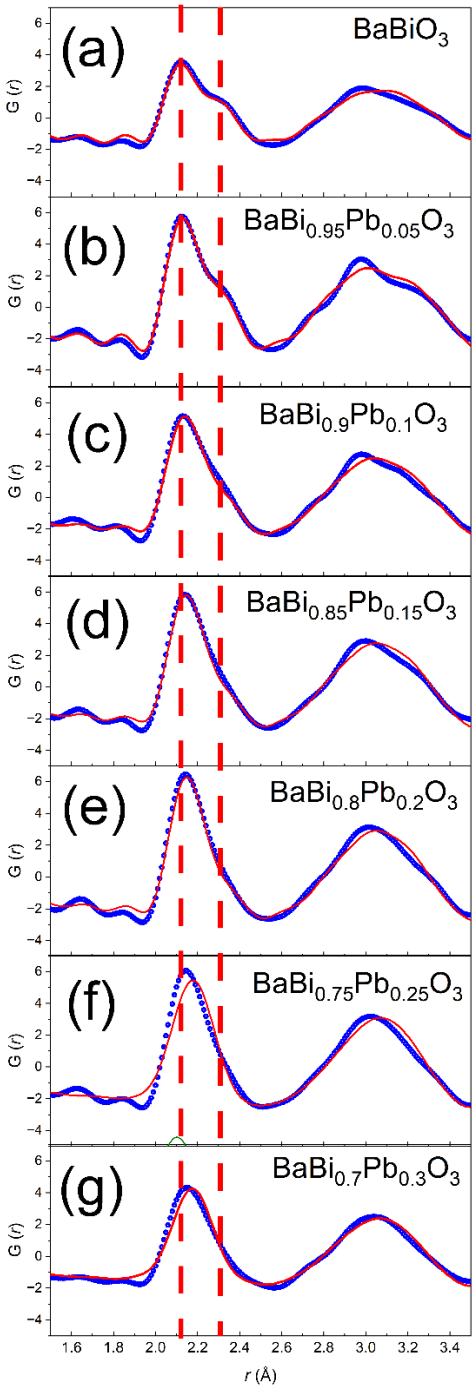

Figure 4.15: Observed and calculated NPDF data for $BaBi_{1-x}Pb_xO_3$ over the regions 1. 5 $\leqslant r \leqslant$ 2.5 Å. The vertical dashed red line shows the expected positions of Bi^{5+}-O and Bi^{3+}-O peaks at ~ 2.168 and 2.30 Å respectively.

Figure 4.16 shows the PDF fitting results of $BaBi_{(1-x)}Pb_xO_3$ with different lead contents. The overall trend indicates an increase in R_{wp} value, it nevertheless remains within acceptable limits. For the NPDF data fit with long-range *I*2/*m* and *Ibmm* structures, a spherical correlation function is applied to model the alteration in B_{iso} with respect to *r*. For $x = 0.0 – 0.2$, the average structure fit with *I*2/*m*, while the local structure maintains a monoclinic distortion. The gradual rise in R_{wp} implies that the fitting process is accommodating the distortion. The excellent fit within range 1.8 - 2.5 Å (Bi-O bond length) confirms the persistence of local distortions in the BiO_6 octahedral. However, the fitting is less satisfactory in the 2.5 - 3.5 Å region, which corresponds to the Ba-O and O-O bond distances. As described in Chapter 3 this region is sensitive to distortion of the BaO_{12} polyhedra. In account for local correlation in local structure disorder, a fit of 1.6 to 30 Å wase applied to explain atom-atom pairs obtained at longer interatomic distances, but it still gave a bad fit. The Ba-O and O-O distribution peak were poorly fit whether adjust *r*-cutoff range or fit with short-range model. For (f) $BaBi_{0.75}Pb_{0.25}O_3$, the fitting with *Ibmm* structure resulted in a poor fit to the local Bi-O bond distance between 1.8 – 2.3 Å, as well as substantial amount of difference determined between 2.5 - 3.5 Å. By altering local range fit with *I*2/*m* model, a better fit in NPDF illustrates long range average structure cannot capture BiO_6 octahedra and BaO_{12} cuboctahedra in local environment, whilst we cannot predict whether Bi^{3+} lone pair electrons affect the distortion or not, as it does not happen at undoped $BaBiO_3$, it assumes the Bi ion in the BiO_6 octahedron perform as 4+ state, it results in a significant bad fit around 2.0 – 2.5 Å peak, which is the primary cause of the high R_{wp}. Although the local structure exhibits CD, the global average structure has transitioned to the orthorhombic *Ibmm* phase. This discrepancy between local and global symmetry is common in perovskites.[18-20] When lead doping ratio approaches to 0.3, the fitting becomes more reasonable.

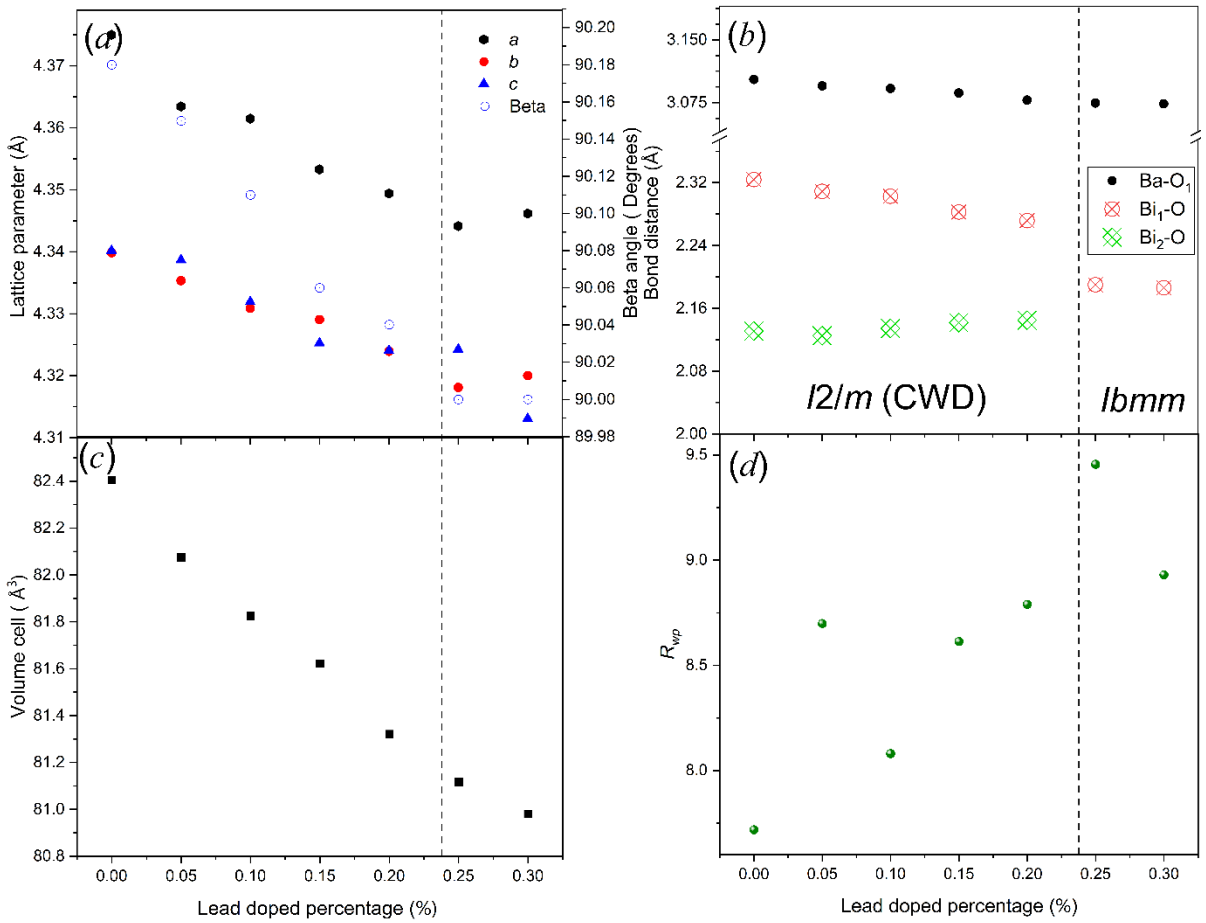

Figure 4.16: Composition dependent results from analysis of the room temperature NPDF data for $BaBi_{(1-x)}$ $PbxO_3$ ($0 \leq x \leq 0.3$). (*a*) and (*c*) are the refined unit cell parameters and volume respectively (*b*) is the cation-oxygen bond lengths where, Bi_1-O represents the distance between Bi^{3+} and O^{2-} and Bi_2 is the Bi^{5+}-O distance. (*d*) is the measure of fit, R_{wp}. The vertical dashed line at x= 0.23 represents the *I2/m* → *Ibmm* phase transition. CWD = charge wave density.

Whilst all data were collected on the same instrument, for the NPDFs shown in Fig 4.15, the data for $BaBiO_3$ and $BaBi_{0.7}Pb_{0.3}O_3$ were measured in a furnace, whilst the remainder were not. This influences the background subtraction and Q_{max}, resulting in slight difference in the PDF peak intensities. A normalization approach is applied to adjust the intensity error between different G(*r*) data, although the normalized G(*r*) shows peaks merging around $0.1 \leq x \leq 0.2$. However, it is obvious that short-range ordering is affected by lead doping, and it does not establish for the expected charge ordering melting around $x = \sim 0.2$. In Figure 4.15 (a) to (g), the first neighbouring peak (1.8 - 2.5 Å) and second peak (2.5 - 3.5 Å) exhibits no significant

change in peak width. The constant peak width suggests that the local scale Bi-O bond distance remain stable and does not display apparent static disorder. Nonetheless, the peak intensity fluctuates between lead doping ratio 0.05 to 0.25, and when combined within the boundary of the CDW region, this behaviour may indicate local distortion induced by Pb^{4+} doping. $BaK_xBi_{(1-x)}O_3$ is an excellent example to describe CO collapse due to the complex superconducting mechanism in $BaBi_{(1-x)}Pb_xO_3$, Charge ordering melting occurs within the potassium doping range of approximately 0.125 to 0.37. DFT calculations illustrate the relationship between multivalent cations and polaron lattice distortion through the demonstration of long range Peierls distortion and local Jahn-Teller effects.[21] The structural characteristics associated with this chapter and their relationship to the superconducting state can be described by hole concentration, with the insulator to semiconductor transition occurring gradually.

Simultaneously, we conducted room-temperature NPDF analysis on samples with varying doping ratios. Considering the lattice parameters and unit cell volume, minimal discrepancies (0.20 – 0.50 $Å^3$) were observed between NPDF and NPD refinement, which fall within an acceptable error range. Both NPDF and NPD results exhibited a contraction with increasing lead doping. The Bi^{3+}-O and Bi^{5+}-O bond lengths in NPDF analysis consistently appeared longer. It is believed that this discrepancy reflects local distortions in $BaBi_{(1-x)}Pb_xO_3$, that are observed by PDF.

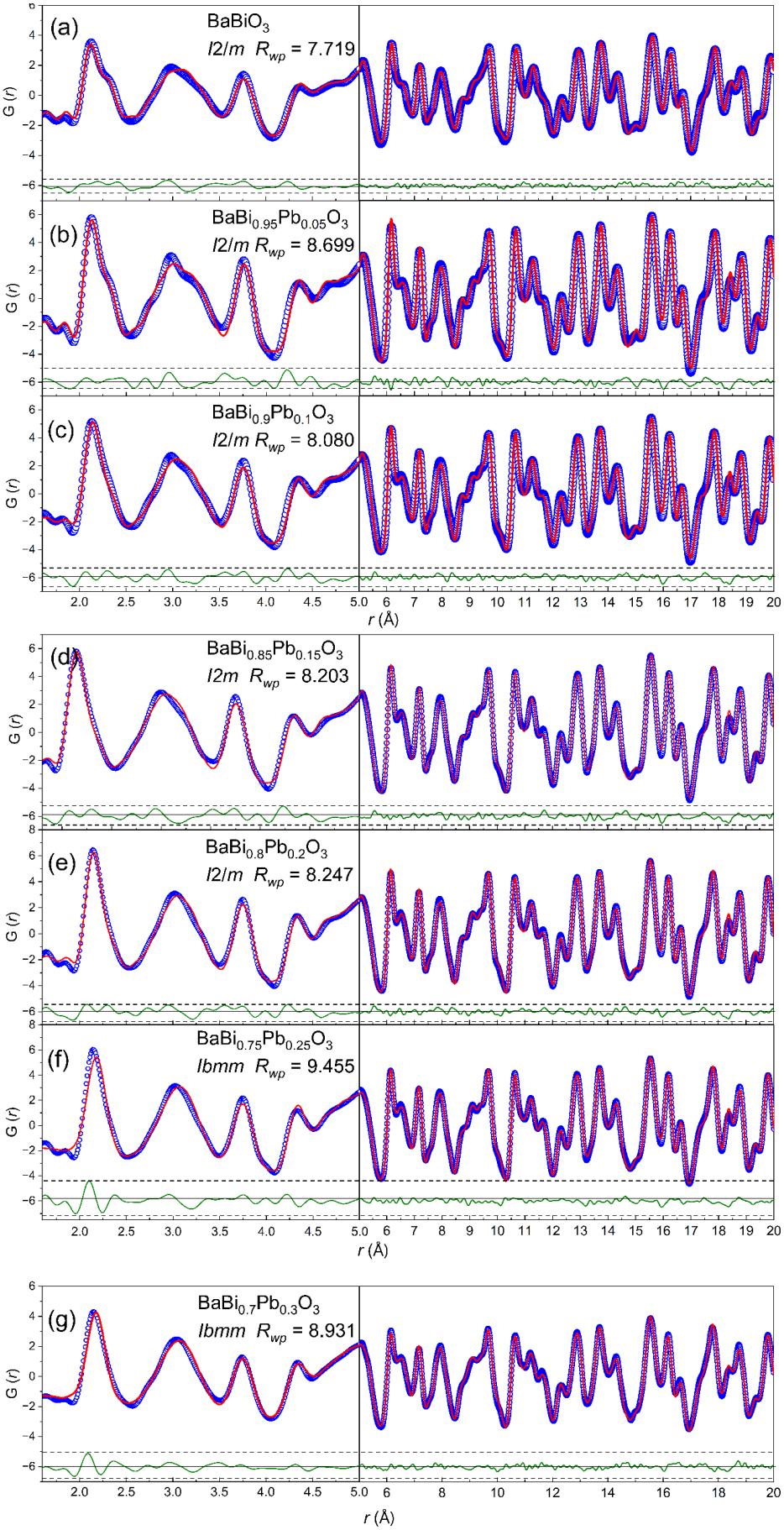
(a)
BaBiO3
I2/m Rwp = 7.719
(b)
BaBi0.95Pb0.05O3
I2/m Rwp = 8.699
(c)
BaBi0.9Pb0.1O3
I2/m Rwp = 8.080
(d)
BaBi0.85Pb0.15O3
I2m Rwp = 8.203
(e)
BaBi0.8Pb0.2O3
I2/m Rwp = 8.247
(f)
BaBi0.75Pb0.25O3
Ibmm Rwp = 9.455
(g)
BaBi0.7Pb0.3O3
Ibmm Rwp = 8.931
G (r)
r (Å)

Figure 4.17: Neutron pair distribution function data fit of $BaBi_{(1-x)}Pb_xO_3$ ($0 \leqslant x \leqslant 0.3$) with anisotropic atomic displacement parameters at 298 K. (a) to (e) monoclinic space group *I*2*m*, (f) orthorhombic space group *Ibmm* and (g) *Ibmm* and *I*4*mcm* two phases co-exist. The blue circles represent the observed data, the red line represents the calculated profile, the green line represents the difference between the two.

4.4 Variable Temperature NPDF Studies of $BaBi_{0.7}Pb_{0.3}O_3$

$BaBi_{0.7}Pb_{0.3}O_3$ has the highest superconducting critical temperature T_c in the $BaBi_{(1-x)}Pb_xO_3$ series discovered by Sleight *et al.* in 1975 and is consequently the most heavily studied example. Furthermore, $BaBi_{0.7}Pb_{0.3}O_3$ serves as a pivotal transition point in the evolution from the insulating state of $BaBiO_3$ to the metallic and superconducting states. In $BaBi_{0.7}Pb_{0.3}O_3$, the breathing mode induced by the ordering of Bi^{3+} and Bi^{5+} is suppressed, leading to higher crystal symmetry.[2, 3, 9]

The crystal structure of $BaBi_{0.7}Pb_{0.3}O_3$ evolved with distinct phase transition pathway upon heating involving three space group: orthorhombic space group *Ibmm*, tetragonal space group *I*4/*mcm* and cubic space group $Pm\bar{3}m$.[9, 22, 23]. The orthorhombic *Ibmm* structure contains the same type of 6-coordinate BiO_6 octahedra and 12-coordinate BaO_{12} cuboctahedra seen in undoped $BaBiO_3$, but now the Pb and Bi are disordered on the same site. As the charge ordering has melted, the BiO_6 octahedra consist of approximately equal Bi-O bond lengths with 2.1860(5) and 2.1814(3) Å, whilst BaO_{12} cuboctahedral remain a polyhedral distortion with five types of Ba-O bond distance in the range 2.702 to 3.446 Å. Upon heating to around 600 K, the orthorhombic structure transforms to a tetragonal structure *I*4/*mcm*. The distortion index correlated with bond length has been regular to 0.00, and Bi-O bond distance is around 2.1632(10) Å. The types of Ba-O merges into three with range approximately between 3.0 – 3.2 Å. The highest symmetry structure cubic $Pm\bar{3}m$ in $BaBi_{0.7}Pb_{0.3}O_3$ requires a phase transition temperature around 750 K, the Ba-O bond distance exhibits similar change as cubic structure $BaBiO_3$ merge into single Ba-O bond length approximately 3.08 Å, whilst the BiO_6

octahedral are made of a single Bi-O bond around 2.18 Å. The crystal structure of $BaBi_{0.7}Pb_{0.3}O_3$ is consistent with that of $BaBiO_3$ doped with different Pb ratio. *Ibmm* structure is the lowest symmetry structure in $BaBi_{0.7}Pb_{0.3}O_3$, while it is significantly more prevalent than *I*2/*m* structure. The tilting angle of polyhedral in $BaBiO_3$ *I*2/*m* is 11.2 degrees ($Bi^{3+}O_6$- BaO_{12}-$Bi^{5+}O_6$), whereas in the *Ibmm* structure at room temperature, it calculates with 9.42 degrees.[24] According to $BaBi_{(1-x)}Pb_xO_3$ phase transition diagram Figure 4.1, we observed that the cubic phase transition temperature decreases from 800 K to 750 K from undoped sample to $BaBi_{0.7}Pb_{0.3}O_3$. This is evidence of the incorporation of Pb and K element doping enhances the symmetry behaviour in BBO system, it exhibits a good agreement to pervious literature.[9]

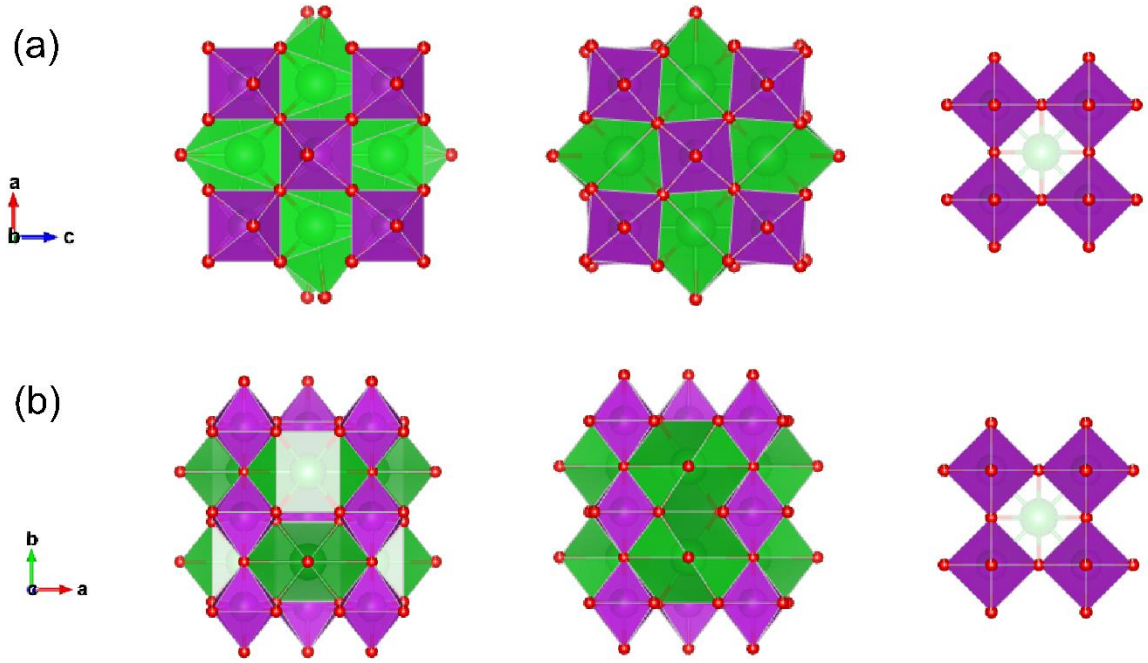

Figure 4.18: The three phases of $BaBi_{0.7}Pb_{0.3}O_3$. The representation includes the phase transition pathway from the orthorhombic structure of space group *Ibmm* (left), then transfer to tetragonal structure of space group *I*4/*mcm* (middle), finally with a cubic structure $Pm\bar{3}m$ (right). (*a*) The first row represents polyhedral rotating along the *b*-axis direction, (*b*) the second row represents polyhedral rotating along the *c*-axis direction. BiO_6 polyhedral is displayed in purple, oxygen is red sphere and barium is green sphere.

The process of charge ordering melting is protracted, which potentially persistent throughout the phase transition. The concept of two-phase co-existence fitting warrants in-depth

consideration as a fitting strategy. The multi-phase fit of $BaBi_{(1-x)}Pb_xO_3$ was substantiated by Climent-Pascual in 2011, they demonstrated that $BaBi_{(1-x)}Pb_xO_3$ exhibits a two-phase co-existence of 2 phase *Ibmm* and *I*4/*mcm* over a lead doping ratio range from 0.7 to 0.95 has been reported previously, but this is well outside the compositional range investigated in this study and there are no other reports of 2 phase compositions in the BBPO series.[25] During the two-phase fitting, we attempted to fit both *Ibmm* and *I*4/*mcm* phase through Bragg peak fit. However, the fitting results resembled the fit of *Ibmm* single phase, it does not observe discernible *hkl* reflections distinguishing two phases, and the contribution of *I*4/*mcm* to peak intensity was minimal. Subsequently, a PDF fitting for *Ibmm* and *I*4/*mcm* two phases are applied and shows similar results to *Ibmm* fit. Two-phase fitting with *I*2/*m* and *Ibmm* represents in Figure 4.19, two-phase fitting shows improved results in 1.8 – 2.5 Å peak, the Bi-O bond length is converging at approximately 2.14 Å. The first neighbouring peak of *Ibmm* phase contributes to peak intensity around 2.18 Å, it results in the shift of first peak in *Ibmm* single phase fit. Whilst the Bi-O peak of *I*2/*m* phase appears at ~2.13 Å.

Orthorhombic and tetragonal space group two-phases fit is modelling in Figure 4.19. The phases ratio within both TOPAS and PDFgui fit results *Ibmm* structure occurs dominated position at 373 K. The distinct between the two is ratio of *Ibmm* structure reaches to 96.88% due to $\boldsymbol{U_{iso}}$ applied in PDFgui, it provides local structure ordering prefer as orthorhombic structure. (d) and (e) exhibit the partial PDF of two-phase fit, Bi-O and Pb-O bond length established with a strong peak around 2.18 Å and 2.19 Å, which does happen visibly splitting in first neighbouring peak. Orthorhombic phase *Ibmm* obtains multiple peak ~ 2.8 to 3.0 Å and contribute second neighbouring peak with two singlets from tetragonal phase *I*4/*mcm*. The two-phases region comparison reveals that in addition to the dominance of *Ibmm* phase at 373 K, the unique strong Ba-Pb bonding in tetragonal phase is associated with the uncommon positional fluctuation of Pb^{4+} in *I*4/*mcm*. Its distinctive melt-quenched state indicates that it severs as a boundary buffer area.

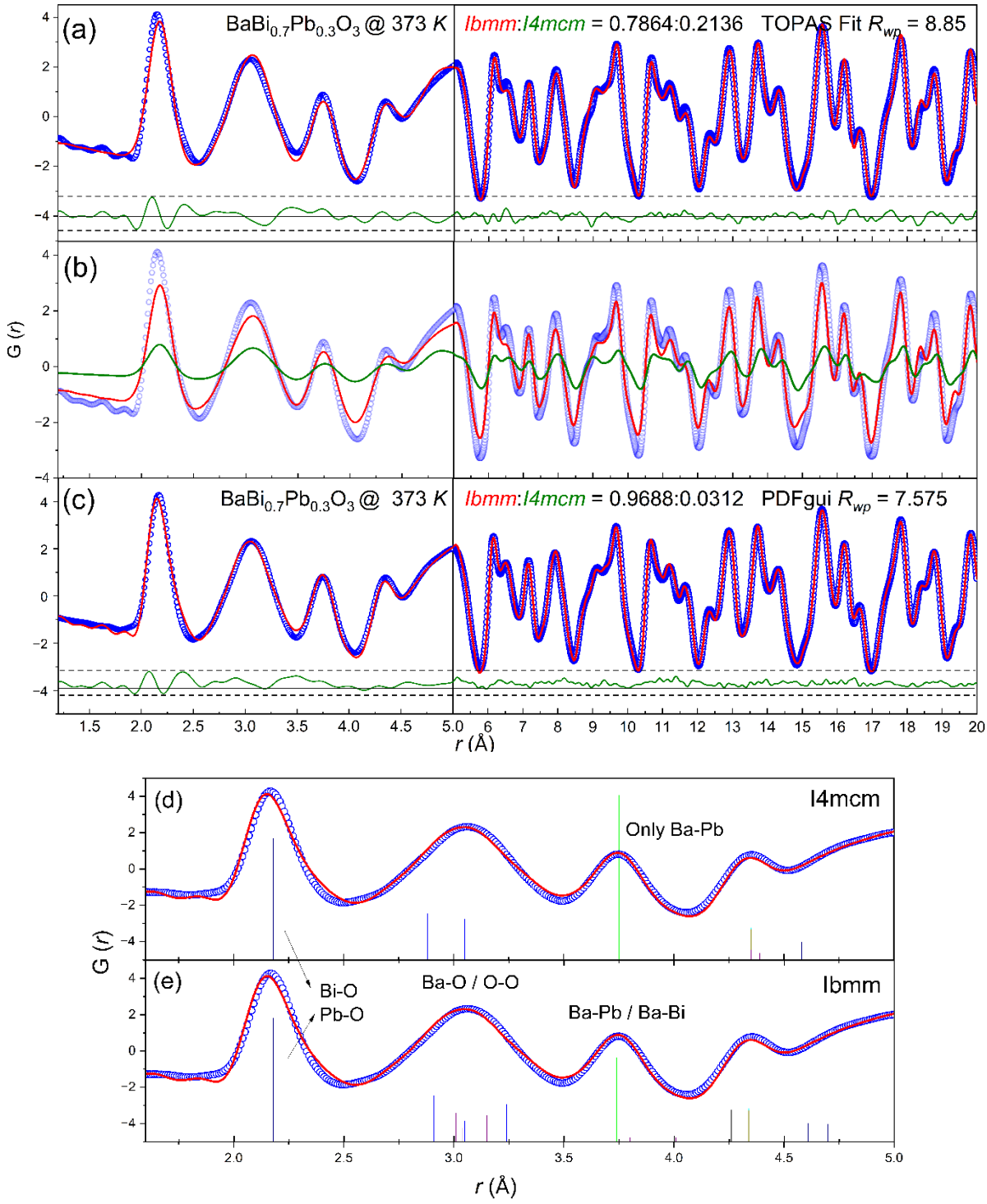

Figure 4.19: The NPDF data for $BaBi_{0.7}Pb_{0.3}O_3$ at 373 K fitting with *I*4/*mcm* (green line) and *Ibmm* (red line) two-phase model. (a) TOPAS fitting model refined with $\boldsymbol{B_{iso}}$ and (b) represent the intensity contribution from two phases. (c) PDFgui fitting model refined with $\boldsymbol{U_{iso}}$. (d) represent the partial PDF results with cation-oxygen bond and cation-cation bond from 1.2-5 Å in *I*4/*mcm* and (e) represent bond distance for *Ibmm*.

The partial PDF of each space group exhibits the key structure characterization correlated between bond length and polyhedral tilting. Bi-O exist in space group *Ibmm* similar to two-phase fit which represent as singlet ~ 2.18 Å, and Pb-O bond does not display a splitting peak around first neighbouring peak, Ba-O bond distances are distributed with multiple peaks over a wide range ~ 2.7 to 3.4 Å, which fit with the multiple coordination range resulted by BaO_{12} tilting. Upon heating, Bi-O evolved with two different bond lengths at 2.16 and 2.19 Å, Pb-O remain overlapping with Bi-O, although partial PDFs in an agreement with same Pb^{4+} and Bi ion bond length, Rietveld refinement explore a strong disorder in Pb^{4+} (higher ADPs). The distribution of O-O bond is relevant centred ~ 3.09 to 3.10 Å, it can be explained through simple tilting mode in tetragonal structure. The largest feature in cubic partial PDF pattern is all bond lengths are simplified: Bi-O/Pb-O at ~ 2.18 Å, Ba-O at ~ 3.09 Å and O-O at 4.37 Å. Although partial PDF RMCprofile without modelling atom movement, the temperature dependence structure change demonstrates local disorder of Pb^{4+}.

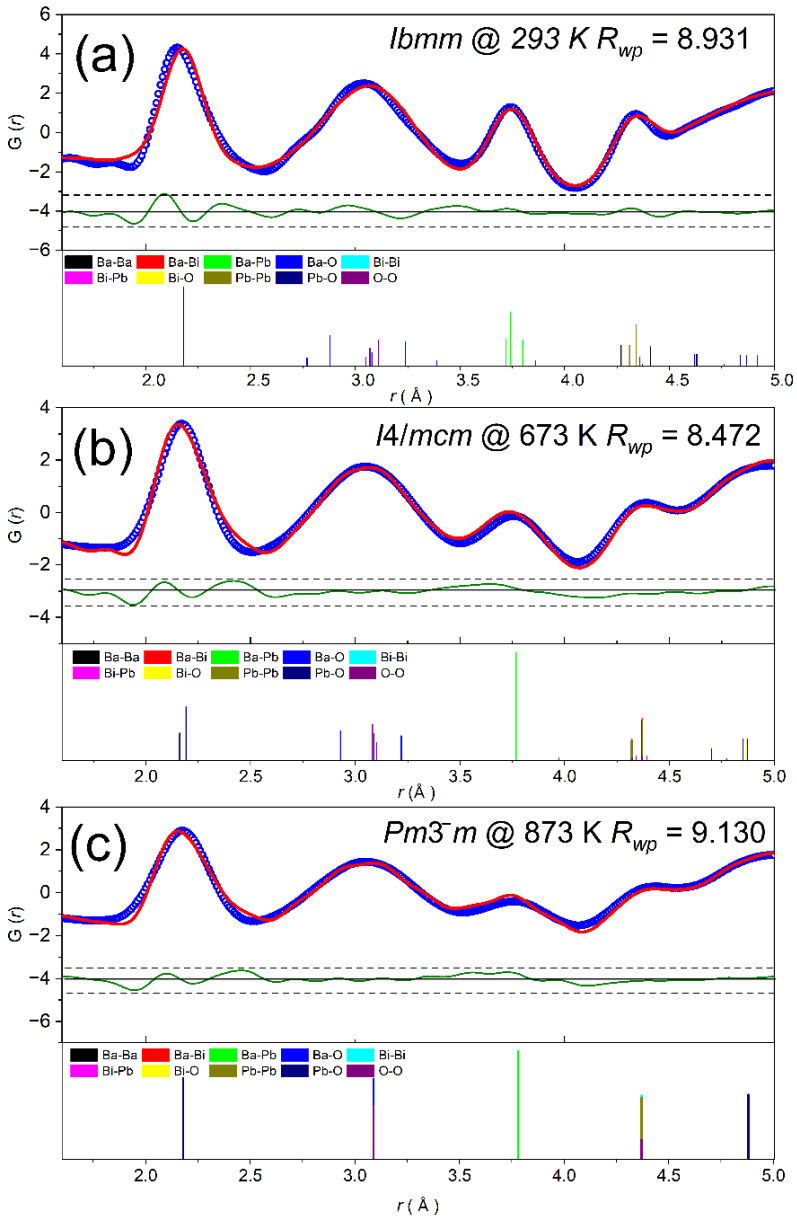

Figure 4.20: Partial neutron pair distribution function data indicates $BaBi_{0.7}Pb_{0.3}O_3$ fitted with (a) orthorhombic *Ibmm* space group at 298 K, (b) tetragonal space group *I*4/*mcm* at 673 K and (c) cubic space group $Pm\bar{3}m$ at 873 K. Data was fitted across from 1.8-20 Å range through PDFgui. The blue circles represent the observed data, the red line represents the calculated profile, the green line represents the difference between the two.

Table 4.4: Cation – cation and cation – oxygen bond distance of $BaBi_{0.7}Pb_{0.3}O_3$ within 1-5 Å range collected from neutron powder diffraction data.

	Ba-Ba	Ba-Bi	Ba-Pb	Ba-O	Bi-Bi	Bi-Pb	Bi-O	Pb-Pb	Pb-O	O-O
Ibmm	4.27- 4.41	3.72- 3.8	3.72- 3.8	2.7-3.4	4.31 4.34	4.31 4.34	2.18 4.62-5.08	4.31 4.34	2.18 4.62-5.08	3.05-3.11 4.36
*I*4/*mcm*	4.32- 4.38	3.77	3.77	2.93- 3.23	4.32 4.37	4.32 4.37	2.16 2.19 4.77-4.87	4.32 4.37	2.16 2.19 4.77-4.87	3.09 3.10 4.34-4.77
$Pm\bar{3}m$	4.37	3.78	3.78	3.09	4.37	4.37	2.18 4.88	4.37	2.18 4.88	3.09 4.37

The temperature dependent study shows that the local distortions in $BaBi_{0.7}Pb_{0.3}O_3$ are influenced by dynamic disorder such as thermal vibrations. Figure 4.21 illustrates the distinction between isotropic and anisotropic displacement parameters at a high-temperature (873 K) fitting, where we observe a significant improvement in the goodness of fit derived from $\boldsymbol{U_{iso}}$. This indicates that atomic vibrations exhibit isotropic fluctuation at elevated temperature, and the displacement of oxygen atoms can be more accurately captured under $\boldsymbol{U_{iso}}$. In the study of mixed-valence oxide perovskite, to capture the ordered/disordered variations of the Bi or Pb atoms, it is essential to eliminate the effects of dynamic disorder and local distortion in oxygen sub-lattice. Consequently, we conducted PDF studies on $BaBi_{0.7}Pb_{0.3}O_3$ at low temperature.

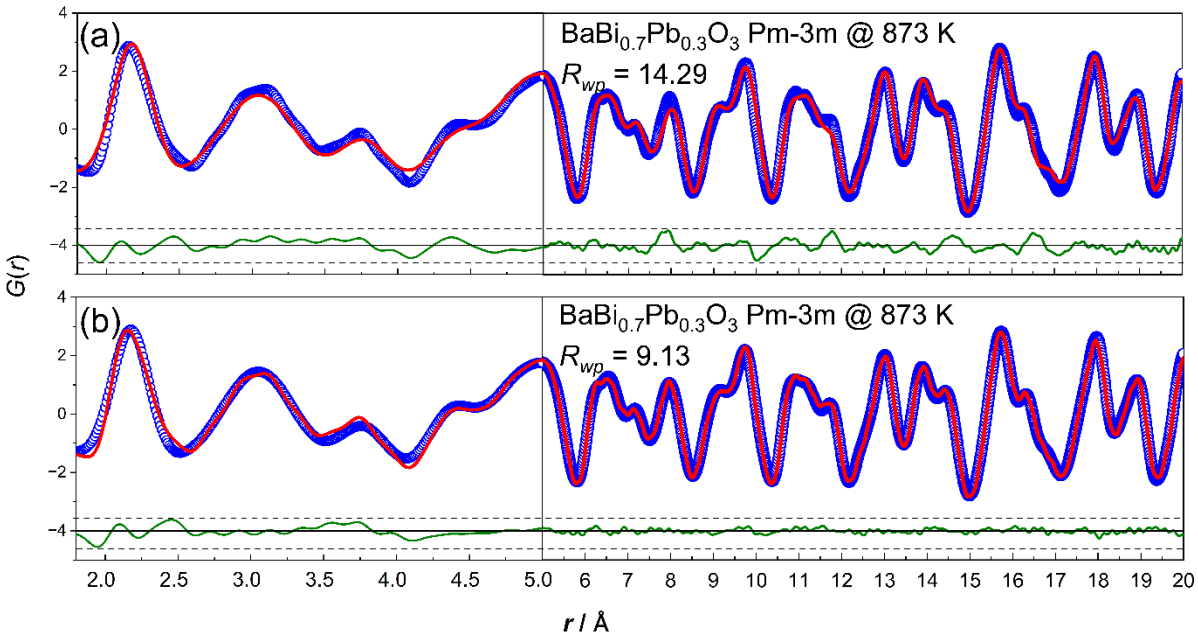

Figure 4.21: Neutron pair distribution function data fit with cubic space group $Pm\bar{3}m$ with anisotropic atomic displacement parameters at 873 K. (a) $BaBi_{0.7}Pb_{0.3}O_3$ NPDF fit with $\boldsymbol{B_{iso}}$, (b) $BaBi_{0.7}Pb_{0.3}O_3$ fit with anisotropic $\boldsymbol{U}$. The data was fitted across a range of 1.8-20 Å. The blue circles represent the observed data, the red line represents the calculated profile, the green line represents the difference between the two.

A good of fit to both the local scale and long-range strucure was obtained against the low temperature data. The Bi-O distances in the BiO_6 octahedra were all approximately equal ~ 2.18 Å, but local distortions were evident in the second neighbouring peak derived by Ba-O and O-O bonds. Long range ordering remains in 10 K $BaBi_{0.7}Pb_{0.3}O_3$, it indicates average structure conforms to the orthorhombic space group. To investigate the role of symmetry lowering on the local structure of $BaBi_{0.7}Pb_{0.3}O_3$, increase structure complexity phase $I2/m$, and $P2_1/n$ models were fit with same 10 K NPDF data. Both $I2/m$, and $P2_1/n$ model obtain better fit at local scale G(r) data, it results by two lower symmetry structure gain greater degrees of local asymmetry and octahedral distortion. Although the small numerical differences in R_{wp} value, the local order caused by Bi-O bonding distortion dominates varies subtly. The Ba-O and O-O peaks exhibit a strong correlation with the oxygen sub-lattice under low-temperature environment. Oxygen sub-lattice undergoes significant changes in response to variations in thermal motion, it is not promising to remain ordering at low temperature. Conversely, the

disorder in the oxygen sub-lattice supports the existence of charge ordering in $BaBi_{0.7}Pb_{0.3}O_3$ at same conditions. Pervious study in this dissertation mentioned that if Bi ions exist in different valence states, the Bi-O bond lengths is varied and forcing adjacent oxygen atoms to shift, it results in distortions of O atom related peaks. However, further evidence is required to substantiate. Figure 4.22 demonstrates that the actual local structure of $BaBi_{0.7}Pb_{0.3}O_3$ at 10 K is more consistent with the monoclinic $P2_1/n$, rather than the *Ibmm* phase supported by pervious literature, it is associated with the symmetry breaking induced by Pb^{4+} dope.[9] The average structure suggest that charge ordering within $BaBi_{0.7}Pb_{0.3}O_3$ at 10 K have collapsed and structure is in a well-described with high symmetric model *Ibmm*. This finding indicates that average structure of $BaBi_{0.7}Pb_{0.3}O_3$ shows an agreement with disordered metallic or superconducting ground state due to Bi-O bond lengths charge disproportionation disappear.

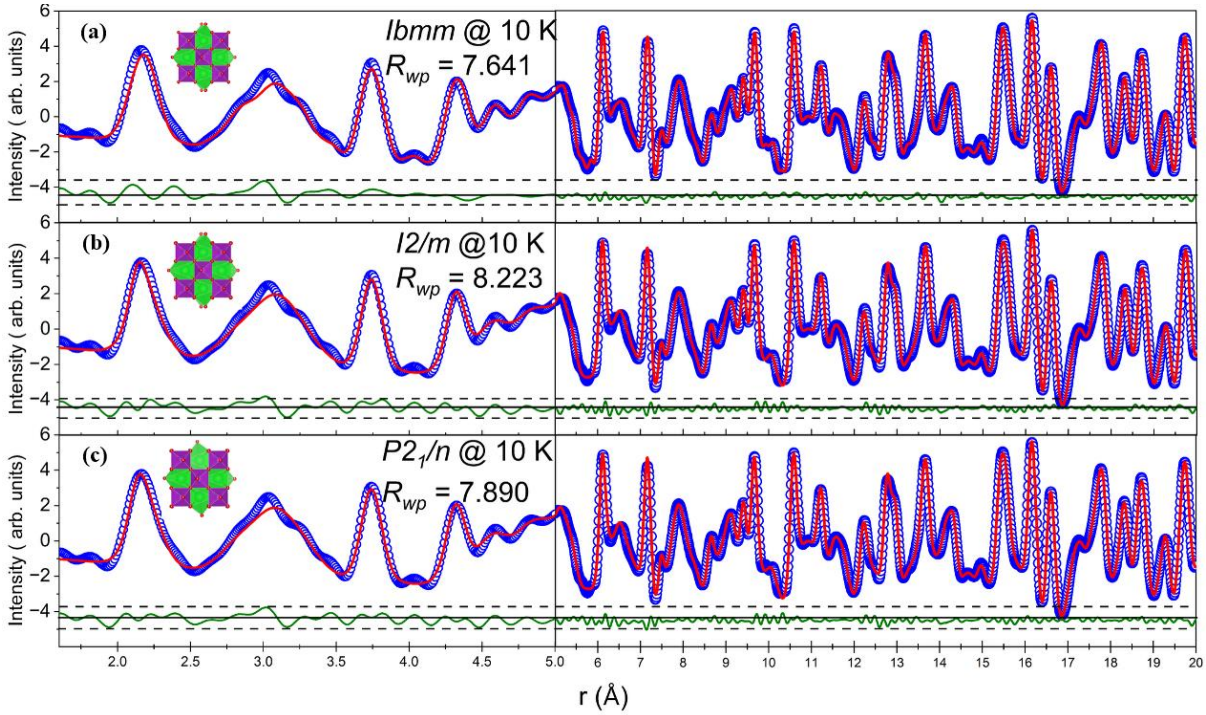

Figure 4.22: Neutron pair distribution function fits of $BaBi_{0.7}Pb_{0.3}O_3$ at 10 K for (a) orthorhombic space group *Ibmm*, (b) monoclinic space group *I2m*, and (c) monoclinic space group $P2_1/n$. The data fits cross a range of 1.6-20 Å, the first half graph presents local distortion from 1.6-5 Å. The blue circles represent the observed data, the red line represents the calculated profile, the green line represents the difference between the two.

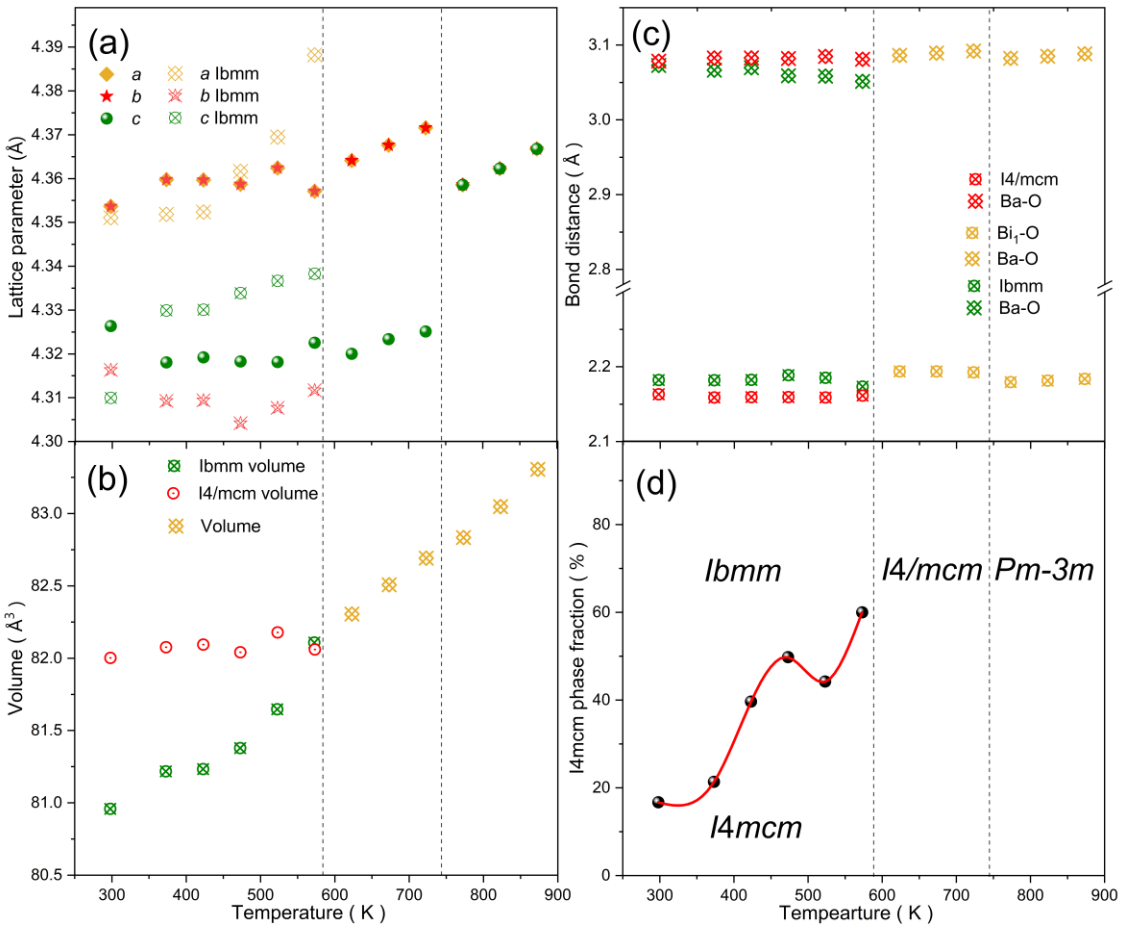

Figure 4.23: Results from the NPDF fit for $BaBi_{0.7}Pb_{0.3}O_3$ varying from 298 K to 873 K.(*a*) and (*b*) indicates lattice parameters and cell volume. (*c*) bond distance change altered by temperature, Bi_1-O represents the average distance between Bi ion and O^{2-}, Ba are representing Ba^{2+}. (*d*) indicates the two-phase region.

4.5 Big-box RMC Modelling

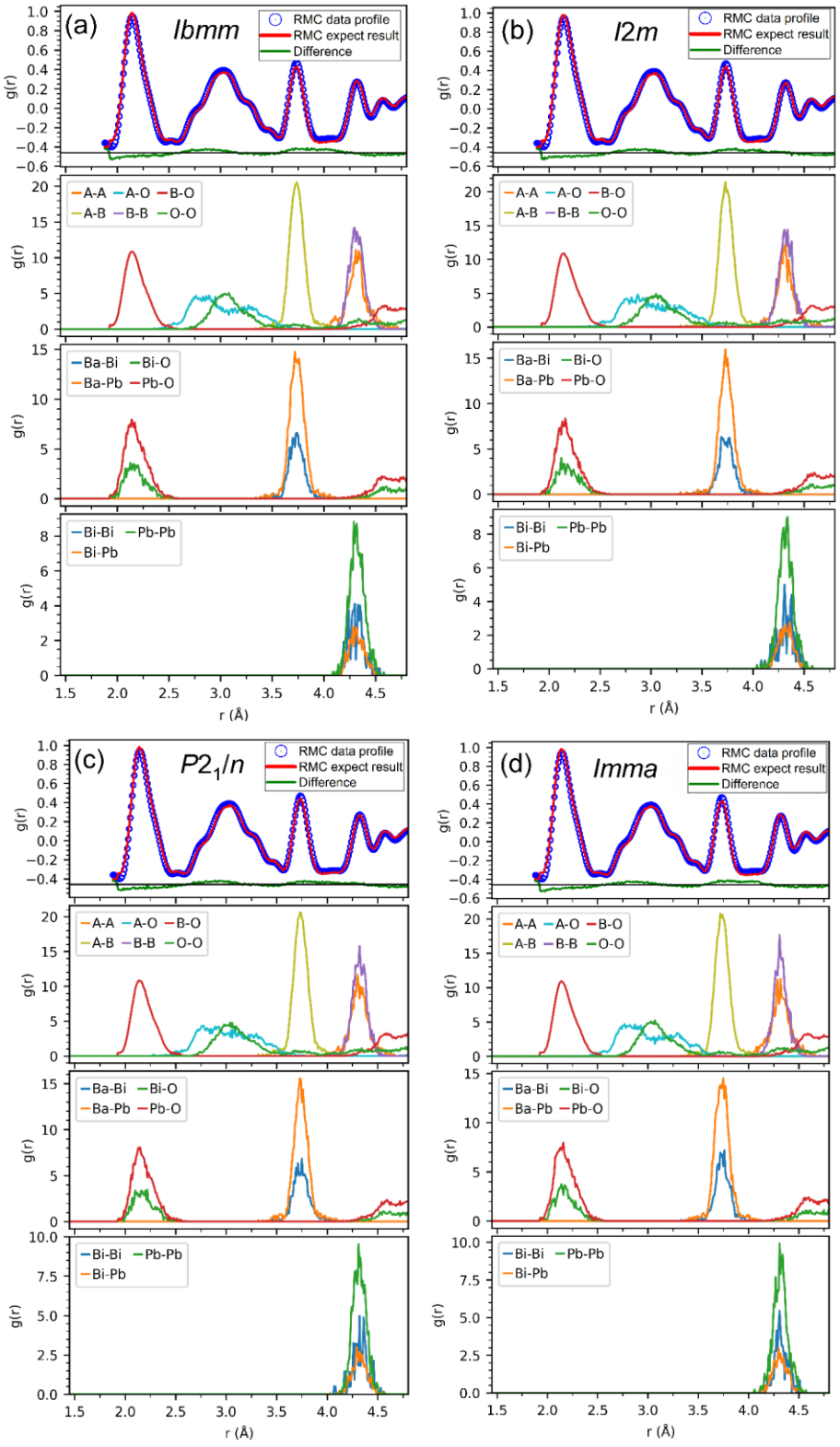

Figure 4.24: Partial PDF data for $BaBi_{0.7}Pb_{0.3}O_3$ at 10 K. (a) orthorhombic space group *Ibmm*, (b) monoclinic space group *I*2/*m*, (c) monoclinic space group $P2_1/n$ and (d) orthorhombic space group *Imma*. The data generated from reverse Monte Carlo method without BVS setting and cross a range of 1.5-5 Å, the second panel represents calculated partial pair distribution function, *A* represent *A*-site cation Ba^{2+}, *B* represents *B*-site cation Bi^{3+}/Bi^{5+} and Pb^{4+}, *O* represents O^{2-}. The rest of subsequent panel stand for various atom-atom distance.

Simulation results from RMCProfile show that different starting structural symmetries do not yield discernible differences. This confirms that the simulations are not strongly dependent on the initial structural configuration, but rather on the imposed valence-state constraints of Bi within a reasonable range, as set by the bond-valence sum (BVS).

The left panel of Figure 4.24 illustrates the RMC simulation of $BaBi_{0.7}Pb_{0.3}O_3$ at 10 K without BVS constraints. In this case, the Pb–O and Bi–O bonds both contribute to the first-neighbour peak at ~2.18 Å. This feature corresponds to a virtual "Bi^{4+}" state, with a peak width of ~0.35 Å, indicative of dynamic delocalization and a mixed-valence state. Importantly, in the absence of explicit Bi charge ordering, the oxygen sublattice does not show significant fitting residuals.

The right panel shows the simulation results with BVS constraints applied. Here, the Bi^{5+}–O bond length appears at ~2.10 Å, characterized by a sharp, intense peak, while the Bi^{3+}–O bond length is ~2.23 Å, appearing as a broader peak. The separation between the two Bi–O peaks ($\Delta r \approx 0.13$ Å) reflects charge disproportionation. The Pb^{4+}–O peak lies between the two Bi–O peaks, effectively preventing complete delocalization of Bi valence states.

Theoretically, Bi charge disproportionation should not produce peaks with such different widths and intensities, since Bi^{3+} and Bi^{5+} are expected to share octahedra with Pb^{4+} in roughly equal proportions. With respect to the second-neighbour peak (O–O and Ba–O contributions), introducing BVS constraints does not yield more reasonable oxygen positions. Notably, the χ^2 value of the unconstrained fit is ~20, whereas the constrained fit gives $\chi^2 \approx 150$. If charge disproportionation were intrinsic to $BaBi_{0.7}Pb_{0.3}O_3$, the BVS-constrained fit would be expected to produce χ^2 values comparable to, or only slightly worse than, the unconstrained case.

The average BVS values from the RMCProfile simulations with BVS constraints are summarized in Table 4.4. The average values for Ba^{2+}, Pb^{4+}, and Bi^{5+} remain within reasonable ranges. In contrast, Bi^{3+} shows an average value of 3.95, which is ~31.5% higher than the expected value. This indicates a distortion in the coordination environment around Bi^{3+}. The corresponding BVS $\chi^2 = 0.254 \times 10^7$, reflecting a strong inconsistency between the imposed BVS constraints and the experimental PDF data. Nevertheless, the results provide supporting evidence that Pb remains in the +4 oxidation state, consistent with its $6s^0$ electronic configuration.

The BVS average of RMCprofile from end BVS result illustrated in Table 4.4. Average BVS value for Ba^{2+}, Pb^{4+} and Bi^{5+} remain within reasonable range, whilst Bi^{3+} gave 3.95 (31.5% higher than expected value), it illustrates a distortion happen to Bi^{3+} coordination environment; BVS $\chi^2 = 0.254 \times 10^7$, which reflect a strict conflict between BVS constrain and experiment PDF. However, there are few valid information provide to support Pb^{4+} remain as 4+ state and fit electronic configuration $6s^0$.

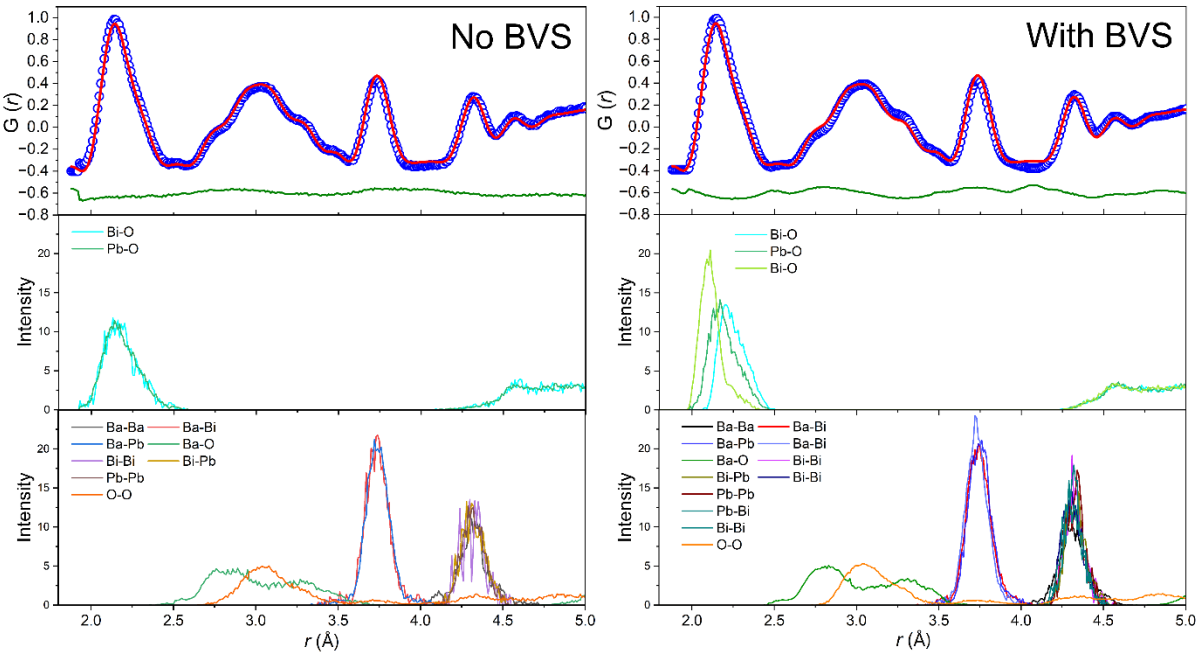

Figure 4.25: Partial PDF data of $BaBi_{0.7}Pb_{0.3}O3$ fit with reverse Monte Carlo (RMC) approach at 10 K. Left panel represents RMCprofile generating movement without bond valence sum constrain, Bi-O

preforms as "Bi^{4+}" in cyan line, right panel represents RMCprofile generating movement with BVS constrain, Bi-O divides into Bi^{3+} -O with cyan line and Bi^{5+}-O with light green line.

Table 4.5: BVS average for each atom after RMCprofile movement generated in $BaBi_{0.7}Pb_{0.3}O_3$ at 10 K.

	Ba^{2+}	**Bi^{3+}**	**Bi^{5+}**	**Pb^{4+}**	**O^{2-}**
Standard value	~ 1.7	~ 3.0	~ 5.2	~ 4.0	~ 1.8
RMC model result	1.8974	3.9464	5.0793	4.9758	2.183

BVS is a crucial metric for quantifying the interatomic distance constraints, which provides further analysis in atomic displacement that substantiates charge disproportionation. The 2D-density displacement patterns of various ions are illustrated in Figure 4.x, where Ba^{2+} as *A*-site cation exhibits minimal displacement variation (< ± 0.05 Å), it consistent with the weak correlation between charge ordering within *B*-site cations. In contrast, three *B*-site cations demonstrate subtle variations: Bi^{3+} and Bi^{5+} exhibit reduced displacement magnitudes from ~0.15 to 0.10 Å compared with BVS results, Bi^{3+} constrained by BVS maintain as 3+ valence state and fix *B*-site position within r_o, it results *O*-site displacement instead. Oxygen sub-lattice undergoes significant distortion, it is transitioning from central concentration to a diffuse distribution along *x*, *y*, *z* axes (from ~0.15 to 0.2 Å), accompanied by positional disorder. This oxygen sub-lattice distortion is coupled with the displacement variation of Bi and Pb ion.

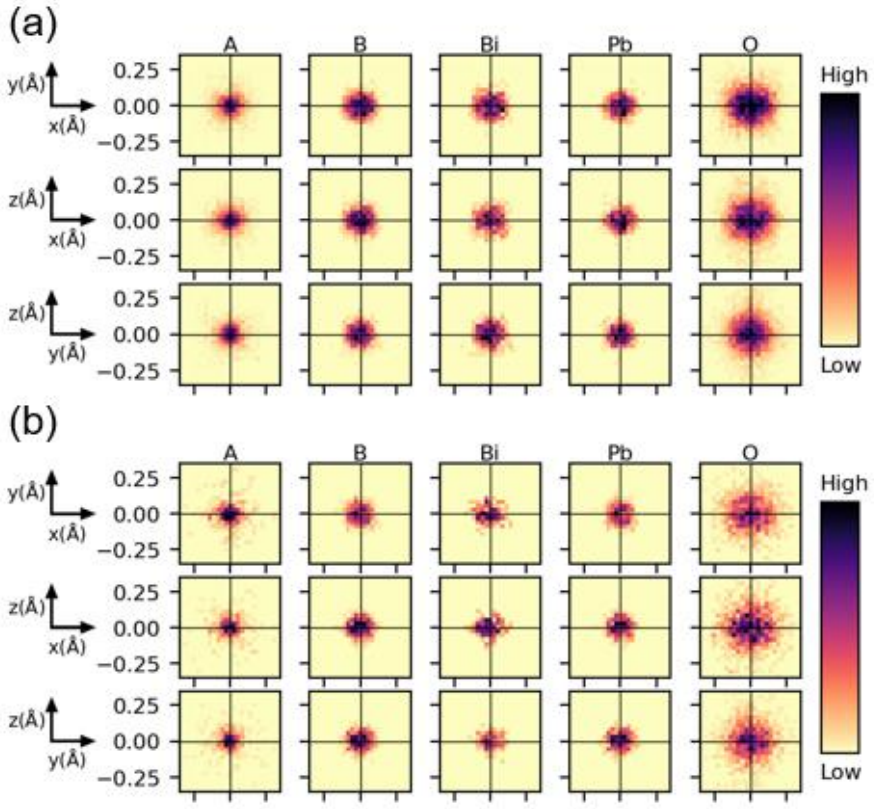

Figure 4.26: The 2D-density pattern derived by RMCprofile. (a) $BaBi_{0.7}Pb_{0.3}O_3$ atom displacement without BVS and (b) $BaBi_{0.7}Pb_{0.3}O_3$ atom displacement with BVS. *A* represents *A*-site atom Ba, *B* and Bi represents *B*-site and *B'*-site atom Bi^{3+} and Bi^{5+} (in BVS plot), *B* in without BVS plot represent to average Bi atom. Pb in without BVS plot represent to average Pb atom, *O* represents to oxygen atom. Three rows visualize the displacement from different axis.

4.6 Conclusion

This work involved neutron powder diffraction (NPD) Rietveld refinements to provide an accurate structural study of the $BaBi_{1-x}Pb_xO_3$ ($0 \leqslant x \leqslant 0.3$) series of compounds at room temperature. The refinement results indicate that $BaBi_{1-x}Pb_xO_3$ crystallizes in either a monoclinic (*I2/m*) or orthorhombic (*Ibmm)* structure, depending on the level of lead doping. The transition between the two structures occurs around $0.20 \leqslant x \leqslant 0.25$ and possibly reflects the presence of BiO_6 octahedral breathing modes. These breathing distortions are gradually suppressed with increasing Pb content. Such behavior is correlated with local charge-density-wave (CDW) instabilities, which are responsible for the semiconducting properties in the $BaBi_{1-x}Pb_xO_3$ series.[26]

Further NPD investigations focused on the temperature-dependent structural evolution of $BaBi_{0.7}Pb_{0.3}O_3$. Rietveld refinements using the orthorhombic *Ibmm* model yielded poor fits between 298 and 573 K, especially in the $Q \sim 4.2–5.0$ Å^{-1} range, indicating the absence of complete long-range order. High-quality refinements confirmed a two-phase coexistence and established the following temperature-dependent phase transition sequence for $BaBi_{0.7}Pb_{0.3}O$:

$$Ibmm\ (\sim 298\ \mathrm{K}) \rightarrow Ibmm + I4/mcm\ (\sim 600\ \mathrm{K}) \rightarrow I4/mcm\ (\sim 750\ \mathrm{K}) \rightarrow Pm\bar{3}m.$$

Neutron total scattering was employed to investigate both the long-range average structure and the short-range local structure of $BaBi_{1-x}Pb_xO_3$. The long-range structures obtained at room temperature are consistent with Rietveld refinement results, while short-range correlations reveal small, but significant, distortions. A structural model consistent with both average and local descriptions was constructed, highlighting distortions that emphasize the complexity of the local structure. This model incorporates polyhedra with varying coordination numbers and inherent disordered tilting, features that are closely linked to the physical properties of Pb-doped compounds, such as superconductivity.

Neutron total scattering also demonstrates exceptional sensitivity to oxygen disorder, making it particularly effective for probing the structural complexity of metal oxides. At relatively high Pb concentrations, the B-site cations remain largely centred, but NPD and NPDF data indicate that oxygen displacements drive polyhedral tilting. This suggests that Bi–O bond-length variations, associated with charge-order melting, are preserved through oxygen disorder.

To further examine oxygen disorder, low-temperature measurements of $BaBi_{0.7}Pb_{0.3}O_3$ were refined in several candidate symmetry space groups, minimizing the influence of thermal motion. Although increasing the number of oxygen degrees of freedom improved short-range fits, low-symmetry models showed significant limitations when describing long-range order. Determining whether short-range disorder in the oxygen sublattice originates from interactions between Bi^{3+} $6s^2$ lone-pair electrons and O 2p orbitals is key to understanding whether charge disproportionation persists in $BaBi_{0.7}Pb_{0.3}O_3$.

Reverse Monte Carlo (RMC) analysis of $BaBi_{0.7}Pb_{0.3}O_3$ NPDF data at 10 K provided a detailed description of atomic arrangements, with B-site atom displacements constrained by bond valence sums (BVS). However, no evidence was found to support the presence of trivalent Bi in $BaBi_{0.7}Pb_{0.3}O_3$. This result mirrors findings from RMC studies of $BaBi_{1-x}Pb_xO_3$, where charge disproportionation of Bi and oxygen-breathing distortions were shown to be independent of the superconducting state. [27]

Bibliography

(1) Bouwmeester, R. L.; Brinkman, A. $BaBiO_3$—From single crystals towards oxide topological insulators. *Reviews in Physics* **2021**, *6*, 100056. DOI: https://doi.org/10.1016/j.revip.2021.100056.

(2) Sleight, A. W.; Gillson, J. L.; Bierstedt, P. E. High-temperature superconductivity in the $BaPb_{1-x}Bi_xO_3$ systems. *Solid State Communications* **1975**, *17* (1), 27-28. DOI: https://doi.org/10.1016/0038-1098(75)90327-0.

(3) Sleight, A. W. Bismuthates: $BaBiO_3$ and related superconducting phases. *Physica C: Superconductivity and its Applications* **2015**, *514*, 152-165. DOI: https://doi.org/10.1016/j.physc.2015.02.012.

(4) Shannon, R. D. Revised effective ionic radii and systematic studies of interatomic distances in halides and chalcogenides. *Acta Crystallographica Section A* **1976**, *32* (5), 751-767. DOI: 10.1107/S0567739476001551.

(5) Sleight, A. W.; Cox, D. E. Symmetry of superconducting compositions in the $BaPb_{1-x}Bi_xO_3$ system. *Solid State Communications* **1986**, *58* (6), 347-350. DOI: https://doi.org/10.1016/0038-1098(86)90802-1.

(6) Giraldo-Gallo, P.; Lee, H.; Zhang, Y.; Kramer, M. J.; Beasley, M. R.; Geballe, T. H.; Fisher, I. R. Field-tuned superconductor-insulator transition in $BaPb_{1-x}Bi_xO_3$. *Physical Review B* **2012**, *85* (17), 174503. DOI: 10.1103/PhysRevB.85.174503.

(7) Wallwork, K. S.; Kennedy, B. J.; Wang, D. The High Resolution Powder Diffraction Beamline for the Australian Synchrotron. *AIP Conference Proceedings* **2007**, *879* (1), 879-882. DOI: 10.1063/1.2436201 (acccessed 4/25/2025).

(8) Foyevtsov, O.; Balandeh, S.; Chi, S.; Sawatzky, G. Structural electronic and magnetic properties of $BaBiO_3$ single crystals. *Physica. B, Condensed matter* **2019**, *570*, 328-333. DOI: 10.1016/j.physb.2019.06.010.

(9) Marx, D.; Radaelli, P.; Jorgensen, J.; Hitterman, R.; Hinks, D.; Pei, S.; Dabrowski, B. Metastable behavior of the superconducting phase in the $BaBi_{1-x}Pb_xO_3$ system. *Physical Review B* **1992**, *46* (2), 1144.

(10) Arshad, M.; Abushad, M.; Azhar, M.; Ahmed, H.; Nadeem, M.; Ansari, A.; Chakradhary, V. K.; Husain, S.; Khan, W. Origin of enhanced dielectric and multiferroic properties in Pb-doped $BaTiO_3$ ceramics. *Applied Physics A* **2022**, *128* (12), 1123. DOI: 10.1007/s00339-022-06239-9.

(11) Li, Z.; Yu, J.; Hao, S.; Janolin, P.-E. Enhancing properties of lead-free ferroelectric $BaTiO_3$ through doping. *Journal of the European Ceramic Society* **2022**, *42* (12), 4693-4701. DOI: https://doi.org/10.1016/j.jeurceramsoc.2022.05.023.

(12) Brown, I. D.; Altermatt, D. Bond-valence parameters obtained from a systematic analysis of the Inorganic Crystal Structure Database. *Acta crystallographica. Section B, Structural science* **1985**, *41* (4), 244-247. DOI: 10.1107/S0108768185002063.

(13) Nicoletti, D.; Casandruc, E.; Fu, D.; Giraldo-Gallo, P.; Fisher, I. R.; Cavalleri, A. Anomalous relaxation kinetics and charge-density-wave correlations in underdoped $BaPb_{1-x}Bi_xO_3$. *Proceedings of the National Academy of Sciences* **2017**, *114* (34), 9020-9025. DOI: 10.1073/pnas.1707079114 (acccessed 2025/07/16).

(14) Liu, S.-Y.; Meng, Y.; Liu, S.; Li, D.-J.; Li, Y.; Liu, Y.; Shen, Y.; Wang, S. Phase stability, electronic structures, and superconductivity properties of the $BaPb_{1-x}Bi_xO_3$ and $Ba_{1-x}K_xBiO_3$ perovskites. *Journal of the American Ceramic Society* **2017**, *100* (3), 1221-1230. DOI: https://doi.org/10.1111/jace.14605 (acccessed 2025/07/22).

(15) Pei, S.; Jorgensen, J. D.; Hinks, D. G.; Dabrowski, B.; Richards, D. R.; Mitchell, A. W.; Zheng, Y.; Newsam, J. M.; Sinha, S. K.; Vaknin, D.; et al. Structural phase diagram of the $Ba_{1-x}K_xBiO_3$ system. *Physica. C, Superconductivity* **1989**, *162-164*, 556-557. DOI: 10.1016/0921-4534(89)91153-2.

(16) Zhang, J.; Bennett, C. J.; Nicholas, M. K.; Mullens, B. G.; Kennedy, B. J. Expected and unexpected structural phase transitions in K_2ReBr_6 and K_2ReI_6. *Journal of solid state chemistry* **2024**, *338*, 124875. DOI: 10.1016/j.jssc.2024.124875.

(17) Sears, V. F. Appendix. Neutron Scattering Lengths and Cross Sections. Vol. 23; Elsevier Science & Technology, 1986; pp 521-550.

(18) Proffen, T.; DiFrancesco, R. G.; Billinge, S. J. L.; Brosha, E. L.; Kwei, G. H. Measurement of the local Jahn-Teller distortion in $LaMnO_{3.006}$. Cornell University Library, arXiv.org: Ithaca, 1999.

(19) Kiryukhin, V.; Koo, T. Y.; Ishibashi, H.; Hill, J. P.; S-W, C. Average Lattice Symmetry and Nanoscale Structural Correlations in Magnetoresistive Manganites. Cornell University Library, arXiv.org: Ithaca, 2003.

(20) Lanzara, A.; Saini, N. L.; Brunelli, M.; Natali, F.; Bianconi, A.; Radaelli, P. G. From manganites to cuprates: a comparative study of the local lattice instability. *Zeitschrift für Physik B Condensed Matter* **1997**, *104* (4), 699-702. DOI: 10.1007/s002570050511.

(21) Franchini, C.; Kresse, G.; Podloucky, R. Polaronic Hole Trapping in Doped $BaBiO_3$. *Physical Review Letters* **2009**, *102* (25), 256402. DOI: 10.1103/PhysRevLett.102.256402.

(22) Asano, H.; Oda, M.; Endoh, Y.; Hidaka, Y.; Izumi, F.; Ishigaki, T.; Karahashi, K.; Murakami, T.; Watanabe, N. Neutron Powder Diffraction from Polymorphs of $BaPb_{0.75}Bi_{0.25}O_3$. *Japanese Journal of Applied Physics* **1988**, *27* (9), 1638-1640. DOI: 10.1143/jjap.27.1638.

(23) Braden, M.; Reichardt, W.; Elkaim, E.; Lauriat, J. P.; Shiryaev, S.; Barilo, S. N. Structural distortion in superconducting $Ba_{1-x}K_xBiO_3$. *Physical Review B* **2000**, *62* (10), 6708-6715. DOI: 10.1103/PhysRevB.62.6708.

(24) Kennedy, B. J.; Howard, C. J.; Knight, K. S.; Zhang, Z.; Zhou, Q. Structures and phase transitions in the ordered double perovskites $Ba_2Bi^{III}Bi^{V}O_6$ and $Ba_2Bi^{III}Sb^{V}O_6$. *Acta Crystallographica Section B* **2006**, *62* (4), 537-546. DOI: 10.1107/S0108768106018842.

(25) Climent-Pascual, E.; Ni, N.; Jia, S.; Huang, Q.; Cava, R. J. Polymorphism in $BaPb_{1-x}Bi_xO_3$ at the superconducting composition. *Physical Review B* **2011**, *83* (17), 174512. DOI: 10.1103/PhysRevB.83.174512.

(26) Jurczek, E.; Rice, T. M. A Charge-Density-Wave Instability in BaBi1-xPbxO3 Caused by Strong Electron-Phonon Coupling. *Europhysics letters* **1986**, *1*, 225. DOI: 10.1209/0295-5075/1/5/005.

(27) Griffitt, S.; Spaić, M.; Joe, J.; Anderson, Z. W.; Zhai, D.; Krogstad, M. J.; Osborn, R.; Pelc, D.; Greven, M. Local inversion-symmetry breaking in a bismuthate high-Tc

superconductor. *Nature communications* **2023**, *14* (1), 845. DOI: 10.1038/s41467-023-36348-9.

Chapter 5 Double Perovskite $Cs_2AgBiBr_6$*[2]

[2] This chapter is based on a manuscript published at *Journal of Solid State Chemistry*.

5.1 Structure Study of $Cs_2AgBiBr_6$

Double perovskites of the ″elpasolite″ family with the general formula $A_2M^IM^{III}X_6$, where M^I = monovalent cation, M^{III} = trivalent cation, X = halide have been proposed as all-inorganic alternatives to Pb containing OIHP.[1] $Cs_2AgBiBr_6$ is one of the more promising examples.[2] In 2016 McClure *et al*. showed that at ambient-temperature $Cs_2AgBiBr_6$ has a cubic structure with a = 11.2711(1) Å described in space group $Fm\bar{3}m$, which accounts for the rock-salt like ordering of the octahedrally coordinated Bi and Ag cations.[3] Shortly thereafter Scade *et al*. confirmed the structure using powder neutron diffraction methods and observed that it undergoes a phase transition to a tetragonal structure near 122 K.[4] This transition is a consequence of the condensation of out-of-phase tilting of the corner sharing octahedra with the tetragonal structure described in space group $I4/m$. The susceptibility of $Cs_2AgBiBr_6$ to such a phase transition can be rationalised by examination of the perovskite tolerance factor $t = \frac{r_A + r_X}{\sqrt{2}(r_B + r_X)}$. Using the ionic radii proposed by Shannon (r_{Cs^+} = 1.88 Å; r_{Ag^+} = 1.15 Å; $r_{Bi^{3+}}$ = 1.03 Å; and r_{Br^-} = 1.96 Å) the tolerance factor is estimated to be t = 0.89.[5] This suggests that the Cs^{1+} cation is too small for the cuboctahedral site in the cubic structure, as also indicated by the bond valence sum (BVS) of 0.73 reported by McClure *et al.*[3]

Despite the Ag^+ cations being appreciably larger than Bi^{3+} (1.15 vs 1.03 Å) McClure *et al*. reported approximately equal Ag-Br and Bi-Br distances of 2.822(5) and 2.813(5) Å respectively. This coupled with the large atomic displacement parameters of the Cs cation raises the possibility of disorder in the structure. To investigate this possibility here we report a variable temperature synchrotron X-ray diffraction study of $Cs_2AgBiBr_6$.

We have confirmed that at room temperature $Cs_2AgBiBr_6$ has a cubic structure described by space group $Fm\bar{3}m$. The structural refinements show the Ag and Bi cations to be fully ordered within the sensitivity of the measurements. The refined lattice parameter of a = 11.26633(3) Å at 300 K is in good agreement with the value of a = 11.2711(1) Å or 11.2784(5) Å reported by

McClure *et al*. and Schade *et al*. respectively.[3, 4] Initially isotropic atomic displacement parameters (ADP) were used, and this gave $\chi^2 = 13.2$. Allowing for anisotropic ADP introduces one addition variable parameter [$U^{11}(Br) \neq U^{22} = U^{33}$; $U^{12}=U^{23}=U^{13} = 0$] but resulted in a significant reduction in χ^2 to 8.9. In the cubic structure there is a single variable atomic position, for the bromide at the 24*e* Wyckoff position (*x*, 0, 0). The refined value for *x* of 0.25056(7) shows the Ag-Br and Bi-Br bond distances to be similar, the refined values being 2.8103(8) and 2.8229(8) Å. This is somewhat surprising since the ionic radius of r_{Ag}^{+} is ~ 0.1 Å larger than that r_{Bi}^{3+}, 1.15 Å and 1.03 Å respectively. This near equality in the Ag-Br and Bi-Br bond distances was also evident from the earlier studies, but this was not discussed further in these. The bond valence sums for the cations were estimated from the refined bond distances and these showed the Cs to be underbonded, 0.74, whereas the values for both Ag 1.27 and Bi 3.20 shows these to be overbonded.[6] This is consistent with the small tolerance factor, $t = 0.89$.[7]

Cooling the sample below ~ 120 K resulted in the splitting of selected diffraction peaks indicative of the lowering of the crystal symmetry to tetragonal with $c/a > 1$. The patterns measured between 80 and 120 K were fit using the tetragonal *I*4/*m* model described by Schade *et al*. [4] Isotropic ADP resulted in an acceptable fit $\chi^2 = 23.5$ that only marginally improved to 22.1 if anisotropic ADPs we used for all atoms (an additional 7 variable parameters) and occasionally resulted in indeterminate values. Consequently, anisotropic ADPs were used only for the Br anions in the final refinement cycles. Cooperative tilting of the octahedra has been found to result in a small distortion of the octahedra and both the $AgBr_6$ and $BiBr_6$ octahedra exhibit slight axial elongation in the tetragonal structure, with this being greater for the $AgBr_6$ octahedra. In the tetragonal structure the Br1 anion is at the 8*h* Wyckoff position ($1/4 + u_1$, $3/4 + u_2$, 0) where $u_1 \sim u_2$ and the angle of the out-of-phase rotation, given by $\tan \phi = 4u_{avg} \sim 5.6°$ at 80 K.[8]

Tilting of the octahedra reduces the volume of the appropriately scaled unit cell and the magnitude of this volume strain (ε_s) was estimated by a linear extrapolation the unit cell volume from the cubic phase into the tetragonal region. The temperature dependence of the excess strain then serves as an order parameter for the tetragonal phase transition and as illustrated in Figure 5.2(c) this was well fit to an expression of the type $\varepsilon_s = \left(\frac{T-T_c}{T}\right)^{\beta}$ where T_c is the cubic

to tetragonal phase transition temperature and β is the critical exponent of the order parameter near the critical point in a continuous phase transition. This fitting gave Tc = 120(2) K and β = ¼ indicative of the second order phase transition. The transition temperature is in excellent agreement with that reported by Schade *et al*.[4]

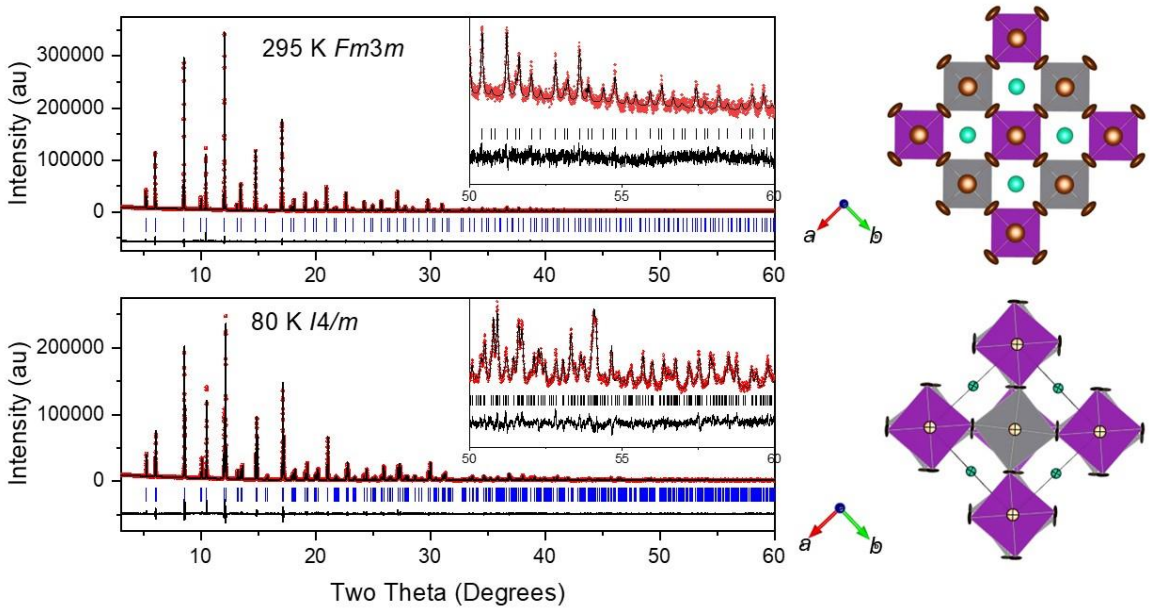

Figure 5.1: Rietveld refinements of the cubic and tetragonal structural models for $Cs_2AgBiBr_6$ against high resolution synchrotron X-ray diffraction patterns collected at 295 and 80 K respectively. The data are represented by the red symbols, and the solid black line through this is the fit. The short vertical markers show the positions of the space group allowed Bragg reflections The difference plot is shown below these. The insets highlight the quality of the data and fit to high angles. The two structures are illustrated, with out-of-phase tilting about the *c*-axis evident in the lower representation.

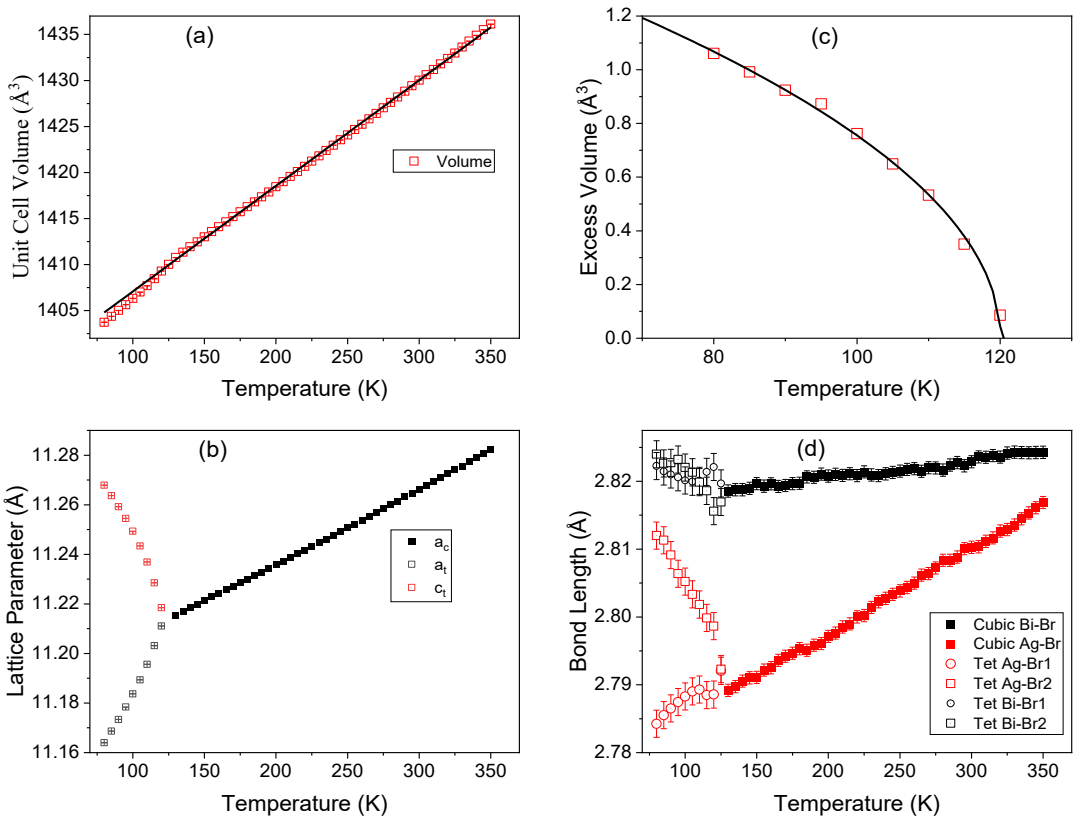

Figure 5.2: Temperature dependence of selected structural features of $Cs_2AgBiBr_6$ obtained from Rietveld refinements. In (a) the experimental unit cell volumes are indicate by the symbols and the solid line is a linear fit to the data measured between 200 and 350 K. (b) shows the appropriately lattice parameters. (c) shows the excess volume and the fit to this as described in the text. (d) shows the Bi-Br and Ag-Br bond lengths were the closed symbols are for the cubic phase and open symbols are for the tetragonal phase.

The temperature dependence of the bond distances in the tetragonal phase is intriguing. As illustrated in Figure 5.2(d) the Bi-Br distances is weakly temperature dependent in the cubic phase, decreasing slightly between 350 and 120 K as expected.[9] Within the precision of the measurements, the distance weakly increases at the transition to the tetragonal structure. In comparison the Ag-Br bond distance shows a noticeable contraction on cooling in the cubic phase and a strong anisotropy between the axial Ag-Br (1) and four equatorial Ag-Br (2) distances in the tetragonal structure with the latter being around 1% longer at 80K. A similar distortion in the $AgBr_6$ is evident from the low temperature (20 K) NPD analysis The average

Ag-Br distance in the tetragonal phase is approximately temperature independent. The difference in the behaviour of the Ag-Br and Bi-Br bond distances can be understood in terms of the differences in the bonding of bromide with the two cations. The Ag^{+} ions are larger than the Bi^{3+} ions and have a greater tendency to form covalent bonds with bromide. It is proposed that this covalent character leads to a more easily distorted $AgBr_6$ octahedra.

The atomic displacement parameters contain information about both static and dynamic disorder. In general, the former is expected to be independent of temperature, whereas the contribution of the latter will increase as the temperature increases reflecting the larger size of the atomic vibrations. The ADPs of the cations all decrease as the temperature decreases suggesting dynamic motions are important. The small discontinuity in the values of these around 120 K is believed to reflect the change in the structural model used at this temperature. That the values of the displacement parameter of the Cs cation, that sits in the cuboctahedra site, is larger than that of the Ag and Bi cation led McClure to postulate that there was dynamic motion of the octahedra, most likely octahedral rotations. The temperature dependence of this observed here is consistent with this hypothesis. The smaller values of the ADPs for the Ag^{+} and Bi^{3+} cations reflects their more confined octahedral environments.

Anisotropic displacement parameters were considered for the Br anions and the temperature dependence of these is illustrated in Figure 5.3. As evident from this figure in the cubic phase the ellipsoids (U^{22}= U^{33}) are largest transverse to the bonding direction in the Ag-Br-Bi chain, see also Figure 5.1, indicating the largest motion is towards the cuboctahedra site. Similar anisotropy has been observed in related halide perovskites.[10-12] In the lower symmetry tetragonal structure there are two crystallographically distinct Br cations (at the 8*h* and 4*e* Wyckoff positions). As illustrated in Figure 5.3 at the transition to the tetragonal structure the transverse ADPs become smaller reflecting the long-range static displacement of the Br anion from the high symmetry position. That the magnitude of the ADPs of the Br decreases once the structure becomes tetragonal, together with the anisotropy in these this is evidence for dynamic tilting of the octahedra in the cubic phase as suggested by McClure.

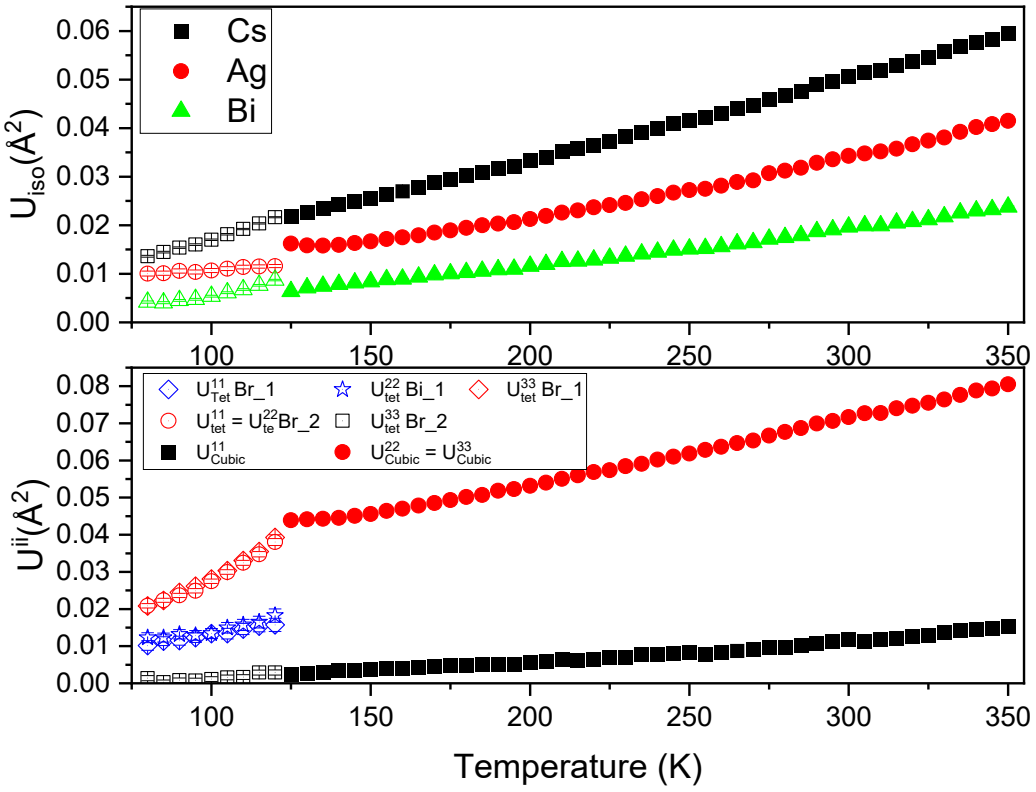

Figure 5.3: Temperature dependence of the atomic displacement panels. For the three cations Cs, Ag and Bi isotropic displacement parameters were refined whereas anisotropic displacement parameters were used for Br. The closed symbols are for the cubic structure and the open symbols are values from the tetragonal structure.

5.2 Conclusion

The structure of $Cs_2AgBiBr_6$ between 80 and 350 K has been determined by Rietveld refinement against high resolution synchrotron X-ray diffraction data. At room temperature the Ag and Bi cations show a rock-salt like ordering, resulting in a doubling of the perovskite unit cell dimensions, and the structure was refined in the cubic space group $Fm\bar{3}m$. The cubic structure is characterised by underbonding of the Cs cation and large anisotropic displacements of the Br ions perpendicular to the Ag-Br-Bi chains. It is reasonable to conclude that this

corresponds to dynamic rotations of the rigid corner sharing octahedra. Such rotations would increase the effective bond valence sum of the Cs cation. Upon cooling below 120 K the structure the dynamic displacements of the Br anions freeze driving a continuous transition to a tetragonal structure described in space group *I*4/*m* resulting in an increase in the bond valence sum of the Cs from 0.73 to 0.85. The cation ordering in $Cs_2AgBiBr_6$ is driven by the charge difference between the Ag and Bi cations, although the Ag^+ cations are appreciably larger than Bi^{3+} (1.15 vs 1.03 Å) paradoxically the observed Ag-Br distance is slightly smaller than the Bi-Br distance 2.8103(8) and 2.8229(8) Å, and corresponding MO_6 polyhedral volumes, whilst in the same order are approximately equal at room temperature. The difference between the distances and between the unit cell volumes increases as the temperature is lowered. It is proposed that the Ag^+ ions have a greater tendency to form covalent bonds with bromide and that this covalent character leads to a more easily distorted $AgBr_6$ octahedra.

Bibliography

(1) Wolf, N. R.; Connor, B. A.; Slavney, A. H.; Karunadasa, H. I. Doubling the Stakes: The Promise of Halide Double Perovskites. *Angewandte Chemie-International Edition* **2021**, *60* (30), 16264-16278. DOI: 10.1002/anie.202016185.

(2) Sirtl, M. T.; Armer, M.; Reb, L. K.; Hooijer, R.; Dörflinger, P.; Scheel, M. A.; Tvingstedt, K.; Rieder, P.; Glück, N.; Pandit, P.; et al. Optoelectronic Properties of $Cs_2AgBiBr_6$ Thin Films: The Influence of Precursor Stoichiometry. *Acs Applied Energy Materials* **2020**, *3* (12), 11597-11609. DOI: 10.1021/acsaem.0c01308.

(3) McClure, E. T.; Ball, M. R.; Windl, W.; Woodward, P. M. Cs_2AgBiX_6 (X= Br, Cl): new visible light absorbing, lead-free halide perovskite semiconductors. *Chemistry of Materials* **2016**, *28* (5), 1348-1354.

(4) Schade, L.; Wright, A. D.; Johnson, R. D.; Dollmann, M.; Wenger, B.; Nayak, P. K.; Prabhakaran, D.; Herz, L. M.; Nicholas, R.; Snaith, H. J.; Radaelli, P. G. Structural and Optical Properties of $Cs_2AgBiBr_6$ Double Perovskite. *ACS Energy Letters* **2019**, *4* (1), 299-305. DOI: 10.1021/acsenergylett.8b02090.

(5) Shannon, R. D. Revised effective ionic-radii and systematic studies of interatomic distances in halides and chalcogenides. *Acta Crystallographica Section A* **1976**, *32*, 751-767. DOI: 10.1107/s0567739476001551.

(6) Brown, I. D. Recent Developments in the Methods and Applications of the Bond Valence Model. *Chemical Reviews* **2009**, *109* (12), 6858-6919. DOI: 10.1021/cr900053k.

(7) Maughan, A. E.; Ganose, A. M.; Almaker, M. A.; Scanlon, D. O.; Neilson, J. R. Tolerance Factor and Cooperative Tilting Effects in Vacancy-Ordered Double Perovskite Halides. *Chemistry of Materials* **2018**, *30* (11), 3909-3919. DOI: 10.1021/acs.chemmater.8b01549.

(8) Howard, C. J.; Kennedy, B. J.; Woodward, P. M. Ordered double perovskites - a group-theoretical analysis. *Acta Crystallographica Section B* **2003**, *59* (4), 463-471. DOI: doi:10.1107/S0108768103010073.

(9) Ning, W.; Zhao, X. G.; Klarbring, J.; Bai, S.; Ji, F.; Wang, F.; Simak, S. I.; Tao, Y.; Ren, X. M.; Zhang, L.; et al. Thermochromic Lead-Free Halide Double Perovskites. *Advanced functional materials* **2019**, *29* (10), n/a. DOI: 10.1002/adfm.201807375.

(10) Bennett, C. J.; Brand, H. E. A.; Yuen, A. K. L.; Nicholas, M. K.; Kennedy, B. J. Structural Properties of Some Vacancy-Ordered Platinum Halide Perovskites. *Inorganic chemistry* **2024**, *63* (10), 4681-4690. DOI: 10.1021/acs.inorgchem.3c04288.

(11) Saura-Múzquiz, M.; Avdeev, M.; Brand, H. E. A.; Kennedy, B. J. Structural and Magnetic Properties of Some Vacancy-Ordered Osmium Halide Perovskites. *Inorganic chemistry* **2022**, *61* (40), 15961-15972. DOI: 10.1021/acs.inorgchem.2c02171.

(12) Zhang, J.; Bennett, C. J.; Nicholas, M. K.; Mullens, B. G.; Kennedy, B. J. Expected and unexpected structural phase transitions in K_2ReBr_6 and K_2ReI_6. *Journal of solid state chemistry* **2024**, *338*, 124875. DOI: 10.1016/j.jssc.2024.124875.

Appendix

Chapter 1

The good of fit R_{wp} is given with various R factors and $\chi 2$ within a dataset against Rietveld curve. Following equations indicate the determination progress:

Profile R factor:

$$R_p = \frac{\sum \left| y_{i(obs)} - y_{i(calc)} \right|}{\sum y_{i(obs)}}$$

Weighted profile R factor:

$$wR_p = \sqrt{\frac{\sum W_i \left(y_{i(obs)} - y_{i(calc)} \right)^2}{\sum W_i \left(y_{i(obs)} \right)^2}}$$

The R-expected profile factor:

$$R_{exp} = \sqrt{\frac{N-P}{\sum w_i y_{i(obs)}^2}}$$

The Bragg R factor:

$$R_B = \frac{\sum \left| I_{K(obs)} - I_{K(calc)} \right|}{\sum I_{K(obs)}}$$

The goodness of fit term:

$$\chi^2 = \frac{\sum W_i\left(y_{i(obs)}\text{-}y_{i(calc)}\right)^2}{\text{N-P}}\left(\frac{wR_p}{R_{exp}}\right)$$

Chapter 3 $BaBiO_3$

Neutron Powder Diffraction – NOMAD @ Oak Ridge National Laboratory

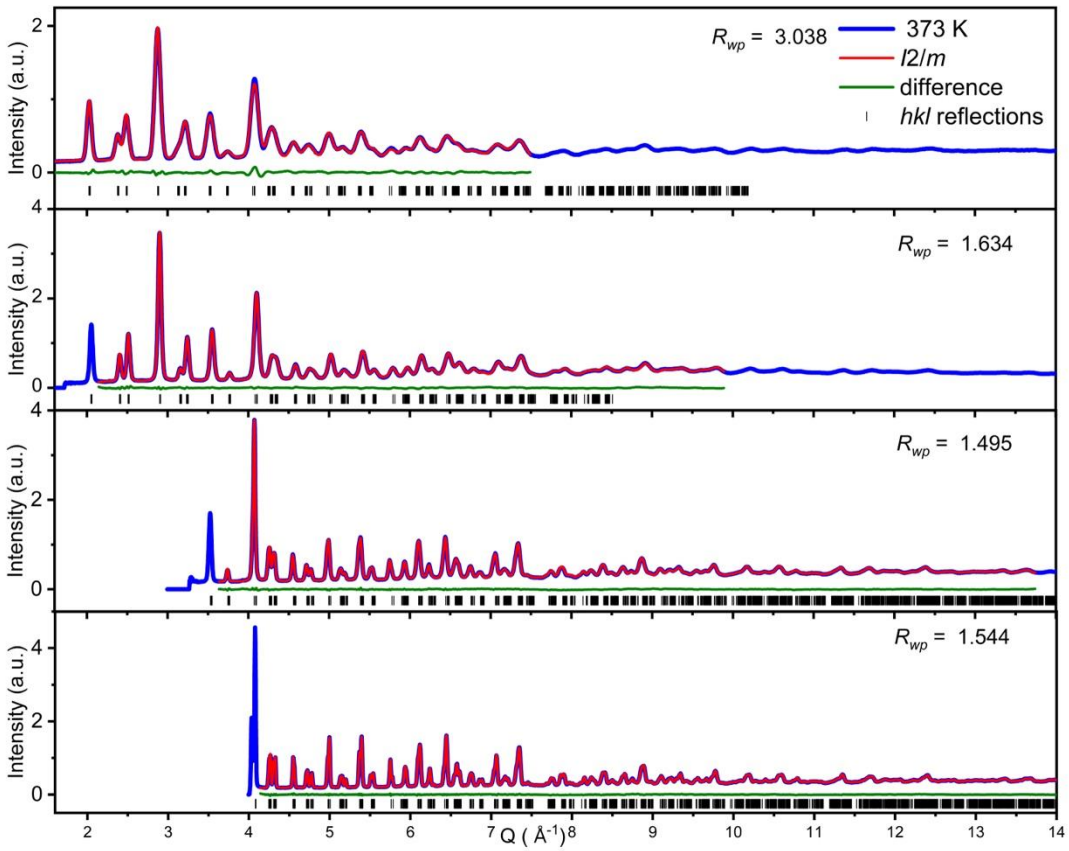

Figure A 1: Neutron powder diffraction data of $BaBiO_3$ collected at the NOMAD beamline at Oak Ridge National Laboratory at 373 K. The blue circles represent the data, the red line is the Rietveld refinement of the data to the monoclinic *I*2/*m* space group, the green line represents the different between the two. The black ticks show the *hkl* reflection allowed by space group.

The NPD Bragg peak Rietveld refinement suggests a better fit in space group $R\bar{3}$ rather than cubic space group $Fm\bar{3}m$.

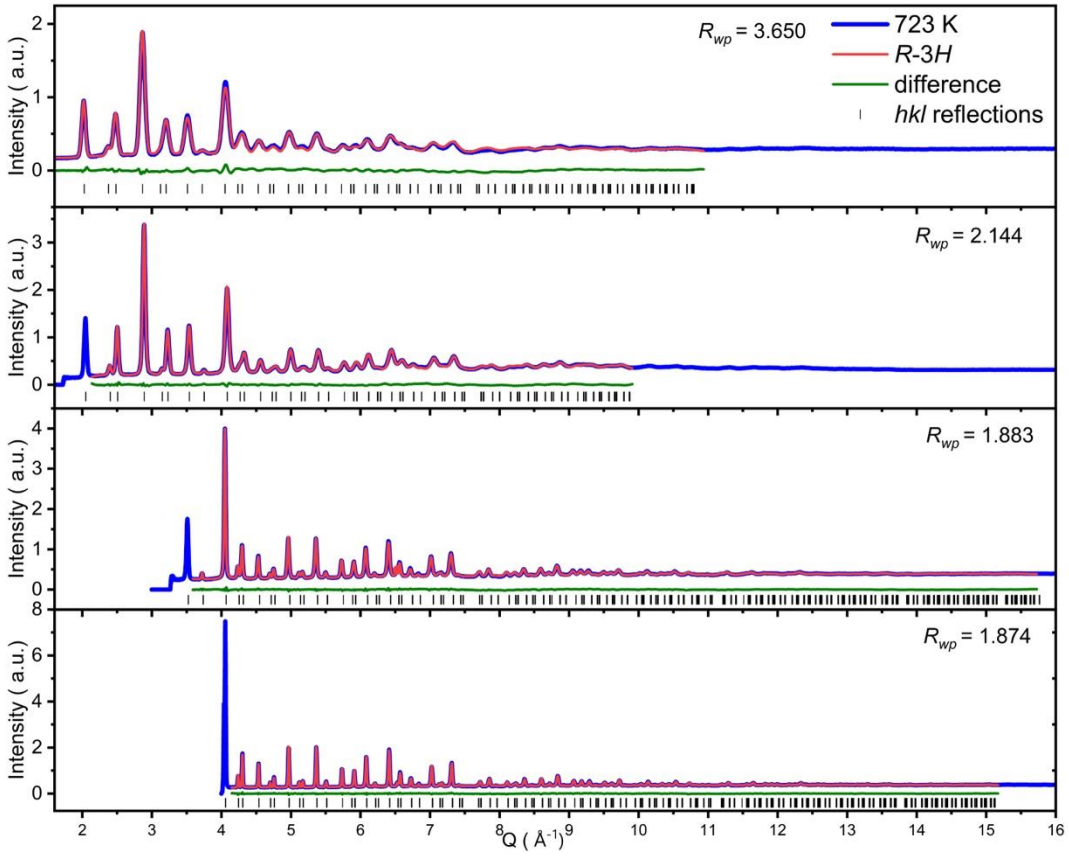

Figure A 2: Neutron powder diffraction data of $BaBiO_3$ collected at the NOMAD beamline at Oak Ridge National Laboratory at 723 K. The blue circles represent the data, the red line is the Rietveld refinement of the data to the rhombohedral $R\bar{3}$ space group, the green line represents the different between the two. The black ticks show the *hkl* reflection allowed by space group.

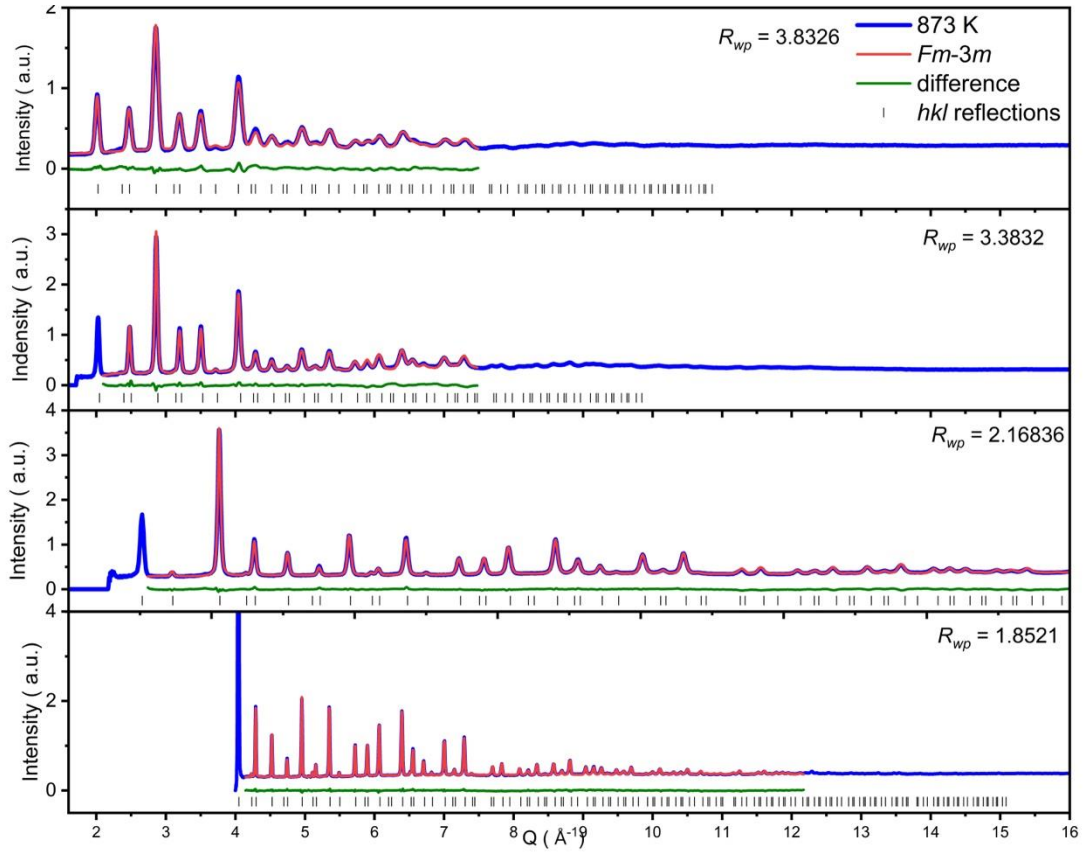

Figure A 3: Neutron powder diffraction data of $BaBiO_3$ collected at the NOMAD beamline at Oak Ridge National Laboratory at 873 K. The blue circles represent the data, the red line is the Rietveld refinement of the data to the cubic $Fm\bar{3}m$ space group, the green line represents the different between the two. The black ticks show the *hkl* reflection allowed by space group.

Neutron Pair Distribution Function – Small Box Modelling

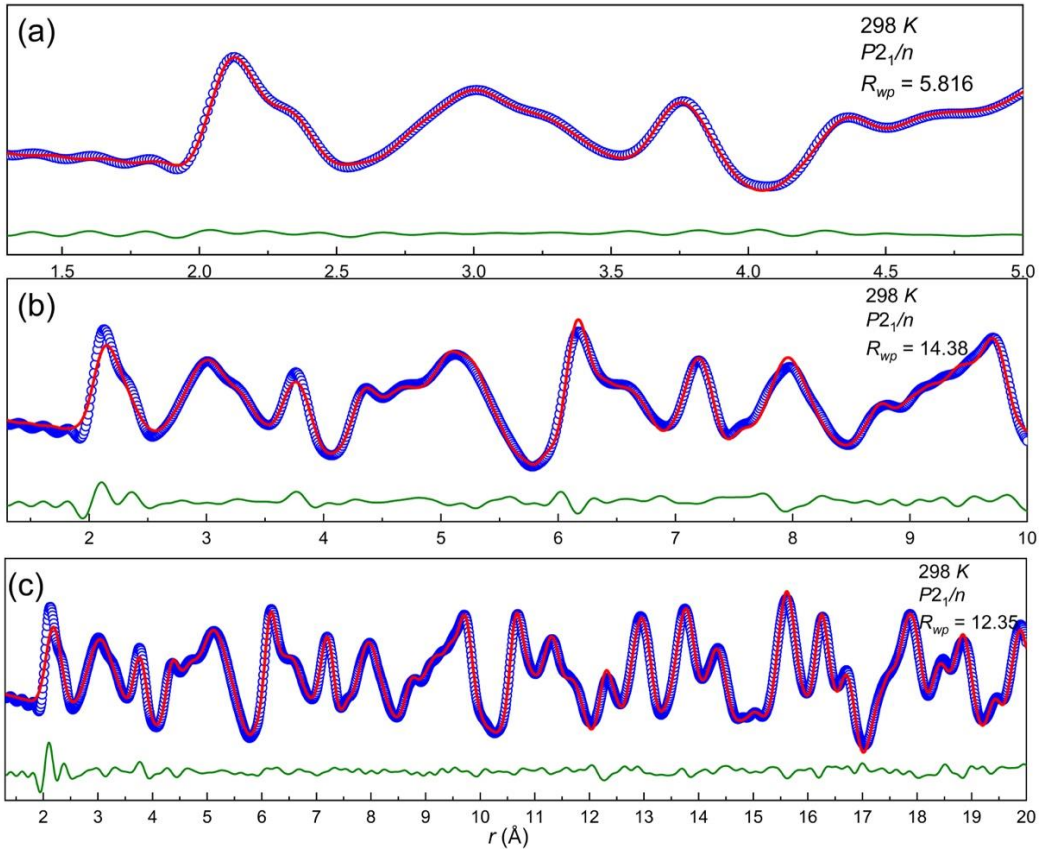

Figure A 4: NPDF data for $BaBiO_3$ at 298 K fitted over a range of (a)1.3 to 5.0 Å, (b) 1.3 to 10 Å and (c)1.3 to 20 Å with space group $P2_1/n$. The blue circles represent the measured data, the red line represents the calculated profile, and the green line shows the difference between the two.

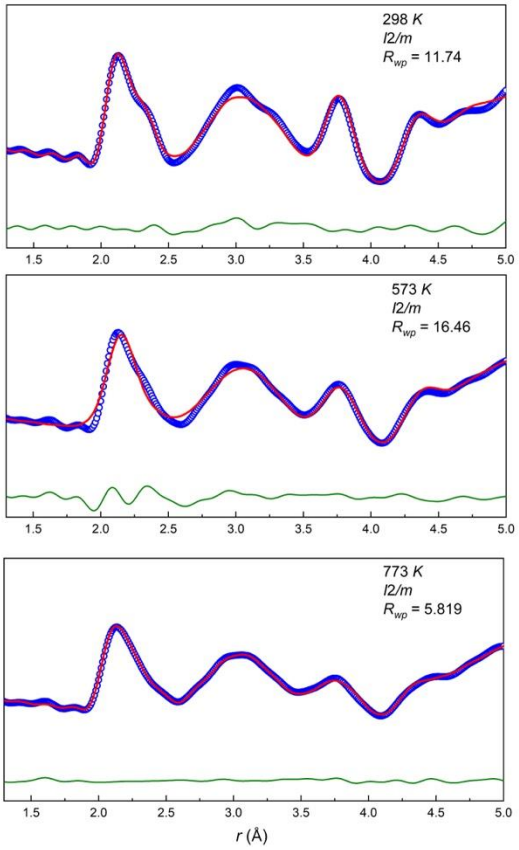

Figure A 5: NPDF data for $BaBiO_3$ at (a)298 K, (b) 573 K and (c) 773 K fitted over a range of 1.3 to 5.0 Å with space group *I*2/*m*. The blue circles represent the measured data, the red line represents the calculated profile, and the green line shows the difference between the two.

Chapter 4 $BaBi_{0.7}Pb_{0.3}O_3$

X-ray Powder Diffraction – STOE @ Sydney Analytical

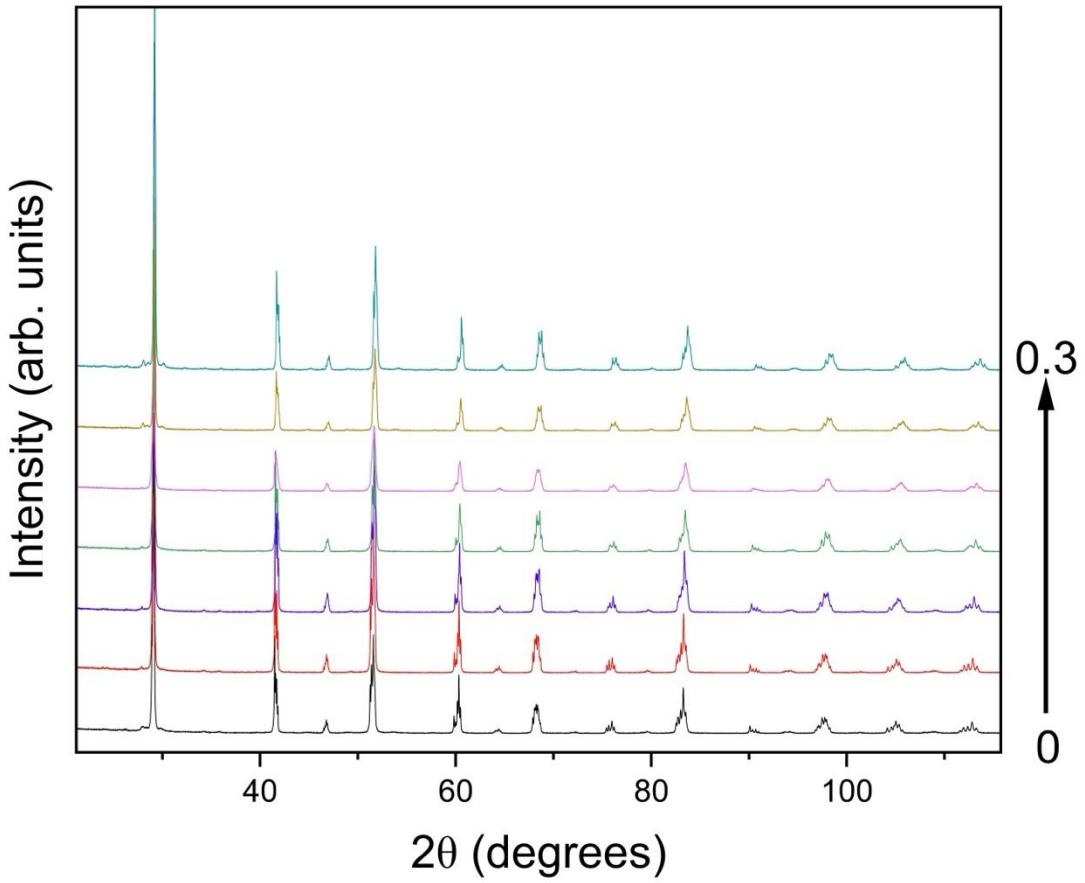

Figure A 6: X-ray diffraction on $BaBi_{(1-x)}Pb_xO_3$ ($0 \leq x \leq 0.3$) composition series collected on a STOE Stadi P monochromatic molybdenum source diffractometer.

Neutron Pair Distribution Function – Small Box Modelling

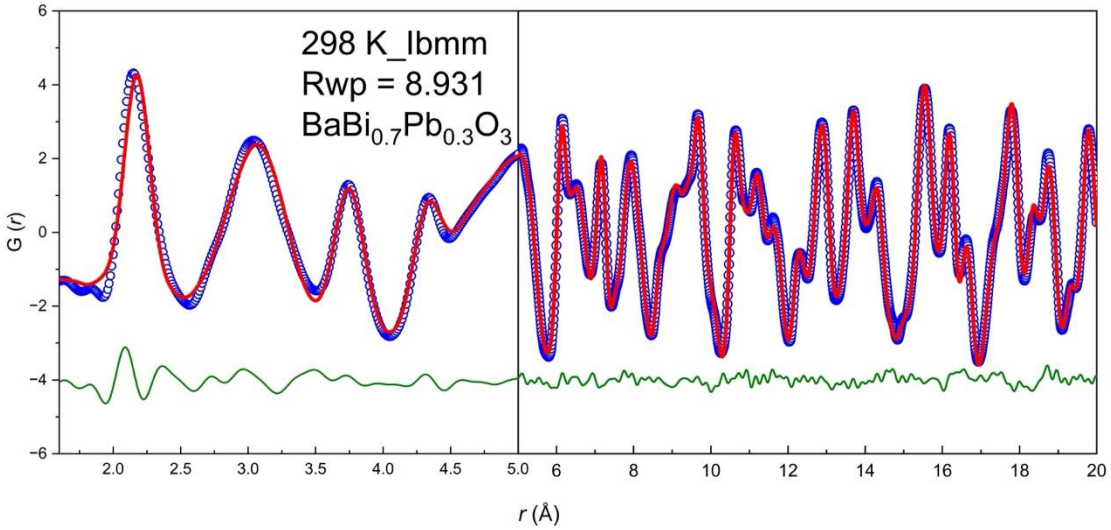

Figure A 7: Neutron pair distribution function data fit for $BaBi_{0.7}Pb_{0.3}O_3$ from 1.6-20 Å assuming the long-range structural model with single orthorhombic *Ibmm* space group at 298 K. The blue circles represent the normalized data, the red line represents the calculated data, and the green line indicates the difference between these.

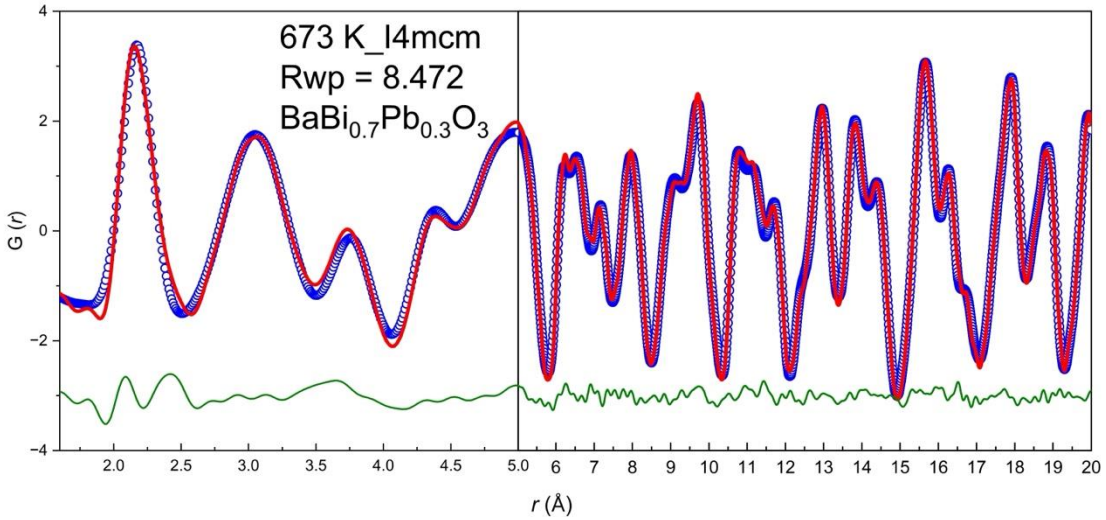

Figure A 8: Neutron pair distribution function data fit for $BaBi_{0.7}Pb_{0.3}O_3$ from 1.6-20 Å assuming the long-range structural model with tetragonal *I*4/*mcm* space group at 673 K. The

blue circles represent the normalized data, the red line represents the calculated data, and the green line indicates the difference between these.

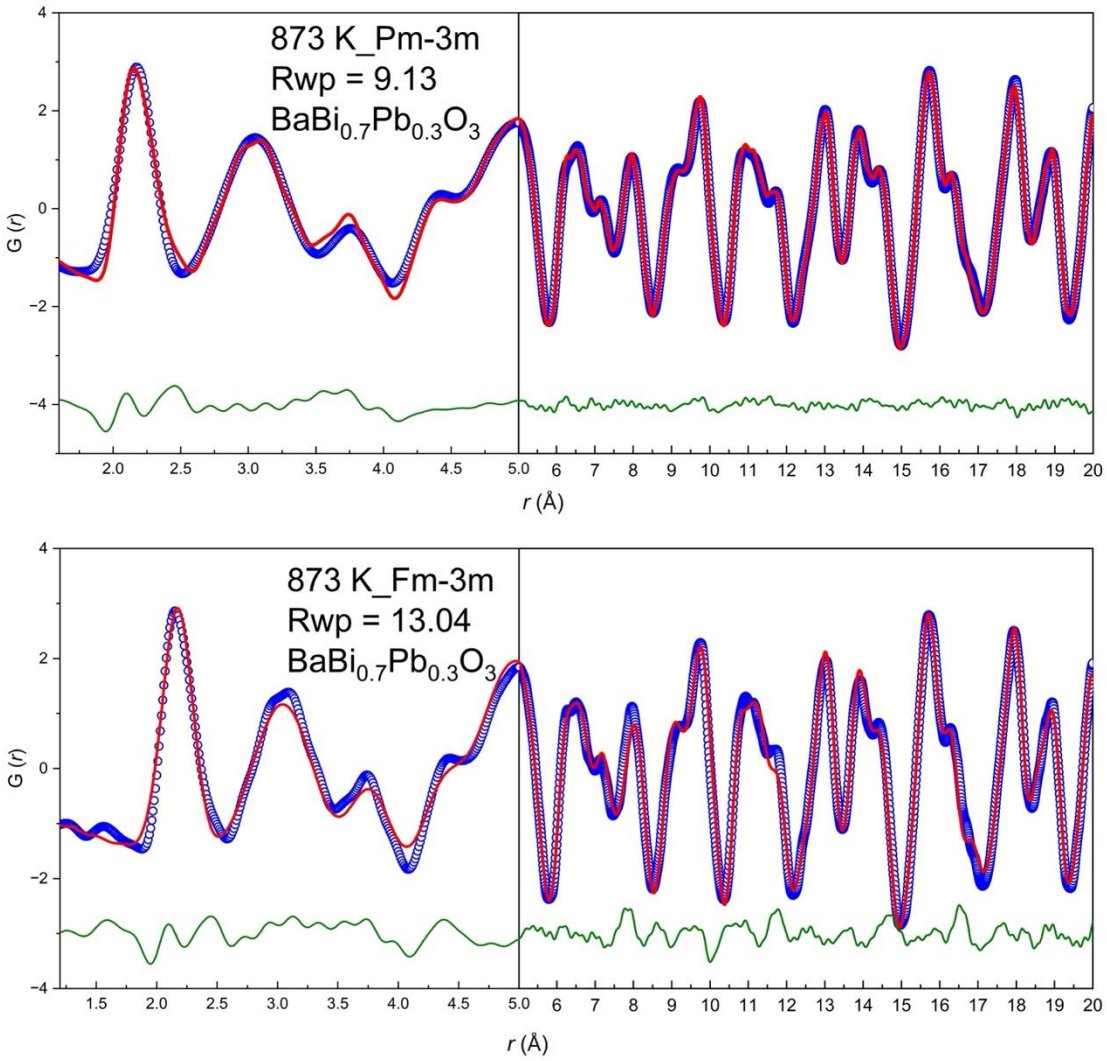

Figure A 9: Neutron pair distribution function data fit for $BaBi_{0.7}Pb_{0.3}O_3$ from 1.6-20 Å assuming the long-range structural model with cubic $Pm\bar{3}m$ (top panel) and $Fm\bar{3}m$ (bottom panel) space group at 873 K. The blue circles represent the normalized data, the red line represents the calculated data, and the green line indicates the difference between these.

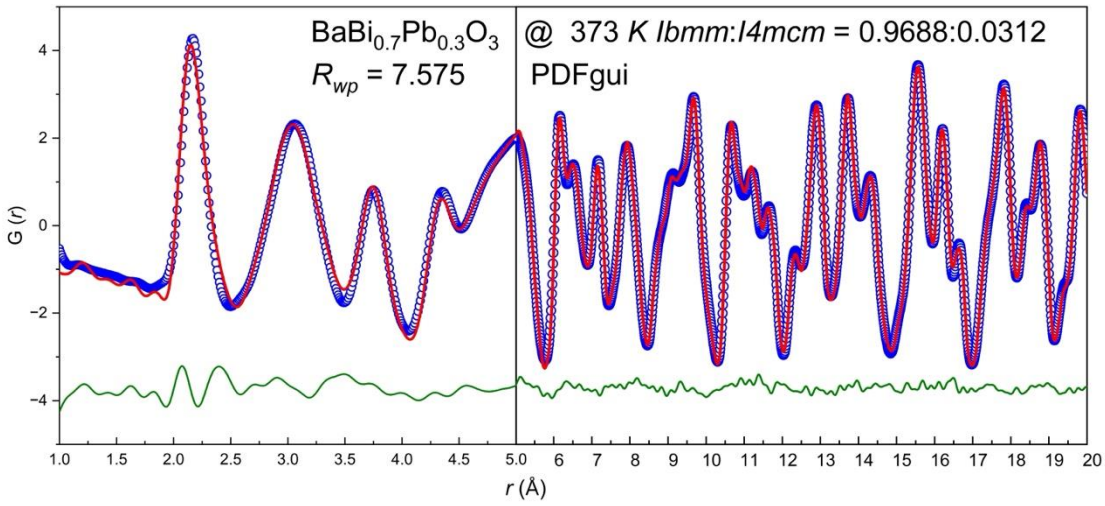

Figure A 10: Neutron pair distribution function data fit for $BaBi_{0.7}Pb_{0.3}O_3$ from 1.6-20 Å assuming the long-range structural model with two-phase orthorhombic *Ibmm* and tetragonal *I*4/*mcm* space group at 373 K. The blue circles represent the normalized data, the red line represents the calculated data, and the green line indicates the difference between these. Data is generated through PDFgui.

Neutron Pair Distribution Function – Big Box Modelling

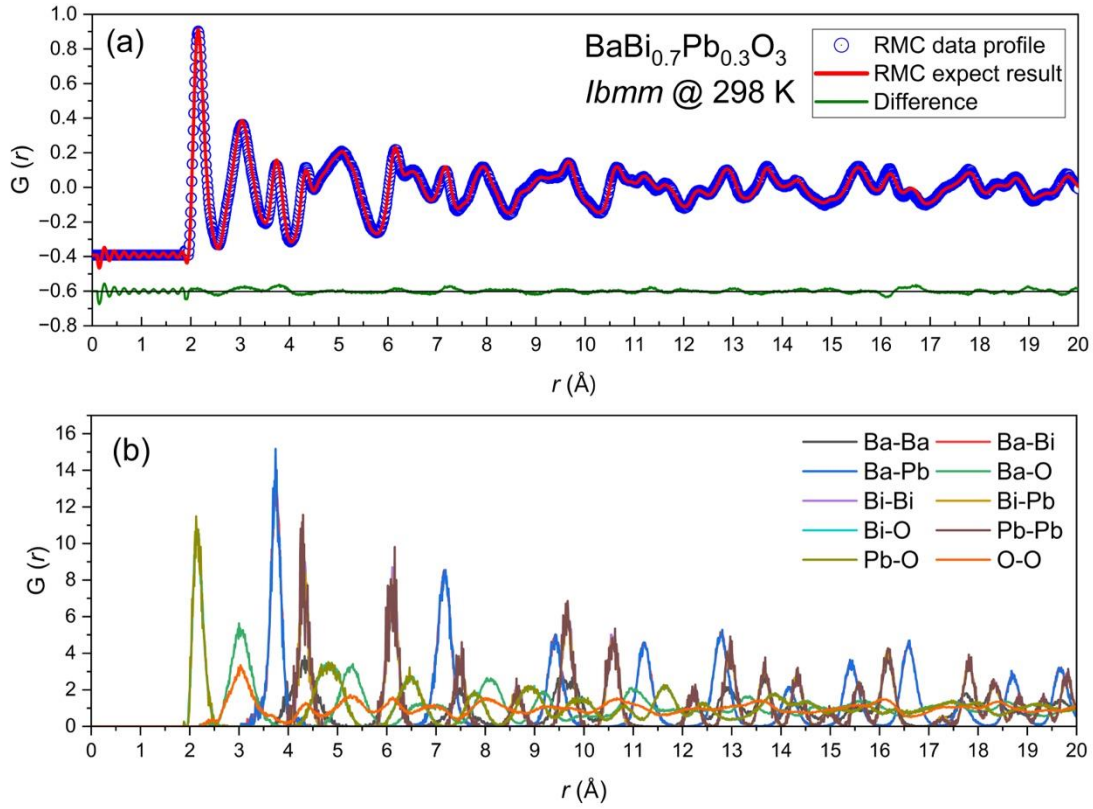

Figure A 11: Neutron pair distribution function data of $BaBi_{0.7}Pb_{0.3}O_3$ at 298 K using the reverse Monte Carlo method. (a) shows the fit to the data, and the (b) show the various atom-atom distances.

Chapter 4 $Ba_{1-x}K_xBiO_3$

$Ba_{1-x}K_xBiO_3$ was originally part of our experimental progress, which differ from $BaBi_{(1-x)}Pb_xO_3$, with K-dope at *A*-site. Traditionally synthesis method applied KO_2, an explosive substance, as potassium contain reagent. Our experiment wants to reduce the risk with replacing alternative low-risk potassium-containing compounds like K_2CO_3. However, even using a solid-state method in a rich-oxygen environment, the *x* ratio in $Ba_{1-x}K_xBiO_3$ is less than 0.05, the measurement result shows below:

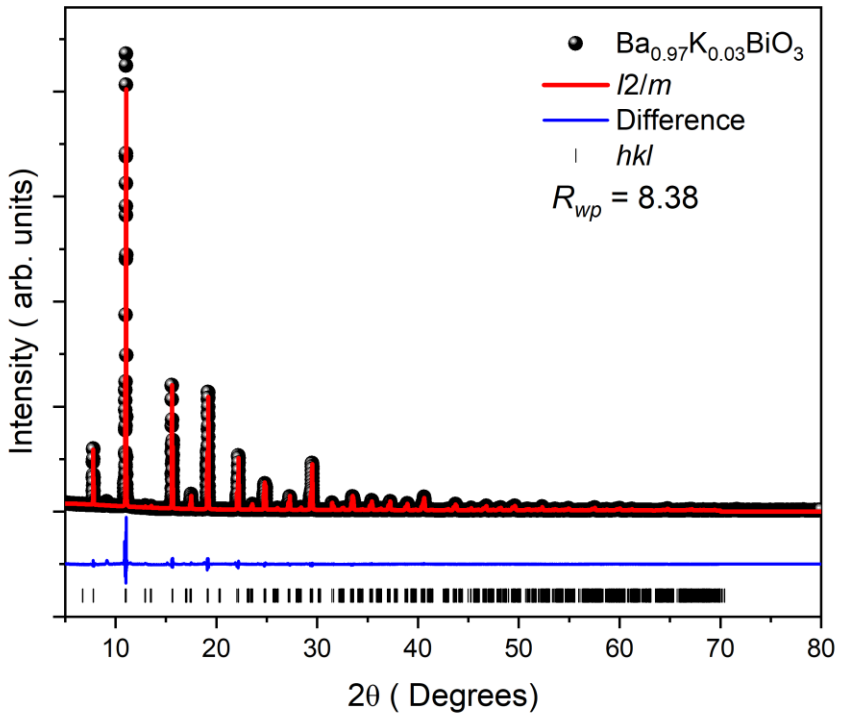

Figure A 12: Rietveld refinement profiles of SXRD data collected for $Ba_{0.97}K_{0.03}BiO_3$ with wavelength 0.561545 Å. Black crosses represent the observed data; red lines indicate the calculated pattern, and the difference plot is shown in blue. Black vertical tick marks show the positions of the space group allowed *hkl* reflections.

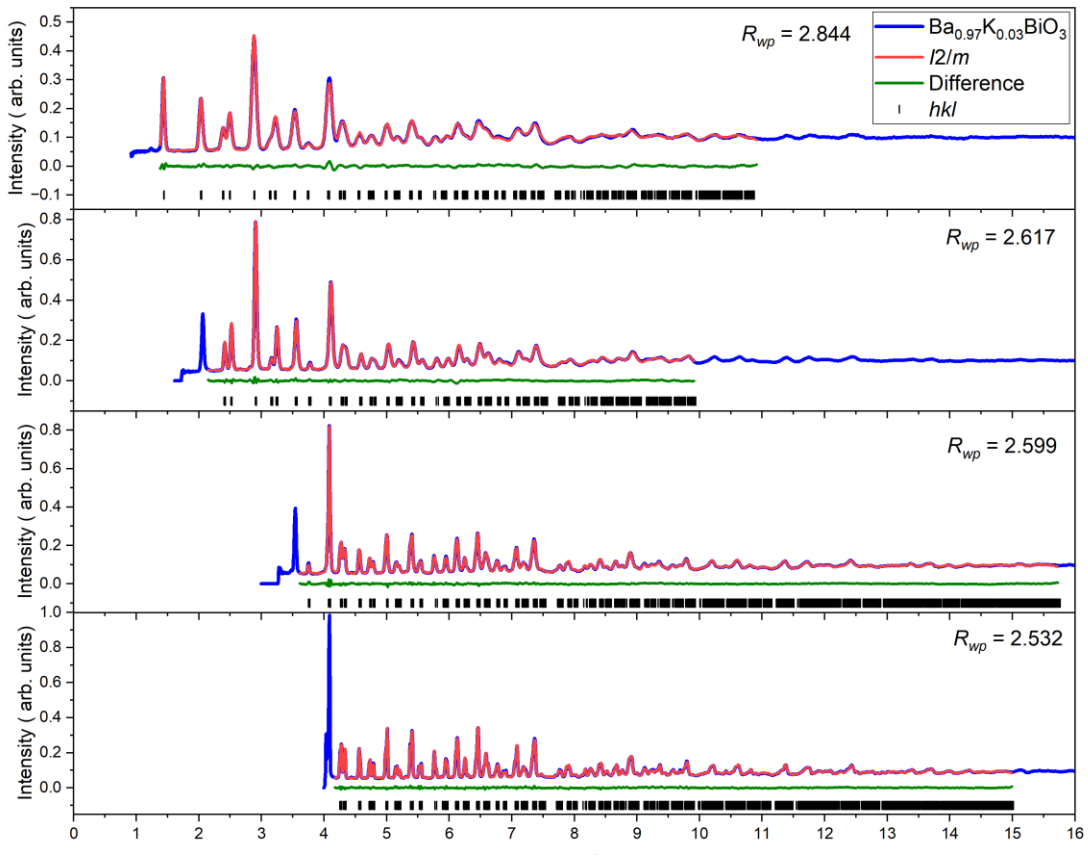

Figure A 13: Neutron powder diffraction data of $Ba_{0.97}K_{0.03}BiO_3$ collected at the NOMAD beamline at Oak Ridge National Laboratory at 298 K. The blue circles represent the data, the red line is the Rietveld refinement of the data to the monoclinic *I*2/*m* space group, the green line represents the different between the two. The black ticks show the *hkl* reflection allowed by space group.

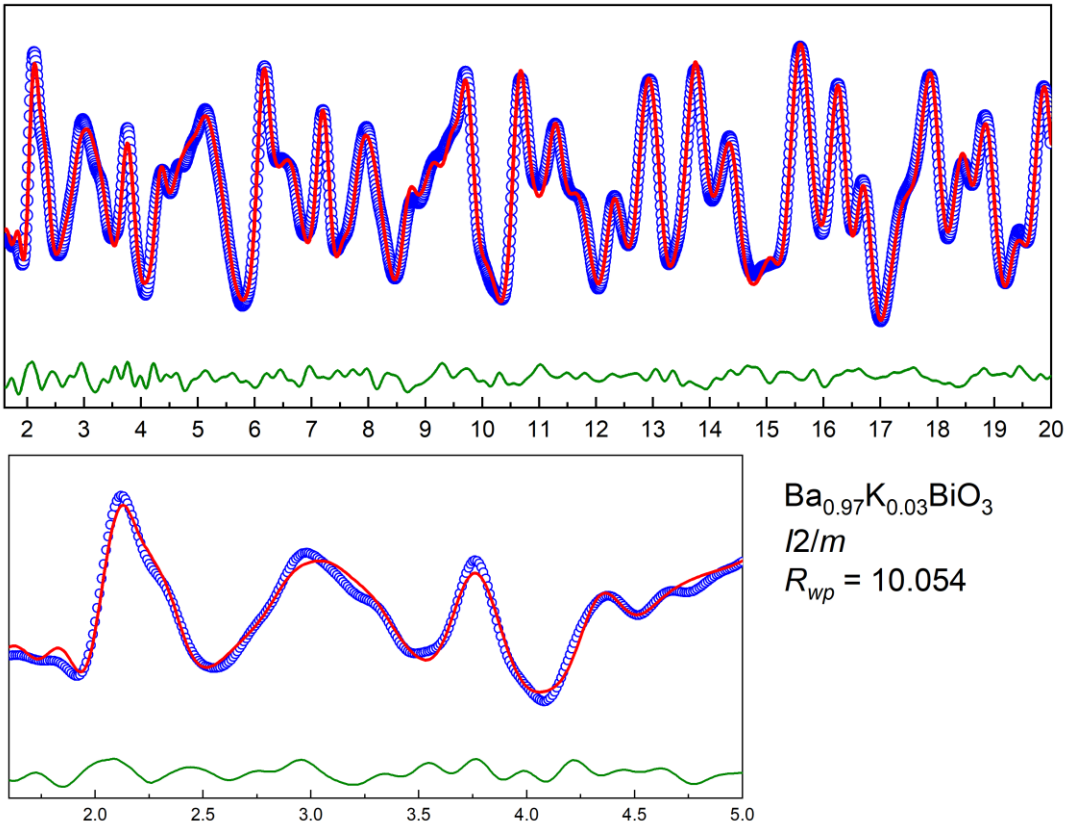

Figure A 14: Neutron pair distribution function data fit for $Ba_{0.97}K_{0.03}BiO_3$ from 1.6-20 Å assuming the long-range structural model with monoclinic *I*2/*m* space group at 298 K. The bottom panel zoom in the local scale distortion with a range over 1.3 – 5.0 Å. The blue circles represent the normalized data, the red line represents the calculated data, and the green line indicates the difference between these. Data is generated through PDFgui.